NATIONAL AERONAUTICS AND SPACE ADMINISTRATION

Technical Report 32-1526

Volume XIII

The Deep Space Network

Progress Report

For November and December 1972

JET PROPULSION LABORATORY
CALIFORNIA INSTITUTE OF TECHNOLOGY
PASADENA, CALIFORNIA

February 15, 1973

NATIONAL AERONAUTICS AND SPACE ADMINISTRATION

Technical Report 32-1526

Volume XIII

The Deep Space Network

Progress Report
For November and December 1972

JET PROPULSION LABORATORY

CALIFORNIA INSTITUTE OF TECHNOLOGY

PASADENA, CALIFORNIA

February 15, 1973

Preface

This report presents DSN progress in flight project support, TDA research and technology, network engineering, hardware and software implementation, and operations. Each issue presents material in some, but not all, of the following categories in the order indicated:

Description of the DSN

Mission Support
- Interplanetary Flight Projects
- Planetary Flight Projects
- Manned Space Flight Projects
- Advanced Flight Projects

Radio Science

Supporting Research and Technology
- Tracking and Ground-Based Navigation
- Communications, Spacecraft/Ground
- Station Control and Operations Technology
- Network Control and Data Processing

Network Engineering and Implementation
- Network Control System
- Ground Communications
- Deep Space Stations

Operations and Facilities
- Network Operations
- Network Control System Operations
- Ground Communications
- Deep Space Stations
- Facility Engineering

In each issue, the part entitled "Description of the DSN" describes the functions and facilities of the DSN and may report the current configuration of one of the five DSN systems (Tracking, Telemetry, Command, Monitor and Control, and Test and Training).

The work described in this report series is either performed or managed by the Tracking and Data Acquisition organization of JPL for NASA.

Contents

DESCRIPTION OF THE DSN

MISSION SUPPORT

Interplanetary Flight Projects

Planetary Flight Projects

RADIO SCIENCE

SUPPORTING RESEARCH AND TECHNOLOGY

Tracking and Ground-Based Navigation

Contents (contd)

Communications, Spacecraft/Ground

Station Control and Operations Technology

Contents (contd)

Contents (contd)

OPERATIONS AND FACILITIES

Network Operations

Network Control System Operations

DSN Functions and Facilities

N. A. Renzetti
Mission Support Office

The objectives, functions, and organization of the Deep Space Network are summarized. The Deep Space Instrumentation Facility, the Ground Communications Facility, and the Network Control System are described.

The Deep Space Network (DSN), established by the National Aeronautics and Space Administration (NASA) Office of Tracking and Data Acquisition under the system management and technical direction of the Jet Propulsion Laboratory (JPL), is designed for two-way communications with unmanned spacecraft traveling approximately 16,000 km (10,000 mi) from Earth to planetary distances. It supports or has supported, the following NASA deep space exploration projects: Ranger, Surveyor, Mariner Venus 1962, Mariner Mars 1964, Mariner Venus 67, Mariner Mars 1969, Mariner Mars 1971, Mariner Venus–Mercury 1973 (JPL); Lunar Orbiter and Viking (Langley Research Center); Pioneer (Ames Research Center); Helios (West Germany); and Apollo (Manned Spacecraft Center), to supplement the Spaceflight Tracking and Data Network (STDN).

The Deep Space Network is one of two NASA networks. The other, STDN, is under the system management and technical direction of the Goddard Space Flight Center. Its function is to support manned and unmanned Earth-orbiting and lunar scientific and communications satellites. Although the DSN was concerned with unmanned lunar spacecraft in its early years, its primary objective now and into the future is to continue its support of planetary and interplanetary flight projects.

A development objective has been to keep the network capability at the state of the art of telecommunications and data handling and to support as many flight projects as possible with a minimum of mission-dependent hardware and software. The DSN provides direct support of each flight project through that project's tracking and

data system. This management element is responsible for the design and operation of the hardware and software in the DSN which are required for the conduct of flight operations.

Beginning in FY 1973 a modified DSN interface has been established with the flight projects. In lieu of the SFOF, a multimission Mission Control and Computing Center (MCCC) has been activated as a separate functional and management element within JPL. This function, as negotiated with each flight project, will provide all computing and mission operations support for missions controlled from JPL. DSN computing support will be provided separately by the DSN. Radio metric, telemetry, and command data interfaces with the DSN are a joint DSN, MCCC, and flight project responsibility. The organization and procedures necessary to carry out these new activities will be reported in this document in the near future.

The DSN function, in supporting a flight project by tracking the spacecraft, is characterized by five network systems:

(1) DSN Tracking System. Generates radio metric data; i.e., angles, one- and two-way doppler and range, and transmits raw data to mission control.

(2) DSN Telemetry System. Receives, decodes, records, and retransmits engineering and scientific data generated in the spacecraft to Mission Control.

(3) DSN Command System. Accepts coded signals from mission control via the GCF and transmits them to the spacecraft in order to initiate spacecraft functions in flight.

(4) DSN Monitor and Control System. Instruments, transmits, records, and displays those parameters of the DSN necessary to verify configuration and validate the network. Provides operational direction and configuration control of the network and primary interface with flight project Mission Control personnel.

(5) DSN Test and Training System. Generates and controls simulated data to support development, test, training and fault isolation within the DSN. Participates in mission simulation with flight projects.

The facilities needed to carry out these functions have evolved in three technical areas: (1) the Deep Space Stations (DSSs) and the telecommunications interface through the RF link with the spacecraft is known as the Deep Space Instrumentation Facility (DSIF); (2) the Earth-based point-to-point voice and data communications from the stations to Mission Control is known as the Ground Communications Facility (GCF); (3) the network monitor and control function is known as the Network Control System (NCS).

I. Deep Space Instrumentation Facility

A. Tracking and Data Acquisition Facilities

A world-wide set of Deep Space Stations with large antennas, low-noise phase-lock receiving systems, and high-power transmitters provide radio communications with spacecraft. The DSSs and the deep space communications complexes (DSCCs) they comprise are given in Table 1.

Radio contact with a spacecraft usually begins when the spacecraft is on the launch vehicle at Cape Kennedy, and it is maintained throughout the mission. The early part of the trajectory is covered by selected network stations of the Air Force Eastern Test Range (AFETR) and the STDN of the Goddard Space Flight Center.[1] Normally, two-way communications are established between the spacecraft and the DSN within 30 min after the spacecraft has been injected into lunar, planetary, or interplanetary flight. A compatibility test station at Cape Kennedy (discussed later) tests and monitors the spacecraft continuously during the launch checkout phase. The deep space phase begins with acquisition by 26-m DSSs. These and the remaining DSSs listed in Table 1 provide radio communications until the end of the mission.

To enable continuous radio contact with spacecraft, the DSSs are located approximately 120 deg apart in longitude; thus a spacecraft in deep space flight is always within the field-of-view of at least one DSS, and for several hours each day may be seen by two DSSs. Furthermore, since most spacecraft on deep space missions travel within 30 deg of the equatorial plane, the DSSs are located within latitudes of 45 deg north and south of the equator. All DSSs operate at S-band frequencies: 2110-2120 MHz for Earth-to-spacecraft transmission and 2290-2300 MHz for spacecraft-to-Earth transmission. An X-band capability is being readied for future missions beginning in 1973.

[1]The 9-m (30-ft) diam antenna station established by the DSN on Ascension Island during 1965 to act in conjunction with the STDN orbital support 9-m (30-ft) diam antenna station was transferred to the STDN in July 1968.

To provide sufficient tracking capability to enable returns of useful data from around the planets and from the edge of the solar system, a 64-m (210-ft) diam antenna subnet will be required. Two additional 64-m (210-ft) diam antenna DSSs are under construction at Madrid and Canberra and will operate in conjunction with DSS 14 to provide this capability. These stations are scheduled to be operational by the middle of 1973.

B. Compatibility Test Facilities

In 1959, a mobile L-band compatibility test station was established at Cape Kennedy to verify flight-spacecraft/DSN compatibility prior to the launch of the Ranger and Mariner Venus 1962 spacecraft. Experience revealed the need for a permanent facility at Cape Kennedy for this function. An S-band compatibility test station with a 1.2-m (4-ft) diameter antenna became operational in 1965. In addition to supporting the preflight compatibility tests, this station monitors the spacecraft continuously during the launch phase until it passes over the local horizon.

Spacecraft telecommunications compatibility in the design and prototype development phases was formerly verified by tests at the Goldstone DSCC. To provide a more economical means for conducting such work and because of the increasing use of multiple-mission telemetry and command equipment by the DSN, a Compatibility Test Area (CTA) was established at JPL in 1968. In all essential characteristics, the configuration of this facility is identical to that of the 26-m (85-ft) and 64-m (210-ft) diameter antenna stations.

The JPL CTA is used during spacecraft system tests to establish the compatibility with the DSN of the proof test model and development models of spacecraft, and the Cape Kennedy compatibility test station is used for final flight spacecraft compatibility validation testing prior to launch.

II. Ground Communications Facility

The GCF provides voice, high-speed data, wideband data, and teletype communications between the Mission Operations Center and the DSSs. In providing these capabilities, the GCF uses the facilities of the worldwide NASA Communications Network (NASCOM)[2] for all long distance circuits, except those between the Mission Operations Center and the Goldstone DSCC. Communications between the Goldstone DSCC and the Mission Operations Center are provided by a microwave link directly leased by the DSN from a common carrier.

Early missions were supported by voice and teletype circuits only, but increased data rates necessitated the use of high-speed and wideband circuits for DSSs. Data are transmitted to flight projects via the GCF using standard GCF/NASCOM formats. The DSN also supports remote mission operations centers using the GCF/NASCOM interface.

III. Network Control System

The DSN Network Control System is comprised of hardware, software, and operations personnel to provide centralized, real-time control of the DSN and to monitor and validate the network performance. These functions are provided during all phases of DSN support to flight projects. The Network Operations Control Area is located in JPL Building 230, adjacent to the local Mission Operations Center. The NCS, in accomplishing the monitor and control function does not alter, delay, or serially process any inbound or outbound data between the flight project and tracking stations. Hence NCS outages do not have a direct impact on flight project support. Voice communications are maintained for operations control and coordination between the DSN and flight projects, and for minimization of the response time in locating and correcting system failures.

The NCS function will ultimately be performed in data processing equipment separate from flight project data processing and specifically dedicated to the NCS function. During FY 1973, however, DSN operations control and monitor data will be processed in the JPL 360/75 and in the 1108. In FY 1974 the NCS data processing function will be partly phased over to an interim NCS processor, and finally, in FY 1975, the dedicated NCS data processing capability will be operational. The final Network Data Processing Area will be located remote from the Network Operations Control Area so as to provide a contingency operating location to minimize single point of failure effects on the network control function. A preliminary description of the NCS appears elsewhere in this document.

[2]Managed and directed by the Goddard Space Flight Center.

Table 1. Tracking and data acquisition stations of the DSN

DSCC	Location	DSS	DSS serial designation	Antenna		Year of initial operation
				Diameter, m (ft)	Type of mounting	
Goldstone	California	Pioneer	11	26(85)	Polar	1958
		Echo	12	26(85)	Polar	1962
		(Venus)[a]	13	26(85)	Az-El	1962
		Mars	14	64(210)	Az-El	1966
—	Australia	Woomera	41	26(85)	Polar	1960
Tidbinbilla	Australia	Weemala (formerly Tidbinbilla)	42	26(85)	Polar	1965
		Ballima (formerly Booroomba)	43	64(210)	Az-El	Under construction
—	South Africa	Johannesburg	51	26(85)	Polar	1961
Madrid	Spain	Robledo	61	26(85)	Polar	1965
		Cebreros	62	26(85)	Polar	1967
		Robledo	63	64(210)	Az-El	Under construction

[a]A research-and-development facility used to demonstrate the feasibility of new equipment and methods to be integrated into the operational network. Besides the 26-m (85-ft) diam Az-El mounted antenna, DSS 13 has a 9-m (30-ft) diam Az-El mounted antenna that is used for interstation time correlation using lunar reflection techniques, for testing the design of new equipment, and for support of ground-based radio science.

DSN Tracking System: Conversion to High-Speed Radio Metric Data

W. D. Chaney and H. E. Nance
DSN Systems Engineering

At the present time, radio metric data are transmitted from the Deep Space Stations via the teletype mode. To meet future requirements, and to update the transmission mode, the operational concept is scheduled to be changed to utilize the high-speed data transmission facilities. This article outlines the implementation schedule and the testing requirements to provide this new capability.

I. Introduction

The transmission of radio metric data from the Deep Space Stations (DSSs) will be changed from the teletype mode to high-speed mode for first use in support of the Mariner Venus/Mercury 1973 Project to meet the requirement of providing 10/s doppler sampling at all stations and dual S/X-band doppler counting at DSS 14. This change involves certain hardware changes, as well as the supporting software packages. The radio metric data will be formatted for high-speed data (HSD) transmission by the station Digital Instrumentation Subsystem (DIS) equipment and transmitted via normal Ground Communications Facility (GCF) HSD circuits.

II. Station Configuration

The present Deep Space Station interface between the Tracking Data Handling (TDH) equipment and the DIS does not provide the required high-rate sampling, the additional doppler count, or the complete status and configuration information. A change to this interface is the first requirement in reconfiguring the stations for the new mode of operation. The necessary Equipment Change Orders (ECOs) have been issued and approved for installation. The implementation of the ECOs will be coordinated with other station changes for the 26-m DSSs and will be included as initial configuration for the new 64-m stations in Australia and Spain (DSS 43 and DSS 63).

III. Configuration Change Schedule

The present schedule for the TDH modification for the station DIS interface calls for the initial implementation at DSS 14. This installation started in the latter part of November 1972 with a tentative completion date of mid-December. Testing will then be conducted at the station to ensure satisfactory operation and make-up of the installation instruction kit. When DSS 14 has demonstrated acceptable operational capability, the instruction kits will

be shipped to the other stations. It is anticipated that the shipment will be made during mid-January 1973, with completion of the installation at all stations by the first of March 1973.

IV. High-Speed Data Interface Testing

Interim testing of the software and hardware will commence shortly after the completion of the installation at DSS 14. The interim testing will be used to allow the programmers for the DSS and the Mission Control and Computing Center (MCCC) to debug the software packages being implemented. This testing is scheduled for the period of December 1972 through mid-February 1973. The initial testing will be limited as to decoding the data block at the MCCC, as the software for this function will not be integrated into the operational software before February 1973. Station hardware and software integration, as well as Deep Space Station testing and acceptance, will take place between the first of April and mid-June 1973. This activity will allow limited interface testing of the capability on a non-interference basis.

V. DSN Combined System Testing

The DSN Combined System Testing for operational acceptance will be initiated in mid-June 1973 and be completed, with the capability turned over to operations, by October 1, 1973. Level 1 and Level 2 testing will be conducted as the stations become available and are accepted. A Level 1 test will consist of one DSS, configured as for an actual tracking period, acquiring a spacecraft in one- or three-way mode, generation of radio metric data, transmitting the radio metric data to the MCCC and Network Control System (NCS) via GCF high-speed data line, and the processing of the data by MCCC and NCS, all in real time. Various sample rates will be used, from 10/s to 1/60 s. Predicts will be generated by the MCCC and transmitted to the station via High-Speed Data Line (HSDL) and used in the Antenna Pointing System (APS) to drive the antenna. Simultaneous telemetry and monitor and operations control data will be transmitted via the HSDL to present a loading factor comparable to a cruise mode condition. When conditions allow, the station will operate in a two-way mode with the spacecraft and command traffic introduced into the system. All processing capabilities will be exercised, including writing of a project tape by MCCC to be checked by project programs. Numerous dumps and displays will be checked to ensure that data and parameters are correct according to inputs.

A Level 2 test will consist essentially of a Level 1 test but will be conducted with two or more DSSs simultaneously. If a spacecraft is not in view for any of the stations, simulated radio metric data will be used. The acceptability of the DSS capability will be based on the acceptance criteria established for the function.

VI. High-Speed Radio Metric Data

The primary objective of the high-speed data mode of operation is to provide 10/s, 1/s, and other high-rate sampling for operations in real time. The current teletype mode for 1/s rate rapidly becomes backlogged and, for high activity phases of operation, limits real-time evaluation and use of data. The HSD mode will also remove the last teletype mode from the DSN operational network. Telemetry, command, and monitor have been operating in this mode for some time, and with the inclusion of radio metric data only administrative traffic will continue to be handled by teletype. The teletype capability will be maintained as backup for radio metric data until January 1, 1974.

The data sample rates included in the high-speed data mode will be 10/s and 1/s and 1 per 2, 5, 6, 10, 20, 30, and 60 s. Twenty samples of data will be included in one HSD block for the 10/s sample rate and four samples for other sample rates. The blocks will be transmitted after a HSD block is complete, according to sample rate, so that the transmission rate to line will be dependent on the sampling rate. X-band and S-band data will be included for both range and doppler data. Necessary configuration information is included to provide complete evaluation of each HSD block.

Helios Mission Support

P. S. Goodwin
Mission Support Office

Project Helios is a joint space endeavor between the United States and West Germany. Its objective is to place two unmanned spacecraft into heliocentric orbits whose perihelion distance will come closer to the sun than any previously or presently planned Free-World deep space undertaking. The West German government is designing and fabricating the spacecraft and will conduct mission operations. NASA will provide the launch vehicle, the launch facilities, and the major portion of the tracking and data acquisition with respect to this program. The launch of the first spacecraft is planned for mid-1974 and the second in late 1975.

To ensure proper technical coordination between the activities in West Germany and in the United States, the International Agreement provides for semiannual Helios Joint Working Group Meetings for the exchange of information and for the proper coordination of the activities leading toward launch and subsequent Mission Operations. This article reports the highlights, with respect to the DSN, of the subjects discussed during the Seventh Helios Joint Working Group Meeting which was held at Porz-Wahn (near Bonn), West Germany, October 25 to 31, 1972.

I. Introduction

The International Agreement between the United States of America and the Federal Republic of West Germany, which formally established Project Helios, specified that the two countries should meet on a semiannual basis to coordinate the technical activities associated with their respective responsibilities regarding this project. These sessions, which are known as Helios Joint Working Group (HJWG) Meetings, are organized as shown in Fig. 1 of Ref. 1, and are held alternately between the United States and West Germany. The seventh such meeting was conducted in Porz-Wahn (near the capitol city Bonn), West Germany, October 25–31, 1972. The previous article in this series (Ref. 2) depicted the significant DSN activities leading to the 7th HJWG Meeting. This article treats the Tracking and Data System highlights that occurred during the 7th HJWG Meeting. Further details of these (as well as other) activities may be found in the official minutes (Ref. 3).

II. TDS Highlights of the 7th HJWG Meeting

At the time of the 7th HJWG Meeting, the Helios Project was approximately 20 months away from its scheduled launch date for the first flight spacecraft. The fundamental design of the spacecraft had been completed and an engineering model of the spacecraft and its associated ground support equipment had been constructed and was undergoing extensive testing. Consequently, the discussion emphasis at the 7th HJWG Meeting was shifting from spacecraft-oriented topics to mission design and operations topics. In addition, the scope of the technical discussions had already transcended the conceptual stage and was now focused upon the detailed definition and understanding of the working interfaces between the various elements of the project. Because of these factors, both the quantity and variety of the agenda topics became too numerous to be efficiently handled during the formal five-day meeting period. As a result, a large portion of the list of TDS agenda topics was shifted to Special Splinter Session Meetings—some of which, due to time limitations, had to be scheduled for the days immediately following the concluding General Session of the 7th HJWG Meeting. Further, many of the agenda topics required participation by representatives from more than two of the formally constituted subgroups. However, for convenience of presentation in this article, the topics are grouped under the headings deemed most appropriate to the subject matter.

A. TDS Subgroup Activities

1. *Initial DSN Acquisition.* As a prelude to the discussions (reported below) regarding the possible "blind acquisition" of the Helios spacecraft, it was necessary to thoroughly understand the procedures and techniques associated with a standard or nominal DSN initial acquisition of the Helios spacecraft after launch. In this regard, certain key factors had been established during the proceedings of the 6th HJWG Meeting (Ref. 4), namely, the selected trajectory would have a 926 km (500 nmi) perigee altitude and would be restricted to the southern launch corridor (Ref. 5, p. 26, Fig. 1). The combination of these two factors greatly reduces the angle and doppler tracking rates associated with the DSN initial acquisition to the point that both are now within standard DSN station capabilities. Consequently, the remaining uncertainties were associated with the interferometer region of the spacecraft's low-gain antenna system (Ref. 1), and the dispersion uncertainties in the injection point due to the TE-364-4 last-stage solid-rocket motor burn. The latter had been studied in detail prior to the meeting (Ref. 2) with the result that the estimate for a successful DSN initial acquisition would be greater than 0.9 (90%) in the nominal case. Further, this probability would occur in a time period (measured in minutes) closely following spacecraft rise at the initial acquisition stations, which are DSS 61 in Madrid, Spain and/or DSS 51 in Johannesburg, South Africa.

2. *Review of the Helios Preliminary NASA Support Plan.* As mentioned in the previous article (Ref. 2), the Helios preliminary NASA Support Plan (NSP) was distributed for review and comment in September 1972. During the 7th HJWG Meeting, the Helios Ground and Operations System (HGOS) (Fig. 1 of Ref. 1) reported that their review of the preliminary NSP had disclosed no significant incompatibilities. Their comments pertained either to the clarity of certain portions of the text material or to the desire for additional detail regarding certain planned capabilities in support of Helios. These comments were accepted by the DSN for inclusion in the final NSP. It was mutually agreed that these HGOS comments would not necessitate the issuance of change pages to the preliminary NSP.

3. *Definition of MDR Content and Format.* The definition of the content and format for the various Master Data Records (MDRs) required for the production of the Helios Experimenter Data Records (EDRs) has been an iterative process over the last several Helios Joint Working Group Meetings. During the 7th HJWG Meeting, this process culminated in the selection of a final format for the telemetry MDR and the near-final agreement upon the format for the Command MDR. In addition, considerable progress was made toward definitizing the Orbit MDR. The major remaining effort concerns the attitude MDR, which, in turn, is dependent upon the outcome of on-going discussions regarding the techniques for attitude determination (see "Special Splinter Meeting Topics," *Subsection E*).

4. *German/U.S. Network Operations Interface.* In a Splinter session, Operations representatives from the DSN and the German Network developed a mutually acceptable Helios Network Operations Management Plan which defines the areas of responsibility, the operating interfaces for inter-Network coordination, as well as the scope and responsibility for documenting Network Operations procedures. By mutual agreement between the TDS and the Mission Analysis and Operations (MA&O) Subgroup Chairmen, this Helios Network Operations Management Plan will be included as a section within the HGOS/JPL Interface Management Plan, mentioned in *Section II-C-1.*

B. TDS/Spacecraft Joint Session

As mentioned in the opening remarks to this section, the Helios spacecraft design has completed its development phase and is heavily involved in the testing and performance evaluation phase of the Engineering Model spacecraft. However, this does not imply a cessation of design effort, but rather it implies that future design effort would be directed toward either overcoming design deficiencies or making significant contributions toward meeting mission objectives. In either event, proposed design changes must be weighed very carefully against their impact upon both schedule and cost limitations. The latter, in effect, creates an atmosphere wherein only the most critical proposed design changes receive project approval. This reality permeated the following discussions:

1. Telecommunications Link Analysis. In September 1972, the Helios Project Office issued an update to their Telecommunications Link Design Document. In the time available prior to the 7th HJWG Meeting, the DSN carefully reviewed each link analysis covering the multitude of operating modes permitted by the Helios spacecraft radio system. By necessity, this review concentrated upon the validation of the various DSN performance parameters assumed in the link calculations, with secondary emphasis being placed upon the techniques and/or assumptions used in conjunction with the spacecraft parameters. During the 7th HJWG Meeting, the DSN reported that its review of the Helios Telecommunications Link Design had *not* disclosed any errors in computation nor any serious errors of omission regarding unidentified losses within the link. It was noted, however, that the September 1972 revision still contained certain assumptions—i.e., design or specification values were employed for those spacecraft parameters for which actual test data are not yet available. This situation is significant because several of the Helios telecommunications links have experienced an erosion of performance margin to the point where any further decrease in performance can begin to jeopardize the accomplishment of mission objectives as they relate to obtaining useable data over those links.

2. DSN Telemetry Performance for Helios. Related to the foregoing activity are the parameters assumed for the performance of the DSN Telemetry System while sequentially decoding the Helios convolutionally encoded telemetry. Since the Data Decoder Assembly (DDA) to be used in support of Helios is still under development by the DSN, it has been necessary to estimate its future performance. The estimates employed in the September 1972 issue of the Helios Telecommunications Link Design were based upon approximately one month of post-launch data obtained from the Pioneer 10 spacecraft, which also uses convolutionally encoded telemetry. However, the Pioneer 10 telemetry frame length is much shorter than the 1152 bits/frame employed for Helios. Therefore, to further refine the estimate of DSN Telemetry System performance for Helios, the DSN performed a computer simulation based upon the Pioneer 10 telemetry performance data but converted to the Helios frame length. This computer simulation was compared to theoretical analyses performed by both JPL and the Helios DFVLR[1] facility. The result was an updated performance estimate for Helios (see Fig. 1) which was presented during the 7th HJWG Meeting. Further updates to this estimate are anticipated as DSN telemetry performance test data become available.

3. Solar Occultation (Blackout). As noted in Ref. 5, p. 28, the Helios trajectory is such that the spacecraft is occulted by the sun several times. These occultations create a radio signal "blackout." The blackout region or angle as viewed from Earth is larger than that dictated by the physical size of the sun, because the solar corona distorts the radio signal in such a manner as to make it more difficult to receive. In addition, the temperature of the sun causes an increase in radio system noise as an antenna looks closer and closer towards the sun. The combination of these two effects increases both the apparent blackout angle and the amount of time the spacecraft must endure without communications from Earth. Because of the latter, it is highly desirable to be able to accurately predict this blackout angle. Unfortunately, this presents a difficult problem since both of the aforementioned effects are dependent upon the level of solar activity which can vary from day to day as well as year to year. Nonetheless, some data are available from near-solar occultations by Pioneer and Mariner spacecraft, and these data have been provided to the Helios Project. During the 7th HJWG Meeting, it was decided that the Helios Project would use these data to develop an assumed model for the telecommunications link performance vs angle from the sun, and that a special meeting would be held at JPL in December 1972 to review and critique this Project-developed model.

---

[1]Deutsche Forschungs und Versuchsanstalt fuer Luft-Und Raumfahrt (German Research and Experimental Institution for Aerospace) at Oberpfaffenhofen, West Germany.

4. Helios/DSN Compatibility Test Plan and Schedule. The DSN/Helios Spacecraft Compatibility Test Plan and Schedule has been discussed from various aspects in previous articles (Refs. 6 to 12). The original plan/schedule as shown in Fig. 3 of Ref. 6 has remained valid in concept even though specific dates and locations have changed slightly from those forecast. The Engineering Model (EM) compatibility tests were conducted in April of 1972 as originally scheduled; however, the test location was transferred from the Compatibility Test Area at JPL, Pasadena (CTA 21) to DSS 71 at Cape Kennedy, Florida. The Test Plan and the Test Results of the EM compatibility test effort are described in Refs. 9, 10, 11, and 12. The prototype compatibility tests are still planned to be conducted at CTA 21; however, the dates have changed from October–November 1973 to February–March 1974. Under the new schedule, compatibility tests with the German Network will be conducted in Germany prior to the shipment of the Prototype to JPL for thermal vacuum chamber and CTA 21 tests, with subsequent reshipment of the Prototype back to Cape Kennedy (as opposed to Germany) where the Prototype can act as a backup to the Flight Spacecraft. The plans for the Flight Model Spacecraft (F-1) remain unchanged from those depicted in Fig. 3 of Ref. 6.

5. Spacecraft Compatibility Test Tapes. As noted in Ref. 10, the EM compatibility tests did not include the spacecraft data-handling equipment portion of the spacecraft radio system. This fact, together with the now delayed arrival of the Prototype Spacecraft, places the first opportunity for Spacecraft/Ground Data System (GDS) compatibility and data-flow testing only four months prior to scheduled launch. Should a serious incompatibility be discovered at this late date prior to launch, the launch schedule could be jeopardized. To reduce the impact of such a possibility, it was decided during the 7th HJWG Meeting to utilize spacecraft Test Tapes obtained during spacecraft checkout with its Ground Support Equipment in Germany in order to replay actual recorded spacecraft telemetry data through the DSN, etc., prior to the arrival of the Prototype for CTA 21 compatibility testing. While it is recognized that such Test Tapes have limitations (i.e., they are not command-responsive, the data are corrupted by tape recorder wow and flutter, etc.), they do permit a significant amount of testing within the Ground Data System in preparation for the Prototype compatibility tests. Consequently such Test Tapes serve as a stepping-stone toward the final demonstration of Ground Data System compatibility/readiness. A preliminary study regarding the possible use of such tapes indicated that compatible playback tape machines were available at JPL; therefore, the DSN accepted an action item to define the tape format and content needed by the DSN in order to accomplish the intended use for these spacecraft Test Tapes.

C. TDS/Mission Analysis and Operations Joint Session

As mentioned above, the Helios Joint Working Group emphasis had shifted by the time of the seventh meeting from Spacecraft Design to the Flight Mission Design. This does not imply that a considerable amount of mission planning had not been accomplished prior to the seventh meeting; it was merely the total emphasis that had shifted. For example, a considerable portion of the Mission Analysis and Operations (MA&O) agenda topics—particularly those with other Subgroups—concerned the detailed, step-by-step operational procedures that would be used during the execution of the mission. The TDS contributed to this effort in two ways: first, the TDS has a representative as a permanent member of the MA&O Subgroup; and second, the TDS Subgroup meets jointly with the MA&O Subgroup at each HJWG meeting to assist in mission planning.

Further, as mission planners, the MA&O Subgroup has a strong interest in all of the subject matter being reported in this article; therefore, the author does not intend to imply that the MA&O participation in the 7th HJWG Meeting was limited to the few topics listed below.

1. Helios Ground and Operations System/JPL Interface Management Plan. By intent, a significant portion of the MA&O Subgroup membership is composed of personnel from the West German Helios Ground and Operations System (HGOS)—(Fig. 1 of Ref. 1). Further, it is evident that the HGOS has a significant operational interface with the JPL Helios support organization (Figs. 2, 3). Therefore, activity was initiated during the 6th HJWG Meeting to develop a HGOS/JPL Interface Management Plan. Considerable progress was made in the interval between that meeting and the 7th HJWG Meeting with the result that near-final agreement was reached upon its contents. At the present time, the final changes/corrections are being incorporated into the manuscript. After proper approval, the plan will be published as a project document. Its contents are shown in Table 1.

2. Ground Data System Test Plan. The TDS Subgroup had long recognized the need to demonstrate compatibility between the various elements of the total Ground Data System (GDS) (Fig. 2) prior to the initiation of Mission Operations Training by the HGOS personnel. Portions of the total Ground Data System will be tested, both within

the U.S. and within Germany, during the spacecraft compatibility tests mentioned in *Paragraph II-B-4*. However, due to the different operational readiness dates for the German, DSN, and Near-Earth Phase Networks (NEPN), the total world-wide Helios Ground Data System could not be demonstrated simultaneously until after the arrival of the Flight (F-1) Spacecraft at Cape Kennedy, Fla. However, significant subdivisions of the total GDS could and should be demonstrated prior to this time. During the 7th HJWG Meeting, the TDS and MA&O Subgroups agreed to develop a coordinated plan leading up to the final total Ground Data System demonstration prior to launch. The JPL effort will be coordinated by the Helios representative from the JPL Flight Project's Operations Support Coordination Office (Fig. 3). This plan is expected to be presented at the 8th HJWG Meeting.

*3. **DSN Command System Redesign.*** During the prelaunch compatibility testing of the Pioneer 10 spacecraft, it became evident that the DSSs' Telemetry and Command Processor (TCP) had become overloaded with ever-increasing project requirements during its lifetime. At the time of Pioneer 10 compatibility testing, the TCP could just handle the Pioneer telemetry and command requirements. Since the Helios telemetry frame length is much longer and commands are sent at 8 symbols-per-second (sps) as opposed to 1 sps for Pioneer, it became evident that a TCP software redesign would be necessary to support Helios. One of the steps currently being taken to reduce total project loading on the TCP is to reapportion the Command System workload between the TCP and the Mission Control and Computing Center (MCCC) 360-75 computers. One of the features of the Pioneer 10 era TCP software design was the ability or flexibility that would permit a project to remotely rearrange or manipulate the Command sequence or "stack" in residence within the station's TCP. This flexibility required a considerable amount of TCP on-site processing. In the new Command System design, such manipulation is done in the MCCC 360-75 computer with only the resultant "command stack" being sent via high-speed data lines to the station's TCP. Considerable TCP processing time has therefore been eliminated without sacrificing the basic Command System flexibility concept. The redesign, however, did affect the operational procedures to be used and the bit-by-bit definition of the high-speed data blocks being used to transfer commands from the MCCC 360-75 to the DSS TCP. These changes were points of discussion during the 7th HJWG Meeting. At the present time, the HGOS organization is reviewing these changes in preparation for a new agreement on the command system interface.

*4. **DSN Experience With the Blind Acquisition of Pioneer 7 Spacecraft.*** As mentioned in *Paragraph II-B-3*, the Helios mission sequence designers are concerned with the ability of the DSN to reacquire the spacecraft signal after the spacecraft emerges from a long-duration solar occultation or blackout. To illustrate the type of techniques that can be employed, the DSN related a recent experience regarding tracking the Pioneer 7 spacecraft.

Because Pioneer 7 was in its Extended Mission Phase, the DSN had not been scheduled to track the spacecraft between July 25 and August 6, 1972. At the latter date, the DSN attempted to locate the Pioneer 7 spacecraft at its predicted frequency without initial success. The condition of the spacecraft, therefore, became unknown. On the assumption that the spacecraft was still transmitting but not on its predicted frequency, a DSN receiver search was made to no avail. Something had therefore happened to the downlink. Commands were then transmitted, using the nominal or predicted uplink frequency, to reinstate the downlink. At that time, Pioneer 7 was 312.2 million km from Earth, which required a round-trip light time of 34.7 min. When this time passed without a successful reacquisition of the downlink, the DSN and the Pioneer Project jointly planned an uplink frequency sweep with simultaneous transmission of commands to the spacecraft. The strategy was to sweep from the predicted uplink frequency in a direction which the spacecraft receiver's frequency would have drifted had the spacecraft temperature decreased because the transmitter had been accidentally turned off. On the third attempt, more than three hours later, the downlink was successfully reestablished. Subsequent telemetry analysis indicated that a spacecraft under voltage protection circuit had actuated to turn off the traveling-wave tube (TWT) RF power amplifier and the science instruments. As a result, the spacecraft receiver had dropped from a temperature of 14.2 to $-13.6°C$. The latter temperature was below the calibrated range of spacecraft receiver rest frequencies; therefore, in developing the transmitter sweep frequency strategy, project personnel had had to estimate the frequency necessary to reestablish the uplink and to command the spacecraft on.

This experience had two major points of significance for Helios. First, assuming a noncatastrophic loss of downlink signal, the DSN can employ operational techniques in an attempt to reestablish communication with the spacecraft; second, it is very important for the project to preflight calibrate the spacecraft receiver's rest frequency over temperature ranges beyond those expected during normal mission operations.

5. DSN Operational Constraints to Mission Design. Due to the nature of station hardware/software design, the DSN does impose certain operational constraints upon mission sequence design. In general, these constraints are not serious, but certainly need to be understood when developing detailed mission sequence procedures. Among others, the following two constraints were noted:

a. Telemetry. The Helios spacecraft has a number of telemetry bit rates available for transmission of data to Earth (Ref. 6). These bit rates change in steps of two, namely, 8, 16, 32, 64 . . . 2048 bps. When the data are convolutionally encoded, each bit becomes two symbols (8 bps becomes 16 sps), with the result that the symbol rates are 16, 32, 64, 128 . . . 4096 sps.

When these symbol streams are received at the DSS, the station's Telemetry System must synchronize to the incoming serial bit stream. This is done in the Symbol Synchronizer Assembly (SSA) which also must be set up or "initialized" in multiples of two centered around the expected downlink symbol rate. Therefore, whenever a Helios telemetry bit rate mode change is commanded, the DSS Telemetry System must be re-initialized at the new symbol rate. Re-initialization can result in the loss of several telemetry frames. This factor should be considered in mission planning, i.e., it is desirable to command telemetry bit rate changes mostly during periods of quiescent spacecraft activity in order to minimize the impact of the lost data.

b. Command. The Helios spacecraft has two command uplink subcarrier frequencies (Refs. 1, 6, and 7). Whenever it is desired to change from one command subcarrier frequency to the other—as for example, during the Step II maneuver (Ref. 5)—it is necessary to interrupt the command modulation and/or the transmission of the command idle sequence (Ref. 7), as well as to switch the actual subcarrier frequencies that are being modulated onto the uplink carrier. This procedure requires the re-initialization of the DSS Command System which can occupy a time period of one to five minutes, depending upon circumstances.

From the above-cited examples, it can be seen that the normal operation of the DSN does place certain constraints upon the mission sequence design. However, if these are properly recognized during mission planning they should have no impact upon mission success.

D. TDS/Experiments Joint Meeting

The major interface between the TDS Subgroup and the Experiments Subgroup lies in the content, structure, and detailed definition of the EDRs to be delivered by the Helios Ground Data System (GDS) to each experimenter. In gross terms, this interface is defined in the project Support Instrumentation Requirements Document (SIRD) and in the responses provided by the NASA Support Plan (NSP) and by the German Support Plan. However, these documents do not define the detailed structure of these EDRs. Further, many of the specifications that do appear in the SIRD and its supporting documents are the direct result of experimenters' requirements. It is a trite truism to say that Experimenters and Ground Data System personnel live and think in different worlds. A good example of this truism is given in the following, which in itself justifies the need for continued TDS/experimenter discussions during the HJWG meetings.

1. Telemetry Master Data Record/Experiment Data Record Completeness Criteria. The Helios SIRD contains a specification that the Telemetry Experiment Data Record (EDR) shall have a bit error rate (BER) no greater than 10^{-5}. This is a very stringent specification and is one of the reasons the Helios Project selected convolutional coding for its telemetry. However, coding alone will not achieve a BER this low; each telemetry mode must contain additional signal margin in its telecommunications link analysis. Further, a BER specification does not apply to lost telemetry frames (e.g., signal dropouts, etc.) so additional completeness criteria are needed. All of these subjects have been repeatedly discussed during previous HJWG meetings; however, the words used by the respective parties were not fully understood by the other. During the 7th HJWG Meeting at least one area of misunderstanding was finally described in words understood by both Subgroups. It relates to both the BER and the completeness criteria:

In the transmission of telemetry data from the DSN stations to the Mission Control and Computing Center (MCCC), (where the data are logged onto the Master Data Record) telephone-type voice/data circuits known as High-Speed Data Lines (HSDLs) are used. These circuits are subject to bursts of noise which in turn obliterate small blocks or chunks of the data being transmitted over the circuit. These noise bursts are random in the sense that they can occur at any time in an unpredictable manner. Prior to the 7th HJWG Meeting, the experimenters had interpreted the word "random" to mean that the noise was more or less uniform—i.e., that it would

affect all data bits being transmitted over the circuit more or less uniformly. Because some experimenters' data are subcommutated within the Helios telemetry frame, those experimenters in particular were alarmed at the discovery that a given HSDL noise burst could obliterate their entire data word. Further, this data word might not be repeated in another measurement until the next Main Frame (one Helios Main Frame is composed of 72 regular 1152 bit Helios frames). The experimenters' concern was even further aggravated by the realization that the mere act of repeating the data transmission from the station would not guarantee that another noise burst would not occur to again affect his data. Unfortunately, this situation can occur in the practical world even though at the same time the Helios Ground Data System is averaging less than 10^{-5} BER and has met a 95–98% completeness criteria. Obviously, the experimenters were not prepared to make an on-the-spot evaluation of the impact of this realization. Nonetheless, it was at least opportune that this realization occurred some 20 months prior to launch —as opposed to after launch, as it did in the case of at least one prior project.

2. *Data Records for Experiments 11 and 12.* Helios has ten major on-board scientific experiments plus two ground-based, passive experiments (Table 2). The latter are Experiments 11 (Celestial Mechanics) and 12 (Faraday Rotation) whose primary data are not contained in the Helios telemetry stream, but rather from measurements taken at the DSN stations. For Experiment 11, the primary data types are doppler and planetary ranging, which are contained in the DSN Tracking System MDR. For Experiment 12, Faraday Rotation, the primary data are recordings of the polarization angle of the incoming Helios carrier signal as received by the DSN 64-m-diam stations. Since neither of these data types fit conveniently into the EDR format structure negotiated with the Experimenters Subgroup for Experiments 1 through 10, action items were jointly assigned to these experimenters and the TDS Subgroup to develop an MDR/EDR Plan specific to Experiments 11 and 12 for presentation at the 8th HJWG Meeting.

3. *Use of Mu Ranging.* The Celestial Mechanics Experiment (No. 11) uses DSN doppler and range data to precisely measure the influence of the sun's gravity upon the Helios trajectory and the propagation of its radio signal. These influences are greatest when the spacecraft is near perihelion and near solar occultation, respectively; however, to completely measure the effect and to get reference points, data are also needed regarding the trajectory well before and after perihelion and occultation passage. During this total time period, the range from Earth to the spacecraft can vary anywhere from 0.6 to 2.0 AU (Ref. 5). Therefore, the DSN Planetary Ranging System must be employed. During the development of the Helios spacecraft, the DSN contemplated employing a "continuous spectrum" (Tau) type of planetary ranging system during the Helios era. However, during the course of this development, flight projects in general expressed an interest in the DSN "discrete spectrum" (Mu) planetary ranging technique, with the result that in July 1972 the DSN made a formal decision to implement both types of planetary ranging systems for operational use in the Helios era. It will now be possible for Helios to use either type of planetary ranging system, with the only constraint being that the project would have to select one or the other ranging system types prior to the beginning of any particular DSN 64-m station pass (planetary ranging is not presently planned for implementation into the DSN 26-m networks). The significance to Helios of this decision is that the *discrete spectrum* (or Mu) Planetary Ranging System permits either or both: (1) less power to be used in the ranging sidebands, or (2) a shorter range code acquisition time (time consumed in making a ranging measurement)—depending upon the project tradeoffs involved.

As mentioned in the discussions regarding link analysis, the Helios telemetry margins, particularly at 2.0 AU, had degraded during the evolution of the spacecraft radio system design. As a result, use of the Tau Planetary Ranging System at 2.0 AU would force a reduction in spacecraft telemetry bit rate when the turnaround ranging mode was activated. In contrast, the use of the Mu Planetary Ranging System under these circumstances could be designed to have only slight effect upon the telemetry data return at 2 AU. A special 7th HJWG Splinter Session investigated this situation in detail and recommended that the planetary ranging modulation index used by the spacecraft be changed from its prior value of 45- to 24-deg phase modulation. This new value should enhance science data return at 2.0 AU, yet still provide capability for Tau Planetary Ranging to a distance of 1.6 AU together with Mu Planetary Ranging capability all the way to 2.0 AU. The latter situation turned out to be completely acceptable to the Experiment 11 representative.

E. Special Splinter Meeting Topics

As mentioned earlier in this article, the 7th HJWG Meeting agenda contained a large number of splinter topics due to the level of detail needed to complete the

various interfaces. While this situation prevailed throughout all Subgroup agendas, it was particularly true for the TDS Subgroup where the number of splinter topics exceeded the number of general session agenda items. Space does not permit the inclusion of even a majority of these topics in this article; therefore, only a few having the greatest significance to the TDS Subgroup activities will be reported in the paragraphs that follow.

1. Blind Acquisition. Just prior to the 6th HJWG Meeting, it was discovered that a possibility exists that the Helios spacecraft might not be transmitting a downlink signal at the time of the initial DSN acquisition. This situation could occur if an unpredicted spacecraft power system overload occurred during launch, which in turn could cause a protective circuit to shut down a number of instruments including the transmitter. Therefore, during the 6th HJWG Meeting, a special study team was constituted to investigate this potential problem in detail and to present their findings at the 7th HJWG Meeting. The DSN participated in this effort both prior to and during the 7th HJWG Meeting. In performing their study, the Team had to make certain key assumptions: the spacecraft failure was not catastrophic; the 926 km (500-nmi) perigee altitude (lofted) trajectory would be employed; the Low-Gain Antenna (LGA or omni) pattern nulls would not exceed 5 db; the Near-Earth Phase Network (NEPN) could provide pointing information to the DSN based on launch vehicle tracking data; and that the DSN initial acquisition station would have an Acquisition Aid Antenna. Of the foregoing, the assumption of -5 dB antenna nulls seemed to be questionable, with the feeling that -40 dB would be a better number. While the DSN agreed to recalculate their predictions based on the -40 dB null criterion, the team concluded that the controlling factor in a successful blind acquisition is the perigee altitude. Altitudes significantly lower than 926 km (500 nmi) would both increase the time required and lower the probability of successfully entering a blind command into the spacecraft to reactivate the downlink. For evaluation purposes, the original assumptions produced the conclusion that the DSN would have a high probability (e.g., 0.9) of successfully establishing communications with the spacecraft by Launch +1 hour. The significant change with respect to a standard initial acquisition (*Paragraph II-A-1*) is, therefore, the time required after spacecraft rise at the initial station for two-way communication to be established.

2. Step II Attitude Determination. A topic of continuing discussion during the past several HJWG Meetings has been techniques for the determination of spacecraft attitude during the Step II maneuver sequence. It has been relatively well understood that the Medium-Gain Antenna (MGA or pancake antenna) pattern characteristics would be used during the final portion of the Step II maneuver to ascertain that the spin axis is pointing to the pole of the ecliptic. This is to be done by monitoring the received signal strength (AGC) at the DSN station. During the 7th HJWG Meeting, it was concluded that the SIRD requirement for sampling DSN AGC values could be reduced from 10/s to 1/s without impacting the Project's ability to perform this maneuver. Since the higher AGC sampling rate would require special implementation within the DSN, it was concluded that the SIRD requirement should be revised to the lower sampling rate to avoid unnecessary cost within the network.

Prior to the 7th HJWG Meeting, there had been concern regarding the initial phases of the Step II maneuver. This regards the determination of whether the spacecraft would start to precess toward the north or toward the south ecliptic pole. While a successful mission could be accomplished with the spin axis oriented toward either pole, the north pole was desired. However, once the precession had gone more than a limited number of degrees, there was insufficient attitude gas reserve to reverse the direction toward the other ecliptic pole. During the 7th HJWG Meeting, it was ascertained that the spin modulation due to the offset of the bottom horn antenna (LGA) would cause a doppler modulation which, in turn, could provide information regarding the direction of orientation—i.e., whether it was precessing toward the north or south ecliptic pole. However, to use this information, it would be necessary to sample the doppler at a rate of 10/s, which is faster than the presently committed DSN maximum sample rate of 1/s. The DSN is contemplating an added capability at selected stations to accommodate 10/s doppler sampling—which if implemented could support Helios, providing this higher rate became a SIRD requirement.

3. Coded vs Uncoded Telemetry at Launch. As mentioned in the previous article (Ref. 1), a major agenda point for the 7th HJWG Meeting was a joint session recommendation regarding whether Helios should be launched in the coded or the uncoded telemetry mode. As might be expected, there were reasonably strong arguments presented in favor of each side of the question. From the DSN viewpoint, either mode could be supported during the initial DSN acquisition, but with the understanding that the coded mode would take slightly longer to process at the station, since telemetry frame

synchronization must take place prior to the data being decoded and processed for transmission to the MCCC. The latter proved not to be a compelling argument, but since the Helios Ground Support Equipment (Helios Test Set—(HTS)) was presently structured only to handle telemetry in the coded mode, the MA&O Subgroup submitted its recommendation that Helios be launched in the coded telemetry mode.

4. Automatic vs Commanded Transponder Coherent Operation. The current design of the Helios spacecraft requires that the transponder be commanded into the coherent mode of operation as opposed to having this function performed automatically upon receipt of an up-link by the spacecraft. Reference 6, p. 23, describes the rationale for the commanded approach. During the 6th HJWG Meeting, an action item was assigned to the DSN to evaluate the operational impact of each approach upon the network as it might relate to Helios mission design. This evaluation was completed, and it was reported during the 7th HJWG Meeting that the commanded technique would not present any significant constraints to network operations over the use of an automatic technique for initiating coherent transponder operation. The project is, therefore, free to select whichever technique best satisfies its mission objectives and/or mission sequence design.

5. Other Topics. There were numerous other topics resolved during the 7th HJWG Meeting—these may be found in the formal minutes (Ref. 3). In addition, there were several on-going topics that were discussed as part of other agenda items. One example of the latter concerns the Low-Gain Antenna (LGA) pattern which was mentioned in relation to several of the agenda topics discussed in this article. There is an obvious need for an early definition of this pattern, particularly with respect to the interferometer region between the dipole and horn antenna elements (Ref. 1)—but, unfortunately, such data are difficult to obtain via Earth-based measurements. Discussions regarding this subject are, therefore, iterative in nature and may be expected to continue through the next several HJWG meetings.

III. Conclusions

This article has treated some of the more significant highlights with respect to the DSN/TDS activity during the 7th HJWG Meeting. The next (8th) Helios Joint Working Group Meeting, is presently scheduled for May 9 through 15, 1973, at Cape Kennedy, Fla. and will emphasize the launch operations aspect of the Helios preparations. In the meantime, the next article in this series will discuss the results of Helios Project technical discussions that were held at JPL during December 1972.

References

1. Goodwin, P. S., "Helios Mission Support," Technical Report 32-1526, Vol. II, pp. 18–27. Jet Propulsion Laboratory, Pasadena, Calif., Apr. 15, 1971.

2. Goodwin, P. S., "Helios Mission Support," Technical Report 32-1526, Vol. XII, pp. 5–9. Jet Propulsion Laboratory, Pasadena, Calif., Dec. 15, 1972.

3. Minutes of the "Project Helios, Seventh Joint Working Group Meeting at GfW, Porz-Wahn, Federal Republic of Germany, 25-31 October 1972" published by the Helios Project Office, Gesellschaft fuer Weltraumforschung, Porz-Wahn, West Germany.

4. Minutes of the "Project Helios, Sixth Joint Working Group Meeting at Jet Propulsion Laboratory, Pasadena, California, April 26 through May 3, 1972," Goddard Space Flight Center, Greenbelt, Md.

5. Goodwin, P. S., "Helios Mission Support," Technical Report 32-1526, Vol. III, pp. 20–28. Jet Propulsion Laboratory, Pasadena, Calif., June 15, 1971.

6. Goodwin, P. S., "Helios Mission Support," Technical Report 32-1526, Vol. IV, pp. 22–31. Jet Propulsion Laboratory, Pasadena, Calif., Aug. 15, 1971.

7. Goodwin, P. S., "Helios Mission Support," Technical Report 32-1526, Vol. V, pp. 17–21. Jet Propulsion Laboratory, Pasadena, Calif., Oct. 15, 1971.

8. Goodwin, P. S., "Helios Mission Support," Technical Report 32-1526, Vol. VI, pp. 25–32. Jet Propulsion Laboratory, Pasadena, Calif., Dec. 15, 1971.

9. Goodwin, P. S., "Helios Mission Support," Technical Report 32-1526, Vol. VII, pp. 17–24. Jet Propulsion Laboratory, Pasadena, Calif., Feb. 15, 1972.

10. Goodwin, P. S., "Helios Mission Support," Technical Report 32-1526, Vol. VIII, pp. 16–19. Jet Propulsion Laboratory, Pasadena, Calif., Apr. 15, 1972.

11. Goodwin, P. S., "Helios Mission Support," Technical Report 32-1526, Vol. IX, pp. 33–34. Jet Propulsion Laboratory, Pasadena, Calif., June 15, 1972.

12. Goodwin, P. S., "Helios Mission Support," Technical Report 32-1526, Vol. X, pp. 14–19. Jet Propulsion Laboratory, Pasadena, Calif., Aug. 15, 1972.

Table 1. HGOS/JPL interface management plan contents

I.	Introduction
II.	Project Management
III.	Project Phases
IV.	Joint Management Policies and Requirements
V.	Task Breakdown and Responsibility Assignment

Table 2. Helios experiments

No.	Experiment	Scientific affiliation
1	Plasma Detectors	
	(A) Proton and Alpha Detector High Angular Resolution	Max Planck Institut fur Extraterrestrische Physik, Garching
	(B) Proton and Alpha Detector Faraday Cup	Ames Research Center
	(C) Electron Detector	
2	Flux-Gate Magnetometer	Tu Braunschweig Institut fur Giophysik und Meteorologie
3	Flux-Gate Magnetometer	Goddard Space Flight Center University of Rome
4	Search-Coil Magnetometer	Tu Braunschweig Institut fur Giophysik und Meteorologie
		Institut fur Nachrichtentechnik
5	(A) Solar Wind Plasma Wave Experiment	University of Iowa University of Minnesota
	(B) Radio Wave Experiment	Goddard Space Flight Center
6	Cosmic Ray Experiment 1 Mev to 1 Gev	University Kiel
7	Cosmic Ray Experiment	
	(A) High Energy Telescope	Goddard Space Flight Center
	(B) Medium Energy Telescope	
	(C) Low Energy Telescope	University of Adelaide
	(D) X-Ray Detector	
8	Electron Detector	Max Planck Institut fur Aeronomie, Lindau/Harz
9	Zodiacal Light Photometer	Landessternwarte Heidelberg
10	Micrometeoroid Detector and Analyzer	Max Planck Institut fur Kernphysik, Heidelberg
11	Celestial Mechanics	Jet Propulsion Laboratory University of Hamburg
12[a]	Faraday Rotation	Jet Propulsion Laboratory

[a]Pending final intergovernmental approval.

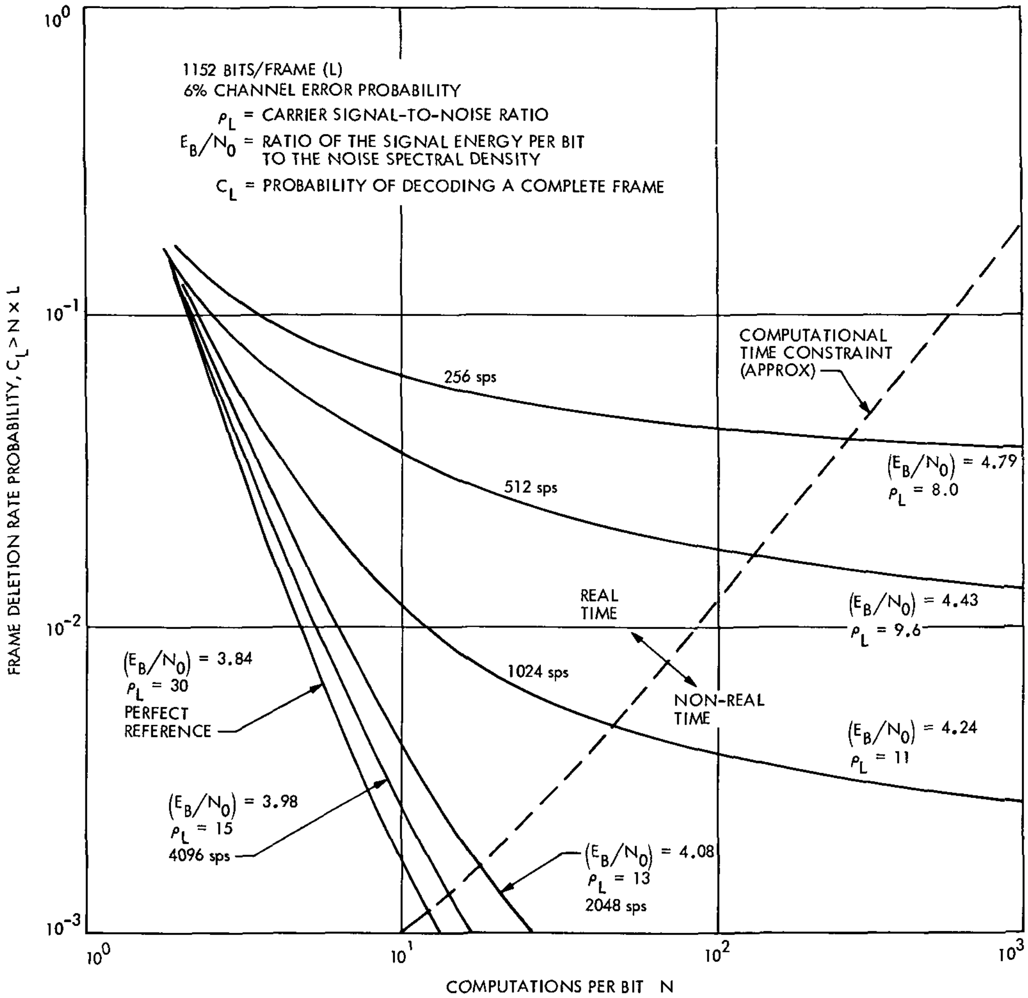

Fig. 1. DSN October 1972 estimate for Helios coded telemetry performance

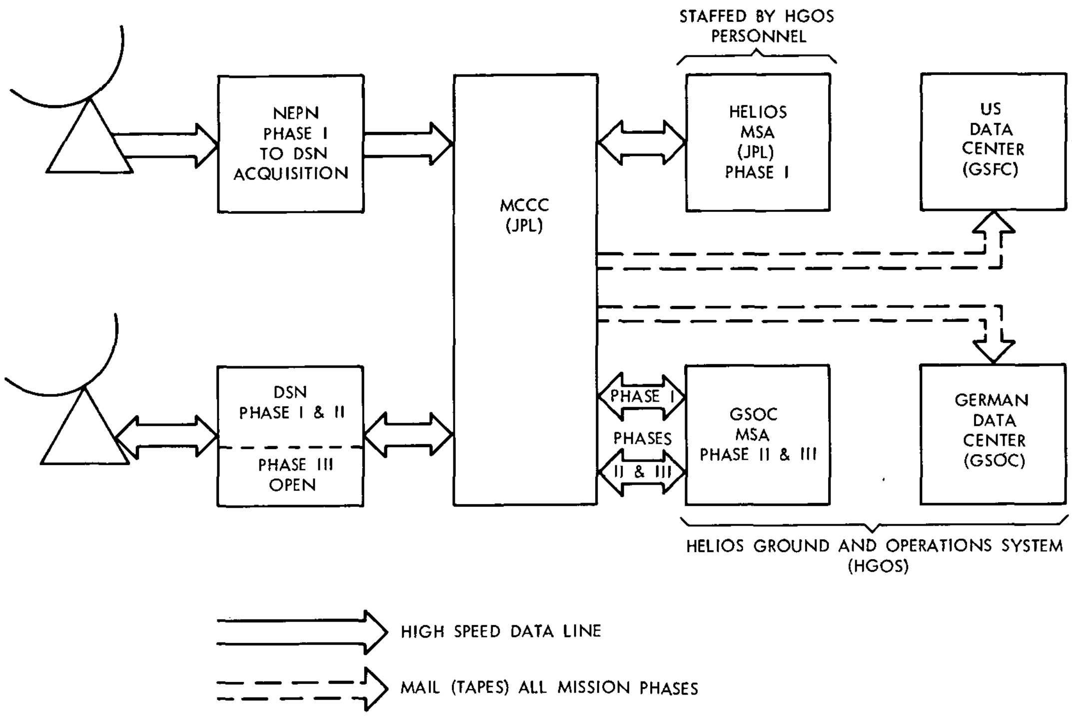

Fig. 2. NASA-TDS Helios data flow

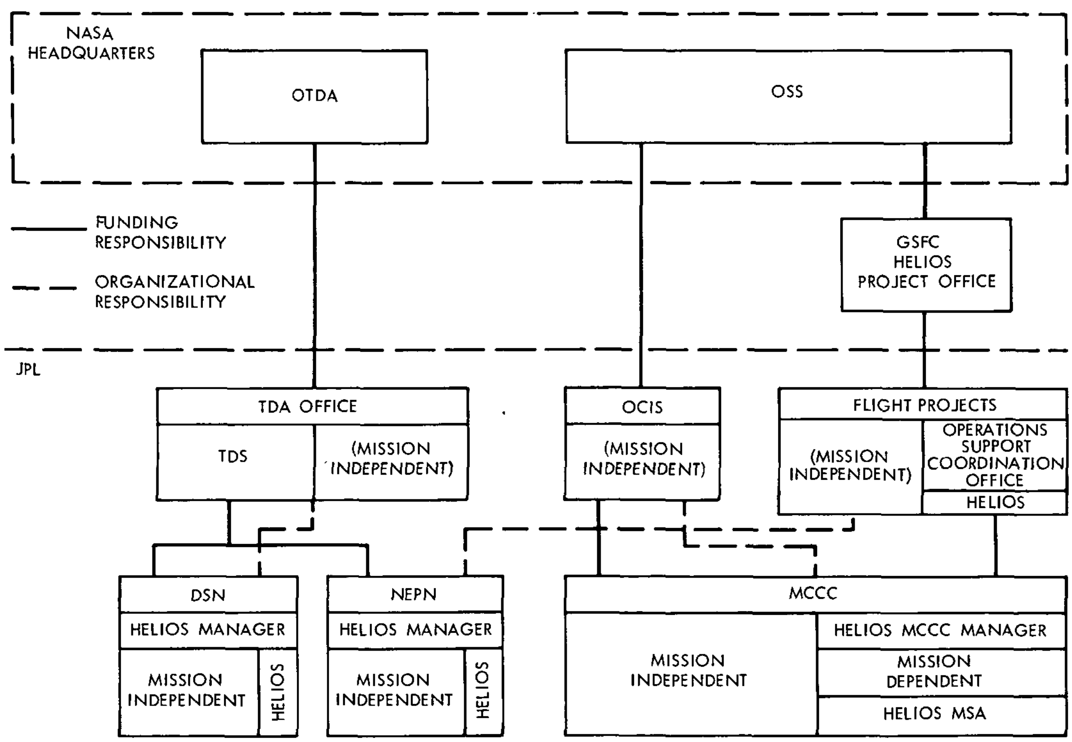

Fig. 3. JPL Helios support functional relationships

DSN Support of the Mariner Mars 1971 Extended Mission

T. W. Howe and D. W. H. Johnston
DSN Operations

Each mission supported by the Deep Space Network is unique. Operations planning normally covers the standard mission only and does not include extended mission operations. This article describes the innovations that had to be made to support this portion of the Mariner Mars 1971 mission.

I. Definition of Extended Mission

The extended Mariner Mars 1971 (MM'71) mission began on February 12, 1972, 90 days after Mariner 9 was inserted into Mars orbit. A revision of the Support Instrumentation Requirements Document (SIRD) and corresponding NASA Support Plan (NSP) was necessary to cover commitments and requirements for the extended mission.

II. Establishment of Extended Mission Requirements

A. Time Period

The SIRD established the period for the extended mission as "Mariner 9 orbit insertion + 90 days to orbit insertion + 365 days." The extended mission of MM'71 was unique in that this was the first Mariner to orbit a planet, and although all nominal mission data taking capabilities remained, the data return capabilities were decreased because of spacecraft antenna pointing and the extreme spacecraft–Earth range.

B. Objectives

Because of the long orbit time of the standard mission and the solar geometry, it was possible to extend the nominal mission and formulate objectives unique to the extended mission. Table 1 (Ref. 1) lists these objectives and the experiments which would achieve them. The NSP indicated that only Deep Space Station (DSS) 14 would be able to support the major portion of the extended mission because of telecommunications constraints. Since DSS 14 was the only 64-m-diameter antenna station available, a loss of this station for any reason meant that all objectives might not be met.

C. Unsupported Requirements

DSS 14 could not give all of the requested coverage because of commitments to other projects. One-way doppler occultation data requirements could not be met for the same reason. Planetary ranging data would be provided at DSS 14 only, using R&D equipment. This configuration would not provide the requested real-time data, but would provide nonreal-time data in the form of punched paper tapes. In addition, all of the original standard mission unsupported requirements remained unsupported in the extended mission.

III. Extended Mission Profile

The extended mission began with no change in the operating mode. DSSs 12, 14, 41, and 62 continued their support 7 days per week. Mapping of the Martian surface continued, and as telecommunications performance degraded, selected features of Mars were re-examined. Table 2 (Ref. 1) lists key milestones and events during the extended mission. By mid-March, RF downlink threshold was reached for the 26-m DSSs, following which they were used only sporadically for uplink purposes. For the remainder of the mission, DSS 14's coverage varied between three and six passes per week.

IV. DSN Support

The innovations required during the extended mission were numerous. Most were needed to correct problems as they occurred in real time. The more significant ones are discussed below.

A. Block Decoder Assembly Threshold

By mid-February, a decrease in telecommunications capability was being observed as a result of the mispointing of the high-gain antenna in position 2 and the increasing range of Mars. The first innovation involved the lowering of the block decoder assembly (BDA) threshold from +2.5 to 0.0 dB signal-to-noise ratio (SNR). This effectively lowered the point at which the BDA would go into an automatic restart, permitting the Project to process pictures at SNRs lower than 2.5 dB. Higher science data rates could then be maintained for longer periods of time and more pictures received per pass, with some degradation in picture quality. This telemetry and command processor (TCP) software option was to remain in effect through the end of the mission.

B. Uplink Tuning

Instances of loss of uplink lock were observed during the latter part of February. The losses occurred during the tuning of the station transmitter exciters. The tuning rates being used at the time were the ones determined during spacecraft compatibility tests conducted before launch. Since station transfers were being performed near periapsis, at times of maximum doppler rate and offset, it was concluded that the standard tuning rate of 15 Hz/min for spacecraft signal levels of -139 to -145 dBm could no longer be used. The tuning rate was lowered on March 1 to 10 Hz/min, and no further anomalies occurred.

C. SDA Bandwidth Settings

The table defining the bandwidth setting for the receiver/subcarrier demodulator assembly was revised for the extended mission. The table covered the various telemetry modes, bit rates, and parts of orbit expected during the extended mission. By periodically zeroing the static error of the phase-locked loops (approximately every 2 h), the telemetry degradation was minimized. A graph was also supplied for members of the Network Analysis Team which defined the optimum SDA bandwidth setting for engineering data for S-band doppler vs. engineering SNR. This allowed the option of changing the bandwidth to cope with real-time conditions.

D. Picture Reception Operations

By mid-March, threshold for 2-kbps data had been reached and a series of high-gain antenna maneuvers had begun. These maneuvers increased the data rate to 8 kbps. For each of the maneuvers, DSS 14 configured for a listen-only mode. In this mode, the diplexer was bypassed and overall system temperature improved. Since DSS 14 could not provide an uplink in this mode, DSS 11 or 12 was called upon to provide an uplink to the spacecraft for the purpose of commanding and also to permit DSS 14 to receive three-way doppler occultation data.

E. Blind Commanding

Blind commanding was introduced during the period of solar occultation when leakage of spacecraft attitude control gas had been observed. DSSs 41, 51, and 62 provided the blind commanding support with the transmission of a series of DC-32s. The DC-32s set a flag in the spacecraft computer and enabled a sequence which conserved gas during the solar occultations. For days on which the DC-32s could be transmitted, 2.81 kg/m^2 of gas would be used per day. Without these commands (no

DSN support), the use rate increased to 12.66 kg/m^2 per day. The commanding was considered blind in that engineering threshold had been reached for the 26-m DSSs, and these stations could not see the results of their commanding effort.

F. Third-Order Tracking Loop Filter

By the end of April, the Block III DSIF receiver had been pushed to the limit of its tracking capability by doppler rates of 25 Hz/s and doppler acceleration rates as high as 0.16 Hz/s. At this point, a third-order loop filter was introduced (Ref. 2). Tests conducted at Compatibility Test Area (CTA) 21 demonstrated a capability of tracking doppler rates in excess of 1000 Hz/s and doppler acceleration as high as 3.8 Hz/s. Installation of the filter in receiver 1 at DSS 14 substantiated the CTA 21 tests. The third-order loop coped with all doppler conditions through the end of the mission.

G. Recording of Occultation Data

As the received signal level approached -164.0 dBm in June, the point of exit occultation could no longer be determined at DSS 14. A procedure was developed whereby the analog recordings of occultation data made at DSS 14 could be sent to CTA 21 and time of exit determined to within less than 1 s. The procedure was unique in that the tapes were played in a reverse direction to determine the point at which the signals disappeared. Determination of this time allowed the occultation experimenters to begin the processing of the prime digital tapes at the exact time of exit and save valuable computer processing time.

H. DSS 14 Antenna Azimuth Bearing

The hydrostatic bearing of the DSS 14 antenna, which had shown signs of degradation in film height as early as December 1971, reached a critical point in June. The final week of July was devoted to a complete regrouting and shimming operation of the degraded area, thereby increasing the possibility of continued antenna operation to the end of the mission. Much needed 400-kW transmitter maintenance was also performed during this period.

I. Coordination of Ranging Operations

A special Mu ranging voice coordination net was established prior to the beginning of the relativity experiment. This separate voice net, which connected the Mu ranging operator at DSS 14 to the ranging advisers located at JPL, was used for technical coordination, exchange of technical information, and the operation of the R&D ranging equipment. The net was used for a 2-month period centered around superior conjunction.

J. Use of Programmed Local Oscillator and 3-Hz Tracking Loop

As superior conjunction neared, excessive solar activity and spectrum broadening were making it difficult to maintain receiver lock. A mixer unit was installed in receiver 2 at DSS 14 which allowed this receiver to be used with a programmed local oscillator (PLO). A 3-Hz tracking loop filter was introduced at the same time. The R&D XDS 930 computer, which had previously been used for Mu ranging, was the input source for the mixer module. Superior conjunction occurred a week after the PLO configuration was first used, and valuable ranging data were obtained on that date.

K. Spacecraft Engineering Test Support

DSS 14 was instrumental in the accomplishment of a series of "end-of-mission" engineering tests. Radio-Frequency Subsystem (RFS) and Flight Command Subsystem (FCS) threshold tests were conducted, and an uplink comparison test was performed. These tests required a precise calibration of the transmitter output power level. Special procedures and operations had to be performed for each of these tests.

V. Summary

The extended mission was completely successful. All of the original objectives were met. The amount of occultation data received was more than doubled during the extended mission. The technique of pointing the high-gain antenna permitted 8-kbps data to be received during the entire extended mission. One hundred percent of the planet was mapped, and selected areas were monitored as possible Viking landing sites. Mariner 9 completed 259 days of extended mission operations and doubled the length of the mission.

Extended missions are seldom planned in advance, and the ability to overcome problems in a relatively short time is extremely important. During the MM'71 extended mission, the DSN demonstrated the ability to react to real-time situations and provide support under adverse conditions.

The extended mission not only enhanced the success of the Mariner 1971 Project but, because of the Mars dust storm during the early portion of the mission, actually became a vital part of the Project itself.

References

1. Textor, G. P., "Mariner Mars 1971 Mission Support," in *The Deep Space Network Progress Report*, Technical Report 32-1526, Vol. IX, pp. 35–37, Jet Propulsion Laboratory, Pasadena, Calif., June 15, 1972.
2. Crow, R. B., "S-Band Receiver Third-Order Loop Demonstration," in *The Deep Space Network Progress Report,* Technical Report 32-1526, Vol X, pp. 168–171, Jet Propulsion Laboratory, Pasadena, Calif., Aug. 15, 1972.

Table 1. Extended mission objectives

Objective	Experiment
Acquire special data	Solar conjunction [S-band, Celestial Mechanics Experiment (CME)]
	High-latitude coverage [TV, Infrared Interferometer Spectrometer (IRIS), Infrared Radiometer (IRR), Ultraviolet Spectrometer (UVS)]
Acquire long-time base data (>90 days)	Meteorology (TV, IRIS, IRR, UVS)
	Celestial Mechanics
Acquire data supplemental to 90-day observations	Repeated spot coverage of areas of interest (TV, IRIS, IRR, UVS)
	Monitor Viking landing sites (TV, IRIS, IRR, UVS)
	Earth occultation (S-band)
	Cooling data (IRR)

Table 2. Extended mission events (Ref. 1)

Event	Date, 1972
Start extended mission	Feb. 12
Complete pre-solar occultation science-taking sequences	Mar. 27
Start solar occultations	Apr. 1
Start orbit edge-on celestial mechanics mass concentration (mascon) period	Apr. 22
Start S-band occultations of polar regions	May 6
Complete orbit edge-on period	June 1
End solar occultations	June 4
Start weekly cycle of high-gain antenna maneuvers with one or two playbacks per week	June 5
End Earth occultations	June 24
Start solar conjunction period (relativity)	Aug. 19
Solar conjunction	Sept. 7
Complete solar conjunction period	Oct. 18
Complete extended mission	Approx. Mar. 1, 1973

Mariner Venus/Mercury 1973 Mission Support

E. K. Davis
DSN Systems Engineering

During November and December 1972, DSN activities have concentrated on finalizing ground system test planning, spacecraft/DSN compatibility test planning, and on continuing implementation. This article summarizes the major accomplishments in the areas of planning, implementation, and testing.

I. Planning Activities

A. NASA Support Plan

NASA Headquarters review of the NASA Support Plan continued during this period. Approval is expected prior to January 1, 1973. Upon receipt of the completed approval page, the DSN will publish and distribute the final plan.

B. Project Master Test Plan

The Mariner Venus/Mercury 1973 (MVM 73) Mission Operations Master Test Plan (JPL internal document 615-97, Sept. 8, 1972) was not published by the Project in final form in November as planned. However, on December 1, 1972, the Project Manager reviewed and approved final Mission Control and Computing Center System (MCCCS), DSN, and Ground Data System test plans, which form the basis for the master document. Material presented in this review does not alter the DSN basic test plan described in the preceding volume of this series.

C. DSN Support Plan

In December 1972, the DSN Support Plan for MVM 73 (JPL internal document 615-15, Oct. 15, 1972) was updated to reflect test requirements and schedules resulting from the test planning activity (Section B). Included in the appendix are schedules and a flow diagram containing guidelines, objectives, and criteria for use by the DSN operations organization in preparing detailed test procedures and schedules for each Deep Space Station. The

update included changing the document title to "DSN Support Requirements for MVM 73" in accordance with revised DSN documentation standard practices.

D. DSN Preparation Plan

The DSN Preparation Plan for MVM 73 contains the technical response to the DSN Support Requirements Document. It communicates detailed information regarding Deep Space Station and Ground Communications Facility configurations, capabilities, and schedules for new implementation. A draft version of this plan was produced and reviewed during this reporting period. The final version is in publication, and approval is planned for early January 1973. Detailed test/training plans and procedures have been excluded from this document. In accordance with revised documentation standard practices, these activities shall be included in the DSN Operations Plan.

E. DSN Operations Plan

The DSN Operations Plan for MVM 73 contains the operational response to the DSN Support Requirements Document, based on existing operational capabilities and on implementation plans described in the DSN Preparation Plan. It communicates detailed plans and procedures for DSN operations, control, data handling, training/testing, performance analysis, and reporting. A draft of the network-level portion of the Operations Plan is under review. Deep Space Station and Ground Communications portions will follow in January 1973.

II. Implementation Activities

A. Ground Communications

Voice, high-speed, and wideband circuits required between Boeing-Kent spacecraft test facilities and the JPL Mission Control and Computing Center have been implemented as required. Goddard Space Flight Center/NASA Communication System-provided terminal and commercial carrier equipment was installed and completed acceptance testing on December 1, 1972. The DSN has provided operational procedures for use in circuit initialization checkout and operations.

Project experimenters at the University of Chicago have requested that data be transmitted to their remote information center in standard ground communication block format instead of the asynchronous word format previously required. Additional terminal equipment is needed to support this mode. The NASA Communications System will provide terminal equipment required at the user end. Existing DSN–JPL terminal equipment will support this requirement subject to use limitations occurring during peak periods of higher-priority operational data traffic.

Procurement and fabrication of terminal equipment for DSN wideband circuit implementation remains on schedule.

B. Deep Space Stations

Implementation for new capabilities required at Deep Space Stations (DSSs) continues on schedule. Following is a status summary of DSS subsystems involved for MVM 73.

1. *Telemetry and Command Subsystem.* The basic command software module for MVM 73 support is completed and being checked out in Compatibility Test Area (CTA) 21. Rearrangement of tables may continue to improve core utilization, but no major problems have been encountered. The new executive for command processing is in work. Software development for the telemetry processor and data decoder assembly is progressing satisfactorily. Medium-rate telemetry block decoding functions have been checked out. Coding for telemetry data formatting for transmission/recording is in work, and initial checks indicate no problems. Data recall processing work has been initiated. Progress is still being made in support of the February 1973 verification test and March 1973 acceptance test schedules. Simulation Conversion Assembly software documents have been completed, and verification testing is under way. Hardware modification kits have been shipped.

2. *Monitor and Control/Digital Instrumentation Subsystem.* The Software Requirements Document has been completed. Coding and checkout to meet baseline requirements are on schedule toward a January 1973 completion date. Additional new requirements for radio metric data handling and telemetry/command initialization changes will be incorporated by February 1973. Station manager console hardware, including silent printers, has been shipped.

3. *Receiver/Exciter Subsystem.* Twenty-four 10-MHz notch filters and alignment procedures have been provided to the assigned stations for Subcarrier Demodulator Assembly interplex mode modifications.

4. *S/X-Band Experiment.* The S-band megawatt transmit (SMT) and S/X-band cones have been removed from DSS 14 and are undergoing metal fabrication work for installation of S/X reflector/feed modifications. Reinstallation is planned in late January 1973 during the

Pioneer 10 low activity period associated with superior conjunction. Re-installation and tests must be completed prior to DSS 14 antenna down time for regrouting beginning February 4, 1973.

5. ***Planetary Ranging.*** Procurement action has been initiated. Responses to the request for bids are due December 21, 1972. This implementation appears to be on a critical schedule since projected delivery dates are very close to committed operational dates. A detailed review will be made in an effort to improve delivery dates.

III. Test Activities

DSN/spacecraft compatibility test planning has been reviewed and revised. The DSN/Spacecraft Compatibility Test Plan was written and is being coordinated. Preparations for Flight Spacecraft 2 subsystem tests in December 1972/January 1973 have been completed. The plan includes spacecraft component–CTA 21 telemetry compatibility tests in April/May 1973, flight spacecraft–CTA 21 tests in July 1973 during thermal-vacuum chamber tests, S/X-band tests at DSS 14 in June 1973 using proof-test model radio and X-band transponder components, and flight spacecraft compatibility verification with DSS 71 during the launch preparation phase.

Viking Mission Support

D. J. Mudgway
DSN Systems Engineering

DSN Support for Viking remains in the transitional phase between planning and commitment, and the early stages of implementation. Existing implementation schedules have been thoroughly reworked to reconcile desired operational readiness dates with anticipated DSN manpower and funding resources. Investigation of downlink interference effects in a dual-carrier environment continued to make progress at Deep Space Station (DSS) 13. The Network configuration for the DSN Test and Training System is described in this article.

I. Introduction

Over the past 2 months DSN support for Viking 1975 (VK75) has been concentrated in a substantial effort to reconcile the existing implementation plans with the operational readiness dates requested by the Project. This effort has taken longer than originally anticipated but is now complete with minor exceptions. As reported in Vol. XII of this series, the resolution of some of the conflicts is related to the definition of working relationships among DSN Operations, DSN Systems Engineering, and the Telecommunications Division.

Tracking and Data Acquisition documentation is also involved to the extent that it reflects the plans, procedures, schedules, and agreements that must be developed among the organizations concerned. This has been accomplished and will be reported in a later issue of the DSN Progress Report.

Investigation of the effects of the dual-carrier environment on DSN performance has made significant progress. The results of this work will be reviewed in mid-December.

II. DSN Test and Training System Configuration

The DSN Test and Training System (TTS), as configured to support Viking 1975, will accomplish the following functions:

(1) Generate and control simulated Deep Space Station (DSS) and spacecraft data streams to support development, testing, training, and fault isolation in the DSN.

(2) Participate in VK75 mission simulation exercises with the Project by controlling data flow within the DSN and generating simulated DSN data to supplement Project simulation data.

It will be possible to accomplish these functions in either the long-loop (via DSSs) or the short-loop [via Ground Communications Facility (GCF) Central Communications Terminal] configurations, as shown in Table 1.

The functional requirements of the DSN Test and Training System, as configured for VK75, are shown in Fig. 1. Unless otherwise stated, these requirements apply to both the 26- and 64-m subnetworks.

The functional capabilities of each of the three elements of the DSN are described below.

A. Deep Space Station Test and Training Functions

The DSSs will accept and process telemetry, command, and radio metric simulation data from the TTS or the Viking Simulation System (VSS) on High-Speed System (HSS) or Wideband System (WBS), as shown in the footnotes to Fig. 1. The capacity of each DSS to handle simulated data will be equivalent to its capacity to handle real-time data, as described in Refs. 1 and 2, except that the data originated in the TTS will be of a simple fixed pattern, whereas the VSS-originated data will be interactive with command and more representative of true flight data.

B. Ground Communications Facility Test and Training Functions

For test and training purposes, the GCF is required to accept simulated telemetry, command, and radio metric data from the TTS and VSS and transfer the data either short-loop or open-loop to the destinations shown in Fig. 1 by HSS and/or WBS as appropriate.

All simulated data will be formatted by the originator to exactly the same standards as for real-time data, as described in Refs. 1 and 2.

C. Network Control System Test and Training Functions

This System includes the Network Control (NC) Test and Training Subsystem, which, when configured for Viking, is required to perform the following functions in support of Project test and training exercises:

(1) Control data flow within the DSN.

(2) Generate simulated DSN data to supplement Project-supplied simulation data.

(3) Accept computer-generated telemetry data from the Viking Mission Control and Computing Center (VMCCC) for transmission to the DSSs.

(4) Accept simulated command data from the VMCCC that is interactive with the telemetry data in item (3).

(5) Provide simulated radio metric data to the VMCCC based on the predicts capability.

The NC Test and Training Subsystem will, in addition, perform the following functions in support of Deep Space Instrumentation Facility (DSIF) development, testing, training, and fault isolation.

(1) Generate DSIF data streams to exercise GCF and NC Subsystems.

(2) Generate fixed telemetry data patterns to exercise DSS subsystems.

These latter functions are used for internal DSN purposes and are described in various DSN Standard Operating Procedures. Other elements of the NC Subsystem, such as the Real-Time Monitors (RTMs), are required for test and training support, but their role is identical to that performed under the real-time data environment.

The NC Test and Training Subsystem interfaces only with the VSS, as shown in Fig. 1, via the GCF Central Communications Terminal (CCT). All simulation data flowing in either direction across this interface will be formatted by the originator, according to the provisions of Ref. 3. Voice and administrative teletypewriter (TTY) circuits between the NC Test and Training Subsystem and the VSS will be provided for DSN/Project coordination of joint test and training exercises.

III. Interfaces

The telecommunication link interfaces between the DSN and the Viking Orbiter and Viking Lander have been fully defined in Refs. 4 and 5. In addition to defining all the telecommunication link parameters, these documents also contain all of the telecommunication link performance data. The documents are now in the formal sign-off process.

A preliminary copy of the DSN to VMCCC System interface agreement is completing its review cycle at present. This document will establish and control all interfaces between the DSSs and the VMCCC that are pertinent to Viking support. It is derived from and is consistent with the DSN System Requirements Document (820-13), Detailed Interface Design.*

IV. Schedules

The need for DSN schedule revisions and reconciliation with current implementation plans as constrained by anticipated budget and manpower resources was discussed in Vol. XII of this series. This work has now been accomplished, and a DSN Implementation Schedule, Level 5, has been released and will serve as the basis for all subsequent implementation planning and testing. The new agreements are depicted in Table 2.

*JPL internal document.

V. Problem Areas

Investigation of downlink interference effects in a dual-carrier environment continues to make good progress at DSS 13. After an extensive cleanup of all waveguide components and taping of all antenna surface joints, the interference effects were still found to be present. Removal of the quadripod and subreflector assemblies resulted in further test data, which suggested that RF leakage around the outer surfaces of the cone and feed horn contributed significantly to the generation of the interference.

These surfaces and the subreflector surfaces have now been welded and reassembled on the antenna, and a further series of test data is being collected. The data will be presented to the Viking Project in December, and will be a critical factor in determining the choice of implementation to be adopted for meeting the dual-carrier requirement.

Other options include the use of dual stations (one 64-, one 26-m) at a single location to provide one carrier each, operation at reduced power levels, and reduction of the available frequency channels from four to three. The conclusions and recommendations from the December review will be reported in the next issue.

References

1. Mudgway, D. J., "Viking Mission Support," in *The Deep Space Network Progress Report*, Technical Report 32-1526, Vol. XI, pp. 19–21, Jet Propulsion Laboratory, Pasadena, Calif., Oct. 15, 1972.

2. Mudgway, D. J., "Viking Mission Support," in *The Deep Space Network Progress Report*, Technical Report 32-1526, Vol. XII, pp. 14–15, Jet Propulsion Laboratory, Pasadena, Calif., Dec. 15, 1972.

3. *Deep Space Network/Viking Mission Control and Computing Center Interface Requirements Document*, JPL Document 619-10, Jet Propulsion Laboratory, Pasadena, Calif. (JPL internal document).

4. *Viking 75 Project Orbiter System, Lander System and Launch and Flight Operations System to TDS Interface Requirements Document, Volume II, Viking Orbiter System to Deep Space Network*, Project Document ID 3703111, Jet Propulsion Laboratory, Pasadena, Calif. (JPL internal document).

5. *Viking 75 Project Orbiter System, Lander System and Launch and Flight Operations System to TDS Interface Requirements Document, Volume III, Viking Lander System to Deep Space Network,* Project Document ID 3703111, Jet Propulsion Laboratory, Pasadena, Calif. (JPL internal document).

Table 1. Deep Space Network Test and Training System configuration modes

Test mode	Data transfer			Flowpaths	
	From	To	Monitored by	HSS	WBS
DSN-long loop	TTS	DSS		1	3
	DSS	RTM		33	33
	DSS		TTS	9	11
	DSS		OCA	26	26
	DSS		VSS[a]	10	12
FOS[b]-long loop	VSS	DSS		2	4
	DSS	VMCCC		25	12
	DSS		VSS	10	12
	DSS		OCA	26	26
	DSS		TTS[a]	9	10
DSN-short loop	TTS	CCT		5	7
	CCT	RTM		33	33
	CCT		TTS	9	10
	CCT		VMCCC	25	12
FOS-short loop	VSS	CCT		6	8
	CCT	VMCCC		25	12
	CCT		VSS	10	12

[a]Desirable capability only.

[b]Flight Operations System.

Table 2. DSN/Viking readiness dates

Facility	Implementation complete	DSN Systems and Operations testing, weeks	Commit to Project support
CTA 21	Feb. 1, 1974	16	June 1, 1974
DSS 71	Aug. 15, 1974	16	Dec. 15, 1974
DSS 11, 14	Aug. 1, 1974	22	Jan. 15, 1975[a]
DSS 12, 42, 61	Nov. 1, 1974	30	June 15, 1975[b] Feb. 1, 1976[a]
DSS 43, 63	Nov. 1, 1974	30	June 15, 1975[b] Feb. 1, 1976[a]
GCF to CTA 21	Feb. 1, 1974	16	June 1, 1974
to DSS 11, 14	Aug. 1, 1974	22	Jan. 15, 1975
to DSS 12, 42, 61, 43, 63	Nov. 1, 1974	24	May 1, 1975
to DSS 71	Aug. 15, 1974	16	Dec. 15, 1974
NC test and training only	Mar. 1, 1974	14	June 15, 1974
NC full system	Oct. 1, 1974	14	Jan. 15, 1975

[a]Full planetary operational configuration.

[b]Cruise configuration only.

Table 3. Telemetry data rates and channel requirements

Data rates			
Telemetry channel	Description	Bit rate	Subcarrier frequency, kHz
Orbiter[a]			
Low-rate	Uncoded engineering data	8⅓ or 33⅓ bps	24.0
High-rate	Coded (32,6) science data	1, 2, 4, 8, or 16 kbps	240.0
Lander[b]			
B	Uncoded data	8⅓ bps	23.3
A	Coded (32, 6) data	250, 500, or 1000 bps	72.0

Required combinations of channels		
Either Lander	Orbiter A	Orbiter B
A and B	Low-rate	Low-rate
A and B	Low-rate	Low- and high-rate (uncoded)
A and B	Low-rate	Low- and high-rate (coded)
A and B	Low- and high-rate (uncoded)	Low- and high-rate (uncoded)
A and B	Low- and high-rate (uncoded)	Low- and high-rate (coded)
A and B	Low- and high-rate (coded)	Low- and high-rate (coded)

[a]Each Orbiter may transmit low-rate only or low- and high-rate channels.

[b]Each Lander will transmit A and B simultaneously, except when ranging.

"Pages missing from available version"

Pgs. 35-36

Radio Science Support

K. W. Linnes
DSN Systems Engineering

Since 1967, radio scientists have used the Deep Space Network 26- and 64-m-diameter antenna stations to investigate pulsars, quasars, and radio galaxies, to study the effect of solar corona on radio signals, and to observe radio emissions from x-ray sources. Very long baseline interferometry (VLBI) techniques have been used for high-resolution studies of quasars. During the reporting period, VLBI obsevations were made of quasars and pulsars as part of the Quasar Patrol. Support was also provided by the 64-m-diameter antenna to search for interstellar molecules and to observe radiation from Jupiter.

I. Introduction

The 26- and 64-m-diameter antenna Deep Space Stations (DSSs) of the DSN have been used for several years to support Radio Science experiments. NASA, JPL, and university scientists have used key DSN facilities whose particular and unique capabilities were required for the performance of the experiments. In order to formalize the method of selecting experiments and experimenters, a Radio Astronomy Experiment Selection (RAES) Panel was formed in 1969. A renewed notice of availability of these facilities was placed in professional journals to inform the scientific community that they were available for limited use by qualified radio scientists (Ref. 1). No charge is made for use of the standard DSN facilities and equipment; special equipment, however, must be provided by the experimenters. A summary of all experiments conducted through August 1972 is reported in Refs. 2 through 8.

II. Radio Science Operations

During the period September through December 1972, approximately 507 h of support were provided to Radio Science experiments (Table 1). Table 2 identifies the experiments supported. The 64-m-diameter antenna at

Goldstone supported all of these experiments; Near-Earth Physics VLBI experiments also made use of a 26-m antenna station at Goldstone (DSS 12). Support in September was limited primarily to those Office of Space Sciences (OSS)-sponsored experiments which could make use of the available time. The major commitment of the 64-m antenna during this period was to the Relativity Experiment of Mariner 9. At the end of the Mariner 9 mission, Radio Science support increased again. An effort was made to obtain as much time on the antenna as possible during October and November because the experimental feed cone containing the X- and K-band equipment was to be removed at the end of November until late in January 1973 to upgrade it for a Mariner Venus/Mercury 1973 flight project S/X-band experiment. For this reason, the Quasar Patrol received two periods of observations in November. One of these was terminated prematurely because of antenna mechanical problems; nevertheless, about half of the nominal 24-h pass produced satisfactory data.

The Quasar Patrol, initiated during a previous reporting period, was continued, although with the schedule modifications mentioned. This activity accounts for most of the time provided to the non-NASA and university radio astronomers under the auspices of the RAES Panel. Results of these observations were included in presentations made by the experimenters at the Sixth Texas Symposium on Relativistic Astrophysics in New York, December 19–22, 1972. The reports discussed changes in the sources observed and demonstrated the need for the regular observations instituted by the Quasar Patrol.

The experiments sponsored by OSS and reported on previously (Refs. 2–9) continued with the search for interstellar microwave lines and observations of Jupiter and Uranus. The latter observations were terminated for the year because of the increasing range to Jupiter. A new observation on the 64-m antenna was that of pulsars at K-band (14.7 GHz). Announcement of this detection is being made to scientific periodicals. Observations were also made at S- and X-band using a 64-m antenna. Regular observations of Venus and Mercury by radar continued for the purpose of providing an improved ephemeris for the Mariner Venus/Mercury 1973 project.

The program on Earth Dynamics, sponsored by the Office of Applications (OA), repeated observations between the 64-m antenna at the Mars DSS and the 26-m antenna at the Echo DSS to obtain statistical data for the determination of the baseline between the stations with greater accuracy. The observations made during previous reporting periods were for the purpose of checking out equipment used to perform these observations.

References

1. Stevens, R., "Use of NASA/JPL Deep Space Network Facilities for Radio Astronomy," *Bulletin of the American Astronomical Society*, Vol. 4, No. 2, 1972, p. 305.

2. Linnes, K. W., Sato, T.; and Spitzmesser, D., "Radio Science Support," in *The Deep Space Network Progress Report*, Technical Report 32-1526, Vol. III, pp. 46–51, Jet Propulsion Laboratory, Pasadena, Calif., June 15, 1971.

3. Linnes, K. W., "Radio Science Support," in *The Deep Space Network Progress Report*, Technical Report 32-1526, Vol. IV, pp. 47–48, Jet Propulsion Laboratory, Pasadena, Calif., Aug. 15, 1971.

4. Linnes, K. W., "Radio Science Support," in *The Deep Space Network Progress Report*, Technical Report 32-1526, Vol. V, pp. 42–44, Jet Propulsion Laboratory, Pasadena, Calif., Oct. 15, 1971.

5. Linnes, K. W., "Radio Science Support," in *The Deep Space Network Progress Report*, Technical Report 32-1526, Vol. VI, pp. 43–45. Jet Propulsion Laboratory, Pasadena, Calif., Dec. 15, 1971

6. Linnes, K. W., "Radio Science Support," in *The Deep Space Network Progress Report*, Technical Report 32-1526, Vol. VII, pp. 29–31, Jet Propulsion Laboratory, Pasadena, Calif., Feb. 15, 1972.

7. Linnes, K. W., "Radio Science Support," in *The Deep Space Network Progress Report*, Technical Report 32-1526, Vol. VIII, pp. 24–28, Jet Propulsion Laboratory, Pasadena, Calif., Apr. 15, 1972.

8. Linnes, K. W., "Radio Science Support," in *The Deep Space Network Progress Report*, Technical Report 32-1526, Vol. X, pp. 52–58, Jet Propulsion Laboratory, Pasadena, Calif., Aug. 15, 1972.

9. Linnes, K. W., "Radio Science Support," in *The Deep Space Network Progress Report*, Technical Report 32-1526, Vol. XI, pp. 26–29, Jet Propulsion Laboratory, Pasadena, Calif., Oct. 15, 1972.

Table 1. DSN support to Radio Science experiments

Month	Hours of support to experiments sponsored by			
	RAES	OSS	OA	Total
September	–	90	–	90
October	32	108.5	15	155.5
November	46.5	102	16	164.5
December	21	76	–	97
Total	99.5	376.5	31	507.0

Table 2. Radio Science experiments involving 64- and 26-m antenna facilities

Experiment	Purpose	Experimenters	DSN facility	Dates
RAES Panel				
Quasar Patrol	To make detailed measurements on radio galaxies and quasars at 2.3, 7.8, and 15.6 GHz; to search for weak compact sources in the nucleus of extended radio galaxies and quasars; to monitor time variations in fine structure and apparent positions of quasars	Group A D. S. Robertson, WRE A. J. Legg, WRE J. Gubbay, WRE A. T. Moffet, Caltech G. Nicholson, CSIR	DSS 14 (used with MIT Haystack and NRAO 42-m antenna)	
		Group B J. J. Broderick, NAIC B. G. Clark, NRAO M. H. Cohen, Caltech D. L. Jauncey, Cornell K. I. Kellermann, NRAO G. H. Purcell, Caltech D. B. Shaffer, Caltech		Oct. 23, 1972 Nov. 25, 1972
		Group C T. A. Clark, GSFC R. M. Goldstein, JPL H. J. Hinteregger, MIT C. A. Knight, MIT G. E. Marandino, Univ. of Maryland G Resch, Univ. of Maryland A. E. Rogers, Haystack Observatory I. I. Shapiro, MIT A. R. Whitney, MIT		Nov. 7, 1972
Ionized hydrogen observations	To detect free-free emission from ionized gas in globular clusters	J. Hills, Univ. of Michigan M. Klein, JPL	DSS 14	May 22, 29, 1972 June 11, 23, 30, 1972 Oct. 11, 1972
Weak radio source observations	To measure the "confusion distribution" of weak radio sources at 2.3 GHz	D. L. Jauncey, Cornell Univ. M. J. Yerbury, Cornell Univ. J. J. Condon, Cornell Univ. D. J. Spitzmesser, JPL	DSS 14	June 5, 12, 1972 July 5, 13, 1972 Dec. 6, 18, 1972

Table 2 (contd)

Experiment	Purpose	Experimenters	DSN facility	Dates
OSS				
Interstellar microwave low-noise spectroscopy	To search for interstellar molecules at 14 GHz	S. Gulkis, JPL T. Sato, JPL B. Zuckerman, Univ. of Maryland D. Cesarsky, Caltech J. Greenstein, Caltech	DSS 14	Apr. 2, 10, 18, 1972 May 2, 6, 14, 17, 1972 June 4, 19, 1972 Aug. 5, 1972 Sept. 5, 14, 19, 1972 Oct. 10, 17, 27, 30, 1972 Nov. 2, 10, 11, 17, 23, 26, 29, 1972
Planetary radio astronomy	To study radio emissions of Uranus and Jupiter at 14 GHz	G. Gulkis, JPL B. Gary, JPL M. Klein, JPL M. Jansen, JPL Resident Research Associate E. Olsen, JPL Resident Research Associate P. Rosenkranz, JPL Resident Research Associate	DSS 14	Apr. 29, 30, 1972 July 14, 1972 Aug. 3, 1972 Sept. 7, 21, 28, 1972 Oct. 3, 4, 21, 28, 31, 1972 Dec. 20, 1972
Pulsar observations	To study emissions from various pulsars at S-, X-, and K-bands	G. Downs, JPL G. Morris, JPL P. Reichley, JPL	DSS 14	Nov. 18, 21, 30, 1972 Dec. 1, 8, 21, 1972
Venus/Mercury radar ranging	To provide improved ephemerides of Venus and Mercury for Mariner Venus/Mercury 1973 Project	J. Lieske, JPL R. Goldstein, JPL	DSS 14	Sept. 1, 15, 19, 26, 1972 Oct. 3, 10, 1972 Nov. 24, 28, 1972 Dec. 1, 5, 8, 20, 26, 1972
OA				
Earth Dynamics VLBI	To demonstrate NRAO Mark II digital recording terminal by measuring the baseline between DSSs 14 and 12	P. MacDoran, JPL J. Fanselow, JPL J. Thomas, JPL J. Williams, JPL	DSS 14 DSS 12	Aug. 15, 1972 Oct. 14, 18, 1972 Nov. 5, 20, 1972

Block IV Subcarrier Demodulator Assembly Acquisition Problem

R. B. Crow
RF Systems Development Section

J. K. Holmes
Communications Systems Research Section

R. C. Tausworthe
Telecommunications Division

The Block IV Subcarrier Demodulator Assembly (SDA) has been designed with four loop bandwidths. Two of these bandwidths are designed with unity damping, while the other two are achieved by increasing the loop gain. Normal tracking can be done in any one of the four bandwidths, or the "high-gain" bandwidths of the set may be used as an acquisition bandwidth. The transition from acquisition to tracking mode should be accomplished by providing a slow reduction in gain in order to limit the peak phase error during the transition time. Excessive phase errors can lead to loss of lock or a greatly diminished quality of data. Experimental evidence and preliminary analysis have shown that the original phase error transient due to acquisition should be allowed to die out before bandwidth reduction is initiated in order to minimize the peak phase error. This article documents the experiments and analysis that led to the bandwidth reduction procedure used in the Block IV SDA so that acquisition is complete 80 seconds after phase lock for the 3.9- to 0.5-Hz configuration and 1300 seconds after phase lock for the 0.23- to 0.03-Hz configuration.

I. Introduction

The Block IV Subcarrier Demodulator Assembly (SDA) has been designed with four loop bandwidths: 0.03, 0.23, 0.5, and 3.9 Hz. Two of these bandwidths (0.03 and 0.5 Hz) have been designed with critical damping and will be called narrow-bandwidth, normal-gain and wide-bandwidth, normal-gain, respectively. These two bandwidths can be increased to 0.23 and 3.9 Hz by increasing the gain by ten to one, and are then called narrow-bandwidth, high-gain and wide-bandwidth, high-gain.

Two fundamental acquisition techniques are possible: (1) change the loop time constants and the loop gain (i.e., keep the damping factor constant) and (2) change only the loop gain (increase the damping factor when the loop gain is raised). The first approach was not used since it is

more difficult to implement. Furthermore, a smooth bandwidth transition is not practical to implement when both time constant and gain are changed in such a manner as to keep the damping constant. The second approach of gain reduction to effect a bandwidth reduction can be accomplished either by an instantaneous gain switch or a gradual change in the gain.

Figure 1 illustrates a series of tests (all testing discussed in this article will be limited to the more difficult narrow-bandwidth case) in which the phase transient was measured after T_1 seconds had elapsed between the last cycle slip and when the gain was switched instantaneously from the high value to the normal value. In this case, the results of this test indicate that if T_1 is made large enough (approximately 1000 seconds), the transient can be held to an acceptably low level, since in the range of anticipated frequency offsets, the effect due to frequency offset is negligible. This test was repeated in the presence of design point noise ($S/N_0 = +8$ dB), and the peak phase error increased to an unacceptable level.

To gain an insight into the problem, a control loop was developed such that the loop gain was held high until the error was reduced to some preset value (ϕ_E), and then the loop gain was allowed to reduce in such a fashion as to keep the phase error constant at ϕ_E. This experiment (see Fig. 2) illustrates that not only must we wait T_1 seconds for the acquisition transient to die out, but that we require T_2 seconds to reduce the gain. Further, it establishes an experimental value for T_2 that will be useful in confirming the analysis that follows.

The preferred acquisition technique is to acquire in the narrow-bandwidth, high-gain mode and allow the acquisition transient T_1 seconds to die out and then smoothly reduce the bandwidth to the narrow-bandwidth, normal-gain mode in T_2 seconds.

Two more experiments were run to confirm the relationship between T_1 and T_2 and the peak phase error. Figure 3 shows T_2 held constant and illustrates that, even with a "soft switch," the initial transient must be allowed to die out. The experiment shown in Fig. 4 was run holding T_1 constant and illustrates the importance of properly controlling the time T_2 allowed for the gain reduction.

II. Analysis

The two aspects of the problem that are analyzed here are the transient settling time T_1 and the time to reduce the gain to 10% of the initial value, which is denoted by T_2. Both calculations are based on the assumption that there is no noise present in the loop. A study is in progress to consider the case in which there is noise. Based on the experimental evidence of Figs. 1–4, it is anticipated that, even at threshold, the two times T_1 and T_2 will not change appreciably from those predicted in this analysis.

A. Transient Response

In order to make the problem amenable to solution, we assume that the phase error is always small enough so that the linear model is applicable. Figure 5 shows the baseband model of a linear phase-locked loop.

If the loop filter is given by

$$F(s) = \frac{(1+\tau_2 s)^2}{(1+\tau_1 s)^2} \tag{1}$$

then the differential equation describing the loop phase error $\phi(t)$ is given by

$$\tau_1^2 \dddot{\phi}(t) + (2\tau_1 + G\tau_2^2)\ddot{\phi}(t) + (1 + 2G\tau_2)\dot{\phi}(t) + G\phi(t) = \dot{\theta}_i + 2\tau_1\ddot{\theta}_i + \tau_1^2\dddot{\theta}_i \tag{2}$$

where $G = K_v K$ is the open-loop gain of the loop and contains the limiter suppression gain as well. The case of interest occurs when the input has a doppler shift Ω_0, so that

$$\frac{d\theta}{dt} = \Omega_0 \tag{3}$$

In order to specify a solution, the three initial conditions must be specified:

$$\begin{aligned} \phi(0) &= \phi_0 \\ \dot{\phi}(0) &= \dot{\phi}_0 \\ \ddot{\phi}(0) &= \ddot{\phi}_0 \end{aligned} \tag{4}$$

Following frequency acquisition, we can arbitrarily define $t = 0$ to be the time at which the initial conditions are specified. Taking Laplace transforms of Eq. (2), we find that the Laplace transform of the phase error $\Phi(s)$ is given by

$$\Phi(s) = \frac{\Omega_{0/s} + \tau_1^2\ddot{\phi}_0 + [\tau_1^2 s + (2\tau_1 + G\tau_2^2)]\dot{\phi}_0}{\tau_1^2 s^3 + (2\tau_1 + G\tau_2^2)s^2 + (1 + 2G\tau_2)s + G} + \frac{[\tau_1^2 s^2 + (2\tau_1 + G\tau_2^2)s + (1 + 2G\tau_2)]\phi_0}{\tau_1^2 s^3 + (2\tau_1 + G\tau_2^2)s^2 + (1 + 2G\tau_2)s + G} \tag{5}$$

From the final value theorem, we can show that the steady-state phase error is given by

$$\phi_{ss} = \lim_{t \to \infty} \phi(t) = \lim_{s \to 0} S\Phi(s) = \frac{\Omega_0}{G} \tag{6}$$

In order to obtain the inverse Laplace transform of $\Phi(s)$, we must factor the denominator of the $\Phi(s)$ polynomial in Eq. (5). Using the parameters of the narrow-band, high-gain mode, $G = 568$, $\tau_1 = 5{,}250$, and $\tau_2 = 148$, and the use of a root finding program the phase error was found to be given by

$$\phi(t) = 0.0176\Omega_0 + Ae^{-0.00603t} + Be^{-0.44075t} + Ce^{-0.00775t} \tag{7}$$

where A, B, and C depend on the loop parameters as well as the initial conditions ϕ_0, $\dot{\phi}_0$, and $\ddot{\phi}_0$, which are unknown. It has been found experimentally that it is necessary to wait until the phase error and its derivatives are very small before the gain is reduced to narrow the loop bandwidth. It is clear that if the first exponential term is reduced to, say, 2% of its final value by waiting until some time T_1, then at that time, $\phi(t)$ is less than or equal to 2% of its initial value. If we arbitrarily select 2% (3.9 time constants) as the required value, then we must wait

$$T_{1\,(\text{narrow})} = 648 \text{ seconds} \tag{8}$$

before the gain is reduced. This value of T_1 has been verified experimentally (see Fig. 3).

In the wide-band, high-gain mode, using the parameters $\tau_1 = 5{,}250$, $\tau_2 = 8.91$, and $G = 2.63 \times 10^6$, we find that

$$\phi(t) = 3.85 \times 10^{-7}\,\Omega_0 + A'e^{-0.10063t} + B'e^{-0.12909t} + C'e^{-0.73454t} \tag{9}$$

where, as before, A', B', and C' depend on the above loop parameters as well as ϕ_0, $\dot{\phi}_0$, and $\ddot{\phi}_0$. We find that the phase error is no larger than 2% of its maximum value just after frequency acquisition in the wide-band acquisition mode when $t = T_1$, where

$$T_{1\,(\text{wide})} = 40 \text{ seconds}$$

B. Required Gain Change to Maintain Constant Phase Error

After the phase error is reduced to a sufficiently small value following acquisition, the gain is reduced to bring the loop into the narrow-bandwidth, normal-gain mode. Generally speaking, a quick reduction of the gain causes the phase error to increase dramatically, with the attendant possibility of losing lock (see Figs. 1 and 4). A reasonable approach to the gain reduction problem is to reduce the gain at a rate such that the phase error does not exceed some maximum value. Under a maximum phase error constraint, the optimal procedure for minimizing the time to reduce the gain to 10% of its initial value is to hold the phase error constant at the maximum value by reducing the gain accordingly. We now derive the loop equation in the case in which the loop gain is a function of time, so that we can determine the optimal gain contour and T_2. In Fig. 6, each low-pass filter has the transfer function

$$H(s) = \frac{1 + \tau_2 s}{1 + \tau_1 s} \tag{11}$$

To simplify the calculations, we let (using $\tau_2 << \tau_1$)

$$H(s) \cong \alpha + \frac{1}{\tau_1 s}, \qquad \alpha = \frac{\tau_2}{\tau_1} \tag{12}$$

We assume that $G(t)$ is an arbitrary function of time. Then, assuming that the initial voltages v_0 and v_1 are stored on the capacitors, we have (for convenience letting $t = 0$ represent the time T_1 s after acquisition)

$$\theta - \phi = \int_0^t \left\{ v_1 + \alpha \left[v_0 + \alpha AK\phi + \frac{1}{\tau_1}\int_0^{t'} AK\phi(t'')\,dt'' \right] + \frac{1}{\tau_1}\int_0^{t'} \left[v_0 + \alpha AK\phi + \frac{1}{\tau_1} AK\phi \right] dt'' \right\} dt' \tag{13}$$

If we normalize time by

$$\tau = \frac{t}{\tau_2} \tag{14}$$

and define a new gain parameter $q(t)$ (the gain contour) by

$$q(t) = \frac{G(t)\,\tau_2^3}{\tau_1^2} \tag{15}$$

then, by suitable differentiation, we can show that Eq. (13) becomes

$$\phi(\tau)\ddot{q}(\tau) + (2\dot{\phi}(\tau) + 2\phi(\tau))\dot{q}(\tau) + (\ddot{\phi}(\tau) + 2\dot{\phi}(\tau) + \phi(\tau))q(\tau) = \dddot{\theta}(\tau) - \dddot{\phi}(\tau) \tag{16}$$

In the case where the phase error and the input phase are constant, the differential equation becomes

$$\ddot{q}(\tau) + 2q(\tau) + \dot{q}(\tau) = 0 \tag{17}$$

The solution is given by

$$q(\tau) = (A + B\tau)\, e^{-\tau}, \qquad \tau \geqq 0 \tag{18}$$

In order to evaluate the unknown constants A and B, we note that at $\tau = 0$ (the time when the phase error is first held constant), the charge on the capacitors is constant. By differentiating Eq. (13) once, normalizing using Eq. (14), and letting $\tau = 0$, we get

$$\dot{\theta}(0) - \dot{\phi}(0) - q(0)\,\phi(0) = (v_1 + \alpha v_0)\,\tau_2 \tag{19}$$

Since the phase error $\phi(t)$ is continuous near zero and v_0 and v_1 are constant at $\tau = 0$, we see that the right-hand side of Eq. (19) is constant. Letting the time 0^- denote the time just before the phase error is held constant and 0^+ the time just after, we obtain from Eq. (19) that

$$q(0^+) = q(0^-) + \frac{\dot{\phi}(0^-)}{\phi(0^-)} \tag{20}$$

By differentiating Eq. (13) twice and using Eq. (14), we have, at $\tau = 0$,

$$\ddot{\theta}(0) - \ddot{\phi}(0) - \dot{q}(0)\,\phi(0) - q(0)\,\dot{\phi}(0) - 2q(0)\,\phi(0) = v_0\alpha\tau_2 \tag{21}$$

Since the right-hand side is constant at $\tau = 0$, we can show that

$$\dot{q}(0^+) = \frac{\ddot{\phi}(0^-)}{\phi(0^-)} + \frac{\dot{\phi}(0^-)}{\phi(0)}\,[q(0^-) - 2] \tag{22}$$

Hence, in order that the phase error be held constant, we require (converting derivatives on τ to derivatives on time) that the optimal gain contour using Eqs. (20) and (22) in Eq. (18) is given by

$$q(t) = \left\{ q(0^-) + \tau_2 \frac{\dot{\phi}(0^-)}{\phi(0)} + \left[q(0^-) + \tau_2^2 \frac{\ddot{\phi}(0^-)}{\phi(0^-)} + \tau_2 \frac{\dot{\phi}(0^-)}{\phi(0^-)} \left(q(0^-) - 1 \right) \right] \frac{t}{\tau_2} \right\} e^{-t/\tau_2} \tag{23}$$

which is valid for $t > 0^+$.

The initial conditions are in general unknown. However, under the assumption that we wait until the phase error has decayed to about 2% of its maximum value obtained after frequency acquisition, it can be shown that both

$$\tau_2 \frac{\ddot{\phi}(0^-)}{\phi(0^-)}$$

and

$$\tau_2 \frac{\dot{\phi}(0^-)}{\phi(0^-)}$$

are close to unity and $q(0^-)$ is 67.5, which is obtained by using Eq. (15) and $G = 568$, $\tau_1 = 5250$, and $\tau_2 = 148$, so that in the narrow-band, high-gain mode we have approximately

$$q(t) = \left(68 + \frac{134t}{\tau_2} \right) e^{-t/\tau_2} \tag{24}$$

Since the bandwidth depends on $q(t)$ by

$$w_l = 0.115 w_{l_0} q \left[\frac{q + 1.5}{q - 0.5} \right] \tag{25}$$

we see that a 10 to 1 reduction in $q(t)$ provides a 7.8 to 1 reduction in bandwidth. Using Eq. (24) we find that for $q(t)$ to drop to 6.75 (10% of 67.5) requires 680 seconds in the narrow-band mode and 41 seconds in the wide-band mode. The actual gain contour used for bandwidth reduction is an approximation to Eq. (24).

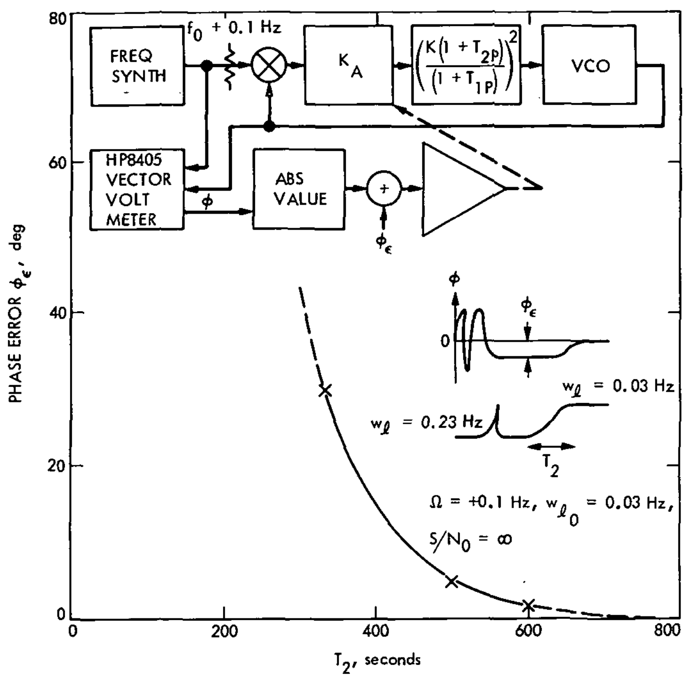

Fig. 2. Controlled phase error ϕ_ε vs. time T_2 to reduce gain to 10% of initial value

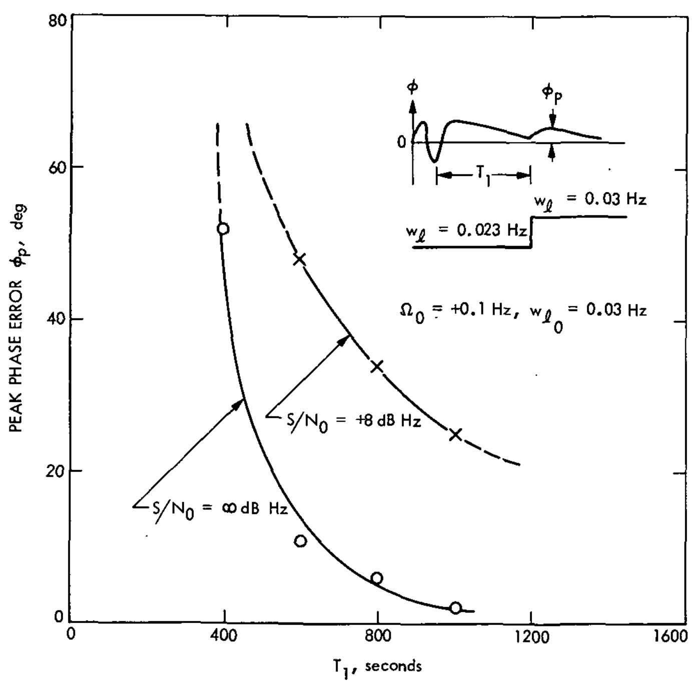

Fig. 1. Peak phase error vs. settling time T_1 for a step change in bandwidth

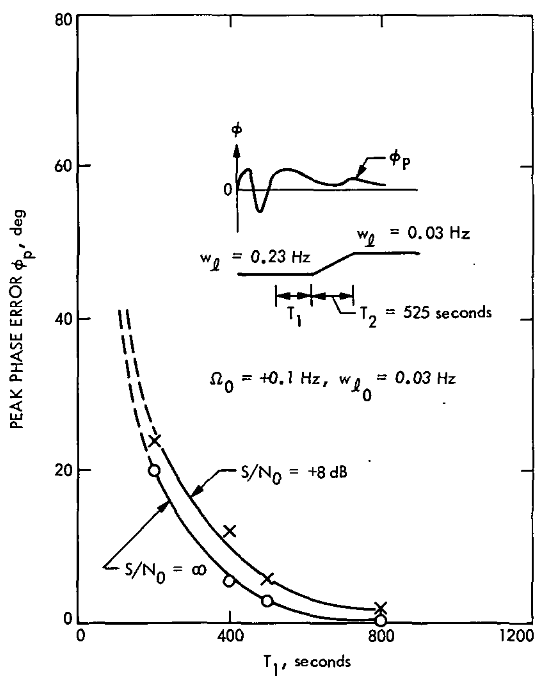

Fig. 3. Peak phase error vs. T_1 for a gradual change (T_2 = 525 s) in bandwidth

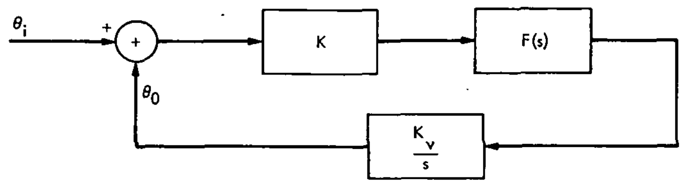

Fig. 5. Linear model of phase-locked loop

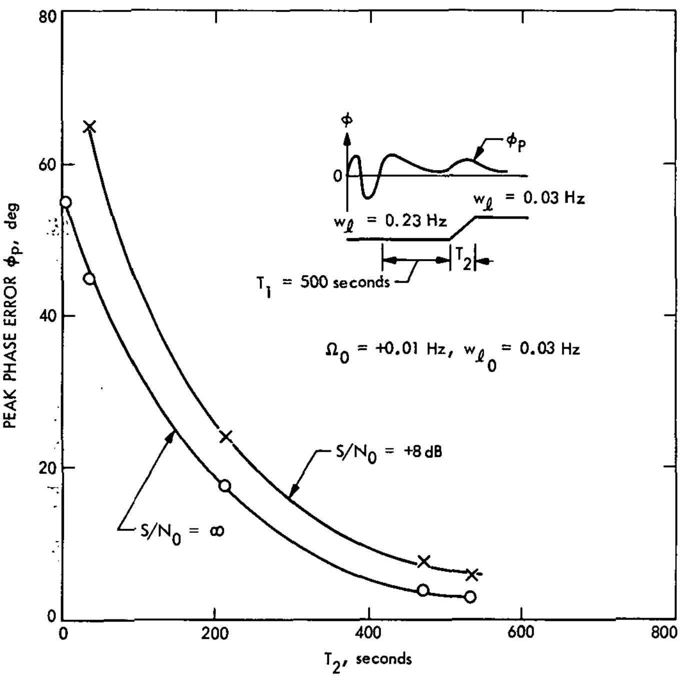

Fig. 4. Peak phase error vs. T_2 after phase transient is allowed to die out (T_1) for 500 s

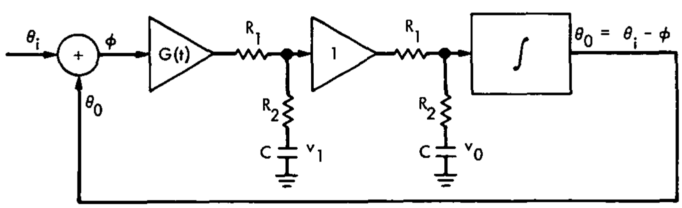

Fig. 6. Model of third-order loop showing initial capacitor voltages

Programmed Oscillator Software Development for High-Doppler-Rate Orbiting Spacecraft

R. Emerson
Communications Systems Research Section

The programmed oscillator (PO) can be used to track spacecraft signals. Orbiting spacecraft impose additional requirements upon the ephemeris used by the programmed oscillator. Modifications to the existing programmed oscillator were made. Experience with the tracking of Mariner Mars 1971 (MM'71) during superior conjunction shows that a receiver, assisted by the signal from the programmed oscillator, permits the tracking of high-doppler-rate signals close to the threshold of the receiver. The advantages of programmed oscillator assisted receiver operation include the reduction of stress upon the loop voltage-controlled oscillator (VCO), obviating the need for more than one VCO per receiver, and the provision of an acquisition aid for the receiver operators. This was demonstrated during the recent Mariner 1971 solar occultation, where no other tracking method could maintain lock.

I. Introduction

This article describes the modifications made to the programmed oscillator (PO) program, the effects of these changes, the source of the information used by the PO, and the additional requirements encountered with this information relative to an orbiting spacecraft. In addition, it discusses the conclusions that can be drawn from the use of the PO in an orbiting spacecraft tracking situation, such as that existing during Mariner 1971 superior conjunction.

It is appropriate to review the nature of the PO. From a hardware point of view, the PO consists of an oscillator that can be controlled remotely, a specialized interface device, a digital computer, and a special real-time program which controls the operation of all the attendant parts. Functionally, the PO is a device which tunes a receiver to the expected carrier frequency of a spacecraft. (For a more detailed description of the PO, see Ref. 1.) The first step in this process is the development of the mathematical model or ephemeris of the spacecraft signal.

II. Orbiting Spacecraft Ephemeris and Special Constraints

An ephemeris, computed from radio metric data, is used to generate predictions of the spacecraft frequency. The program used to perform this function is called the JPL PREDICTS SYSTEM (Ref. 2). The output of this program aids the station in tracking the spacecraft.

Because of the limited I/O and memory capacity of the MAC-16 computer used to drive the PO, it is necessary to condense the input to it. The form chosen is 14th-order Chebyshev polynomial. The ephemeris produced by the JPL PREDICTS SYSTEM is converted to the polynomial form by a Sigma 5 program, TRANSPOLY, which fits the point-by-point data of the ephemeris to a closed-form interpolating function.

The orbiting of a spacecraft around Mars or any planet produces rapid changes in doppler at periapsis. The effect of these rapid changes is a doppler curve over a pass for which the derivatives do not die out fast enough. Attempting to fit a 14th-order polynomial to these data results in residual errors that exceed acceptable limits. If, however, the ephemeris for the pass is segmented into small enough parts, each part will become fittable by a 14th-order polynomial.

The PO control program pre-computes values of the ephemeris. If, in attempting to compute such a value, the program finds that the argument of time is past the range of the polynomial, it signals for the next segment. The next segment will be loaded if the actual time of loading falls within its range of arguments. This constrains the successive segments to overlap in time.

These two segmentation modifications were added to the TRANSPOLY program along with the capability to produce a configuration deck. The configuration deck specifies parameters to the PO control program about the specific tracking situation.

III. Ephemeris Information Processing

Figure 1 gives an overall view of the ephemeris information flow. There are two separate inputs to this ephemeris processing diagram. The information flow will be described, assuming that the ephemeris is available from the orbit determination program on ephemeris tapes.

The requirements for an experiment or tracking situation are determined and submitted to the Tracking Group of the Network Analysis Team (NAT TRACK) as a request for predicts. NAT TRACK is responsible for translating these requirements into parameters acceptable to the JPL PREDICTS SYSTEM 360/75 program. The requirements and the planetary and spacecraft ephemeris information are combined in this program to produce a transmission file on a mass storage device. This file contains a point-by-point tabulation of the spacecraft tracking predicts, e.g., angular position, expected transmitter frequency (one- and two-way), best-lock uplink frequency, etc. When the transmission file is completed, it is dumped onto nine-track magnetic tape. This tape is copied to seven-track tape format by a utility 360/75 program so that it can be used by the Sigma 5 TRANSPOLY program for the next step in the process. The limited file space for the transmission file on the 360/75 may require the merging of several tapes into one for processing by TRANSPOLY. The program which performs this function is a Sigma 5 program called TAPMRG.

TRANSPOLY converts the information contained in the transmission file into a deck of cards containing one or more sets of polynomial constants. Furthermore, it will optionally produce the configuration deck for the Multi-Application Computer* programmed oscillator (MAC-PO).

The resulting deck of cards is further processed by the XDS 930 program EPHGEN, which converts the card images to paper tape and appends checksum information. This permits the tape to be verified for correct punching prior to its required use. When the experiment is ready to proceed, the paper tape is read and checked by the MAC-PO control program, and the information is used to control the oscillator.

IV. TRANSPOLY Program

Figure 2 shows some of the details of the TRANSPOLY program. This program is based on a 7094 FORTRAN IV SUBROUTINE package developed by C. Lawson of the Science and Engineering Computing Section. When the program is entered, it reads a control deck which specifies parameters for the run (e.g., observable(s) to be output, number of points per segment, number of points to overlap, etc.). Using this information, the program reads the Transmission file from tape, converting it to the required format. The program may optionally list the Transmission file. If an end-of-file is encountered during the reading, processing is terminated. The Transmission file format is described in Ref. 3. If the end-of-pass has not been reached, the program returns to the reading operation. When enough points have been read to delineate a segment or the end-of-pass is encountered, the program computes the fitting polynomial constants by the least-squares method. The data are fit to a 14th-order Chebyshev polynomial with uniform weighting. A configuration deck is output if required; then the appropriate polynomial constants deck is punched, together with a listing of the

*Lockheed trade name.

residuals if desired. The program computes outputs for segments until the end-of-pass. Although it is not explicitly shown in the figure, the program will continue to run passes until the control deck signals the end of the job.

V. Modifications to the PO Program

The PO program, as initially written, assumed that the ephemeris for a pass would be in one segment only, that the doppler rate would not change sign during the pass, that the doppler excursions would be limited to 20 kHz over a pass, and that the doppler rate would not exceed 21.55 Hz/s. All of these assumptions are violated by orbiting spacecraft tracking requirements. This change in requirements necessitated the following modifications to the PO program.

The most significant change to the program is one that enables it to recognize the end of a segment and take the appropriate action. With each set of ephemeris information in polynomial form, there are parameters that give the time interval over which this set of data is valid. When the program is running, it has calculated values for the ephemeris ahead of those needed. These values lie between 96 and 128 s in the future. A new calculation is made every 32 s. When a calculation is attempted that lies outside the bounds for which the polynomial constants are valid, the program, as modified, requests the next segment of ephemeris polynomial constants. It takes 3.2 s to read the new segment into the computer. During this time, a portion of the normal processing must be suspended. The effect on the output of the PO is as follows.

During the time that the computer is reading the new data, no new control values are given to the PO control interface. Since the control value is a rate in frequency, the PO continues to track at the last rate supplied. For MM'71, the expected maximum doppler acceleration was estimated at 0.013 Hz/s^2. This represents a phase transient of at most 54 deg at S-band.

The effect of this transient on an open-loop receiver is not detectable when such a receiver is used for observing the spectra of the received signal. Its effect on a closed-loop receiver is also undetectable, since the tracking loop continues to track the signal.

After the new ephemeris has been read, normal processing is resumed, and the new data are converted for use within the computer. At the next request for a future value, the program finds that the new ephemeris set has replaced the old; therefore, the requested time is within the bounds of the ephemeris constant set, and processing continues without further interruption.

Because of the higher doppler rates and extremes encountered while tracking an orbiting spacecraft, it was necessary to change the range of control of the PO. This was accomplished by inserting the search oscillator into the next higher decade, i.e., the 1000-Hz instead of the 100-Hz decade, thus permitting the continuous tracking of doppler extremes to ± 96 kHz, and doppler rates to 215.5 Hz/s. Under these conditions, the least increment of phase control is 0.18 deg.

The change in sign of the doppler rate at periapsis requires that the initial value of the search oscillator be at its midpoint. This permits the longest possible tracking time before a decade change is required of the PO.

VI. Results of PO-Assisted Tracking

The modified PO control program was employed during MM'71 superior conjunction. The output of the PO was used to control two open-loop receivers and one closed-loop receiver at the same time. The open-loop receivers measured the doppler spreading in both the left- and right-circular polarized modes. The closed-loop receiver gathered ranging information for the relativity experiment.

In order to determine the validity of the closed-loop-assisted (synchronous-assist) mode of tracking, experiments were designed to determine the effect, if any, of the PO on the doppler residuals. The uplink transmitter was interrupted for a time to ascertain the effect of loss of signal upon the doppler residuals. One round-trip light time later, it was possible to determine, from the doppler residuals alone, that loss of signal had occurred. A comparison of the doppler residuals with and without PO assistance showed no detectable difference between the two conditions.

By monitoring the performance of the closed-loop receiver, the doppler residuals, and the PO output when ephemeris segments were read into the PO computer, it was determined that no degradation of the overall performance occurred. Similar studies of the performance of the open-loop receivers also showed no degradation.

VII. Conclusions

The use of the MAC-PO to assist in the tracking of an orbiting spacecraft by a closed-loop ground receiver

has been shown to be practical and necessary. The synchronous-assist mode of receiver operation has proven successful in the tracking of high-doppler-rate signals close to the threshold of the receiver. Although the receiver was modified to permit this type of operation, none of its essential characteristics were changed (in those situations in which other tracking techniques could be applied). For example, a comparison of the doppler residuals with and without the PO assist showed no discernible effect by the PO. Also, in the absence of signal, the doppler residuals behaved in an identical way with or without the PO.

An expansion of the PO-assisted system can provide both one- and two-way tracking ability, as well as relaxing the constraints upon the ground receiver loop VCO. In the PO-assisted mode, the VCO will be required to track only the residuals of doppler (the difference between the predicted and the actual doppler), which cover a far smaller frequency range than the doppler itself. (The worst case during MM'71 was ±500 Hz at S-band or ±5.2 Hz at the VCO frequency with PO assist, compared to doppler extremes of ±26,000 Hz at S-band or ±270 Hz at the VCO frequency without PO assist.) Typical values for the residuals of MM'71 were ±15 Hz at S-band or ±0.156 Hz at the VCO frequency at periapsis during conjunction.

The use of this technique can obviate the need for more than one VCO per receiver for all tracking situations. In addition, since there is but one model predicting the doppler for a given spacecraft, one PO can provide the primary tracking information for any number of receivers assigned to a spacecraft. The PO can also aid in the acquisition of the spacecraft signal by providing real-time doppler residuals at each site.

References

1. Winkelstein, R., "Minicomputer-Controlled Programmed Oscillator," in *JPL Quarterly Technical Review*, Vol. 1, No. 3, pp. 79–87, Jet Propulsion Laboratory, Pasadena, Calif., Oct. 1971.

2. "The JPL Predict System," in *Multimission Real-Time Tracking Subsystem User's Guide—Model 5*, 900-444; Rev. C, Section 5, pp. 5–1 ff, Jet Propulsion Laboratory, Pasadena, Calif., Mar. 1972 (JPL internal document).

3. "TRK-2-2 DSN Tracking System Interfaces," in *Deep Space Network System Requirements—Detailed Interface Design*, 820-13; Rev. A; Change 31, Jet Propulsion Laboratory, Pasadena, Calif., Nov. 1972 (JPL internal document).

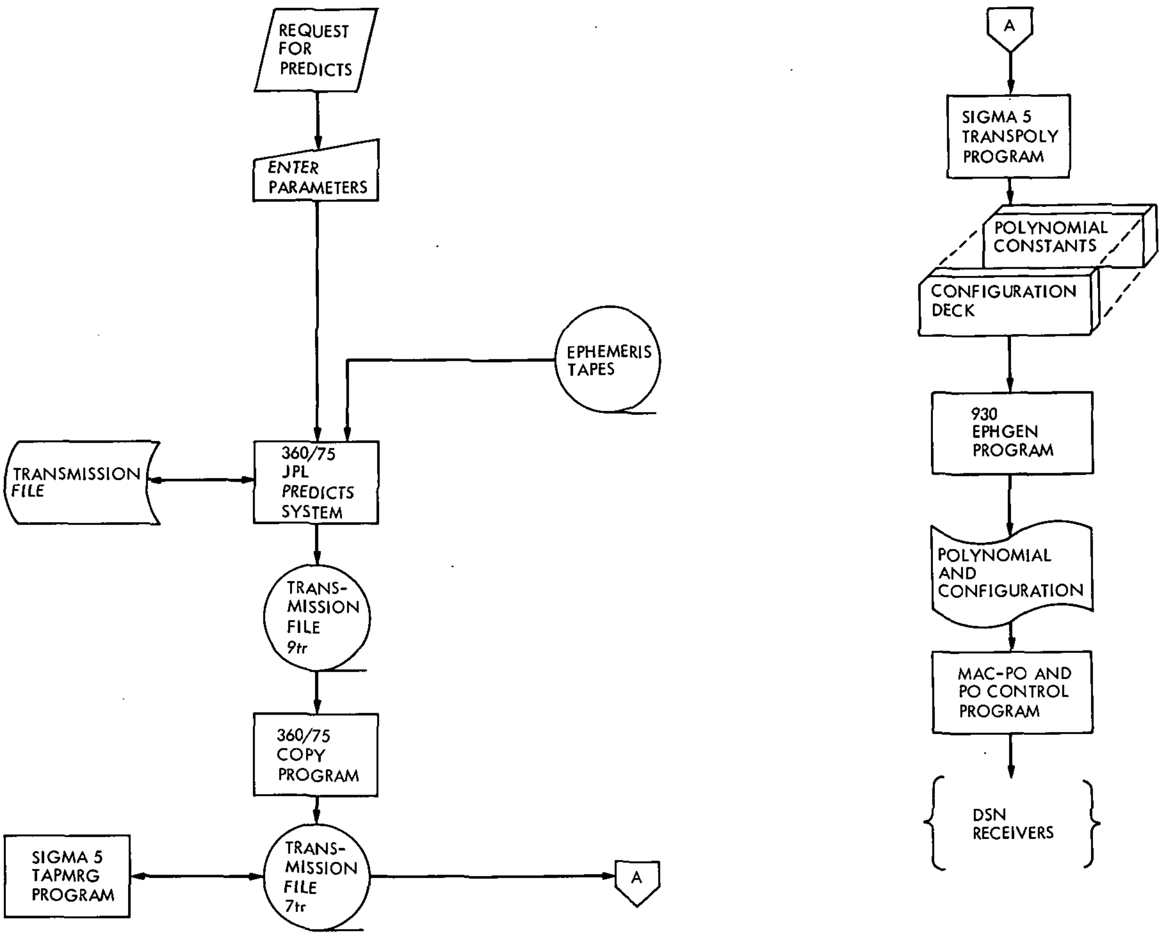

Fig. 1. Ephemeris information flow diagram

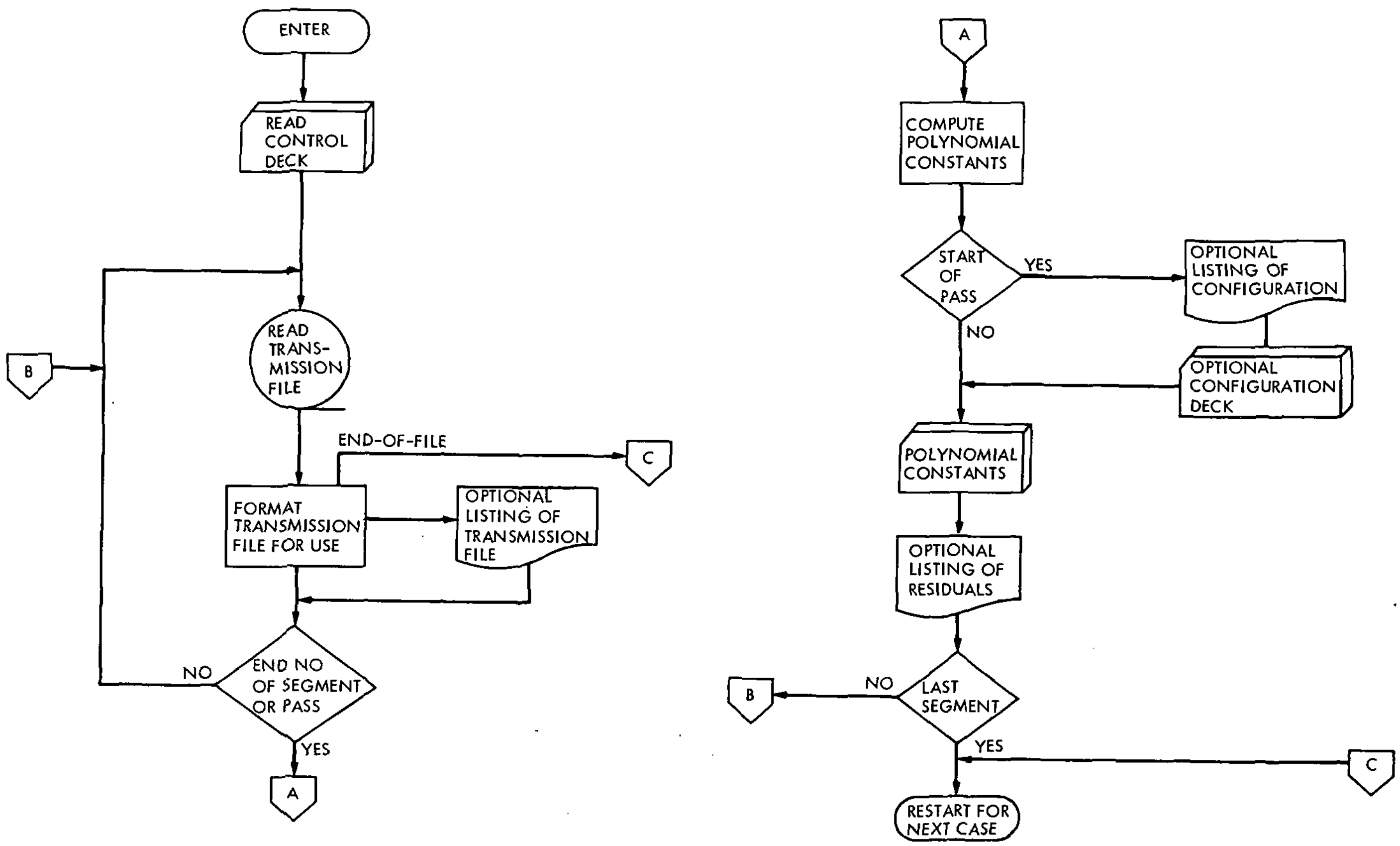

Fig. 2. TRANSPOLY block diagram

Programmed Oscillator Tracking Accuracy Measurements

R. F. Emerson
Communications Systems Research Section

The programmed oscillator has previously been shown to accurately track the low doppler rates encountered in cruise phase spacecraft and planetary radar situations. To determine whether the programmed oscillator (PO) would be able to track the high doppler rates encountered with orbiting spacecraft such as Mariner Mars 1971, further tests were conducted which demonstrated that the PO does have that capability. These tests further showed that the precision of the computations within the program used to drive the oscillator is of such a degree that no significant degradation in tracking ability is contributed by them.

I. Introduction

The programmed oscillator (PO) is an electronic frequency generation system that automatically produces a changing frequency as a precalculated function of time (Ref. 1). Tests of this device had shown its suitability for high-phase-stability tracking situations. Further tests were needed, and an experiment was designed which would determine the ability of the PO to reproduce the required frequency function of time for both low and high doppler rate conditions. Ephemerides for both Mariner Mars 1971 (MM'71) and Venus planetary radar were obtained and used to drive the PO. The output of the PO was measured, recorded, and compared to the ephemeris. These comparisons indicated that the error in tracking accuracy of the PO is less than the errors introduced by the high-quality measurement system; hence, the tracking error added is zero or negligible.

II. Measurement System

The measurement system block diagram is shown in Fig. 1. The PO receives the tracking information from the ephemeris paper tape. A 5-MHz reference signal provides a coherent reference for both the PO and the counter. A 1-s tick provides synchronization for the clock internal to the PO and for the arming of the counter for measurement. A modulo-N divider divides the 1-s tick to permit the repetitive sampling of the PO signal at known intervals. The printer records the results of the measurement for later processing.

The modulo-N divider was constructed specifically for these tests, but it has general utility. Referring to Fig. 2, this device consists of four functional units. The input buffer stage determines the trigger point and polarity of the input signal to be used by the divider circuit. It also provides proper drive for the divider circuit. The divider circuit produces one output pulse for every N input pulse as set by the manual entry switches. This output signal is buffered to provide two types of output: a 'trigger' signal, which is a replica of the buffered input signal, and a 'gate' signal, which is a square wave of frequency $1/2N$ times the input frequency. When grounded, the reset signal forces the divider to the value of N, the manual set point. *An output is produced N pulses after the reset line is released from ground.*

Two types of tests were performed with this system. In the first, the total output of the PO was measured once a minute and averaged for 10 s. In the second type, the expanded search oscillator (SO) output was measured and averaged for 1 min every other minute. While this latter test provides several orders of magnitude improvement in resolution, it does not measure the entire PO system.

III. Analysis of the Measurement System

The resolution of a counter measurement is determined by the duration of the measurement. The counter used in these tests was a Hewlett-Packard Computing Counter Model 5360A, which has a relative accuracy (Ref. 2)

$$\frac{\Delta f}{f} = \frac{\pm 1 \times 10^{-9}}{\text{measurement time}}$$

It was not possible to use arbitrarily long measurement times because the frequency being measured has an acceleration term. The error contributed by this acceleration term is derived below.

Assume that

$$f(t) = F_0 + \dot{F}t + \frac{\ddot{F}t^2}{2}$$

represents the frequency at time t. The average frequency over a period T is then

$$\bar{f}_T = \frac{1}{T}\int_t^{t+T} f(t)dt$$

$$= F_0 + \dot{F}\left(t + \frac{T}{2}\right) + \frac{\ddot{F}}{2}\left(t^2 + tT + \frac{T^2}{3}\right)$$

The frequency at the midpoint of the period is, however,

$$f(t_m) = F_0 + \dot{F}\left(t + \frac{T}{2}\right) + \frac{\ddot{F}}{2}\left(t^2 + tT + \frac{T^2}{4}\right)$$

and the error using this as an estimate of the average frequency is

$$\epsilon = \bar{f}_T - f(t_m) = \frac{1}{24}\ddot{F}T^2$$

If both Δf and ϵ can be made small enough, it is possible to use the instantaneous value of the ephemeris at the midpoint of the measurement interval for tracking accuracy comparisons. From the MM'71 ephemeris, it was determined that the maximum acceleration would not exceed 0.072 mHz/s^2 at the PO output, and that the PO output frequency for the MM'71 tracking situation is nominally 22 MHz. Table 1 shows counter (Δf) and acceleration (ϵ) error values in mHz for these parameters as a function of sample duration. The minimum of the sum of the two error terms was used to select the near-optimum sample duration of 10 s.

With the increase in resolution of 2×10^5 for the high-resolution test, an evaluation of the errors for this test yields a Δf of less than ± 0.1 mHz and an ϵ bounded by ± 11 mHz. The latter error term prohibits the use of the midpoint comparison described above. Therefore, the process of averaging was simulated with a computer program and this new ephemeris used to provide comparison values for this high-resolution test. By comparing results of these simulations with both 0.1- and 0.01-s integration steps, it was determined that the 0.1-s step produced values of sufficient accuracy for the comparisons.

IV. Results

The tests were conducted in April 1972 using both MM'71 and Venus radar ephemerides for the overall tests, and only the Venus ephemeris for the high-resolution test. Figures 3 and 4 plot the doppler rate and acceleration error (ϵ) for Venus planetary and MM'71 targets, respectively. Table 2 lists the extremes of doppler rate and ϵ for each target. Figures 5 and 6 are plots of the tracking error (measured–predicted) for the two targets. The maximum error encountered with Venus as the target was 0.006 Hz at the PO frequency. Translated to S-band, this represents a tracking error of 0.38 Hz at 2388 MHz. The same values for MM'71 are 0.003 Hz at the PO and 0.29 Hz at 2296 MHz. These figures serve to bound the tracking error but do not measure it well because they are of the same magnitude as the errors in measurement.

The bounds indicate, however, that the PO is able to track the ephemeris.

To determine how well the PO was tracking the input ephemeris, a high-resolution test was performed, and provided an increase in resolution of 2×10^5. The results of this measurement with Venus as the target were 150×10^{-9} Hz error at the PO output frequency, or 9.6×10^{-6} Hz at S-band (2388 MHz).

V. Conclusions

The two tests described above measure two different aspects of the PO. Each of these aspects indicates the tracking accuracy from a different point of view. The overall test of the PO demonstrates that it is capable of tracking both high and low doppler rates accurately. By measuring only the SO output, the high-resolution test ignores the effects of the fixed part of the synthesizer on the total output frequency. In effect, this test measures the software's ability to control the closed-loop portion of the PO.

Taken together, the two tests show that the PO is highly capable of tracking the high doppler rates of an orbiting spacecraft such as MM'71 and that the software does not significantly contribute to the tracking error.

References

1. Winkelstein, R., "Minicomputer-Controlled Program Oscillator," in *JPL Quarterly Technical Review*, Vol. 1, No. 3, pp. 79–87, Jet Propulsion Laboratory, Pasadena, Calif., Oct. 1971.
2. *Computing Counter 5360A Training Manual*, Hewlett-Packard, pp. 35–49.

Table 1. Counter (Δf) and acceleration (ϵ) errors for various sample durations

Sample duration	Δf $\times 10^{-3}$ Hz	ϵ $\times 10^{-3}$ Hz	$\Delta f + \epsilon$ $\times 10^{-3}$ Hz
100 ms	220	3×10^{-6}	220
1 s	22	3×10^{-3}	22
10 s	2.2	0.03	2.23
100 s	0.22	3	3.22

Table 2. Extrema of doppler rate and ϵ

Target	Doppler rate $\times 10^{-3}$ Hz/s	ϵ, Hz
Venus	-6.1	-1.2×10^{-6}
MM'71	-18	-0.3×10^{-3}

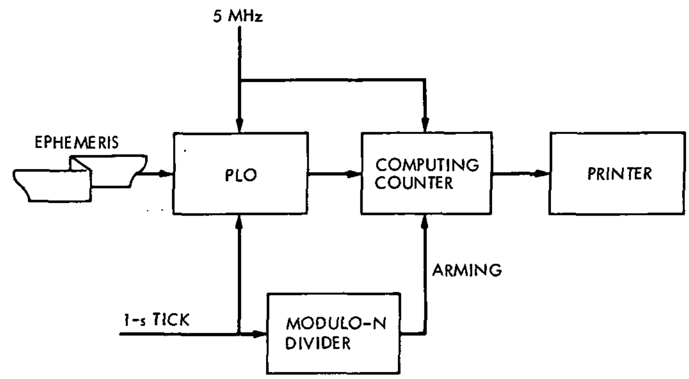

Fig. 1. Measurement setup

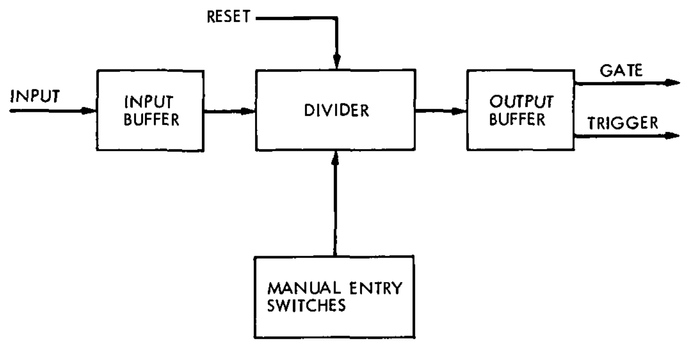

Fig. 2. Modulo-*N* divider block diagram

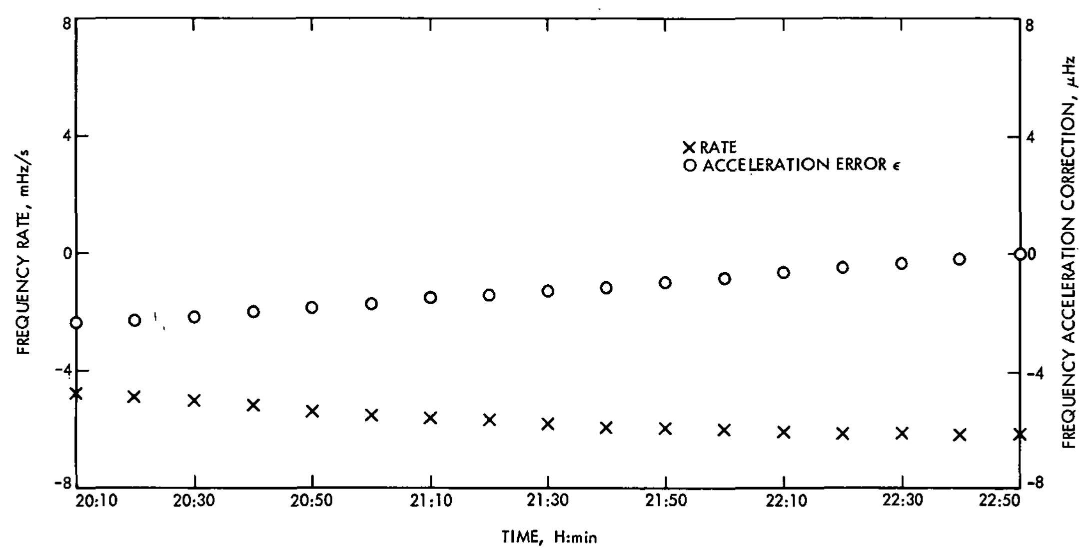

Fig. 3. Frequency functions—Venus

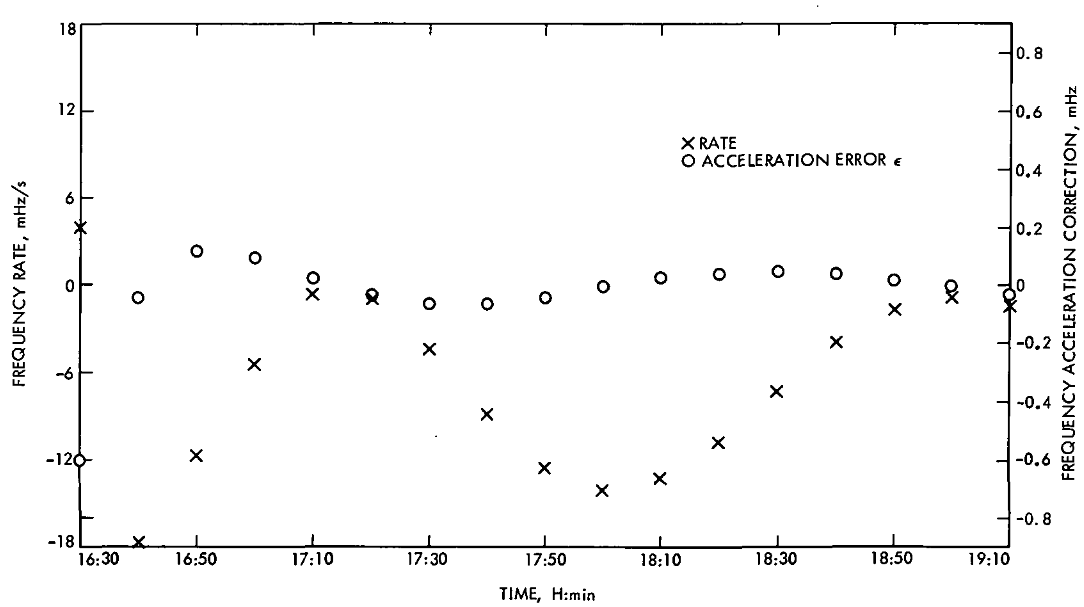

Fig. 4. Frequency functions—MM'71

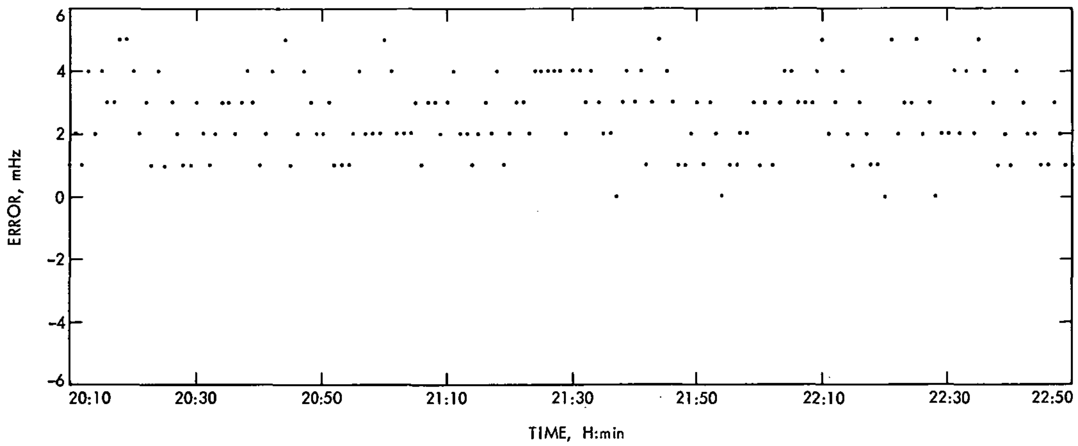

Fig. 5. PO tracking error—Venus

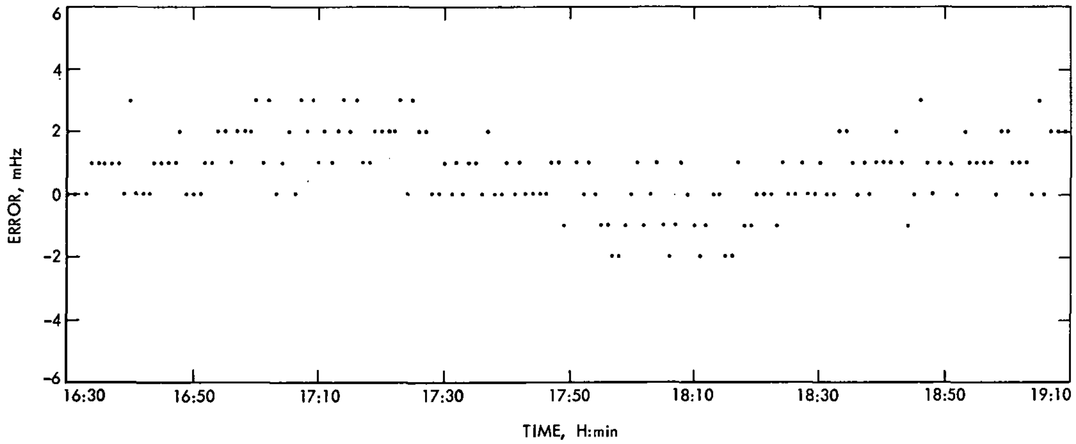

Fig. 6. PO tracking error—MM'71

Low-Noise Receivers: Microwave Maser Development

E. Wiebe
Communications Elements Research Section

This article summarizes the operational status of the closed-cycle refrigerators (CCRs) used to cool traveling-wave masers in the DSN. The improved CCRs have now replaced virtually all the old Model 210s. The reliability of the new system has lived up to all expectations. A continuing effort is made to simplify the system in order to further improve its reliability. The second part of this article describes a simple way of eliminating the oil pump which is used to cool and lubricate the compressor.

I. Performance of Closed-Cycle Refrigerators

In order to provide the Deep Space Instrumentation Facility with reliable operational equipment, the closed-cycle refrigerators (CCRs) developed at JPL (Ref. 1) have undergone extensive testing at JPL and at Goldstone for the past 6 years. Ten of these units were tested in R&D programs at JPL and at Deep Space Stations (DSSs) 13 and 14. A total of 333,000 h were logged on the running time meters located in the compressor assemblies. All units generally substantiate the specification that mechanical maintenance will not be required more than once a year.

An R&D X-band traveling-wave maser (TWM) was installed on the 64-m antenna at DSS 14 some 3 years ago and was used for many radio science experiments. It was also used to life test the refrigerator system, and no mechanical maintenance was performed during the test period. When it was recently removed from the antenna (because of DSS 14 scheduling), it had logged 23,000 h of trouble-free operation.

A charcoal trap in the helium gas supply line was serviced regularly, and proper start-up procedures were followed after each shut down, e.g., after electrical power outages.

Fourteen of the new CCRs have been installed as operational equipment in the DSN over the past 2 years, and these have logged over 100,000 h. Thus, a grand total of nearly half a million hours have been logged.

II. Oil-Lubricated Compressor

An ordinary air-conditioning compressor unit is used to supply the recirculating helium gas which is required in the CCR. The only modifications made in the unit are the addition of a small oil pump to the main drive shaft, and

the rearrangement of the valves for cascade operation of the two cylinders, which are normally in parallel.

The oil pump is used to inject oil into the helium gas to cool the compressor, as well as to prevent blow-by, and to provide upper cylinder lubrication. Filters easily separate the oil from the gas, and clean helium gas is supplied to the CCR. Occasionally, the positive-displacement, gear-type oil pump has failed and caused some worry. In a continuing effort to simplify and improve reliability in the system, a scheme has been developed for eliminating the oil pump. Extensive testing is now underway to prove the practicality of the method.

Figure 1 shows a simplified schematic of the gas and oil flows in a system which uses an oil pump. The oil pump takes oil at crankcase pressure p_2 and delivers oil at p_3 ($p_3 - p_2 \approx 310\,\mathrm{kN/m^2}$) to the metering block A and heat exchanger 1; the bulk of the oil is returned to the crankcase and helps to cool the compressor. However, a small portion of the oil is fed through metering blocks A and B back to the first- and second-stage intake ports. It is noted that the second-stage intake pressure is the same as the crankcase pressure p_2. Thus, although oil flow can be maintained to the first-stage intake at p_1 without the oil pump, an oil pump is required to inject oil into the second stage. The oil separator eventually supplies most of the oil required for the second stage. However, it is incumbent on the system to be self-priming.

Figure 2 shows one simple way in which the oil pump may be eliminated. Oil from the crankcase is cooled by heat exchanger 1 and injected into the first stage of the compressor. The discharge from the first stage is cooled by heat exchanger 2 and returned to the crankcase via a relief valve V, which is set to approximately 172 $\mathrm{kN/m^2}$. Thus, oil at $p_2 + 172\,\mathrm{kN/m^2}$ is now available and may be injected into the second-stage intake port.

The additional work done by the first stage of the compressor is negligible, since the second stage performs most of the operation. However, there is a small increase in compressor temperature, since no cooling oil is available. Table 1 shows a typical set of temperatures for two systems operating side by side in otherwise identical operating conditions. The important parameter is the second-stage output temperature, which should be kept below 100°C to prevent decomposition of the oil.

Figure 3 shows the relief valve and tee which comprise the modification. The oil pump end plate is also modified by removal of the pump and substitution of a simple thrust bearing. Figure 4 shows an end view of the modified compressor assembly.

Reference

1. Higa, W. H., and Wiebe, E., "A Simplified Approach to Heat Exchanger Construction for Cryogenic Refrigerators," *Cryogenic Technology*, March/April 1967.

Table 1. Typical operating temperatures

	First-stage exhaust temperature, °C	Second-stage exhaust temperature, °C	Compressor housing temperature, °C
Compressor without oil pump	67	82	78
Compressor with oil pump	94	82	57

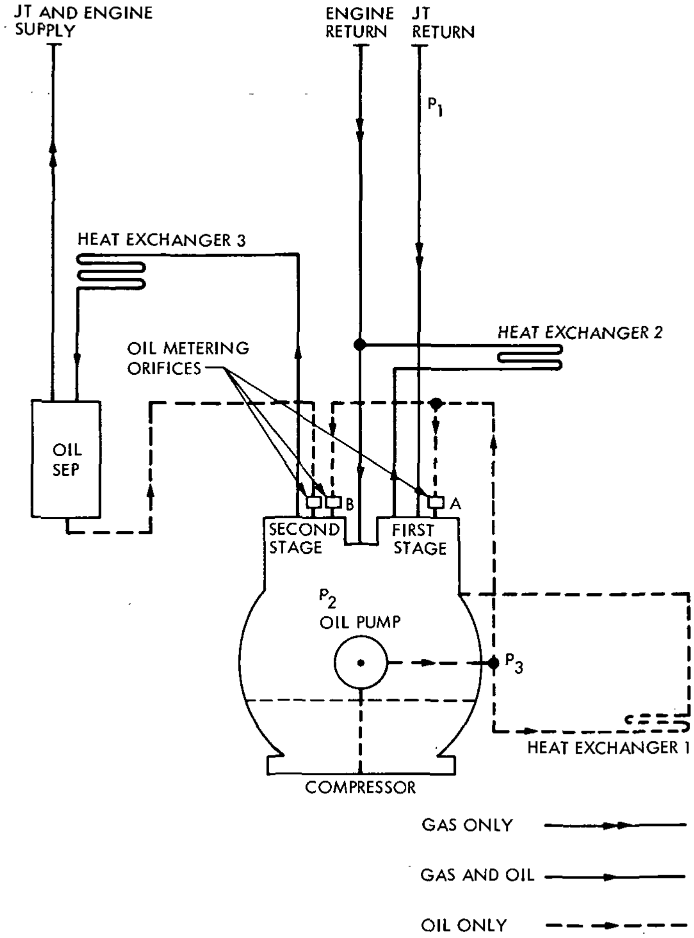

Fig. 1. Gas and oil in compressor assembly with oil pump

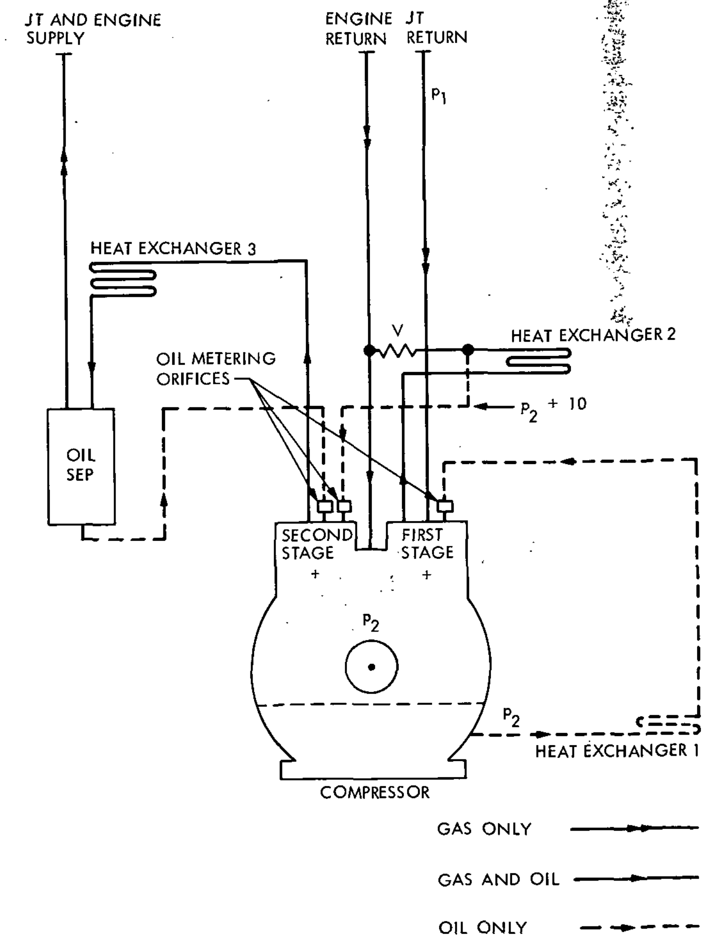

Fig. 2. Gas and oil flows in system without oil pump

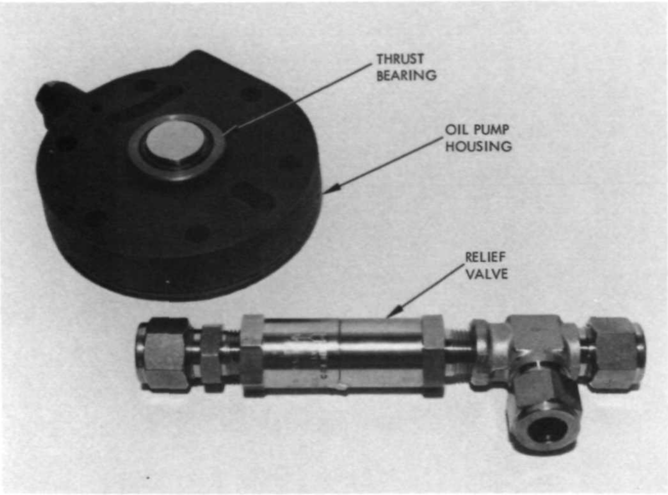

Fig. 3. Components required for modifications in compressor

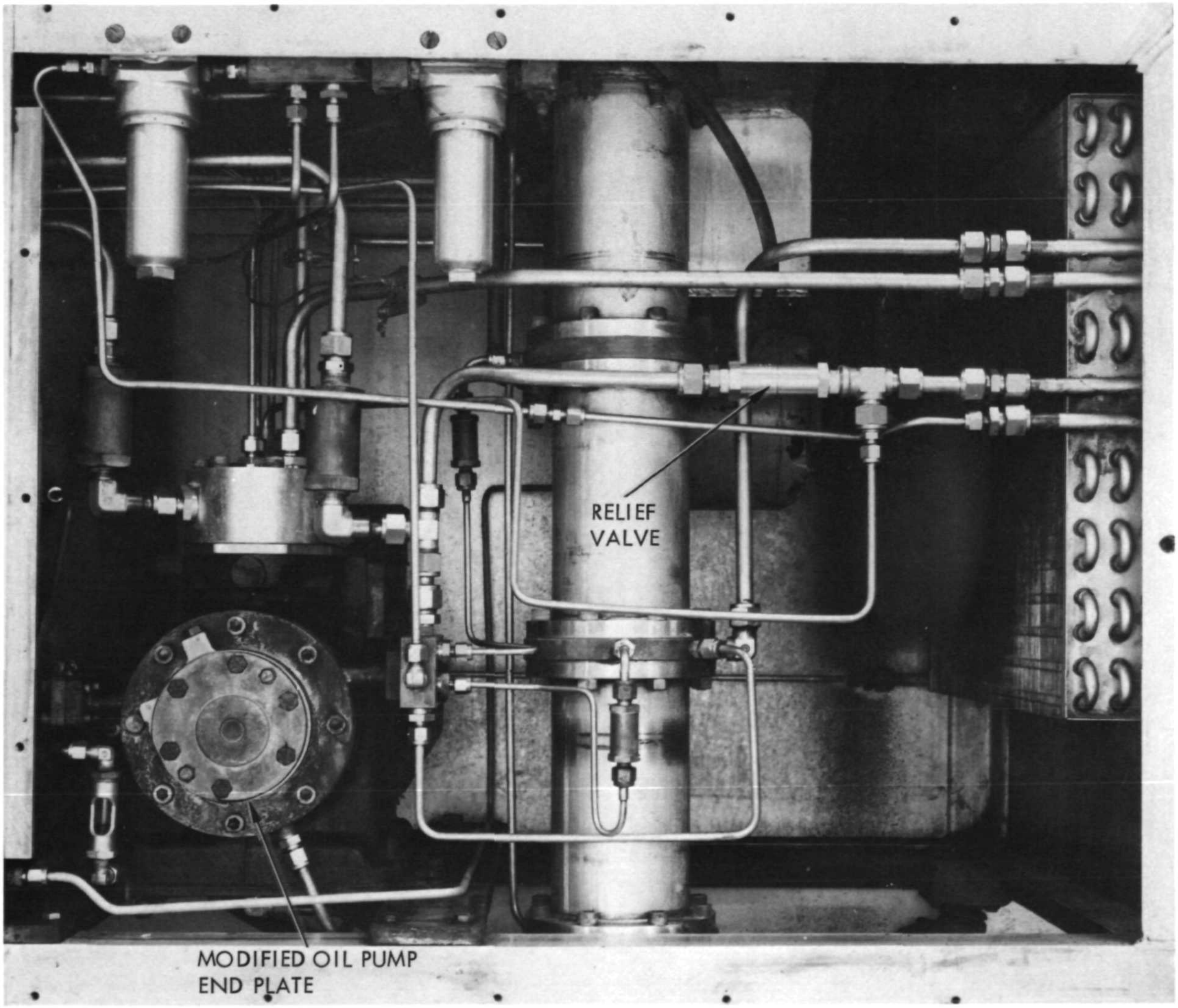

Fig. 4. End view of compressor with modifications installed

Filtering Dual-Frequency Radio Metric Data

K. H. Rourke
Tracking and Orbit Determination Section

This article introduces a technique for reducing the effect of ionospheric and space plasma charged particles on radio metric measurements. Development of the method is motivated by the difficulty in obtaining complete, two-way range calibrations when dual-frequency measurements are available for only the radio downlink. Using least-squares theory, estimation techniques are derived that allow the downlink calibration to, in effect, be "fed back" to correct unobserved uplink errors. Plausible numerical examples are presented, indicating that such techniques are applicable to precision range measurements for the initial applications of two-station tracking.

I. Introduction

Several articles (Refs. 1, 2, and 3) have discussed the use of dual-frequency radio measurements in calibrating the effects of ionospheric and space plasma charged particles. Currently envisioned dual-frequency systems involve a single-frequency uplink/dual-frequency downlink configuration. As stated in Refs. 1, 2, and 3, downlink-only dual-frequency measurements cannot provide complete doppler and range calibrations since, because of the time-varying character of the ionospheric and space plasma electron content, the downlink charged-particle effects cannot be directly related to the uplink effects. There does exist, however, a calculable, statistical relationship between the uplink and the observable downlink effects; and this relationship can be expected to permit a statistical determination to be made of the total uplink/downlink effect. Such a treatment will require the processing of the dual-frequency measurements over an extended period of time (one round-trip time, for instance). Thus, in essence, one filters the dual-frequency measurements to obtain estimates of the charged-particle effect or, more importantly, estimates of the principal quantities of interest, doppler and range.

The following section presents a short discussion of the statistical properties of two-way radio measurements. These results provide a basis for forming statistical estimates of measured quantities, doppler and range, in the

presence of errors due to space- and time-varying wave propagation effects. The analysis is concluded with a simplified yet concrete example of estimating the round-trip range to a spacecraft, in the presence of errors due to ionospheric and space plasma charged particles.

II. Statistical Properties of Two-Way Radio Measurements

The following discussion is restricted to range measurement, i.e., round-trip delay measurement, to simplify the argument. The methods may, however, be applied to round-trip range rate, i.e., doppler, measurements.

The delay measurement, based on a single-frequency uplink, and downlink, can be expressed as a function of reception time:

$$z(t) = \varepsilon_U(t) + \varepsilon_D(t) + 2R + n(t)$$

where R is the one-way range to a spacecraft, and ε_U and ε_D are the respective uplink and downlink error contributions due to charged-particle refractive index variations along the ray path. The quantity n represents other error sources, such as instrumentation uncertainties. To simplify the analysis, the spacecraft range shall be assumed constant. This assumption is not restrictive, since in applications, the range change can be tracked with doppler measurements. The range change can be unambiguously determined by comparison of the doppler and range measurements [as in differenced range vs. integrated doppler (DRVID)].

In a dual-frequency downlink configuration, there are two measurements, $z_1(t)$ and $z_2(t)$, where z_1 can be expressed as above and

$$z_2(t) = \varepsilon_U(t) + \alpha\varepsilon_D(t) + 2R + n_2(t)$$

where α is a proportionality factor expressing the difference between the downlink charged-particle effects for the two frequencies. For instance, assuming an S-band uplink with X- and S-band downlinks, z_1 can be represented as the S-up and -down measurement, and z_2 the S-up and X-down measurement. In this case, α is approximately 1/16 (see Ref. 3). The downlink charged-particle effect can be isolated as follows:

$$\frac{z_1(t) - z_2(t)}{1-\alpha} = \varepsilon_D(t) + \frac{n_1(t) - n_2(t)}{1-\alpha}$$

A complete calibration of the range measurement is not available, however, since the uplink and downlink effects cannot be directly related. Nevertheless, it is shown in the following that a statistical relationship between uplink and downlink can be determined, and that spacecraft range measurements can be improved through statistical processing methods, i.e., filtering.

A general statement of the problem is: Estimate R from $z_1(t)$ and $z_2(t)$ for $t_1 \leqq t \leqq t_1 + T$. Conventional least-squares estimation techniques should suffice; therefore, second-order moments of z_1 and z_2 are required to compute the estimates. As indicated in Ref. 3, the z_1 and z_2 propagation errors, ε_U and ε_D, can be expressed as

$$\varepsilon_U = \int_0^{R_0} U\left(x, t - \frac{(2R_0 - x)}{v}\right) dx$$

$$\varepsilon_D = \int_0^{R_0} U\left(x, t - \frac{x}{v}\right) dx$$

where $U(x,t)$ is the time-varying refractive index function along the ray path, $0 \leqq x \leqq R_0$, and v is the propagation rate. (R_0 is the "nominal" range to the spacecraft.) The quantity $U(x,t)$ can be related to charged-particle density, as indicated in Ref. 3. This function shall be assumed in the following to be a random variable depending on x and t. The expected product functions of the uplink and downlink errors shall be expressed as follows:

$$\left.\begin{aligned} r_{UU}(s) &= E\left[\varepsilon_U(t)\,\varepsilon_U(t+s)\right] \\ &= \iint_0^{R_0} F\left(\Delta x, s - \frac{\Delta x}{v}\right) dx_1 dx_2 \\ r_{UD}(s) &= E\left[\varepsilon_U(t)\,\varepsilon_D(t+s)\right] \\ &= \iint_0^{R_0} F\left(\Delta x, s + \frac{2(R_0 - \bar{x})}{v}\right) dx_1 dx_2 \end{aligned}\right\} \qquad (1)$$

with

$$\Delta x = x_1 - x_2 \text{ and } \bar{x} = \frac{x_1 + x_2}{2}$$

where it is assumed that $U(x,t)$ is a mean-zero, temporally and locally spatially stationary random variable with covariance function

$$F(\Delta x, s) = E\left[U(x,t)\,U(x + \Delta x, t + s)\right]$$

This assumption is indeed restrictive and not actually necessary for a general development. It would probably be quite sufficient in practice, however, and makes the

following analysis more understandable. (The above assumption coincides with the assumptions for the space plasma analysis techniques described in Ref. 4.) Observe from the above development that

$$E\left[\varepsilon_D(t)\,\varepsilon_D(t+s)\right] = r_{UU}(s)$$

and

$$r_{DU}(s) = E\left[\varepsilon_D(t)\,\varepsilon_U(t+s)\right] = r_{UD}(-s)$$

One may argue that such a model is unrealistic; however, this type of model is often sufficient in filtering problems provided that gross effects have been accounted for (i.e., average ionospheric and plasma charged-particle densities have been removed).

III. Filtering

The particular problem of estimating the constant range R from the dual-frequency data z_1 and z_2 is most easily treated in the familiar parameter estimation format, i.e.,

$$\bar{z} = Ay + \varepsilon$$

with

$$\bar{z} = \begin{pmatrix} z_1(t_1) \\ z_2(t_1) \\ z_1(t_2) \\ z_2(t_2) \\ \cdot \\ \cdot \\ \cdot \end{pmatrix}, \qquad A = \begin{pmatrix} 2 \\ 2 \\ \cdot \\ \cdot \\ \cdot \end{pmatrix}, \qquad y = R$$

and

$$\bar{\varepsilon} = \begin{pmatrix} \varepsilon_1(t_1) \\ \varepsilon_2(t_1) \\ \varepsilon_1(t_2) \\ \varepsilon_2(t_2) \\ \cdot \\ \cdot \\ \cdot \end{pmatrix}$$

where discrete measurements of z_1 and z_2 are obtained at times $t_1, \cdots, t_n$, and

$$\varepsilon_1(t) = \varepsilon_U(t) + \varepsilon_D(t) + n_1(t)$$

$$\varepsilon_2(t) = \varepsilon_U(t) + \alpha\varepsilon_D(t) + n_2(t)$$

The solution for y is given by the Gauss-Markov theorem (Ref. 5) and can be represented as follows:

$$\hat{y} = (A^T \Lambda_{\bar{\varepsilon}}^{-1} A)^{-1} A^T \Lambda_{\bar{\varepsilon}}^{-1} z \tag{2}$$

where

$$\Lambda_{\bar{\varepsilon}} = E\left[\bar{\varepsilon}\bar{\varepsilon}^T\right]$$

the variance of the error in estimating y is given by

$$\sigma_{\hat{y}}^2 = E\left[(\hat{y} - y)^2\right] = (A^T \Lambda_{\bar{\varepsilon}}^{-1} A)^{-1}$$

Note that $A^T \Lambda_{\bar{\varepsilon}}^{-1} A$ is a scalar for this problem and that the real difficulty in estimating y is forming $\Lambda_{\bar{\varepsilon}}^{-1}$, since

$$\Lambda_{\bar{\varepsilon}} = \begin{pmatrix} \gamma_{11}(0) & \gamma_{12}(0) & \gamma_{11}(t_1 - t_2) & \gamma_{12}(t_1 - t_2) & \cdots \\ \gamma_{21}(0) & \gamma_{22}(0) & \gamma_{21}(t_1 - t_2) & \gamma_{22}(t_1 - t_2) & \cdots \\ \cdot & \cdot & \gamma_{11}(0) & \gamma_{12}(0) & \cdots \\ \cdot & \cdot & \gamma_{21}(0) & \gamma_{22}(0) & \cdots \\ \cdot & \cdot & \cdot & \cdot & \cdots \\ \cdot & \cdot & \cdot & \cdot & \cdots \end{pmatrix} \tag{3}$$

where the above components are given by

$$\gamma_{11}(s) = E\left[\varepsilon_1(t)\,\varepsilon_1(t+s)\right] = r_{UU}(s) + r_{UD}(s) + r_{DU}(s) + r_{DD}(s) + \sigma_{n_1}^2 \delta(s)$$

$$\gamma_{12}(s) = E\left[\varepsilon_1(t)\,\varepsilon_2(t+s)\right] = r_{UU}(s) + \alpha r_{UD}(s) + r_{DU}(s) + \alpha r_{DD}(s) + \sigma_{n_1 n_2} \delta(s)$$

$$\gamma_{22}(s) = E\left[\varepsilon_2(t)\,\varepsilon_2(t+s)\right] = r_{UU}(s) + \alpha\left(r_{UD}(s) + r_{DU}(s)\right) + \alpha^2 r_{DD}(s) + \sigma_{n_2}^2 \delta(s)$$

with $\gamma_{21}(s) = \gamma_{12}(-s)$. Note that the data noise functions $n_1(t)$ and $n_2(t)$ are assumed to be white with the indicated covariance weightings. Numerical procedures that are more efficient than the direct inversion of Eq. (3) can be developed, particularly in this case of stationary noise processes (see Ref. 6). These considerations are not pursued here, since the principal interest in this analysis is a numerical assessment of the filtering techniques for hypothetical error models.

IV. Error Models

To avoid the complexities of the double integrals in Eq. (1), assume that the charged-particle densities are constant over N specified "cells" along the ray path, and

that the densities are statistically independent from cell to cell and individually exponentially correlated. Thus,

$$\varepsilon_U(t) = \sum_{k=1}^{N} U_k\left(t - \frac{2R_0 - x_k}{v}\right)$$

$$\varepsilon_D(t) = \sum_{k=1}^{N} U_k\left(t - \frac{x_k}{v}\right)$$

where $U_k(t)$ is the time-varying charged-particle effect (measured in meters, for instance) that is localized at x_k. A visualization of this model is presented in Fig. 1. Functions that correspond to those in Eq. (1) are given by

$$\left.\begin{aligned} r_{UU}(s) &= \sum_{k=1}^{N} F_k(s) \\ r_{UD}(s) &= \sum_{k=1}^{N} F_k\left(s + \frac{2(R_0 - x_k)}{v}\right) \end{aligned}\right\} \qquad (4)$$

with

$$F_k(t) = \sigma_k^2 e^{-|t|/\tau_k}$$

where σ_k and τ_k characterize the statistical properties of the kth cell.

V. Numerical Examples

In the following, three numerical examples are investigated. In each example, the Earth–spacecraft range is assumed to be 2 AU. The charged-particle effect is divided into 10 cells along the ray path. The first cell is located at $x_1 = 0$, and the remaining cells are uniformly distributed between 0 and 2 AU. The three models are illustrated in Fig. 2. In the first model, the particle effect is uniformly distributed along the ray path. Models 2 and 3 include a large ionospheric effect located at $x = 0$, and Model 3 includes a solar corona effect near $x = 1$ AU.

Figure 3 presents the S-up, S-down round-trip autocovariance functions for the three models. Note that the standard deviations for the models are 6.1, 16.2, and 19.7 m, respectively. These values represent the expected round-trip range errors for uncalibrated S-band range measurements. Of particular significance are the peaks for Models 2 and 3 at a lag equal to 2000 s, the signal round-trip time. It is of interest that the formation of estimated signal autocovariance functions, based on actual radio measurements, is a technique for estimating space plasma densities (see Ref. 4).

Figure 4 presents round-trip range error standard deviations, $2 \times \sigma_{\hat{y}}$, for the three models as a function of filter length, i.e., the amount of data incorporated into the estimates. It is seen that consistent improvement occurs with dramatic error reductions after one round-trip time. This relates how a filter can remove a large part of the ionospheric error as a result of the special way it influences the radio signals, as indicated in Fig. 3. This property is further illustrated in Fig. 5, recalling that $\varepsilon_U(t)$ and $\varepsilon_D(t)$ are the uplink and downlink effects on the signal received at time t. It is seen that large cross correlations exist for Models 2 and 3 for round-trip time lags. Thus, a filter can effectively feed back the downlink errors (measurable with the dual-frequency data) to recover some of the unobserved uplink errors.

VI. Implications

The principal intent of this analysis is not to develop a general theory but to introduce, with a specific example, a promising approach to the problem of treating radio measurement charged-particle errors. This approach need not be restricted to two-way range measurements with dual-frequency data. Straightforward extensions of it can be applied to dual- or single-frequency range or doppler measurements.

Regarding the results of the numerical examples, one observes that the dual-frequency filtering yields large reductions in two-way range measurements provided that one allows for sufficiently long filtering periods (up to the signal round-trip time). The 5-m round-trip range accuracies, based on plausible charged-particle density models, are suitable for the initial two-station tracking applications (see Refs. 7 and 8 concerning near-simultaneous ranging). Note that, for the respective models, the quoted filter performances are optimistic in that statistical model mismatching can be expected to degrade the errors from their optimal values.

References

1. Von Roos, O. H., and Mulhall, B. D., "An Evaluation of Charged Particle Calibration by a Two-Way Dual Frequency Technique and Alternatives to this Technique," in *The Deep Space Network Progress Report,* Technical Report 32-1526, Vol. XI, pp. 42–52, Jet Propulsion Laboratory, Pasadena, Calif., Oct. 15, 1972.

2. Von Roos, O. H., "Analysis of the DRVID and Dual Frequency Tracking Methods in the Presence of a Time-Varying Interplanetary Plasma," in *The Deep Space Network Progress Report,* Technical Report 32-1526, Vol. III, pp. 71–76, Jet Propulsion Laboratory, Pasadena, Calif., June 15, 1971.

3. Von Roos, O. H., "The S/X Band Downlink Only or Uplink Controversy Revisited," TM 391-239, Jet Propulsion Laboratory, Pasadena, Calif., Oct. 13, 1971 (JPL internal document).

4. Thiede, E. C., and Lusignan, B. B., "A Technique to Study Randomly Varying Media," *IEEE Trans. Antennas and Propagation,* Vol. AP-18, No. 1, Jan. 1970, pp. 99–103.

5. Luenberger, D. G., *Optimization by Vector Space Methods,* Wiley and Sons, New York, 1969.

6. Robinson, E. A., *Multichannel Time Series Analysis with Digital Computer Programs,* Holden–Day, San Francisco, 1967.

7. Rourke, K. H., and Ondrasik, V. J., "Application of Differenced Tracking Data Types to the Zero Declination and Process Noise Problems," in *The Deep Space Network Progress Report,* Technical Report 32-1526, Vol. IV, pp. 49–60, Aug. 15, 1971.

8. Rourke, K. H., "Viking Orbit Determination Analysis Bi-Monthly Report," IOM 391.2-280, March 22, 1972 (JPL internal document).

Fig. 1. Charged-particle density model

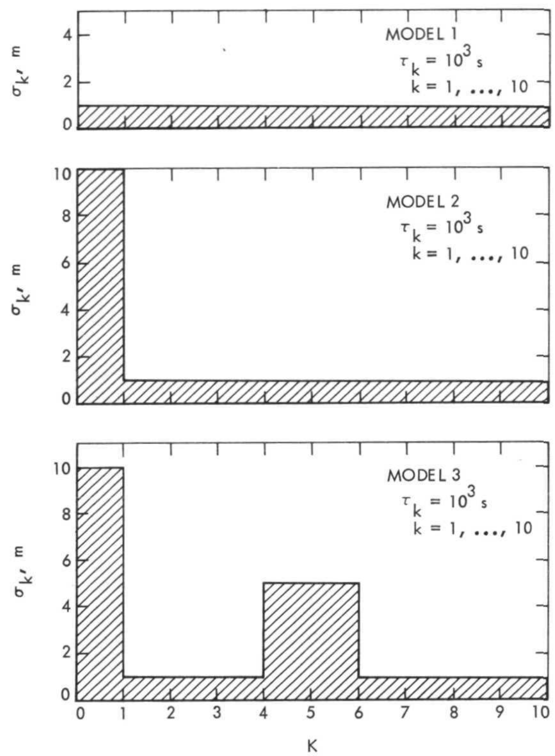

Fig. 2. Specific charged-particle density models

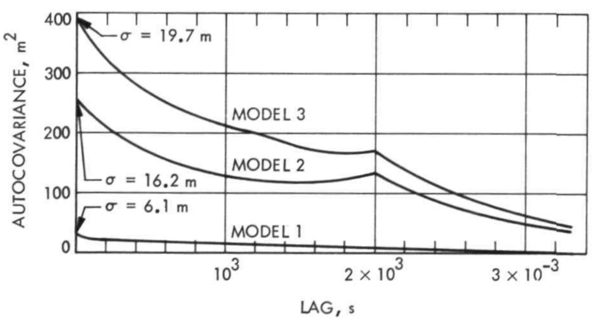

Fig. 3. Two-way range error autocovariance functions, $E[\varepsilon_1(t)\,\varepsilon_1(t+s)]$

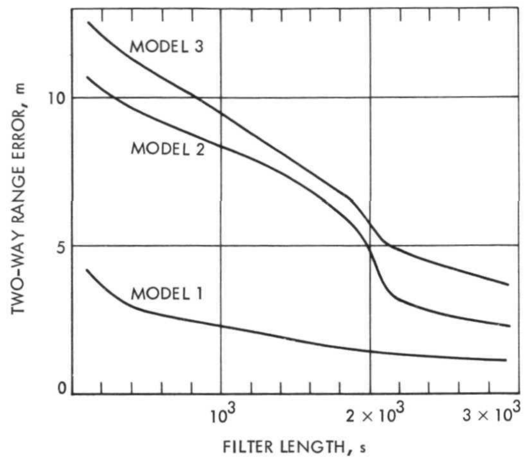

Fig. 4. Two-way range estimation error, $2 \times \sigma_{\hat{y}}$

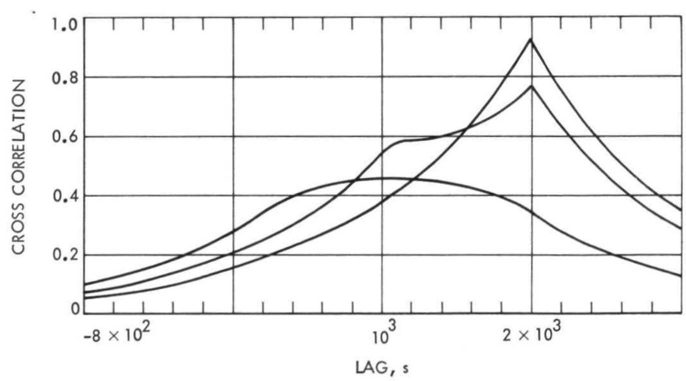

Fig. 5. Uplink/downlink cross correlation, $E[\varepsilon_D(t)\,\varepsilon_U(t+s)]/\sigma_{\varepsilon_D}\sigma_{\varepsilon_U}$

S/X-Band Experiment: Development of Special Telecommunications Development Laboratory Support Test Equipment

T. Y. Otoshi and O. B. Parham
Communications Elements Research Section

This article documents the design of an X-band down converter and a doppler extractor receiver that were specially developed and supplied to the Telecommunications Development Laboratory in July 1971. The special equipment enabled preliminary tests to be made on the performance of a combined S/X-band radio system similar to that which will be used for the Mariner Venus/Mercury 1973 mission.

I. Introduction

The S/X-band experiment to be performed with the Mariner Venus/Mercury 1973 (MVM 73) spacecraft is a dual-frequency experiment to measure the electron content of the interplanetary media between Earth and the planets Venus and Mercury (Ref. 1). An uplink signal of approximately 2113 MHz will be transmitted to the spacecraft from the 64-m-diameter antenna at DSS 14. This uplink signal as received by the spacecraft radio system will be coherently multiplied by ratios of 240/221 and 880/221 to produce S- and X-band carrier frequencies of approximately 2295 MHz and 8415 MHz. The coherent S- and X-band signals will then be transmitted back to the DSS 14 ground system. A measurement of the dispersiveness of the S- and X-band phase and range data as received back at the ground station provides scientific information required for determining total interplanetary electron content.

A Block IV ground radio system currently being developed by the Division will be installed at DSS 14 for the S/X experiment. The Block IV system will be a phase-stabilized system enabling simultaneous reception of S- and X-band frequencies and will yield dispersive S/X doppler and S/X range data.

At the time the preliminary tests were conducted (September through October 1971), the Block IV system having S/X capability was not yet available. Therefore, it was necessary to utilize a Block III system that had only S-band capability. The Block III system was converted into an X-band phase-locked loop receiver by means of

an X-band to 50-MHz down converter, which will be described in this article. As was shown in a report by Brunn (Ref. 2), the preliminary ranging and carrier phase test data were successfully obtained.

II. X-Band Down Converter

A block diagram of the X-band down converter is shown in Fig. 1. An input X-band signal (in the frequency range of 8400 to 8450 MHz) is down converted to produce a 50-MHz intermediate frequency (IF) output signal. This output signal is then fed into the 50-MHz IF input stage of a Block III receiver. The Block III phase-locked loop VCO output (nominally 23.4 MHz) is fed back into the down converter assembly, doubled, and then added to a coherent bias signal of approximately 51.7 MHz, which is produced by a frequency synthesizer and a 5-MHz frequency standard. An output signal of approximately 98.6 MHz is then filtered and multiplied by 85 to provide a phase-locked local oscillator frequency that is 50 MHz lower than the input X-band signal. Many of the mixers, amplifiers, and multipliers are of the same design as those implemented in the Block IV system. The Telecommunications Development Laboratory (TDL) X-band receiver system was purposely designed to be similar to the Block IV system so that preliminary test data would give a valid indication of MVM 73 S/X radio system performance.

Figure 2 shows the front, top, and rear views of the fabricated assembly. Table 1 shows typical noise figure and image rejection data of this assembly as measured in the laboratory. After installation at the TDL, a noise figure measurement was again made on the X-band down converter. The single sideband noise figure of the converter for the Channel 19 X-band input frequency (8421.79 MHz) was determined to be (10.2 ± 0.5) dB as defined at the Type N input port of the converter assembly. The increase in noise figure was attributed to minor adjustments made after data of Table 1 had been obtained.

III. X-Band Doppler Extractor Receiver

X-band doppler data were obtained by use of an S/X translator and an X-band doppler extractor receiver similar to that which will be used in the Block IV system.

A block diagram of the TDL X-band doppler extractor system is shown in Fig. 3. The doppler extraction method is similar to that of the Block IV system except that the first IF is 50 MHz instead of 325 MHz.

Figure 4 shows the fabricated receiver portion of the TDL X-band doppler extractor system. A special purpose S/X translator (zero delay device) is currently being fabricated and will be supplied to TDL for S/X test purposes.

IV. Acknowledgment

The equipment described in this article was developed with the cooperation and assistance of R. MacClellan, C. Johns, and H. Donnelly of the RF Systems Development Section. R. Clauss of the Communications Elements Research Section developed the low-loss waveguide X-band filter.

References

1. Levy, G., Dickinson, R., and Stelzried, C., "RF Techniques Research: S/X Band Experiment," in *Supporting Research and Advanced Development,* Space Programs Summary 37-61, Vol. III, pp. 93–95, Jet Propulsion Laboratory, Pasadena, Calif., Feb. 20, 1970.

2. Brunn, D. L., "S/X Band Ranging and Phase Tests," Interoffice Memo No. 3396-72-060, Jet Propulsion Laboratory, Pasadena, Calif., Feb. 23, 1972 (JPL internal document).

Table 1. Noise figures and image rejections of X-band down converter

Frequency, MHz	Single-sideband noise figure, dB	Image rejection, dB
8400	12.2	41
8405	11.2	39
8410	11.0	37
8415	10.6	37
8420	9.6	36
8425	8.6	35
8430	8.5	34
8435	9.2	31
8440	10.0	30
8445	11.2	28
8450	12.4	25

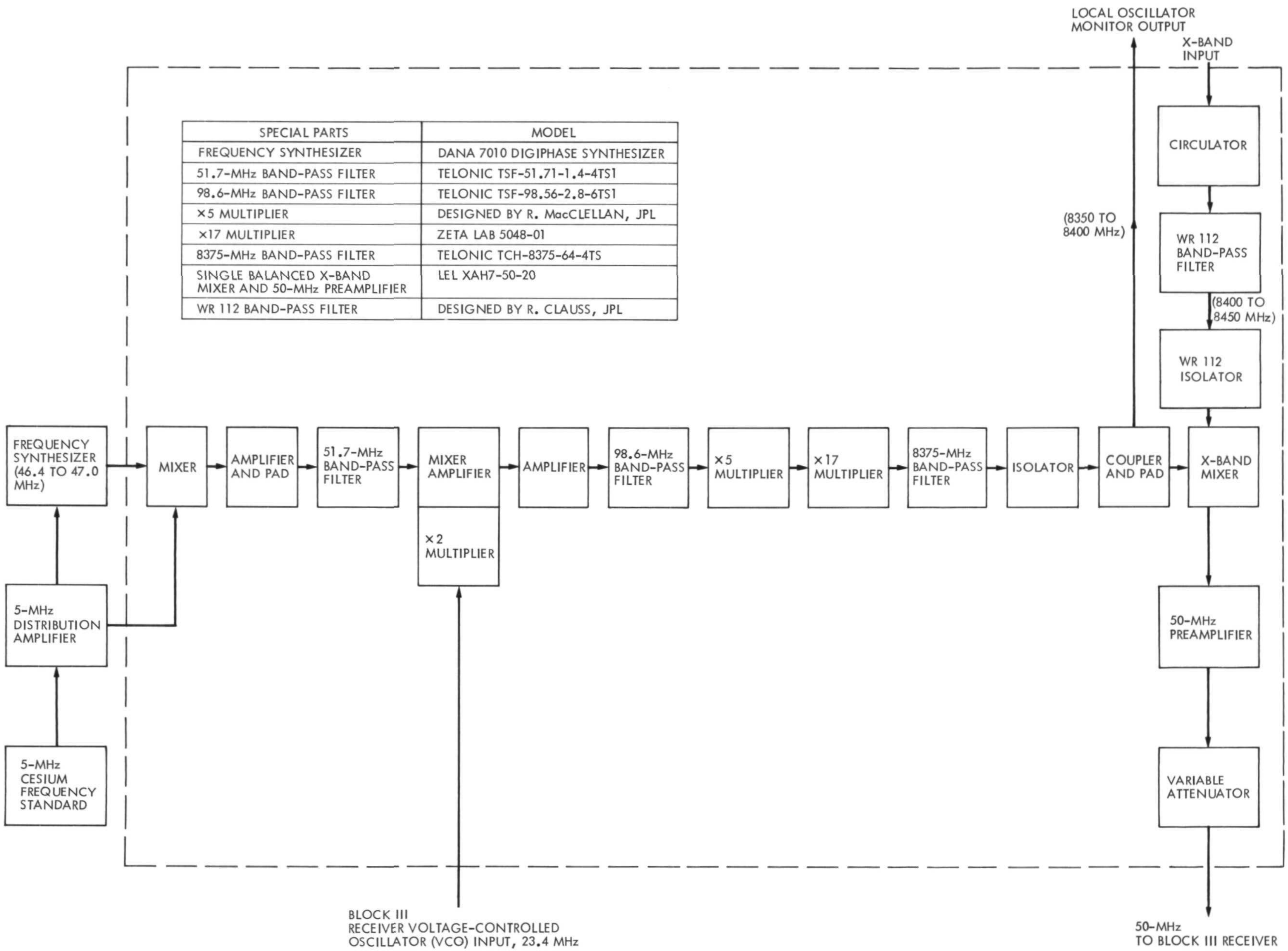

SPECIAL PARTS	MODEL
FREQUENCY SYNTHESIZER	DANA 7010 DIGIPHASE SYNTHESIZER
51.7-MHz BAND-PASS FILTER	TELONIC TSF-51.71-1.4-4TS1
98.6-MHz BAND-PASS FILTER	TELONIC TSF-98.56-2.8-6TS1
×5 MULTIPLIER	DESIGNED BY R. MacCLELLAN, JPL
×17 MULTIPLIER	ZETA LAB 5048-01
8375-MHz BAND-PASS FILTER	TELONIC TCH-8375-64-4TS
SINGLE BALANCED X-BAND MIXER AND 50-MHz PREAMPLIFIER	LEL XAH7-50-20
WR 112 BAND-PASS FILTER	DESIGNED BY R. CLAUSS, JPL

Fig. 1. Block diagram of TDL X-band to 50-MHz down converter

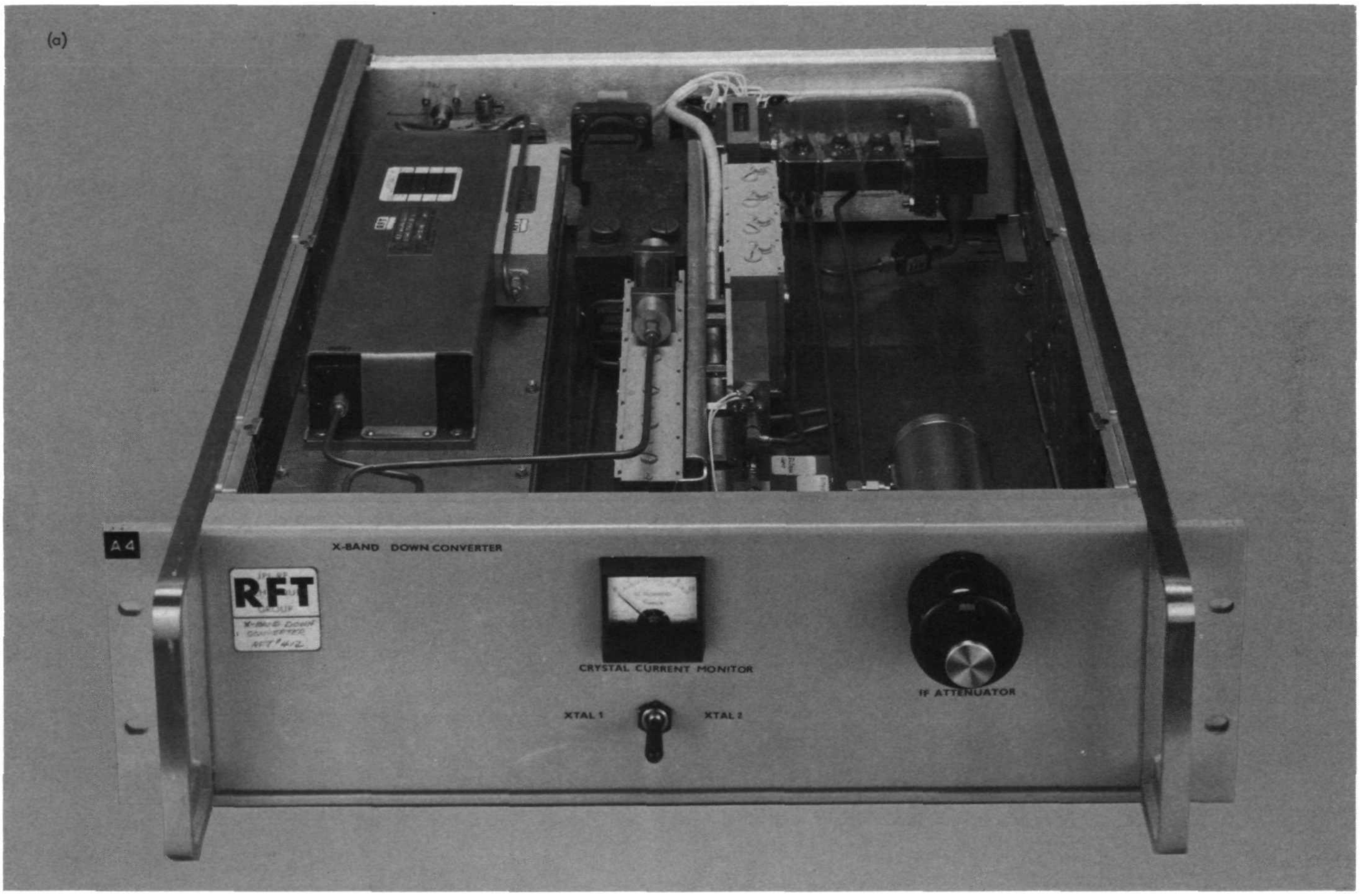

Fig. 2. TDL X-Band to 50-MHz down converter: (a) front view; (b) top view; (c) rear view

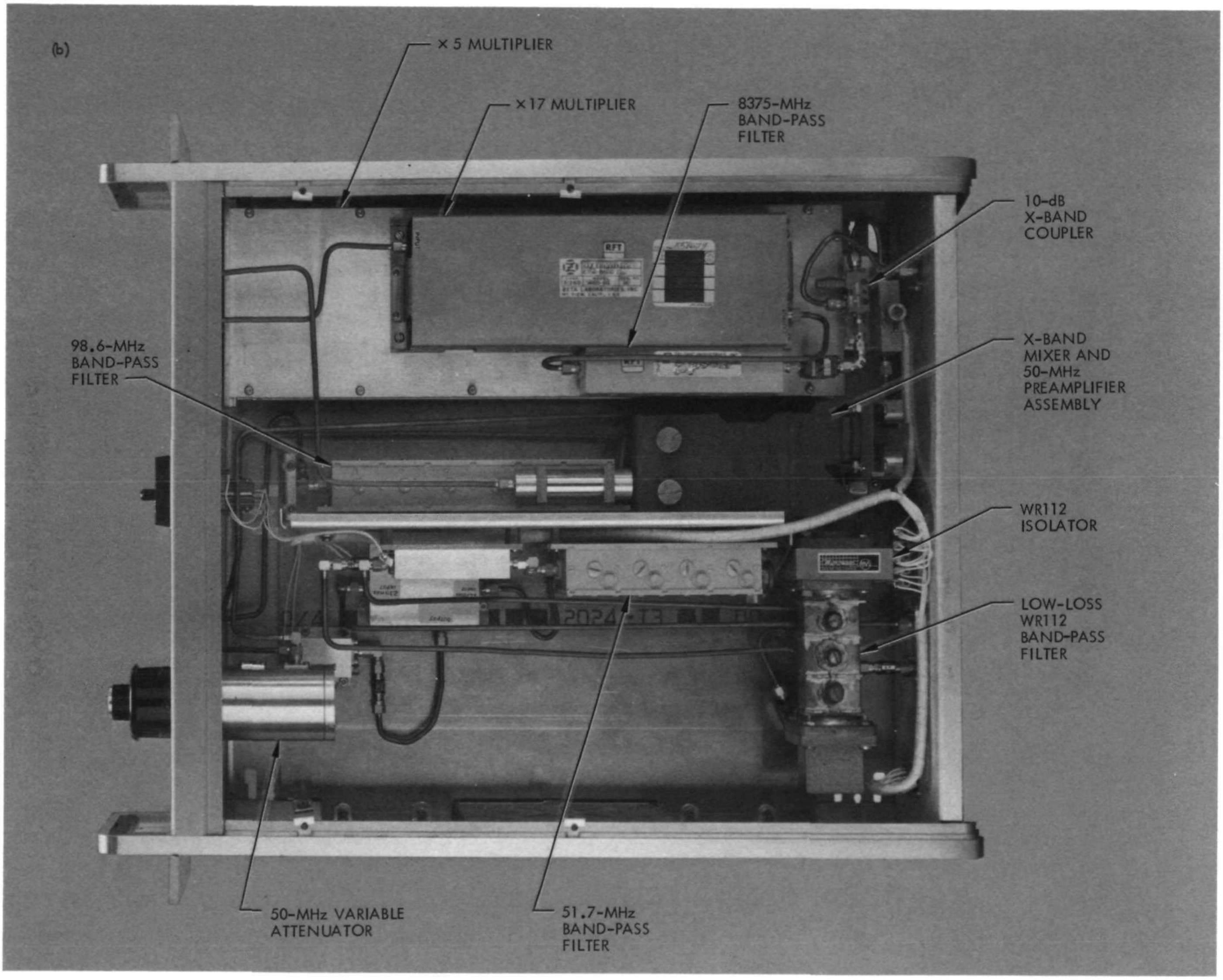
(b)
× 5 MULTIPLIER
× 17 MULTIPLIER
8375-MHz
BAND-PASS
FILTER
10-dB
X-BAND
COUPLER
98.6-MHz
BAND-PASS
FILTER
X-BAND
MIXER AND
50-MHz
PREAMPLIFIER
ASSEMBLY
WR112
ISOLATOR
LOW-LOSS
WR112
BAND-PASS
FILTER
50-MHz VARIABLE
ATTENUATOR
51.7-MHz
BAND-PASS
FILTER

Fig. 2 (contd)

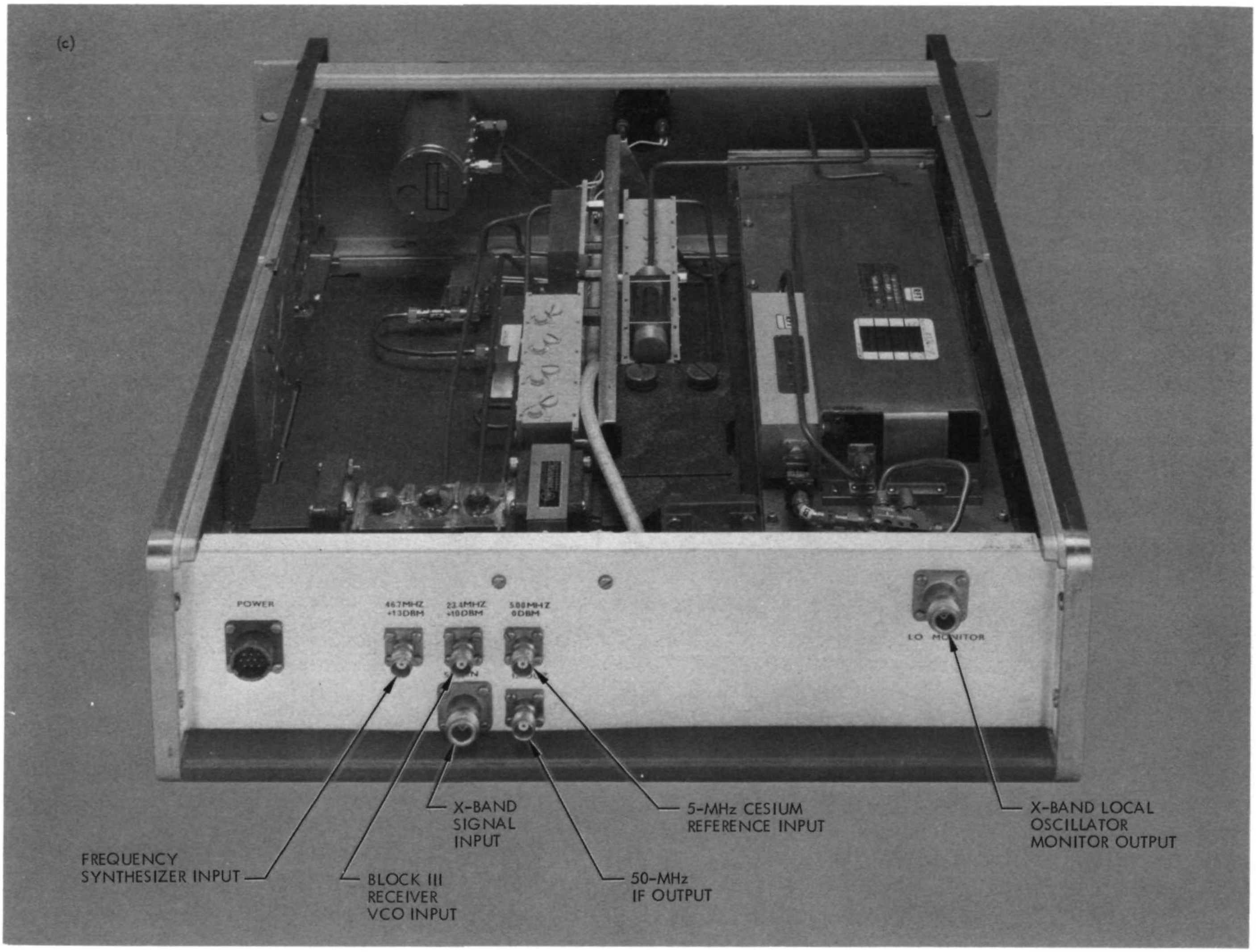
(c)
POWER
LO MONITOR
X-BAND SIGNAL INPUT
5-MHz CESIUM REFERENCE INPUT
X-BAND LOCAL OSCILLATOR MONITOR OUTPUT
FREQUENCY SYNTHESIZER INPUT
BLOCK III RECEIVER VCO INPUT
50-MHz IF OUTPUT

Fig. 2 (contd)

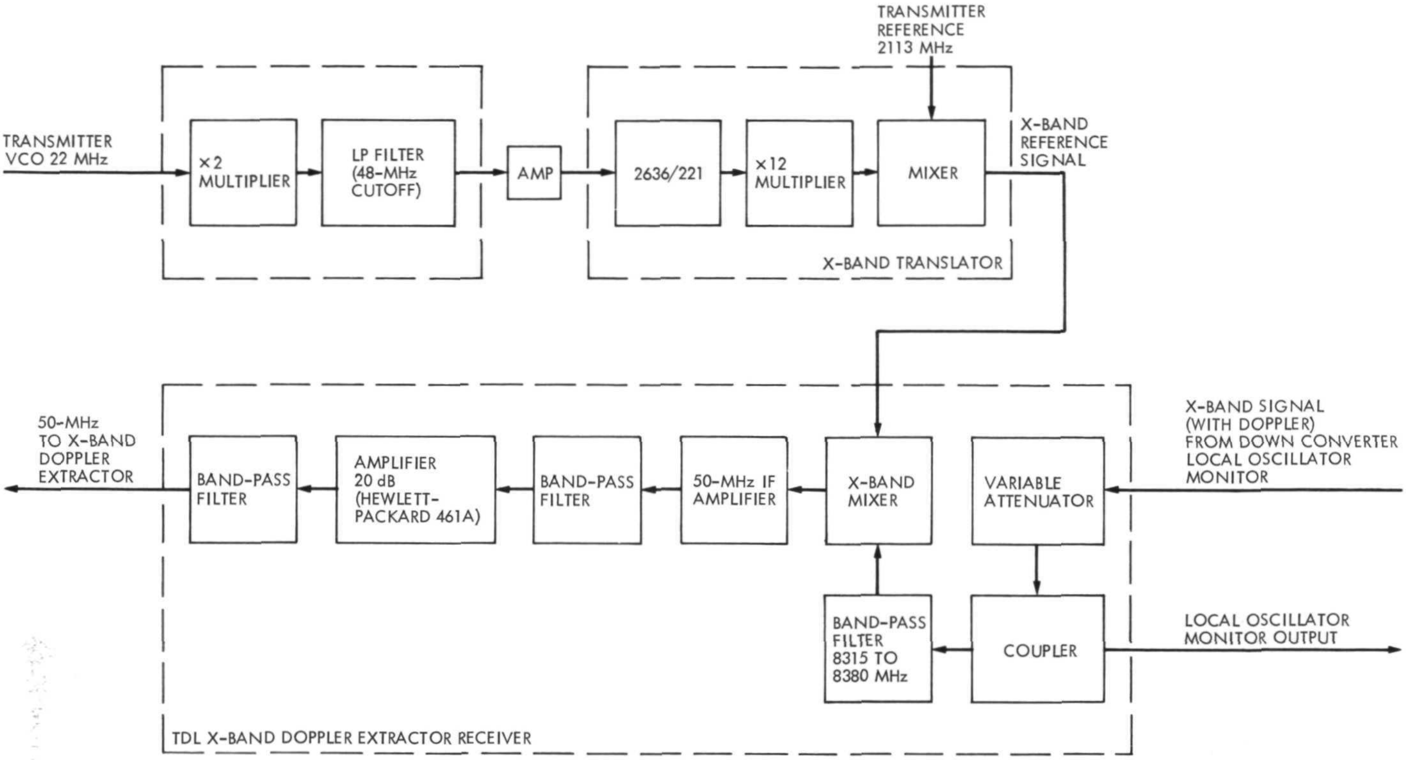

Fig. 3. Block diagram of TDL X-band doppler extractor system

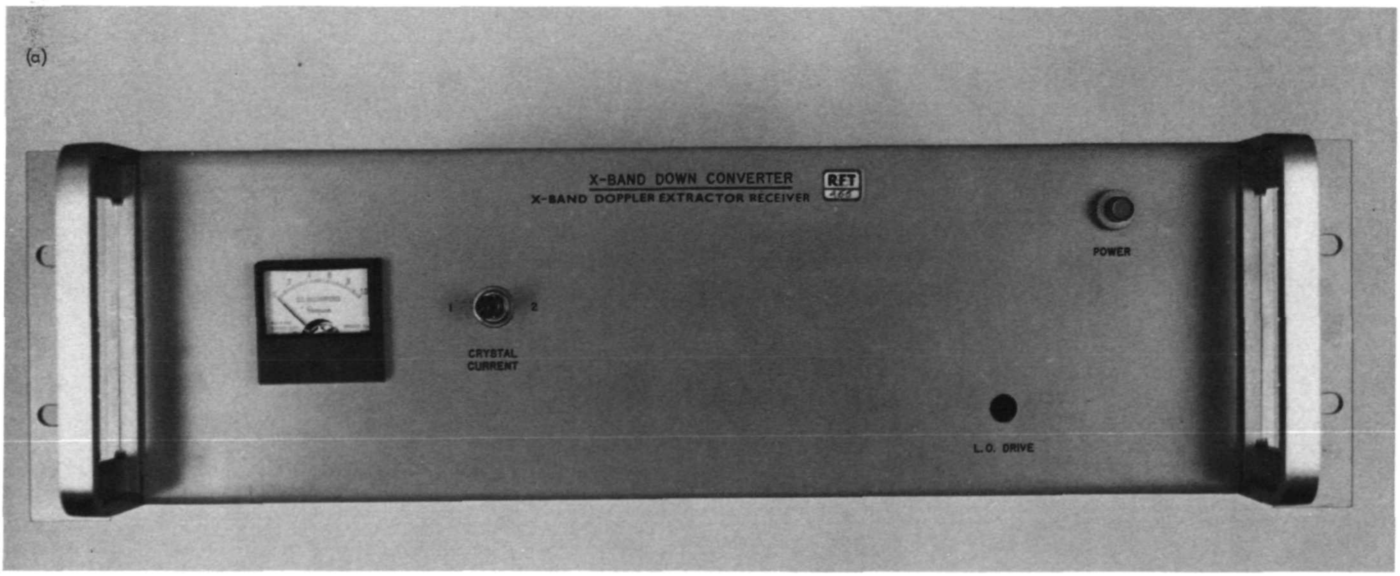

Fig. 4. TDL X-band doppler extractor receiver: (a) front view; (b) top view; (c) rear view

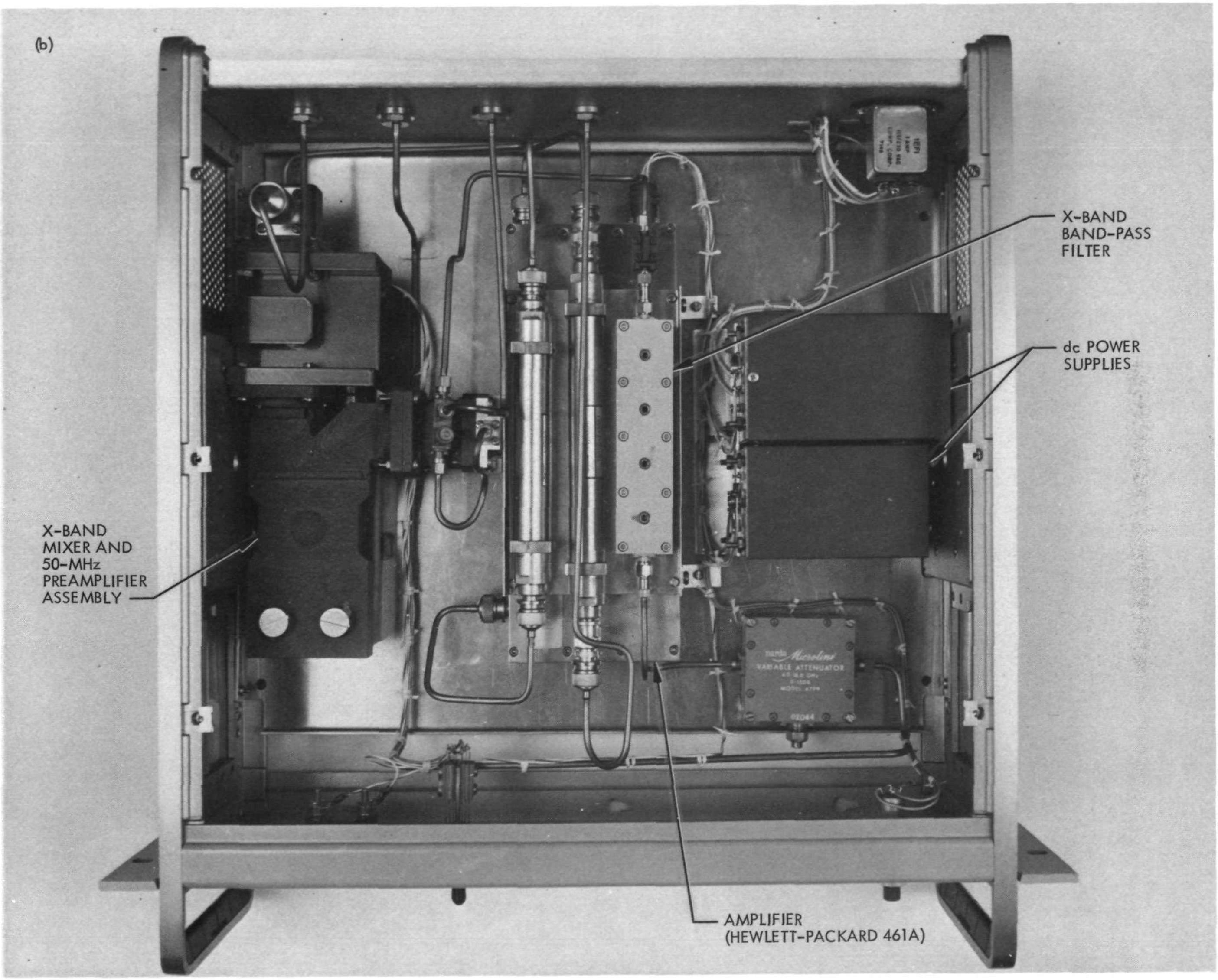
(b)
X-BAND
BAND-PASS
FILTER
dc POWER
SUPPLIES
X-BAND
MIXER AND
50-MHz
PREAMPLIFIER
ASSEMBLY
AMPLIFIER
(HEWLETT-PACKARD 461A)

Fig. 4 (contd)

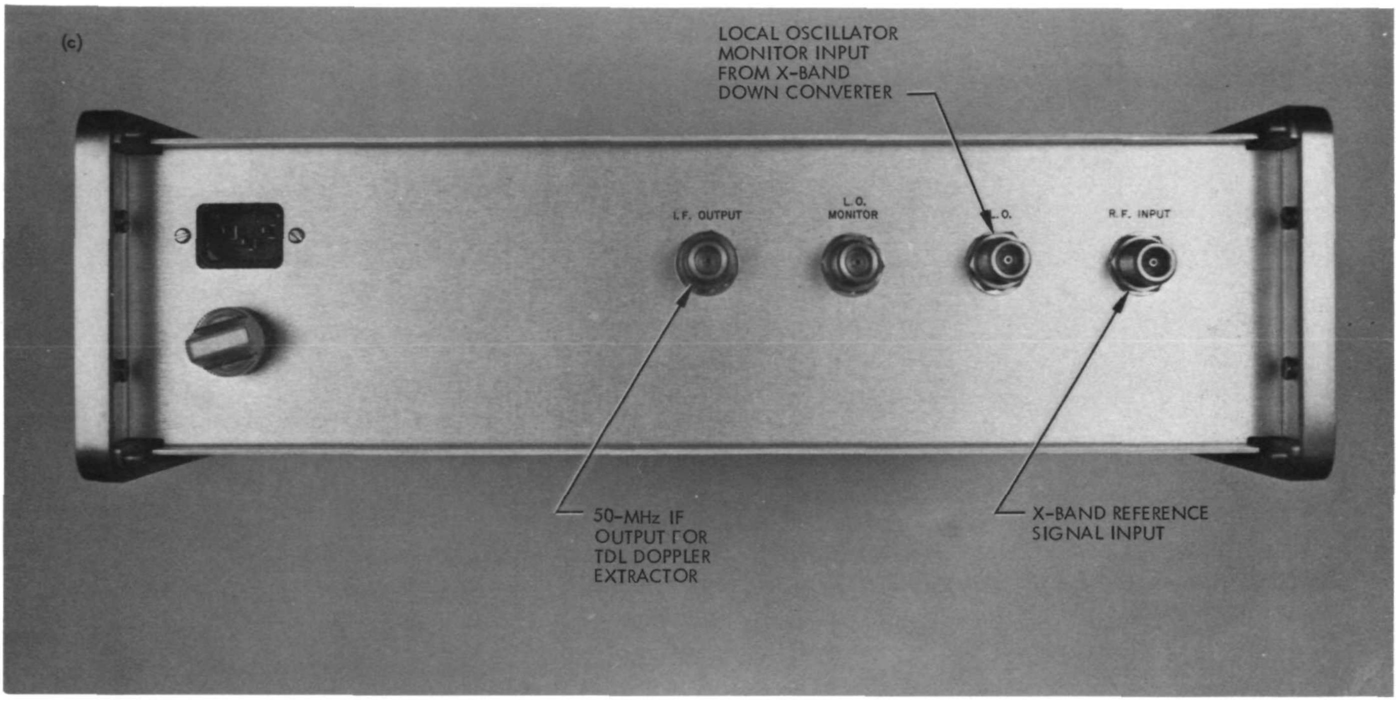
(c)
LOCAL OSCILLATOR MONITOR INPUT FROM X-BAND DOWN CONVERTER
I.F. OUTPUT
L.O. MONITOR
L.O.
R.F. INPUT
50-MHz IF OUTPUT FOR TDL DOPPLER EXTRACTOR
X-BAND REFERENCE SIGNAL INPUT

Fig. 4 (contd)

Performance of Coded, Noncoherent, Hard-Decision MSFK Systems

I. Bar-David and S. Butman
Communications Systems Research Section

The capacity of noncoherent multifrequency shift keying (MFSK) systems that use a hard decision receiver is determined as a function of the predetection signal-to-noise ratio (ST/N_0). For any given predetection signal-to-noise ratio there is an optimum number of frequencies that maximize the system capacity. This optimum number decreases as the predetection signal-to-noise ratio decreases. However, it is shown here that this number is never less than 7. This means that binary frequency shift keying, a commonly used modulation technique at very low data rates, is suboptimum by at least 2.2 dB, compared to the performance obtainable with 7 signals. Similar results are obtained for the computational cut-off R_{comp}, when convolutional coding with sequential decoding is used over such an MFSK channel. These channels are expected to arise in planetary entry missions into thick atmospheres, such as those of Venus and Jupiter.

I. Introduction

Noncoherent reception is necessary when the receiver cannot determine the phase of the received signals. This situation is likely to occur in missions that enter thick atmospheres of planets such as Venus, Jupiter, Saturn, and Uranus. Usually this is due to random phase changes that are too large to ignore and too rapid to estimate accurately, i.e., the signal-to-noise ratio (SNR) in the predetection filter, ST/N_0, is too low, where S is the rms power of the received signal, N_0 is the one-sided noise density and T is the time interval over which the phase is relatively constant albeit unknown. Causes of this type of behavior in planetary entry are turbulence, dispersion, attenuation and residual doppler.

Roughly speaking, the time T corresponds to the inverse bandwidth of the random phase process. The phase variations cannot be tracked by a phase-locked loop of lower bandwidth, while the signal-to-noise ratio in this minimum loop bandwidth is too low. It is well known (Refs. 1, 2, and 3) that communication under the described conditions requires transmission of signals that

are orthogonal over a time interval T or less, and their reception by means of a square-law receiver. Performance curves plotting the error probability for detecting one of $M = 2^K$ equiprobable signals (corresponding to a rate of K/T bits/s) as a function of bit signal-to-noise ratio $ST_B/N_0 = ST/KN_0$, have been computed by Lindsey (Ref. 1). Also, in the limit as T and M approach infinity, with M growing exponentially, Turin (Ref. 2) has proved that zero error probability can be attained for all rates up to the capacity of the infinite bandwidth coherent channel $C_\infty = 1.44\ S/N_0$ bits/s. This behavior in the limit is not surprising because allowing T to grow arbitrarily large means that the phase tends to an unknown constant (between $-\pi$ and π). Thus, it can be estimated with arbitrarily high accuracy by diverting a small fraction, ε, of the power to a phase reference signal, since $\varepsilon ST/N_0 \to \infty$. Consequently, a coherent receiver can be used and it is well known (Ref. 3) that C_∞ can then be achieved with a coded sequence of short duration antipodal signals ($M = 1$) instead of the very special orthogonal signal set.

It is not difficult to show that noncoherent signaling by itself cannot achieve arbitrarily low error rates when ST/N_0 is bounded. In fact the error probability increases as the number of signals, M, increases. Nevertheless, arbitrarily reliable communication is still possible at a nonzero rate (but less than C_∞) by employing an additional level of coding (concatenating) on the channel created by the orthogonal signals and the noncoherent receiver. Theoretically, error-free transmission is possible at rates up to the capacity of this noncoherent channel.

The purpose of this article is to investigate the capacity of the above noncoherent channel as a function of M and ST/N_0, and to draw conclusions pertaining to the design of coded, noncoherent communication systems.

II. The Noncoherent Multiple Frequency Shift Keying Channel

Multifrequency shift keying (MFSK) refers to the case in which orthogonal signals over time T are harmonics of the frequency $1/T$. Usually the orthogonal signals are modulated onto a high-frequency carrier and it is the phase of the carrier as opposed to the phase of the signals that cannot be tracked. In that case the maximum number of orthogonal signals that can be distinguished in a system of bandwidth W is approximately $M = 2WT$, since both $\sin(2\pi kt/T)$ and $\cos(2\pi kt/T)$ $k = 1, 2, \cdots, WT$ can be used. However, if the phases of the signals are also unknown, then only $M = WT$ signals can be distinguished by the receiver: the sine terms, for instance, must be dropped to avoid confusion with phase-shifted cosines. The model assumes that the carrier phase is statistically independent every T seconds.

Figure 1 is a block diagram of a noncoherent MFSK system. During each interval of time T one of $M = 2^K$ orthogonal signals $x_m(t)$; $m = 1, 2, \cdots, M$ with unit energy is modulated onto a carrier $\cos \omega t$ and arrives in the presence of additive Gaussian noise $n(t)$ as

$$r(t) = \sqrt{2S}\, x_m(t) \cos(\omega t + \theta) + n(t) \qquad (1)$$

where θ is an unknown phase shift uniformly distributed between $-\pi$ and π.

The optimum receiver (Ref. 4) for this system computes the M dimensional test statistic $r = (r_1, r_2, \cdots, r_M)$ where

$$r_k = \frac{2}{\sqrt{N_0 T}} \left[\left(\int_0^T r(t)\, x_k(t) \cos \omega t\, dt \right)^2 + \left(\int_0^T r(t)\, x_k(t) \sin \omega t\, dt \right)^2 \right]^{1/2} \qquad (2)$$

It is possible to show (Ref. 4) that the conditional density of r_k is

$$P(r_k | x_m(t)) = \begin{cases} r_k \exp\left(-\frac{1}{2} r_k^2\right) & \text{if } k \neq m \\ r_m \exp\left(-\frac{1}{2} r_m^2 - \frac{1}{2}\alpha^2\right) I_0(\alpha r_m) & \text{if } k = m \end{cases} \qquad (3)$$

where

$$\alpha^2 = 2\, ST/N_0 \qquad (4)$$

and $I_0(\alpha r)$ is the modified Bessel function of the first kind

$$I_0(\alpha r) = \frac{1}{2\pi} \int_{-\pi}^{\pi} \exp(\alpha r \cos\theta)\, d\theta \qquad (5)$$

Now, if no further coding is used, the optimum decoding rule is to declare x_m received when r_m is largest. In Ref. 1 it is shown that the probability of being correct is

$$P_c = \int_0^\infty \left[1 - \exp\left(-\frac{1}{2}x^2\right) \right]^{M-1} \times \exp\left[-\frac{1}{2}(x^2 + \alpha^2)\right] I_0(\alpha x)\, dx \qquad (6)$$

and the data rate is

$$R = \frac{\log_2 M}{T} = \frac{K}{T} \text{ bits/s} \tag{7}$$

It is now well known (Refs. 2, 3, and 4) that

$$\lim_{T \to \infty} P_c = \begin{cases} 1 & \text{if } R < C_\infty = S/N_0 \log_2 e \\ 0 & \text{otherwise} \end{cases} \tag{8}$$

however, the bandwidth W grows exponentially as

$$W = \frac{M}{2T} = \frac{2^{RT}}{2T} \tag{9}$$

Moreover, as already mentioned, letting T grow to infinity assumes a constant phase. This means that coherent communication was possible in the first place, and that C_∞ could have been achieved with binary signals of duration approaching zero as $\frac{1}{2}W$, where $W \to \infty$ *independent of* T. However, the problem, in general, is not a dearth of bandwidth; rather it is a lack of ST/N_0.

Examination of Eq. (6) reveals that $P_c < 1$ if ST/N_0 is finite and decreases ultimately as $1/M$, as M increases. Therefore, additional coding is required if the error probability for a given ST/N_0 and M is to be reduced further. The maximum rate of transmission at which the error probability can be made arbitrarily small by use of additional coding is, of course, the capacity of the inner, MFSK channel, and the main concern of this article.

III. Capacity of the *M*-ary, Noncoherent MFSK Channel

When the receiver makes a decision as to which one of M signals is received and discards all other information the result is an M-ary symmetric channel with crossover probability $(1 - P_c)/(M - 1)$. The capacity of such a channel is easy to compute (Ref. 5).

$$C = \frac{1}{T} [\log_2 M + P_c \log P_c + (1 - P_c) \log_2 (1 - P_c) - (1 - P_c) \log_2 (M - 1)] \text{ bits/s} \tag{10}$$

$$= IR \tag{11}$$

where

$$I(M, ST/N_0) = P_c + \frac{P_c \log_2 P_c + (1 - P_c) \log_2 (1 - P_c)}{\log_2 M} - \frac{(1 - P_c) \log_2 (1 - 1/M)}{\log_2 M} \tag{12}$$

is the information per input bit of the MFSK channel.

Normalizing with respect to $C_\infty = S/N_0 \log_2 e$ yields

$$\frac{C}{C_\infty} = \frac{I \ln 2}{(ST_B/N_0)_{\text{MFSK}}} \tag{13}$$

where

$$(ST_B/N_0)_{\text{MFSK}} \triangleq \frac{ST}{N_0 K} = \frac{S}{N_0 R} \tag{14}$$

is the signal-to-noise ratio per input bit of the MFSK channel.

Figure 2 is a plot of the normalized capacity versus MFSK signal-to-noise ratio for $K = 1, 2, \cdots, 10, 15, 20$ and $K \to \infty$. The $K \to \infty$ curve is obtained from the fact that $P_c \to 1$ if $ST_B/N_0 < \ln 2 = 0.693$, and $P_c \to 0$ otherwise; therefore,

$$\lim_{K \to \infty} \frac{C}{C_\infty} = \begin{cases} 0 & \text{if } (ST_B/N_0)_{\text{MFSK}} < \ln 2 = 0.693 \\ \ln 2/(ST_B/N_0) & \text{otherwise} \end{cases} \tag{15}$$

This reveals, incidentally, that MFSK signaling approaches C_∞ in a nonuniform manner as $K \to \infty$, as opposed to the uniform convergence obtained over the coherent binary input, infinite quantized (no hard decisions) Gaussian channel. The nonuniform convergence is in accord with the threshold effect that is observed in nonlinear receivers.

Figure 3 is a plot of the minimum required energy-to-noise ratio per coded bit (E_b/N_0) coded vs ST/N_0 for various k,

$$\left(\frac{E_b}{N_0}\right)_{\text{coded}} = \frac{C_\infty}{C} \ln 2; \qquad \frac{ST}{N_0} = K \frac{ST_B}{N_0}$$

Note that the performance with $K = 1$ (2 signals) and $K = 2$ (4 signals) is always worse than with $K = 3$ (8 signals) for all values of ST/N_0. This is proved in the appendix.

IV. Convolutional Coding and Decoding Limit

As a guide to the performance obtainable when a convolutional code is used over the MFSK channel, it is of interest to evaluate the computational limit on the decodable rate R_{comp}. Without going into the details treated adequately in Ref. 3, it can be shown that the expected number of computations necessary to decode a convolutional code using a sequential decoding algorithm becomes infinite if the rate exceeds R_{comp}. Thus, R_{comp} is an effective measure of the rate achievable with convolutional codes. Note that R_{comp} here is R_0' in eqn. 6.62b of Ref. 3. For the M-ary symmetric channel

$$R_{\text{comp}} = -\frac{1}{T}\log_2\left[\frac{1}{M}\left(\sqrt{P_c} + (M-1)\sqrt{\frac{1-P_c}{M-1}}\right)^2\right] \tag{16}$$

$$= RI_{\text{comp}} \tag{17}$$

where

$$I_{\text{comp}} = 1 - \frac{2\log_2\left(\sqrt{P_c} + \sqrt{(2^K-1)(1-P_c)}\right)}{K} \tag{18}$$

Therefore

$$\frac{R_{\text{comp}}}{C_\infty} = \frac{I_{\text{comp}}\ln 2}{(ST_B/N_0)_{\text{MFSK}}} \tag{19}$$

yields the normalized computational limit for sequential decoding per input bit of the MFSK channel, and is plotted in Fig. 4 per various values of K.

The curves in Fig. 5 are plots of the minimum required bit energy-to-noise ratio vs ST/N_0 for various K:

$$\left(\frac{E_b}{N_0}\right)_{\text{comp}} = \frac{C_\infty}{R_{\text{comp}}}\ln 2$$

Again, as in the capacity case, we see that the use of 2 and 4 signals is everywhere inferior to using 8 signals for the inner MFSK channel.

Figures 6 and 7 are plots of the optimum performance achievable for given K after optimizing over ST/N_0, and for given ST/N_0 after optimizing over K. From Fig. 6 it is evident that improvement with increasing M is very slow for $M > 1000$ ($K > 10$). Since larger values of M are too complex it also means that when $ST/N_0 > 10$ orthogonal signaling must be replaced by some other scheme; such as by partially coherent schemes, or by schemes involving "soft" decisions in the inner MFSK channel.

Investigation of "soft" decision MFSK systems is currently under way for both large and small values of ST/N_0. Better performance is to be expected from the fact that more information is retained when soft rather than hard decisions are made.

V. Conclusions

This article established performance limits theoretically achievable over noncoherent channels perturbed by additive Gaussian noise using orthogonal signals and a hard-decision MFSK receiver. The performance is, not surprisingly, a function of the signal-to-noise ratio ST/N_0 in the MFSK correlators. These correlators can be thought of as a predetection filter and ST/N_0 as the predetection signal-to-noise ratio. The performance improves as ST/N_0 increases provided the bandwidth, as measured by the number of orthogonal signals, can be increased.

The result of greater practical import, however, concerns operation at moderate and low values of the predetection signal-to-noise ratio, $ST/N_0 < 1.0$, where it was found that the best results are to be obtained by using about 8 signals.

VI. Acknowledgment

The numerical computations were programmed and run on a digital computer by I. Eisenberger, to whom our thanks are addressed.

References

1. Lindsey, W. C., "Coded Noncoherent Communications," *IEEE Transactions on Space Electronics and Telemetry*, Vol. SET 10-11, pp. 6–13, March 1965.

2. Turin, G. L., "The Asymptotic Behavior of Ideal *M*-ary Systems," *IRE Proceedings*, Vol. 47, pp. 93–94, January 1959.

3. Wozencraft, Z. M., and Jacobs, I. M., *Principles of Communications Engineering*, J. Wiley and Sons, New York, N.Y., 1965.

4. Viterbi, A. J., *Principles of Coherent Communication*, McGraw-Hill, New York, N.Y., 1966.

5. Fano, R. M., *Transmission of Information*, J. Wiley and Sons, New York, N.Y., 1961.

Appendix
Capacity at Very Small Values of ST/N_0

We will show that

$$\frac{C}{C_\infty} \to \frac{ST}{N_0}\left(\sum_{m=2}^{M} \frac{1}{m}\right)^2 \Big/ 2(M-1) \qquad \text{as } \frac{ST}{N_0} \to 0 \tag{A-1}$$

The coefficient multiplying ST/N_0 on the right hand side has a maximum value of 0.211 at $M = 7$. However, the maximum is quite broad and is 0.2107 at $M = 8$. Therefore, the optimum mode of communication in a hard-decision MFSK system at very low signal-to-noise ratios is to use 8 signals (a power of 2 is always convenient). The comparative performance of 2, 4, 8, 16, and 32 signals is as 0.1250, 0.1956, 0.2107, 0.1895, 0.1508. In particular the performance of a binary hard decision frequency shift keying (FSK) system is 2.28 dB below that of the optimum 7 or 8 frequency system.

To prove the above relationship we note that

$$P_c \to \frac{1}{M} \qquad \text{as } ST/N_0 \to 0$$

Therefore, it is convenient to introduce

$$\varepsilon_M = MP_c - 1 \tag{A-2}$$

Then

$$I \ln M = \frac{1}{M}(1 + \varepsilon_M)\ln(1 + \varepsilon_M) + \frac{M-1}{M}\left(1 + \frac{\varepsilon_M}{M-1}\right)\ln\left(1 + \frac{\varepsilon_M}{M-1}\right)$$

$$\approx \frac{\varepsilon_M^2}{2(M-1)} \qquad \text{for } \varepsilon_M << 1 \tag{A-3}$$

Since $C/C_\infty = I \ln M/(ST/N_0)$ it is necessary to show that

$$\varepsilon_M \approx \frac{ST}{N_0}\sum_{m=2}^{M}\frac{1}{m}$$

In Ref. 1 it is noted that the probability of a correct decision is also given by

$$P_c = 1 - \frac{1}{M}\sum_{j=2}^{M}(-1)^j \binom{M}{j} \exp\left[-\frac{ST}{N_0}\left(1 - \frac{1}{j}\right)\right] \tag{A-4}$$

$$= -\frac{1}{M}\sum_{j=1}^{M}(-1)^j \binom{M}{j} \exp\left[-\frac{ST}{N_0}\left(1 - \frac{1}{j}\right)\right] \tag{A-5}$$

Therefore

$$\varepsilon_M - \varepsilon_{M-1} = -\sum_{j=1}^{M-1}(-1)^j \binom{M-1}{j}\left(1 - \frac{M}{M-j}\right) \times \exp\left[-\frac{ST}{N_0}\left(1 - \frac{1}{j}\right)\right] - (-1)^M \exp\left[-\frac{ST}{N_0}\left(1 - \frac{1}{M}\right)\right] \tag{A-6}$$

$$= -\frac{1}{M}\sum_{j=1}^{M}(-1)^j \binom{M}{j} \times \exp\left[-\frac{ST}{N_0}\left(1 - \frac{1}{j}\right)\right] \tag{A-7}$$

$$= \exp[-ST/N_0]\int_0^{ST/N_0} \exp[x]\, P_c(x)\, dx \tag{A-8}$$

$$= \frac{\exp[-ST/N_0]}{M}\int_0^{ST/N_0} \exp[x]\,[1 + \varepsilon_M(x)]\, dx \tag{A-9}$$

Now, $\varepsilon_M(0) = 0$ and increases with x, therefore

$$\left(\frac{1 - \exp[-ST/N_0]}{M}\right) \leq \varepsilon_M - \varepsilon_{M-1} \leq \left(\frac{1 - \exp[-ST/N_0]}{M}\right)(1 + \varepsilon_M) \tag{A-10}$$

or

$$\frac{ST}{N_0}\frac{1}{M} \leq \varepsilon_M - \varepsilon_{M-1} \leq \frac{ST}{N_0}(1 + \varepsilon_M)\frac{1}{M} \tag{A-11}$$

However, from the left hand inequality we have $\varepsilon_M \geqq \varepsilon_m$ for any $m \leqq M$. Therefore

$$\frac{ST}{N_0}\frac{1}{m} \leqq \varepsilon_m - \varepsilon_{m-1} \leqq \frac{ST}{N_0}\frac{1}{m}(1 + \varepsilon_M); \qquad m \leqq M \tag{A-12}$$

Summing from 2 to M yields

$$\frac{ST}{N_0}\sum_{m=2}^{M}\frac{1}{m} \leqq \varepsilon_M \leqq \left(\frac{ST}{N_0}\sum_{m=2}^{M}\frac{1}{m}\right)(1 + \varepsilon_M) \tag{A-13}$$

thus

$$\frac{ST}{N_0}\sum_{m=2}^{M}\frac{1}{m} \leqq \varepsilon_M \leqq \frac{\dfrac{ST}{N_0}\displaystyle\sum_{m=2}^{M}\frac{1}{m}}{1 - \dfrac{ST}{N_0}\displaystyle\sum_{m=2}^{M}\frac{1}{m}} \tag{A-14}$$

provided the denominator on the right hand side is positive. Since the upper and lower bounds approach each other as $ST/N_0 \rightarrow 0$ the desired result is established.

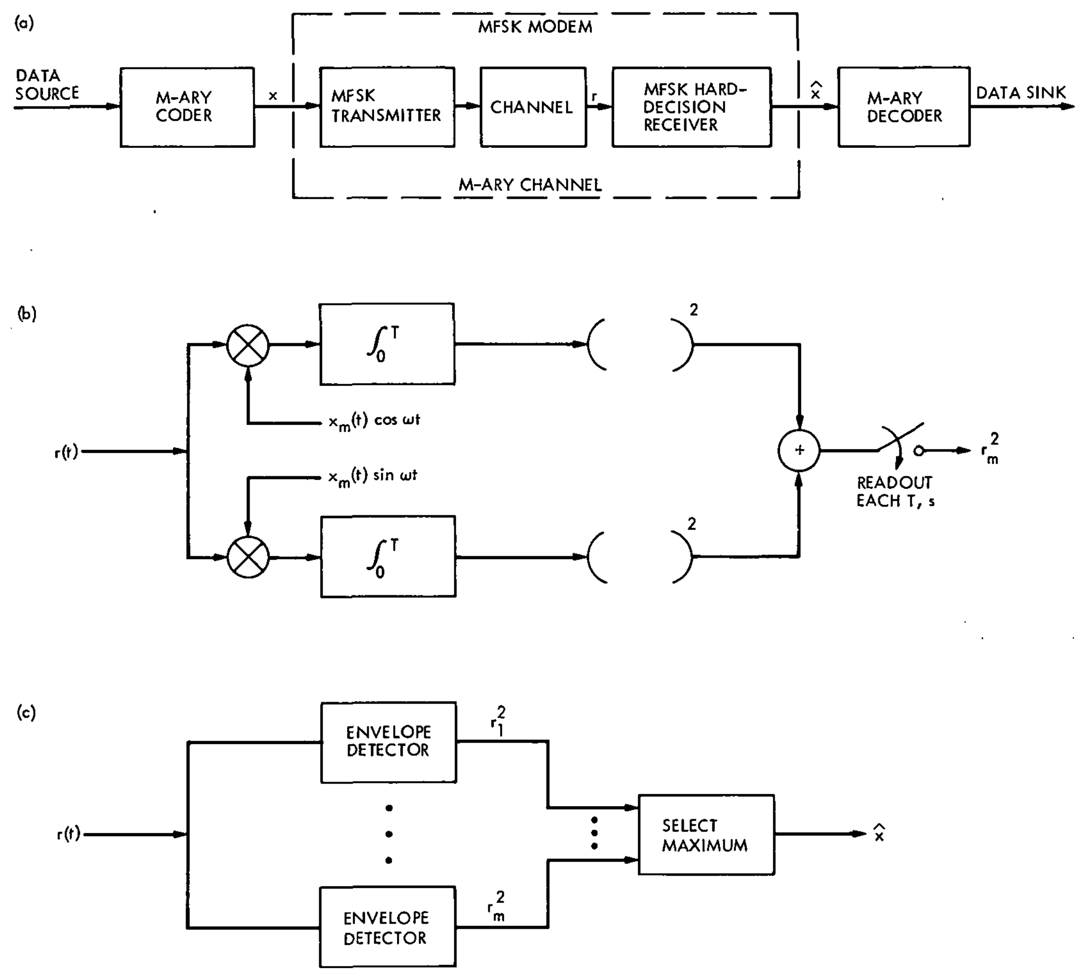

Fig. 1. Coded hard-decision MFSK system diagram: (a) coder and modem; (b) envelope detector; (c) hard-decision MFSK receiver

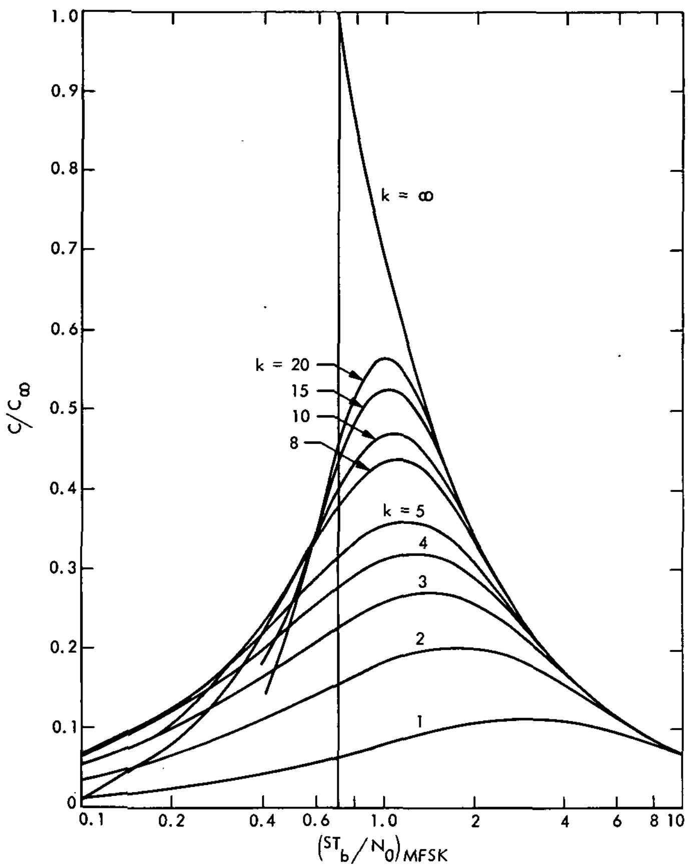

Fig. 2. Capacity vs MFSK bit SNR

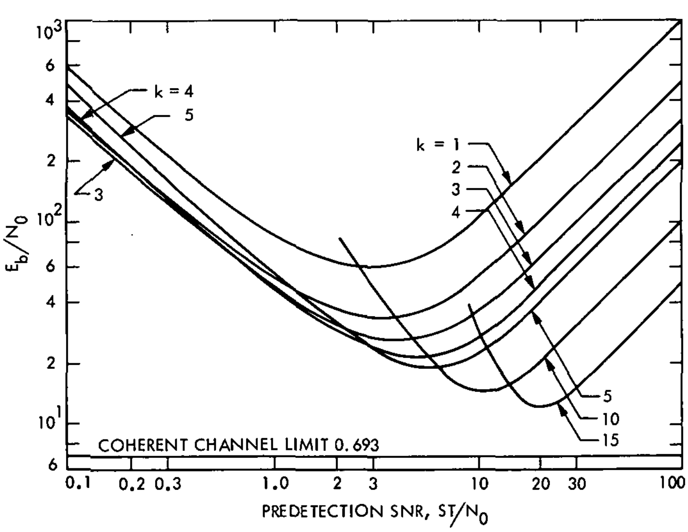

Fig. 3. Minimum SNR per coded bit vs predetection SNR

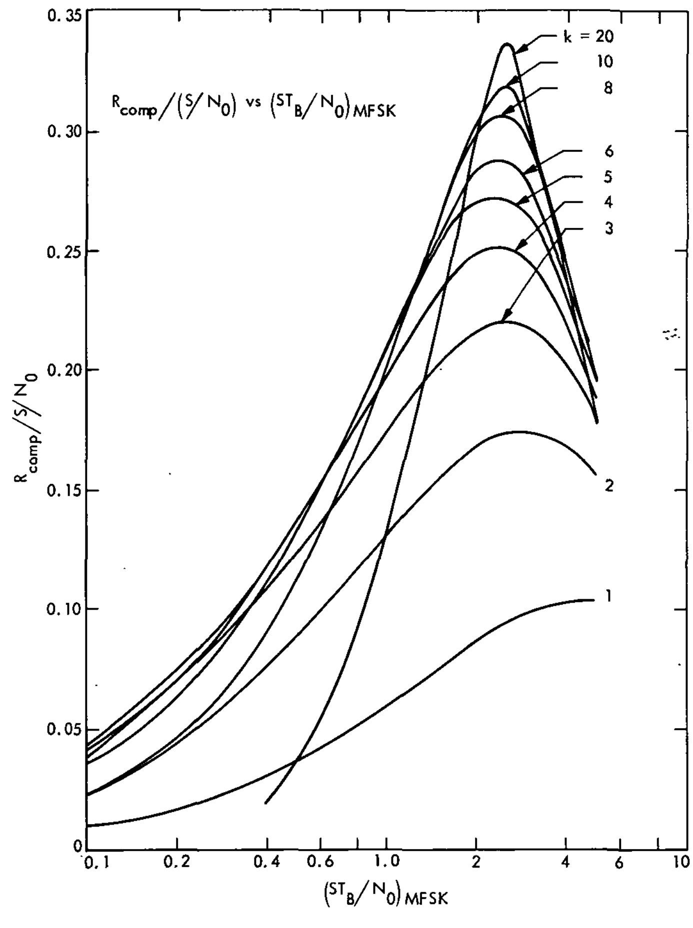

Fig. 4. R_{comp} vs MFSK bit SNR

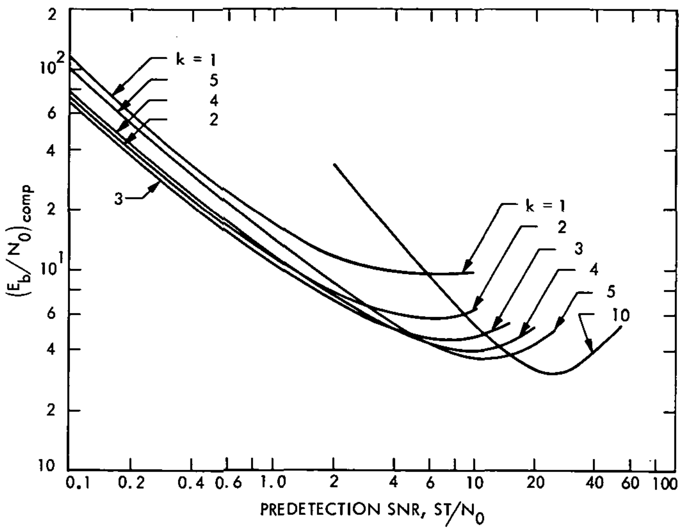

Fig. 5. (E_b/N_0) comp vs predetection SNR

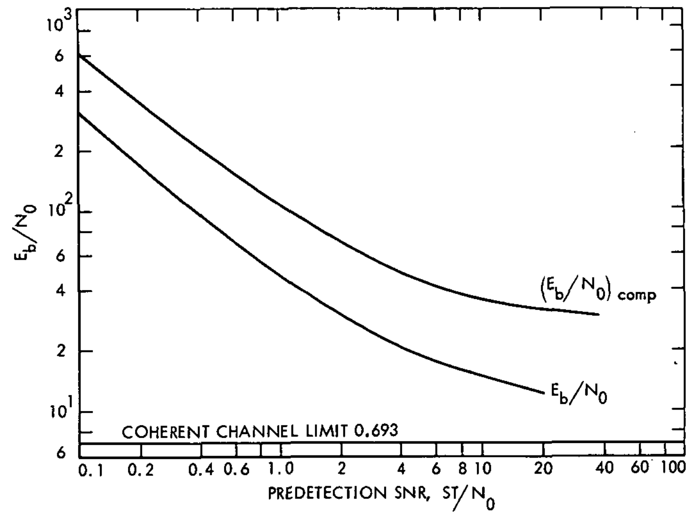

Fig. 7. Performance vs predetection SNR

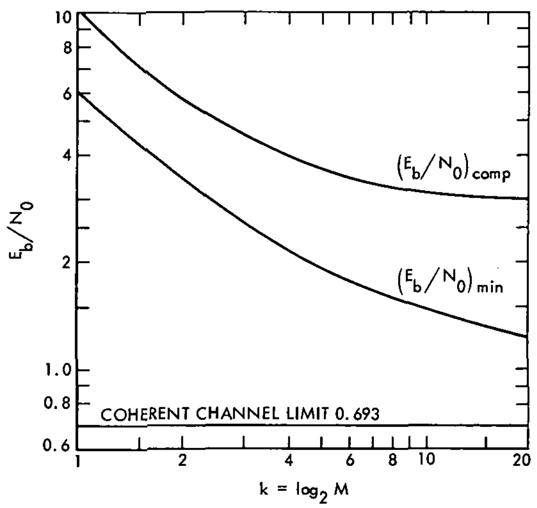

Fig. 6. Performance vs number of MFSK signals

Efficient Antenna Systems: A New Computer Program for the Design and Analysis of High-Performance Conical Feedhorns

P. D. Potter
Communications Elements Research Section

It is well known that paraboloidal antenna aperture efficiency is enhanced by providing aperture illumination which approaches uniformity in amplitude, phase, and polarization. For dual-reflector antenna systems, such as those used in the DSN, a high degree of uniformity is possible by use of specially shaped reflector surfaces (Ref. 1). As a long-range solution to the problem of achieving high aperture efficiency, this approach is attractive because it is inherently broadband and requires only a simple feedhorn of the type presently being utilized in the DSN. An alternate approach for achieving high aperture efficiency (suggested by D. Bathker of the Communications Elements Research Section) involves use of the existing antenna reflecting surfaces together with a more complex multimode feedhorn. This approach is attractive from an implementation standpoint. Preliminary experimental results (obtained by R. Thomas of the Communications Elements Research Section) are promising. The multimode technique does, however, suffer from bandwidth difficulties, at least with presently known mode-generation techniques. To assist and guide the multimode feedhorn experimental effort, a new computer program has been developed which computes horn radiation patterns and bandwidth properties as a function of horn geometry. This article describes the analytical technique utilized and agreement with existing experimental data.

I. Introduction

For the case of conical horns with modest or small flare angles, the amplitude patterns may be calculated to good accuracy by expanding the aperture fields in cylindrical waveguide modes and utilizing the radiation pattern formulas given by Silver (Ref. 2). An early but definitive work on the effect of neglecting the horn flare angle by Ludwig (Ref. 3) showed that the propagation characteristics of conical waveguide modes differ from those of cylindrical waveguide modes in a simple and predictable way. In a detailed analysis of the differences in aperture illumination functions between cylindrical and conical modes, Narasimhan and Rao (Ref. 4) demonstrate that, for semi-flare angles up to 20 deg, the fields on a spherical cap in the horn aperture are very well approximated by the standard cylindrical (Bessel function) fields.

The first good conical feedhorn to be developed was the dual-mode horn reported by Potter (Ref. 5). This horn has many desirable performance features, together with a convenient physical configuration, but suffers from a bandwidth problem. The dual-mode horn concept was extended by Ludwig (Ref. 6) to the case of many modes. Ludwig used cylindrical waveguide functions and showed good experimental results for a four-mode horn. Later, Minnet and Thomas (Ref. 7) reported a new technique for achieving the same performance as the dual-mode horn (Ref. 5) but over a large bandwidth. This method consists of utilizing a high-impedance wall in the horn, physically realized by circumferential grooves approximately one-quarter wavelength deep. The two modes in such a horn (TE_{11} and TM_{11}) propagate with the same velocity and are both necessary in a certain phase and amplitude relationship to satisfy the horn wall boundary conditions. The two modes are therefore called a single hybrid mode, designated the HE_{11} mode. A horn of this type is presently the standard design for the DSN 64-m-diameter antennas (Ref. 8).

B. Mac A. Thomas later extended his hybrid-mode horn analysis to the case of multiple hybrid modes (Ref. 9). In order to get closed-form solutions for the modal radiation patterns, Thomas assumed a planar aperture with cylindrical hybrid modes. A definitive review of hybrid-mode propagation and aperture radiation for both cylindrical and conical configurations has been published by Clarricoats and Saha (Refs. 10 and 11).

Clarricoats et al. (Ref. 12) developed a spherical wave technique for computing hybrid-mode horn radiation patterns and showed good agreement with experimental data. Professor Clarricoats was kind enough to send a copy of the computer program developed by his group for performing these radiation pattern calculations. Unfortunately, his program (written in ALGOL) was not easily adaptable for use with the JPL Scientific Computing Facility (SCF). Additionally, certain extra features were desired in the program. For these reasons, a new program was written in FORTRAN IV for use on the SCF Univac 1108 computer. This program utilizes Clarricoats' spherical wave technique (Ref. 12) and his cylindrical hybrid-mode equations (Ref. 10) but uses a spherical cap aperture with the field approximation of Ref. 4. This procedure produces very accurate results for small flare-angle horns such as those employed in DSN antennas. The new computer program has been checked out and results have been compared with experimental data. The program is described in the next section.

II. Computer Program Description

Figure 1 shows the selected horn geometry. The phasing section may have zero length as a special case, or may be utilized to phase a pair of hybrid modes for proper relationship. The computer program, HYBRID-HORN, assumes that the amplitude of the hybrid modes in the aperture is known and has an input for adjustment of mode amplitudes; in actual practice, the mode amplitudes are controlled by the mode-generator geometry. The phases of the hybrid modes at the input of the phasing section (mode generator) are also input. The resulting phases at the aperture are computed by numerical integration of the propagation constants in the phasing section and flare. The propagation constants in the flare are calculated using the cylindrical-guide-arc length technique developed by Ludwig (Ref. 3). The only other program inputs are the horn physical geometry and various output options. A typical case (one geometry at one frequency) takes about 20 s of SCF Univac 1108 execution time.

The program presently assumes unity ($m = 1$) azimuthal field variation, although it could easily be upgraded for modes with arbitrary azimuthal variation. The $m = 1$ variation is that which is normally desired in an antenna feed. The field equations in the horn plane are given by (Ref. 10):

$$\mathbf{E}_{rn} = (E_n)\,[J_1(x)]\sin\phi\,\mathbf{a}_r \tag{1a}$$

$$\mathbf{H}_{rn} = -\left(\frac{E_n}{Z_0}\right)(\mathrm{BAL}_n)\,[J_1(x)]\cos\phi\,\mathbf{a}_r \tag{1b}$$

$$\mathbf{E}_{\theta n} = -j(E_n)\left(\frac{k}{K_n}\right)\left[\frac{J_1(x)}{x}\right] \times [\bar{\beta}_n \cdot F_m(x) + \mathrm{BAL}_n]\sin\phi\,\mathbf{a}_\theta \tag{1c}$$

$$\mathbf{E}_{\phi n} = -j(E_n)\left(\frac{k}{K_n}\right)\left[\frac{J_1(x)}{x}\right] \times [\bar{\beta}_n + F_m(x)\cdot \mathrm{BAL}_n]\cos\phi\,\mathbf{a}_\phi \tag{1d}$$

$$\mathbf{H}_{\theta n} = +j\left(\frac{E_n}{Z_0}\right)\left(\frac{k}{K_n}\right)\left[\frac{J_1(x)}{x}\right] \times [\bar{\beta}_n \cdot \mathrm{BAL}_n \cdot F_m(x) + 1]\cos\phi\,\mathbf{a}_\theta \tag{1e}$$

$$\mathbf{H}_{\phi n} = -j\left(\frac{E_n}{Z_0}\right)\left(\frac{k}{K_n}\right)\left[\frac{J_1(x)}{x}\right] \times [\bar{\beta}_n \cdot \mathrm{BAL}_n + F_m(x)]\sin\phi\,\mathbf{a}_\phi \tag{1f}$$

where

$$F_m(x) \equiv x \left[\frac{J_1'(x)}{J_1(x)} \right]$$

J_1 = Bessel function of the first kind and order 1

J_1' = derivative of J_1 with respect to the argument

k = free-space propagation constant

$x = K_n r$

Z_0 = free-space characteristic impedance

$$F_m(x_1) - \frac{\bar{\beta}_n^2}{F_m(x_1)} = \left(\frac{K_n}{k} \right)^2 S_m(x_1', x_0') \qquad (2)$$

$$F_m(x_1) = x_1 \left[\frac{J_1'(x_1)}{J_1(x_1)} \right]$$

$x_1 = K r_1$

$$\bar{\beta}_n^2 \equiv 1 - \left(\frac{K_n}{k} \right)^2$$

$$S_m(x_1', x_0') \equiv x_1' \left[\frac{J_1'(x_1') \cdot Y_1(x_0') - J_1(x_0') \cdot Y_1'(x_1')}{J_1(x_1') \cdot Y_1(x_0') - J_1(x_0') \cdot Y_1(x_1')} \right]$$

Y_1 = Bessel function of the second kind and order 1

Y_1' = derivative of Y_1 with respect to the argument

$x_1' = k r_1$

$x_0' = K(r_1 + \text{GROOVE})$

GROOVE = groove depth

$$\text{BAL}_n = - \frac{\bar{\beta}_n}{F_m(x_1)}$$

The normalized longitudinal propagation constant $\bar{\beta}$ is determined by numerical solution of Eq. (2). The wall reactance, ZGROOV, is given by

$$\text{ZGROOV} = - \frac{(Z_0) x_1'}{S_m(x_1', x_0')} \qquad (3)$$

At the frequency of operation for which BAL_n *is* ± 1, the hybrid mode is said to be *balanced*. Modes for which the BAL_n are positive quantities are normally desired and are designated HE_{1n}. At the balance frequency, the HE_{1n} modes exhibit almost perfect symmetry between *E*- and *H*-planes. Modes for which the BAL_n are negative are designated EH_{1n} modes and are normally undesirable since they are grossly unsymmetrical between *E*- and *H*-planes.

An interesting and important special case of Eqs. (1a)–(1f) is that for which the groove depth approaches zero, i.e., the horn becomes a standard smooth-wall horn. For this case, BAL_n approaches a positive zero (HE_{1n} modes) or a negative infinity (EH_{1n} modes). Examination of the equations for smooth-wall cylindrical waveguides (Ref. 2) shows that Eqs. (1a)–(1f) become the smooth-wall equations, with HE_{1n} modes becoming TM_{1n} modes and EH_{1n} modes becoming TE_{1n} modes. The case of TE_{11} and TM_{11} is of particular interest since it corresponds to the dual-mode conical horn (Ref. 5), for which good experimental data are available and which is still being used for special applications such as gain standards. The computer program HYBRIDHORN has an internal switch so that it will handle the case of zero groove depth (smooth-wall horn).

III. Comparison with Experimental Data

Figure 2 shows a comparison of HYBRIDHORN computed data (TE_{11} and TM_{11} modes only) for the smooth-wall JPL/NBS Standard Gain Horn (Ref. 13), which is a scale model of the original dual-mode horn design (Ref. 5). The *H*-plane agreement is almost perfect. The minor discrepancies in *E*-plane are not presently understood. An attempt was made to improve agreement with experimental data by addition of radiation from currents at the edge of the horn aperture. Significant improvement was not obtained, however. One possibility for the *E*-plane discrepancies not yet investigated is the presence of significant amounts of modes other than TE_{11} and TM_{11} – the TE_{12} in particular. Although the horn design (Ref. 5) is such that higher-order modes are severely attenuated, the exact degrees of attenuation and the generated amplitudes have not been calculated or measured.

Figure 3 shows a comparison of HYBRIDHORN computed and measured data for the DSIF single hybrid-mode corrugated horn (Ref. 8). These recently obtained measured patterns were taken by R. Thomas and O. Hester of the Communications Elements Research Section, using

the JPL Mesa Antenna Range Facility, with the same basic setup described in Ref. 13. The excellent agreement between computed and measured patterns demonstrates the high quality of the experimental data and the implied accuracy of the HYBRIDHORN computer program.

Figure 4 shows computed and measured amplitude patterns (phase data were not available) for an experimental dual hybrid-mode horn.*

Section IV briefly discusses a novel use of the DSIF standard corrugated feedhorn design, in conjunction with the HYBRIDHORN program.

IV. Possible Use of the DSIF Corrugated Feedhorn Design as a Gain Standard

The HYBRIDHORN computed pattern shown in Fig. 2 was numerically integrated; the computed directivity is 21.990 dB. Despite the minor pattern discrepancies, this number compares favorably with the JPL/NBS horn calibration directivity of 22.04 ± 0.10 dB, 3σ, quoted in Ref. 13. The computed directivity of the single hybrid-mode horn pattern shown in Fig. 4 is 22.370 dB (at 8.448 GHz). Because this horn is a single-mode horn, there is no question of whether the HYBRIDHORN program has the correct inputs; thus the confidence level in the 22.370-dB number is high. As a gain standard, the corrugated horn has a number of attractive features relative to the JPL/NBS horn, including lower dissipative loss, lower E-plane aperture edge illumination (hence less exterior currents), broad bandwidth, and more accurately calculable performance. These features bear further examination.

*The computed data are for HE_{11} and HE_{12} modes only. The possibility of additional modes in the experimental data exists.

Acknowledgement

It is a pleasure to acknowledge many helpful discussions on this project with R. Thomas, A. C. Ludwig, and P. W. Cramer, all of the Communications Elements Research Section.

References

1. Potter, P. D., "Antenna Study: Performance Enhancement," in *The Deep Space Network Progress Report*, Technical Report 32-1526, Vol. X, pp. 129–134, Jet Propulsion Laboratory, Pasadena, Calif., Aug. 15, 1972.
2. Silver, S., *Microwave Antenna Theory and Design*, Chapter 10, McGraw-Hill Book Co., Inc., New York, 1949.
3. Ludwig, A., "Antennas for Space Communications: Antenna Feed Research," in *Supporting Research and Advanced Development*, Space Programs Summary 37-22, Vol. IV, pp. 184–189, Jet Propulsion Laboratory, Pasadena, Calif., Aug. 31, 1963.
4. Narasimhan, M. S., and Rao, B. V., "Hybrid Modes in Corrugated Conical Horns," *Electronic Letters*, Vol. 6, No. 2, Jan. 22, 1970, pp. 32–34.
5. Potter, P. D., "A New Horn Antenna with Suppressed Sidelobes and Equal Beamwidths," *Microwave J.*, June 1963.
6. Ludwig, A. C., "Radiation Pattern Synthesis for Circular Aperture Horn Antennas," *IEEE Trans. on Antennas and Propagation*, Vol. AP-14, No. 4, July 1966, pp. 434–440.
7. Minnett, H. C., and Thomas, B. Mac A., "A Method of Synthesizing Radiation Patterns with Axial Symmetry," *IEEE Trans. on Antennas and Propagation*, Vol. AP-14, 1966, pp. 654–656.
8. Brunstein, S. A., "A New Wideband Feed Horn With Equal E- and H-Plane Beamwidths and Suppressed Sidelobes," in *The Deep Space Network*, Space Programs Summary 37-58, Vol. II, pp. 61–64, Jet Propulsion Laboratory, Pasadena, Calif., July 31, 1969.
9. Thomas, B. Mac A., "Theoretical Performance of Prime-Focus Paraboloids Using Cylindrical Hybrid-Mode Feeds," *Proc. IEE (British)*, Vol. 118, No. 11, Nov. 1971.
10. Clarricoats, P. J. B., and Saha, P. K., "Propagation and Radiation Behavior of Corrugated Feeds – Part 1. Corrugated Waveguide Feed," *Proc. IEE (British)*, Vol. 118, No. 9, Sept. 1971, pp. 1167–1176.
11. Clarricoats, P. J. B., and Saha, P. K., "Propagation and Radiation Behavior of Corrugated Feeds – Part 2. Corrugated-Conical-Horn Feed," *Proc. IEE (British)*, Vol. 118, No. 9, Sept. 1971, pp. 1177–1186.
12. Clarricoats, P. J. B., et al., "Near-Field Radiation Characteristics of Corrugated Horns," *Electronic Letters*, Vol. 7, No. 16.
13. Ludwig, A., et al., *Gain Calibration of a Horn Antenna Using Pattern Integration*, Technical Report 32-1572, Jet Propulsion Laboratory, Pasadena, Calif., Oct. 1, 1972.

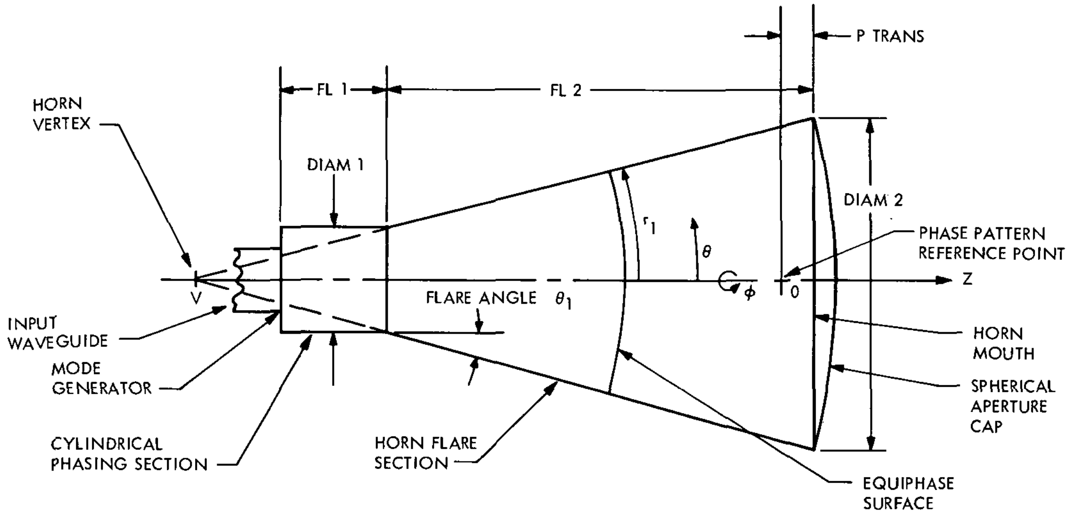

Fig. 1. Horn geometry

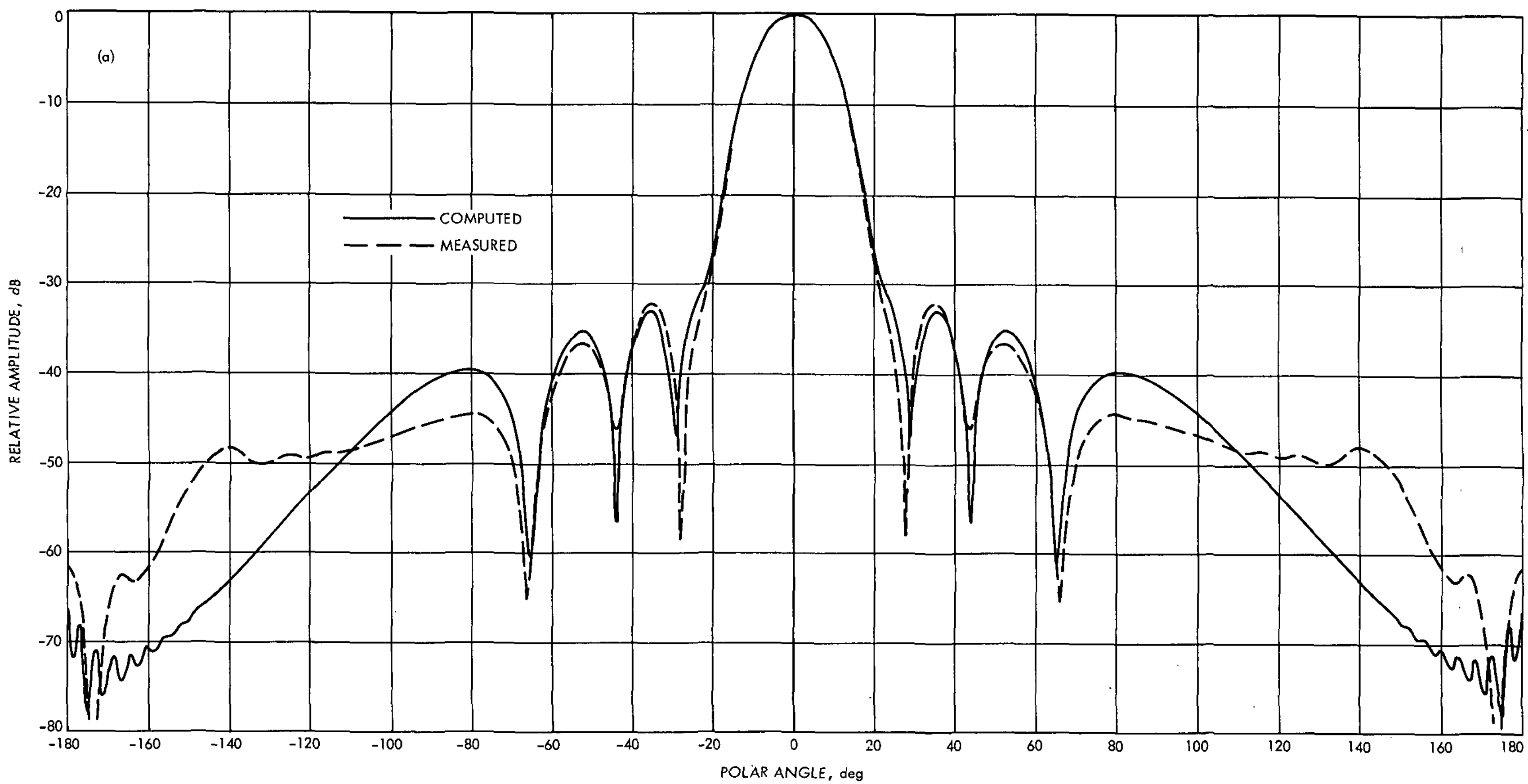

Fig. 2. Computed and measured patterns about phase center, NBS standard gain horn: (a) E-plane amplitude, (b) E-plane phase, (c) H-plane amplitude, (d) H-plane phase

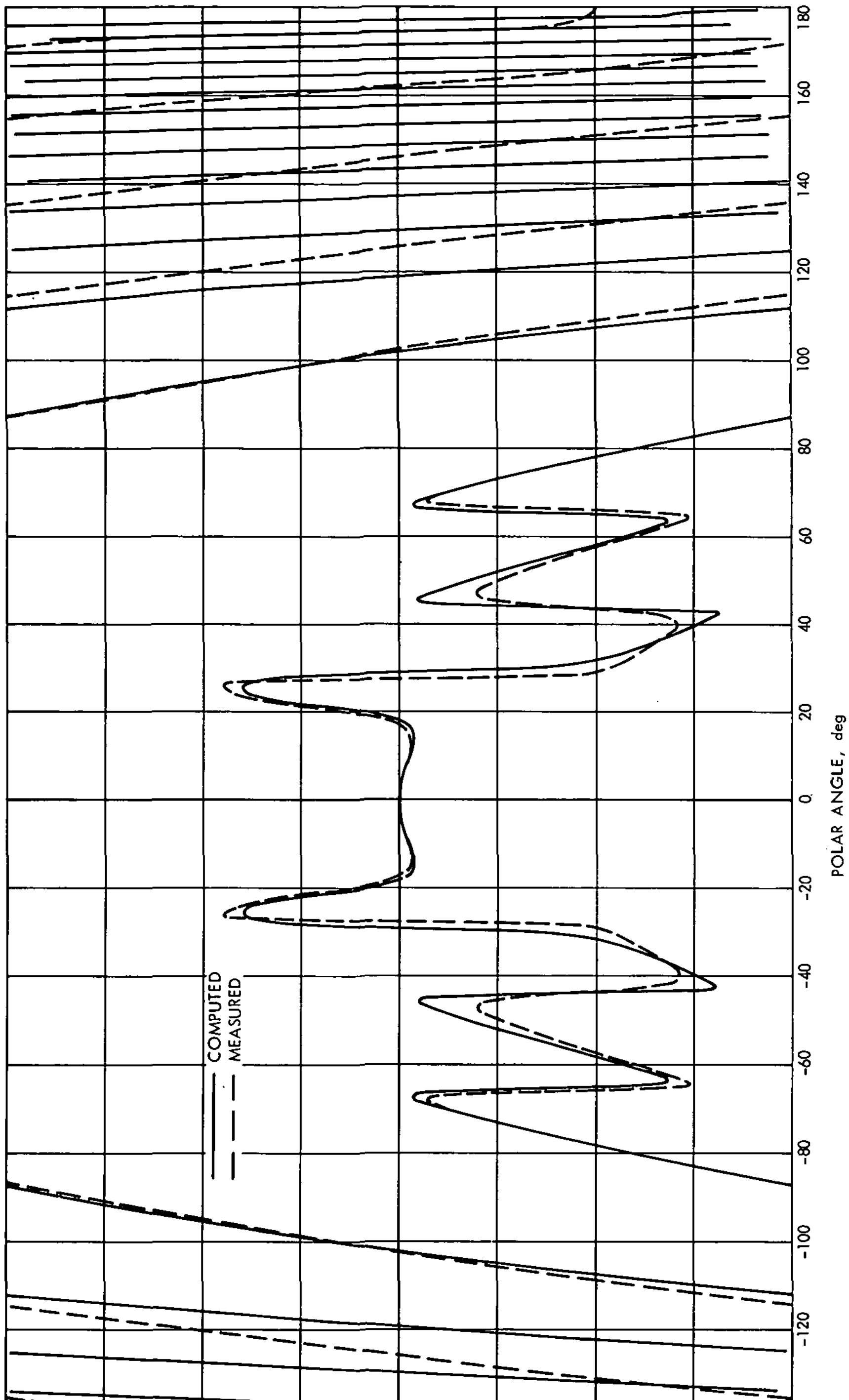
(b)
COMPUTED
MEASURED
POLAR ANGLE, deg
PHASE, deg
-180
-160
-140
-120
-100
-80
-60
-40
-20
0
20
40
60
80
100
120
140
160
180
180
135
90
45
0
-45
-90
-135
-180

Fig. 2 (contd)

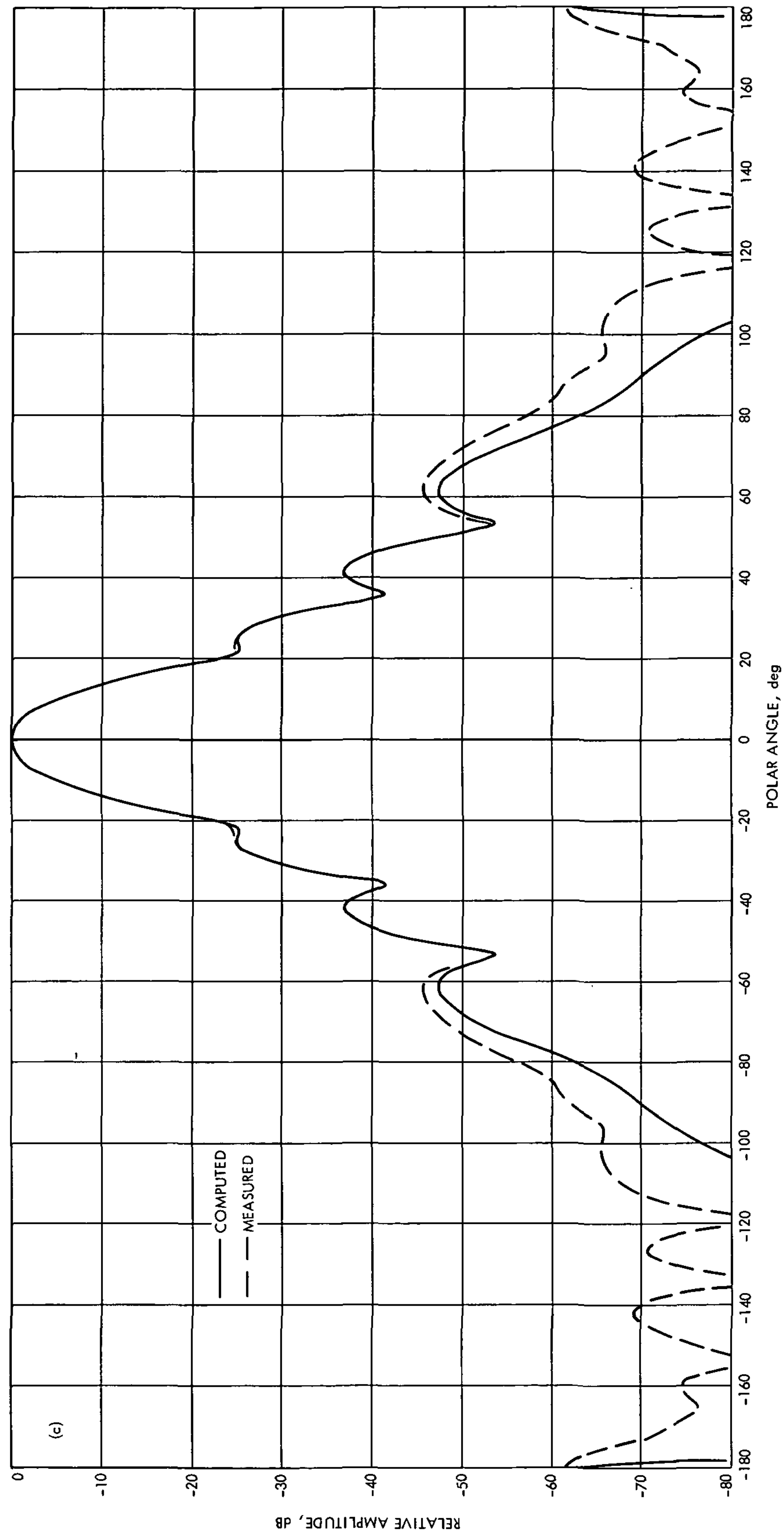
(c)
COMPUTED
MEASURED
POLAR ANGLE, deg
RELATIVE AMPLITUDE, dB
0
-10
-20
-30
-40
-50
-60
-70
-80
-180
-160
-140
-120
-100
-80
-60
-40
-20
0
20
40
60
80
100
120
140
160
180

Fig. 2 (contd)

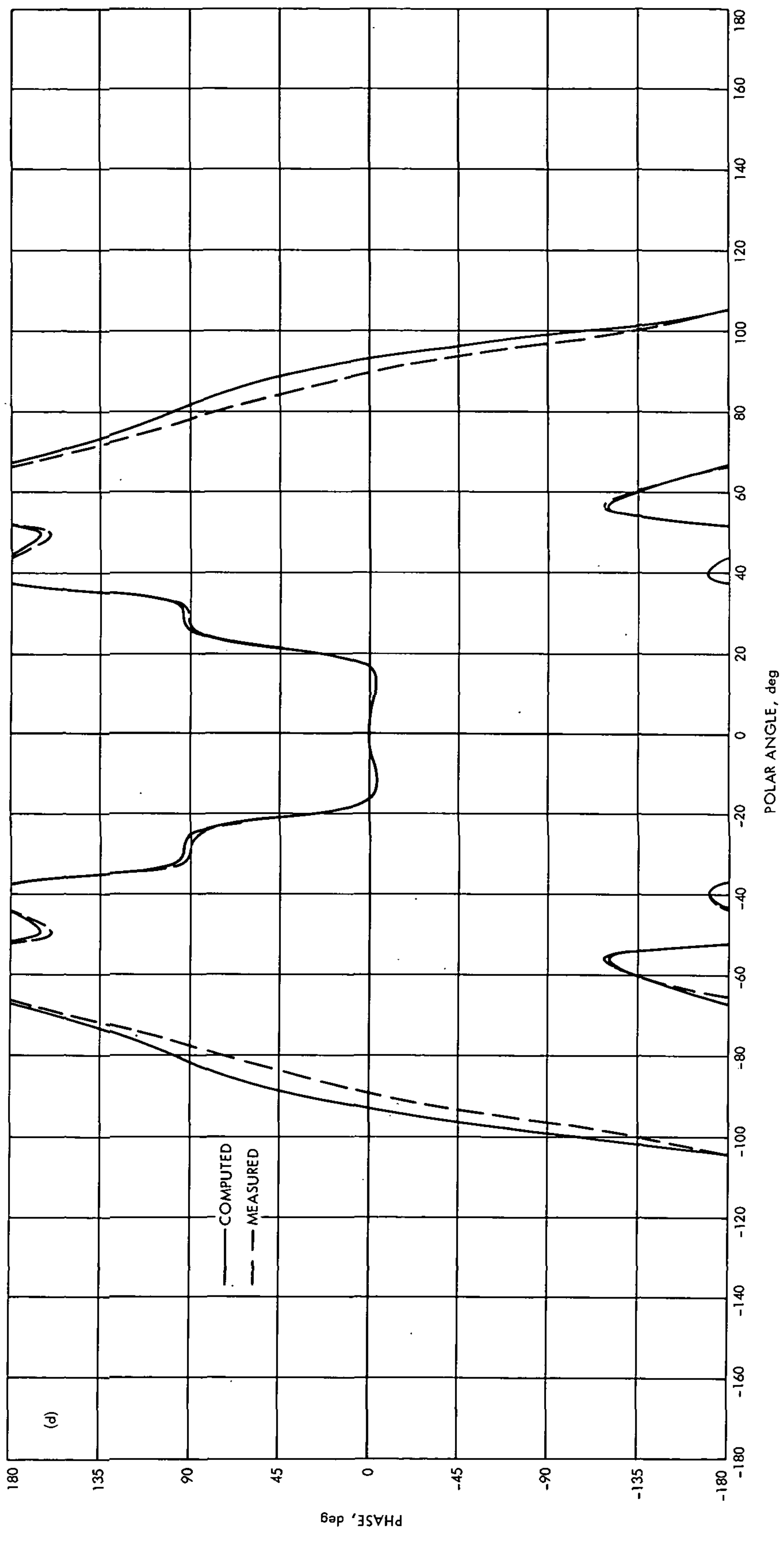
(d)
COMPUTED
MEASURED
POLAR ANGLE, deg
PHASE, deg
-180
-160
-140
-120
-100
-80
-60
-40
-20
0
20
40
60
80
100
120
140
160
180
-135
-90
-45
45
90
135

Fig. 2 (contd)

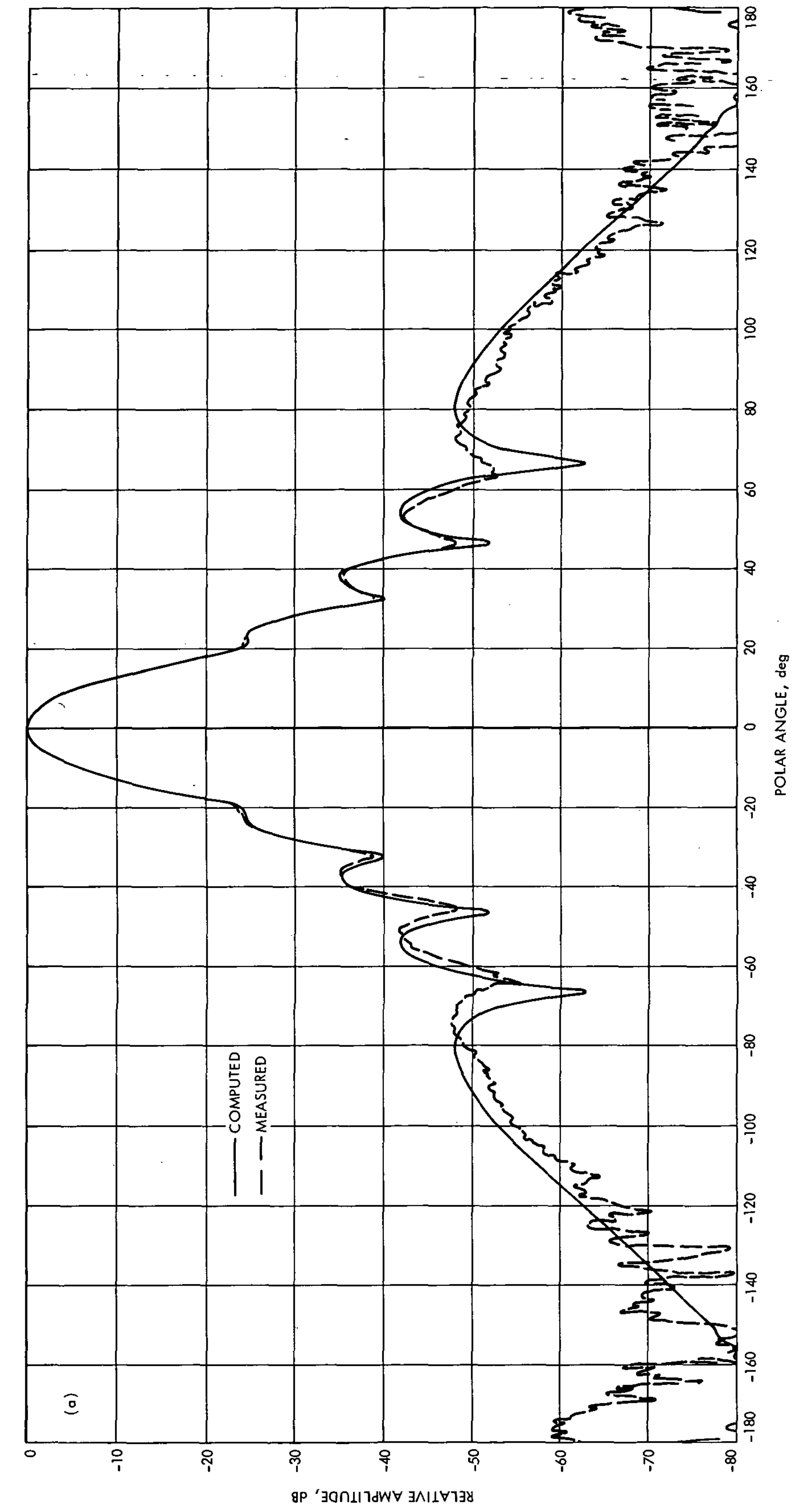

Fig. 3. Computed and measured patterns about phase center, standard DSIF single *hybrid-mode* horn: (a) E-plane amplitude, (b) E-plane phase, (c) H-plane amplitude, (d) H-plane phase

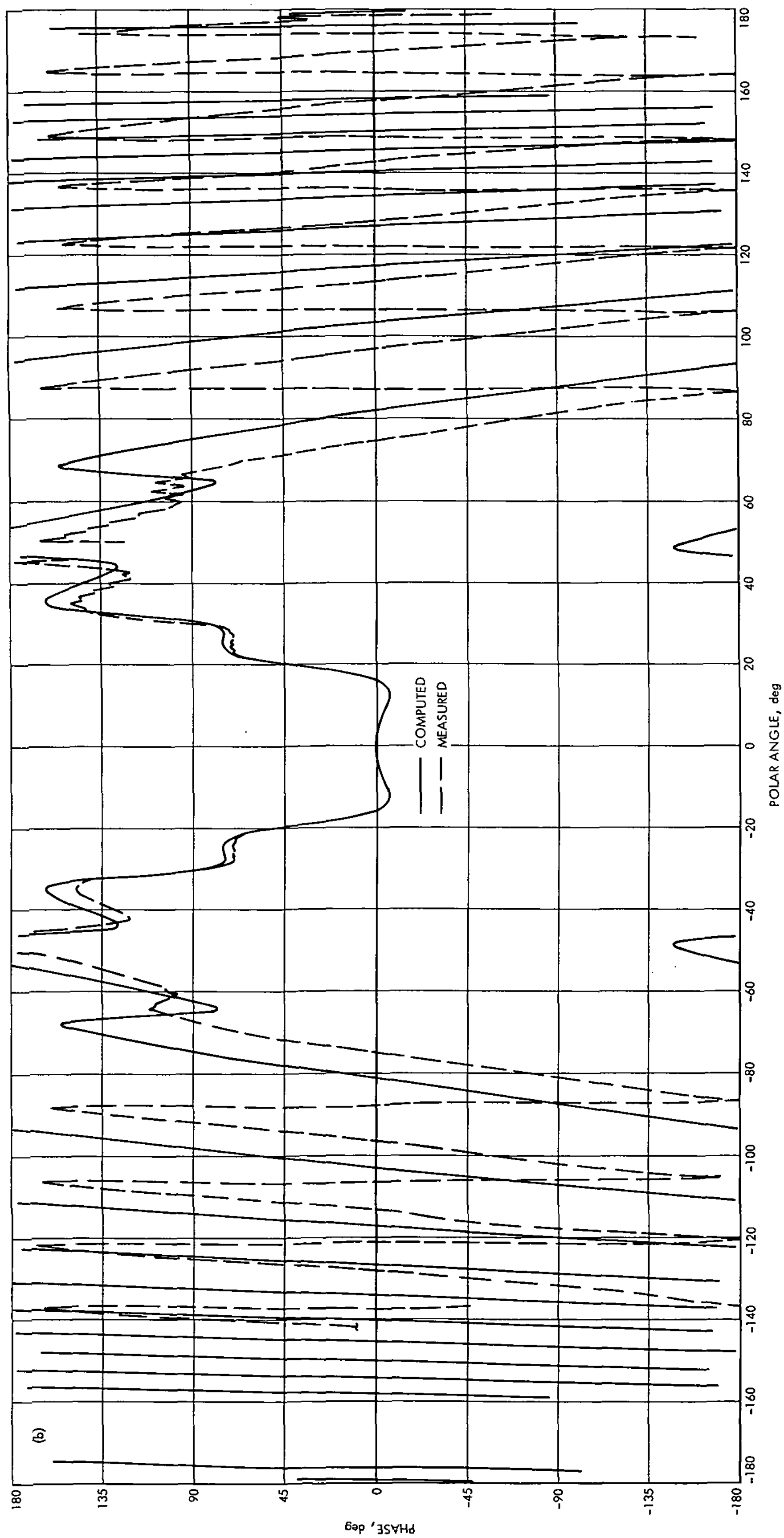

Fig. 3 (contd)

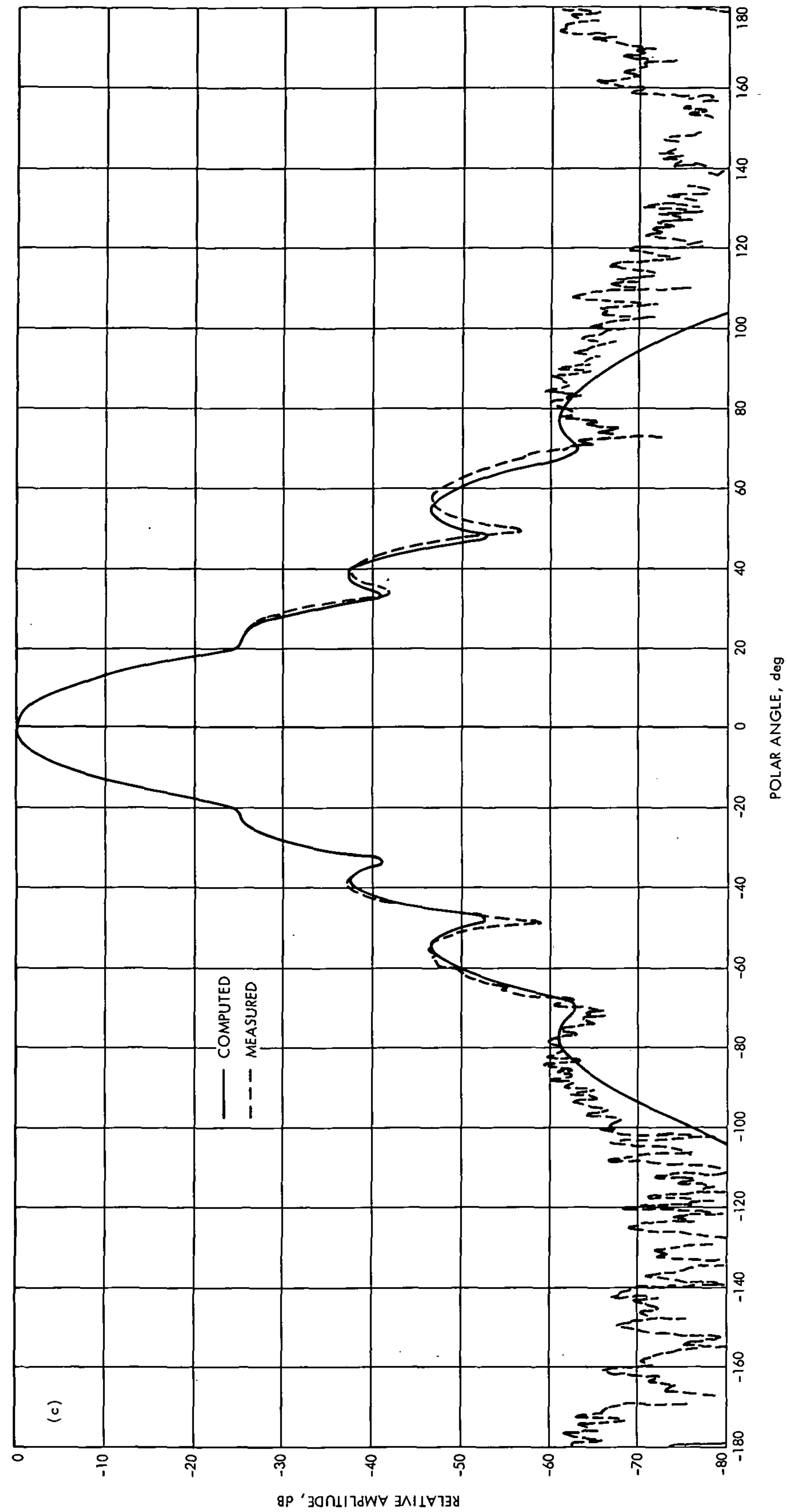
(c)
COMPUTED
MEASURED
RELATIVE AMPLITUDE, dB
0
-10
-20
-30
-40
-50
-60
-70
-80
POLAR ANGLE, deg
-180
-160
-140
-120
-100
-80
-60
-40
-20
0
20
40
60
80
100
120
140
160
180

Fig. 3 (contd)

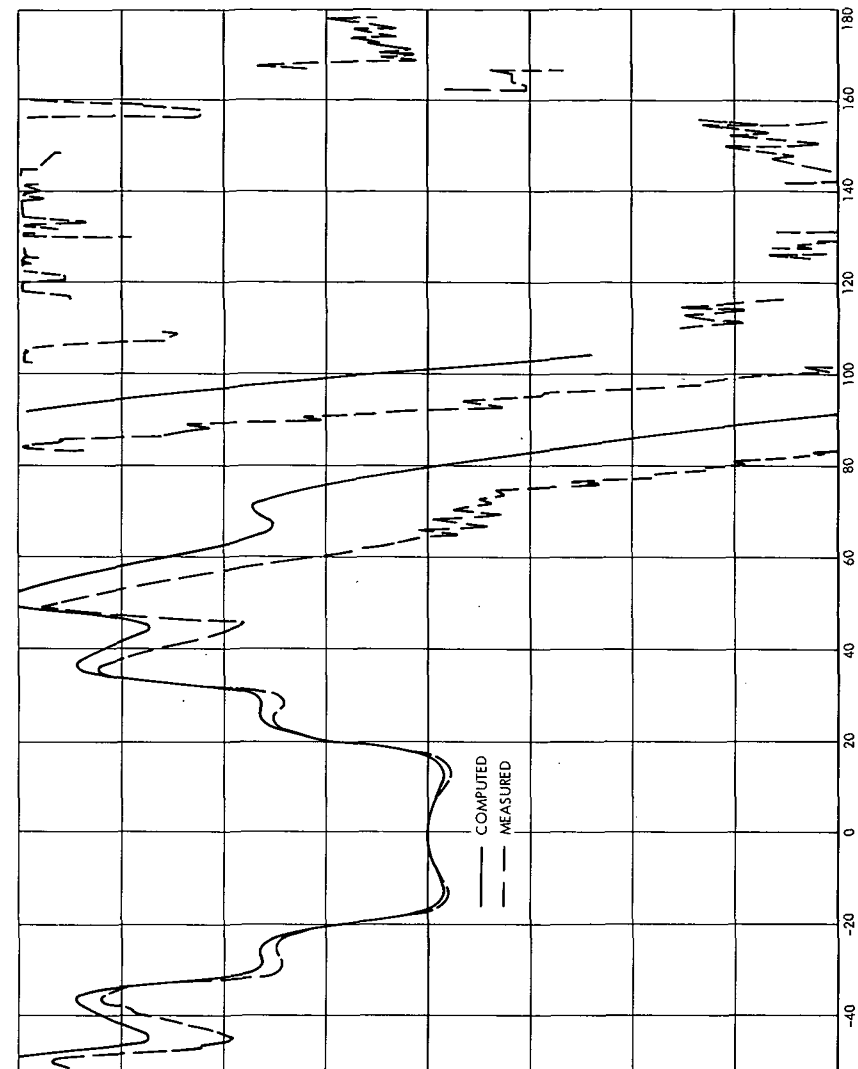
(d)
COMPUTED
MEASURED
POLAR ANGLE, deg
PHASE, deg
-180
-160
-140
-120
-100
-80
-60
-40
-20
0
20
40
60
80
100
120
140
160
180
-135
-90
-45
45
90
135

Fig. 3 (contd)

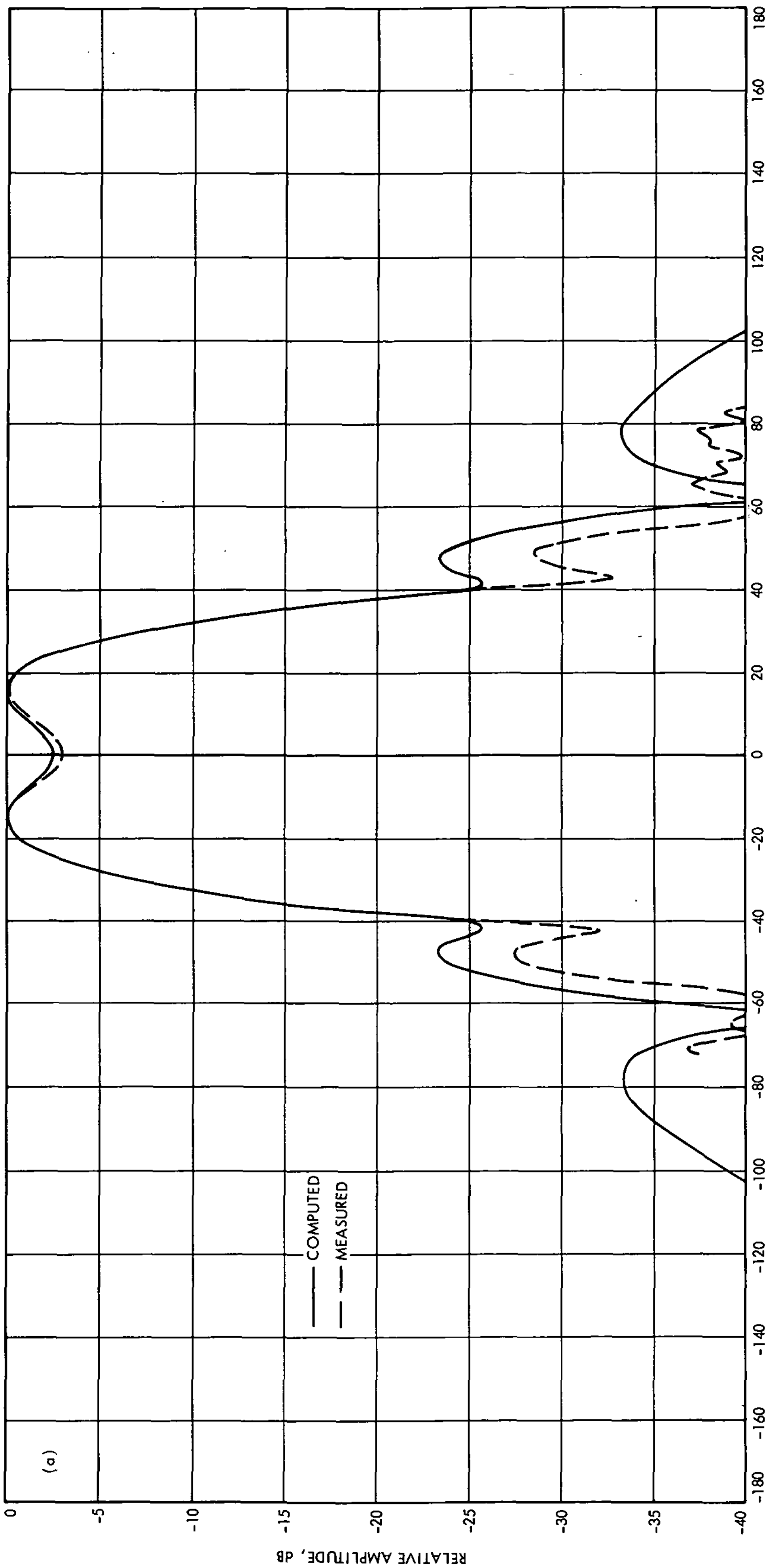

Fig. 4. Computed and measured patterns, experimental dual hybrid-mode horn: (a) E-plane amplitude, (b) H-plane amplitude

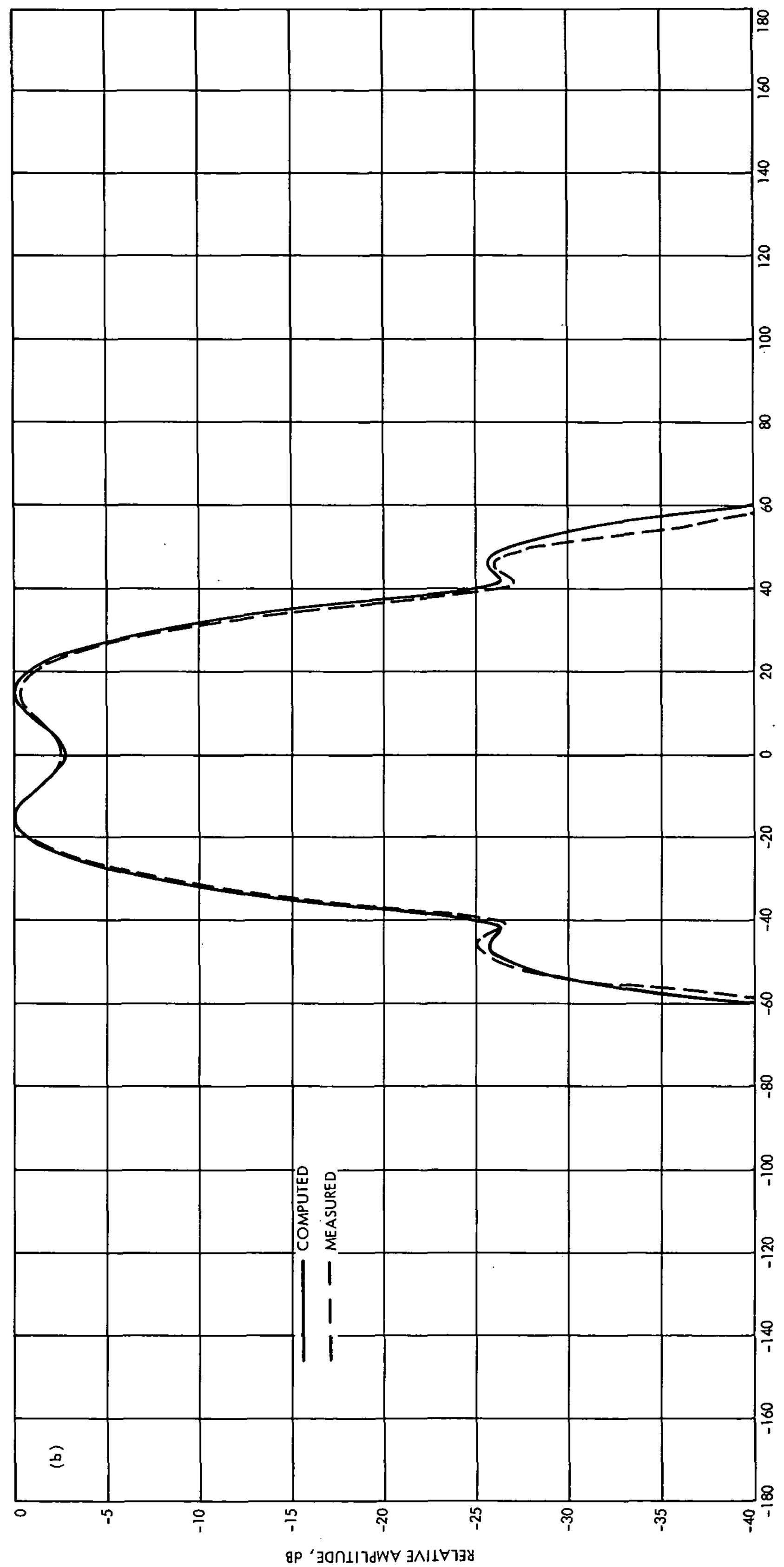
(b)
COMPUTED
MEASURED
POLAR ANGLE, deg
RELATIVE AMPLITUDE, dB
-180
-160
-140
-120
-100
-80
-60
-40
-20
0
20
40
60
80
100
120
140
160
180
0
-5
-10
-15
-20
-25
-30
-35
-40

Fig. 4 (contd)

Radial Extension Study of the 64-m-Diameter Antenna

M. S. Katow
DSIF Engineering Section

An increase in the paraboloidal RF capturing area of the 64-m-diameter antenna with minimal increase of the surface distortion may be attractive from the operations standpoint. A study of the problems involved in increasing from a 64-m-diameter to a 68-m-diameter and the resulting distortion increase due to gravity loadings is described. It is planned to document the effects of calculated wind and thermal loadings in future reporting.

I. Introduction

One of the major factors that determines the RF performance of the 64-m-diameter antenna is the size of its paraboloidal reflecting surface. An increase of its diameter over the present 64-m-diameter size with minor deterioration of the surface distortions from gravity, wind, and thermal loadings may result in a more effective ground antenna. To evaluate this possibility, a study was made of the structural modifications required to extend the diameter by 4 m (64- to 68-m-diameter total) and compute distortions of the reflective surface resulting from the environmental loadings.

In this article, a description of the extension of the hyperboloid's diameter is outlined. Also, the plan for adding the extension to the reflector structure is described along with the computed distortion rms due to gravity loadings only. In future reporting, the rms distortions from wind and thermal loadings will be described.

II. Extension Geometry

Figure 1 describes the extension geometry required on the paraboloid and Fig. 2 shows the extension required on the hyperboloid.

On the hyperboloid, there is presently a flat of about 0.3 m (12 in.) attached to its periphery. The extension would require a hyperboloid surface varying from 0.207-m (8.165-in.) to 0.253-m (9.973-in.) widths with again a flat or cone surface of 0.3 m (12 in.) attached.

One method of extending the surface would be to remove the present flat and attach the required hyperboloid surface and the flat. Some connections to the backup structure will be necessary to insure stiffness of the new surfaces.

This increase in the hyperboloid diameter decreases the clearances to the quadripod structure to a minimum, if

allowance for focusing and a full 10-cm (4-in.) lateral Y adjustments are necessary in the future.

III. Reflector Structure Extension

The reflector structure of the 64-m-diameter antenna is basically a structural arrangement of radial trusses connected by hoop trusses as shown in Figs. 3 and 4. There are other trusses interconnected to it to serve as supports for the quadripod, the elevation wheel structure, and the elevation bearing, which are not affected by the modification under discussion.

The two functions of the hoop trusses near the outer edge are (1) to provide supports for the surface panels between the main radial rib trusses at the intermediate rib positions; the air and gravity loadings at node B in Fig. 3 are transferred to the radial ribs at nodes A and H; and (2) to provide hoop restraints as the radial rib nodes increase or decrease in circumferential length from the radial component of the deflections caused by environmental loads. These hoop forces provide distortion restraints.

One practical structural arrangement for a radial extension is shown by dotted lines in Fig. 4. An outside hoop for circumferential stiffness is provided by a typical rod DHM and the stiffness for the localized environmental normal loadings at node H will be transferred to the radial rib by the truss LHP typically.

IV. Computer Analysis Description and Analysis

The extension trusses were added to the ½ model of the reflector structure that includes all the structural members of the tipping assembly about the elevation axis with the exception of the intermediate rib. Since the intermediate rib is not a truss, it was replaced by an equivalent weight to reduce the size of the model. Therefore, the extension was modeled only with the addition of a truss addition (LMP of Fig. 4) to all of the radial ribs and hoops DM between each extension. The equivalent weights of the additional trusses were then added at nodes L, M, and P.

The gravity "off" to "on" loadings for the zenith and horizon looks were applied and the resulting displacements of the reflector nodes where the surface panels are supported from the NASTRAN computer analysis were best fitted and the residuals contour plotted by the rms program (Ref. 1).

V. Results and Conclusions

An unexpected result occurred for the zenith look gravity loading case where there was an improvement in rms value from 1.05 mm to 0.98 mm. The explanation is that the additional peripheral loadings from the extension trusses are in the direction resulting in a better fit to the best fit paraboloid. This is shown in the contour map of Fig. 5 of the best fit residuals of the zenith or symmetric loading. Inspection shows that the major part of the periphery of the reflector where the extensions are added are still high. It will be interesting to pursue further this weight addition method of improving the overall distortion figure.

The results of the horizon look or antisymmetric gravity loading show expected discontinuities of the contour lines near the periphery of the reflector caused by the deflections of the added nodes (Fig. 6). However, the magnitude of the added deflections at this moment appears to be larger than that consistent with the added diameter. Additional study of the modeling of the extension will be made to check for this case of the loading vectors out of the plane of main rib trusses.

The computed distortions based on the existing modeling are documented and compared to the existing 64-m-diameter computed rms distortions in Table 1.

For the extreme elevation angle cases where the reflective surface panels are set at 45°, the rms distortions stated are the changes in the reflector structure distortions from zero rms at 45° due to gravity loadings only. Therefore, the panel manufacturing errors as well as the equivalent rms loss due to feed mismatch with the focal points as well as the distortion due to wind and thermal loads must be added to form the complete distortion figure.

Also, an area weighting function based on the RF illumination amplitude was used as per Fig. 7 in computing the rms figure.

Reference

1. Katow, M. S. and Schmele, L. W., "Antenna Structures: Evaluation Techniques of Reflector Distortions" in *Supporting Research and Advanced Development,* Space Programs Summary 37-40, Vol. IV, pp. 176–184. Jet Propulsion Laboratory, Pasadena, Calif., Aug. 31, 1966.

Table 1. Computed distortion rms—reflector structure only

	Elevation position	Loading case	Best fit—rms 64-m-diameter mm	(in.)	68-m-diameter mm	(in.)
1	Zenith look	Gravity off/on	1.04	(0.041)	0.99	(0.039)
2	Horizon look	Gravity off/on	2.06	(0.081)	2.26	(0.089)
3	Zenith look	Panels set at 45° elevation	1.55	(0.061)	1.65	(0.065)
4	Horizon look	Panels set at 45° elevation	1.02	(0.040)	1.04	(0.041)

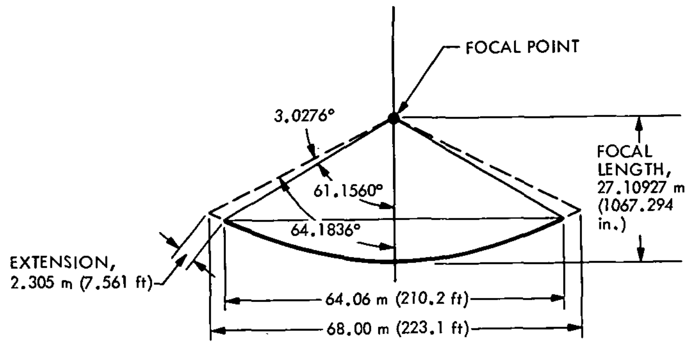

Fig. 1. Paraboloid geometry

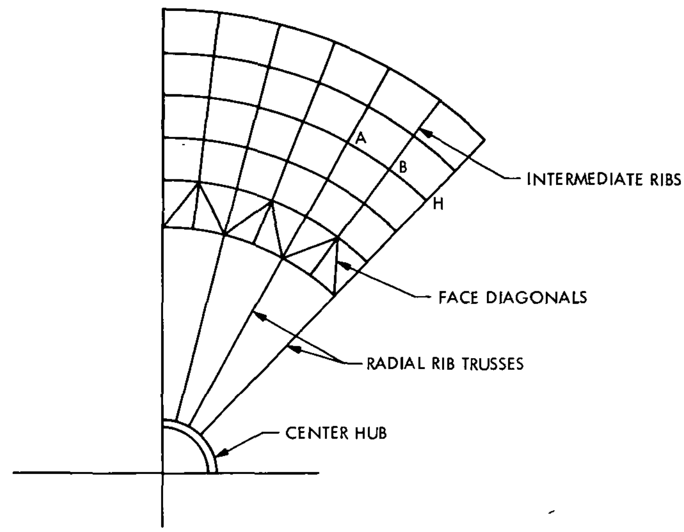

Fig. 3. Reflector structure, partial plan view

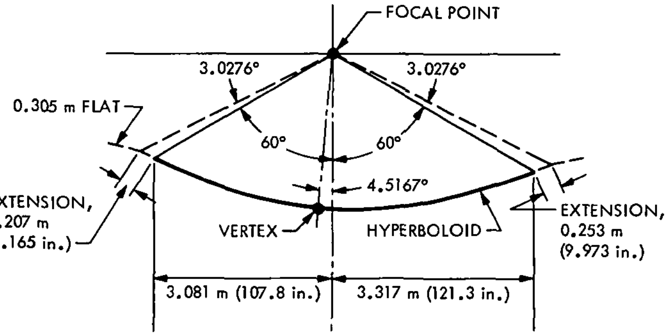

Fig. 2. Hyperboloid geometry

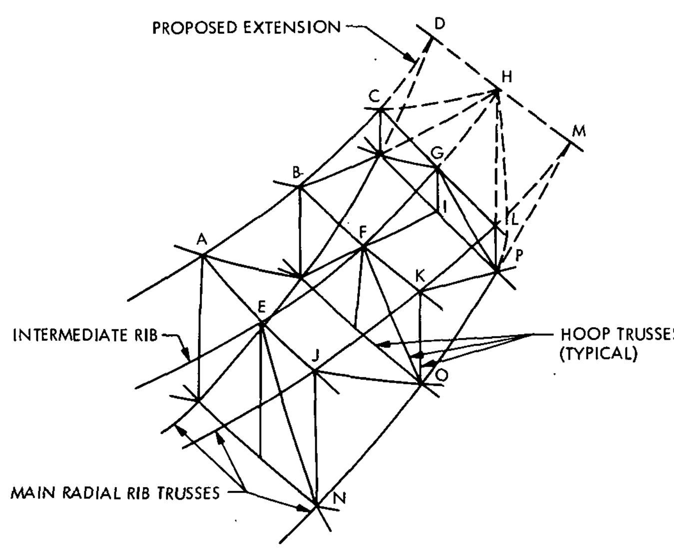

Fig. 4. Reflector structure between two radial rib trusses

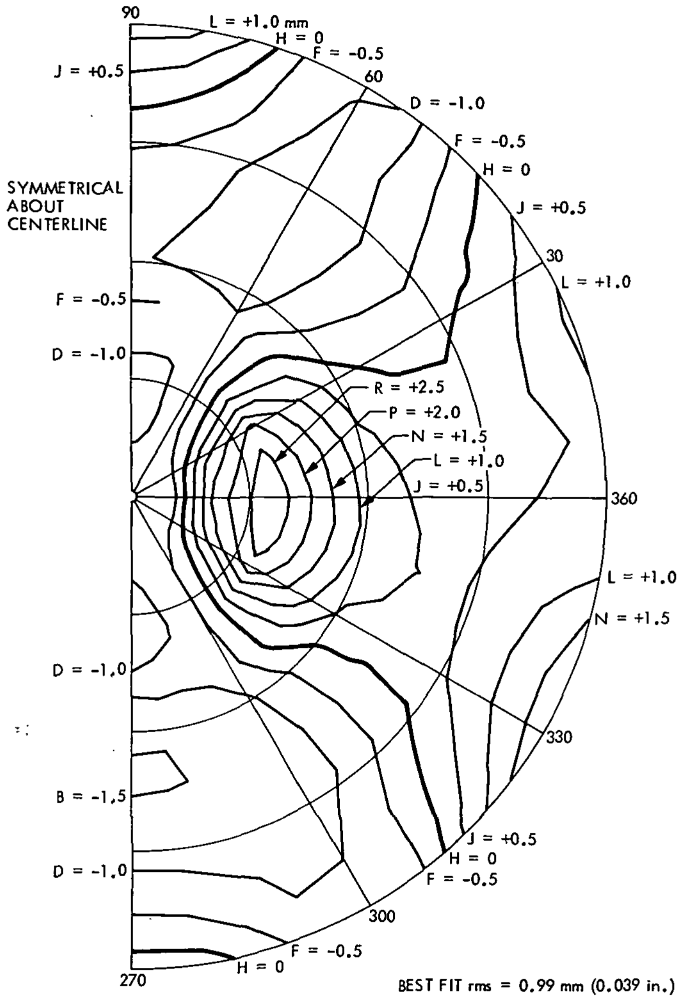

Fig. 5. 68-m-diameter loading case: zenith look gravity off/on contour map of the normal errors after best fit

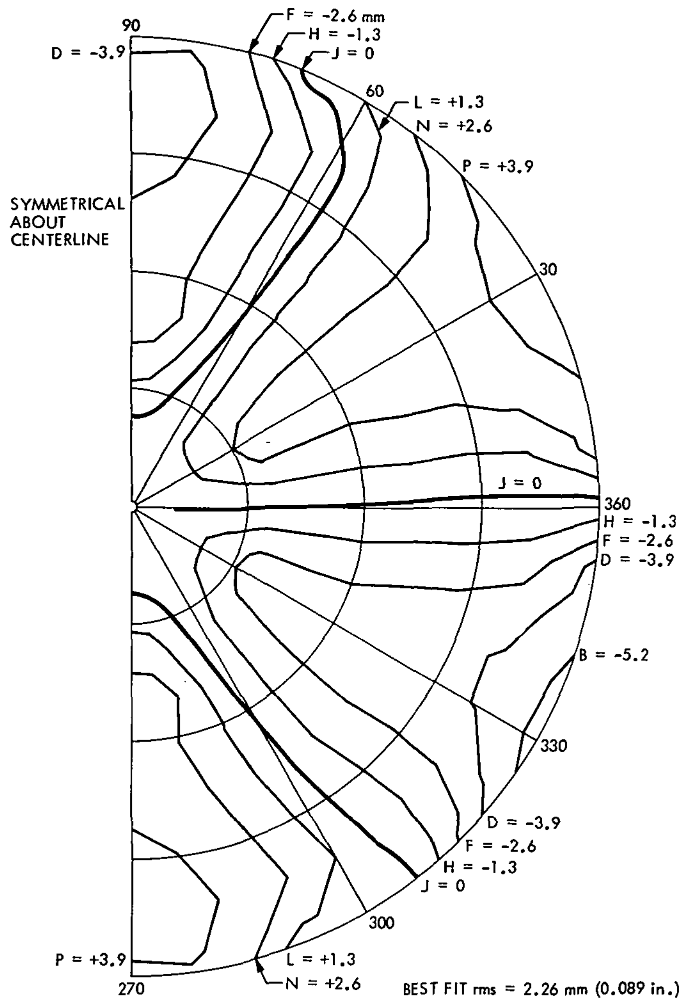

Fig. 6. 68-m-diameter loading case: horizon look gravity off/on contour map of the normal errors after best fit

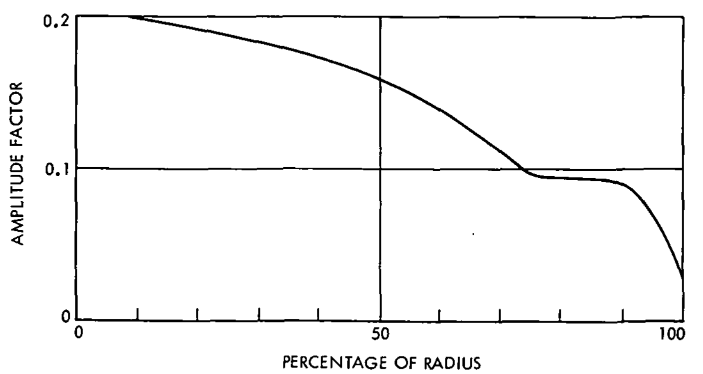

Fig. 7. RF amplitude illumination factor

Convolutional Codes With a Frequency-Shift-Keying Modem

C. L. Weber[1]
Communications Systems Research Section

An analytic approximation to the probability of error per bit for the Viterbi maximum likelihood decoder of convolutional codes which employs an arbitrary modem is presented. The effect of limited path memory of the decoder on performance is determined. The method is applied in particular to the quantized binary frequency-shift-keying modem. This may be useful for entry direct links.

I. Introduction

The performance of the Viterbi maximum likelihood decoding algorithm at memory lengths where it is practical has been determined via digital simulation by Heller and Jacobs (Ref. 1) and Layland (Ref. 2). The channels that were assumed in these simulations consisted of the Binary Symmetric Channel (BSC) and the additive white Gaussian noise (AWGN) channel with a binary phase-shift-keying (PSK) modem.

We determine the performance for the Viterbi decoding algorithm with limited path memory and any encoder memory length. We are motivated since there has as yet been no analytic description of the effect of decoder memory size in the maximum likelihood decoder. This is clearly an important design consideration and a parameter which cannot be arbitrarily chosen. In addition, one clearly cannot build or simulate a decoder under all channel conditions and parameter settings.

Although the derived performance applies to any modem, emphasis is placed on the frequency-shift-keying (FSK) modem. The FSK modem is applicable, for example, in a descending atmospheric entry probe which is communicating directly to Earth where it is doubtful that a coherent RF reference phase can be maintained.

Expressions are derived which estimate the performance of a given time-invariant convolutional code for which the decoder is assumed to implement the maximum likelihood Viterbi algorithm. The results can be used to carry out a system design since the trade-off between the distance parameters of the code, the number and spacing of the quantization levels, the type of modem, and the size of the decoder memory can be analytically determined from these expressions.

[1]Consultant from the University of Southern California for the Communications Systems Research Section.

Some of these variations are presented. For example, the effect of the finite decoder memory is the addition of a term in the expression of probability of error per bit which decreases exponentially to zero as decoder memory size increases. This additional term is the dominant contribution to the probability of error for small decoder memory. The size of decoder memory at which the two terms are of the same order of magnitude is dependent on the distance parameters of the code and the signal-to-noise ratio in the modem.

Of importance in the development of the expressions for performance is an enumeration of all paths which have merged with the correct path, whose path length is less than or equal to the decoder memory. Also, an enumeration of all paths which have not merged with the correct path is required, whose path length is equal to that of the decoder memory. These enumerations are determined via transfer functions, from which approximations on the first event error probability 3 and the probability of error per bit are determined. These expressions are then applied to the binary PSK and binary FSK modem.

II. Transfer Functions for a Finite Memory Decoder

Techniques to obtain bounds on the probability of first-event error and probability of error per bit for maximum likelihood decoding have been introduced and developed by Viterbi (Ref. 3). In so doing, Viterbi introduced the transfer function of the code to enumerate the lengths of paths, the number of input *ones* corresponding to the paths, and the weight of the paths leaving the all-*zero* state and returning to the all-*zero* state at some later time. In general, the transfer function, $T(M, L, N)$ is a power series whose ijkth terms is $a_{ijk}M^i L^j N^k$, where a_{ijk} is the number of paths that pass through the modified state diagram in j branches with k input *ones* and with metric or weight i. The use of the transfer function to determine upper bounds on the bit error probability over any memoryless channel is presented in detail by Viterbi for an *infinite path memory*, maximum likelihood decoder.

Suppose now that the decoder path memory is restricted to some finite length ℓ. To now enumerate all paths which have *merged* with the all-*zero* state, again let the exponent of the dummy variable L be equal to the length of a path and the exponent of the dummy variable N be equal to the number of input *ones* corresponding to the path. For the moment we shall be concerned with the transfer function $T_\ell(L, N)$, which is to be determined so as to enumerate all paths through the modified state diagram up to length ℓ.

There is one path that leaves the all-*zero* state and returns after $K + 1$ input bits. This path is represented by NL^{K+1} since the first input bit for the path is a *one*, followed by K *zeros*. There is one path leaving the all-*zero* state and returning after $K + 2$ input bits. This path is represented by N^2L^{K+2} since it corresponds to two input *ones* followed by K *zeros*. For $K + 2 \leq \ell \leq 2K + 1$, there are $2^{\ell-(K+2)}$ paths leaving the all-*zero* state and returning after ℓ input bits. These paths have an initial input *one* corresponding to the path leaving the all-*zero* state, and there is a final input *one* followed by K *zero* input digits, so as to guarantee the return of the path to the all-*zero* state in exactly ℓ steps. The remaining $\ell - (K + 2)$ input bits can therefore be chosen arbitrarily with a distinct path corresponding to each of these input sequences. The transfer function of all paths which merge with the all-*zero* state up to length ℓ, for $K + 2 \leq \ell \leq 2K + 1$, is given by

$$T_\ell(L, N) = NL^{K+1} + N^2L^{K+2} \times \sum_{i=0}^{\ell-(K+2)} (1 + N)^i L^i \qquad K + 2 \leq \ell \leq 2K + 1 \tag{1}$$

For $\ell > 2K + 1$, some paths then contain a sequence of K consecutive *zero* input bits among the $\ell - (K + 2)$ input bits so that the path would merge with the all-*zero* state before ℓ steps. To circumvent this, recall that the Viterbi maximum likelihood decoding algorithm rejects paths with low likelihood at the point where the path first merges with the correct path. Therefore, if the all-*zero* vector is considered to be the transmitted sequence, then only paths that return to the all-*zero* state for the first time at a given decoding step are considered. Let

$$\phi_j(N) = \begin{cases} N, & j = 1 \\ N^2(1 + N)^{j-2}, & 2 \leq j \leq K + 1 \end{cases} \tag{2}$$

represent the enumeration of paths with information sequences of total length $j + K$, the last K input bits being zero. As the information length is increased from $j - 1$ to j, there are $\phi_{j-1}(N)$ paths for the added input being a *one* and also the same for being a *zero*. For $j > K + 1$ and $\ell > 2K + 1$, however, some of the paths of length j which result from the additional input bit being a *zero* will have K consecutive *zeros* in the $j - 2$ input bits between the initial input *one* and the final input *one*. These paths are just the paths of length j with an initial input *one* followed

by K *zeros* followed by a path of length $j - (K+1)$. The final $j - (K+1)$ path segment necessarily begins with a *one*. These paths that return to the all-*zero* state before the end of the path therefore are enumerated by $N\phi_{j-(K+1)}$ and correspond to paths that must be eliminated when enumerating all paths whose input sequence is of length exactly equal to $j + K$ through the modified state diagram. Thus for $j > K + 1$, the following recursion relationship is obtained for $\phi_j(N)$:

$$\phi_j(N) = (1+N)\,\phi_{j-1}(N) - N\phi_{j-(K+1)}(N), \qquad j > K+1 \tag{3}$$

The transfer function which enumerates all paths that have merged with the all-*zero* sequence up to length ℓ is thus given by

$$T_\ell(L,N) = L^K \sum_{j=1}^{\ell-K} \phi_j(N)\,L^j, \qquad \ell > K+1 \tag{4}$$

In the special case where infinite memory is assumed, $\ell \to \infty$ and the resulting transfer function can be expressed in closed form via direct summation, namely,

$$T(L,N) \triangleq \lim_{\ell\to\infty} T_\ell(L,N) = \frac{NL^{K+1}(1-L)}{1 - L(1+N) + NL^{K+1}}$$

This infinite memory transfer function has been given previously by Viterbi (Ref. 3) using a different approach.

For finite path memory ℓ input bits *must* be decoded and released to the data user after ℓ steps of decoding. Therefore, assuming the all-*zero* vector was transmitted, all paths leaving the all-*zero* state and *not returning* after ℓ input bits must be compared to determine if one of these paths has a likelihood greater than the path with the largest likelihood of all paths that have returned to the all-*zero* state at the decoding time specified. We enumerate these paths in a manner similar to that used to determine $T_\ell(L,N)$. We need to determine the transfer function

$$V_\ell(L,N) \triangleq \Psi_\ell(N)\,L^\ell \tag{5}$$

which enumerates all paths of length ℓ which leave the all-*zero* state at the outset and have not returned after ℓ input bits. Direct observation yields the fact that $\Psi_1(N) = N$, and $\Psi_\ell(N) = N(1+N)^{\ell-1}$, $\ell = 2, \cdots, K$. In order to be guaranteed that no path contains a sequence of K *zeros*, $\Psi_\ell(N)$ must satisfy the same recursion relationship as $\phi_j(N)$ in Eq. (3), namely

$$\Psi_\ell = (1+N)\,\Psi_{\ell-1}(N) - N\Psi_{\ell-(K+1)}(N)$$

for $\ell \geqq K+1$, where the initial condition $\Psi_0(N) = 1$ is needed to completely specify $\Psi_j(N)$. The recursion relationship for both types of input sequences is the same, the only difference being the sets of initial conditions.

III. Approximations to Probability of Error

Upper bounds on the probability of first event error and probability of error per bit can be obtained by direct application of the transfer functions in the previous section. These bounds are rather poor bounds, however, primarily due to the assumption that the distance between paths is set equal to the minimum distance. This assumption is quite gross, and produces tractable, but weak, upper bounds.

For short code memory length K, the complete distance structure of the code can be used to achieve tight upper bounds. In order to retain the use of only simple distance properties and improve the estimate of the probability of error, the following approximations are made to the complete distance structure of the code. To begin, consider the truncation term $V_\ell(L,N) = \Psi_\ell(N)\,L^\ell$ described above. One method to obtain an upper bound is to replace L^ℓ by $M^{d_0\ell+d_1}$, thereby replacing the distance in every path by a uniform lower bound on the minimum distance. In the above representation of the uniform lower bound, namely $d_0\ell + d_1$, we have the following definitions:

The term ℓ is the path length in branches, which in our applications will be set equal to the path length corresponding to the size of the decoder memory.

The term d_0 is the minimum average weight per branch of the code. Upper and lower bounds on d_0 for binary convolutional codes of rate $1/n$ are presented in Ref. 4. For example, $d_0 \leqq 1/2$ for rate 1/2 codes and $d_0 \leqq 1$ for rate 1/3 codes; these bounds are attainable by certain codes.

The term d_1 is a small bias. It represents an offset of the minimum distance from uniform growth with path length. The bias compensates for a concentration of weight over the path from the all-*zero* state to the average weight per branch cycle and compensates additionally for a concentration of weight over any part of this cycle.

With this prelude, the approach to the approximation is as follows. Various paths in the tree will have various weights. We know that for any length ℓ, the path of smallest weight is lower bounded by $d_0\ell + d_1$. The path with maximum weight is estimated by $n\ell$. We approximate all

intermediate weight paths of length ℓ by appropriate combinations of these two extreme weights as follows. Consider first the path of length $\ell = 1$. All paths into the modified state diagram begin with a *one*. We estimate the weight of the path of length equal to one branch by the transfer function $A_1(M, N)$, namely,

$$A_1(M,N) \triangleq NM^{d_0+d_1} \tag{6}$$

the N being present because all error sequences begin with a *one*, and $d_0 + d_1$ estimates the weight in this first branch. We equally well could have estimated the weight in this first branch by n; the difference will be negligible when long input sequences are considered. For $\ell = 2$, the two possible input sequences are 11 and 10. We elect to estimate the weight of the two $\ell = 2$ paths via the transfer function

$$A_2(M,N) = NM^{d_0+d_1}(NM^{d_0} + M^n) \tag{7}$$

In so doing, we assume that the added *one* in the 11 input sequence produces a small weight increase, namely d_0, and that the added *zero* in the 10 sequence produces a larger weight increase, which we estimate by n. When we add the third digit, we reserve this assumption, so that

$$A_3(M,N) = NM^{d_0+d_1}(NM^{d_0} + M^n)(NM^n + M^{d_0}) \tag{8}$$

The idea is now established; in general, therefore,

$$A_\ell(M,N) = NM^{d_0+d_1}(NM^{d_0} + M^n)^{\lceil(\ell-1)/2\rceil} \times (NM^n + M^{d_0})^{\lfloor(\ell-1)/2\rfloor} \tag{9}$$

where the $\lceil\ \rceil$ notation indicates the greatest integer in the enclosed expression and the $\lfloor\ \rfloor$ notation, the smallest integer.

This approach to averaging distances of all paths which do not return to the all-*zero* state in ℓ branches involves the same addition of extra paths as in the previous section, since no attempt has been made to remove such paths by use of the recursion relationship for $\Psi_\ell(N)$.

For small decoder memory, there exist many more non-return-to-zero paths than return-to-zero paths. The truncation term $A_\ell(M,N)$ is therefore the dominant contribution to the probability of error for small decoder memory. For large decoder memory, the effect of decoder memory decreases exponentially to zero, so that the $B(M,N)$ term to be described below for the return-to-zero paths becomes the dominant contribution to the probability of error.

By expanding $A_\ell(M,N)$ in a power series, we obtain

$$A_\ell(M,N)\Big|_{\substack{N=1\\ M^k=P_k}} = \sum_{i=0}^{\lceil(\ell-1)/2\rceil}\binom{\lceil(\ell-1)/2\rceil}{i}\sum_{j=0}^{\lfloor(\ell-1)/2\rfloor}\binom{\lfloor(\ell-1)/2\rfloor}{j}P_k \tag{10}$$

where

$$k = \lceil d_1 + d_0(1+i+j) + n(\ell - 1 - i - j)\rceil \tag{11}$$

and where we have substituted P_k for M^k. The probability P_k is the probability of first event error between two merging paths which differ in k positions. For the approximation of probability of error per bit, we use the power series

$$\frac{\partial A_\ell(M,N)}{\partial N}\Big|_{\substack{N=1\\ M^k=P_k}} = \sum_{i=0}^{\lceil(\ell-1)/2\rceil}\binom{\lceil(\ell-1)/2\rceil}{i}\sum_{j=0}^{\lfloor(\ell-1)/2\rfloor}\binom{\lfloor(\ell-1)/2\rfloor}{j} \times\left(1+i-j+\frac{\ell-1}{2}\right)P_k \tag{12}$$

where k is again given by Eq. (11). Equations (10) and (12) provide the contribution to the probability of first event error and probability of error per bit respectively from all paths of length ℓ which have not merged with the all-*zero* state. The length ℓ is set equal to the size of the decoder path memory.

Using similar techniques as used for the truncation term, $A_\ell(M,N)$, we now estimate the portion of the probability of error which comes from the undetected error term, which we designate as $B_\ell(M,N)$. First consider the path of length $\ell = K + 1$. The minimum distance for this path length is approximated by d_{free}. Therefore, we estimate the weight of the path of length $K + 1$ by the transfer function $B_{K+1}(M,N)$, namely,

$$B_{K+2}(M,N) \triangleq NM^{d_{free}} \simeq NM^{d_0\bar{\ell}+d_1} \tag{13}$$

where $\bar{\ell}$ is defined as follows. For a convolutional code with minimum average weight per branch d_0, bias d_1, and free distance d_{free}, there is a path length $\bar{\ell}$ such that all

paths through the modified state diagram with length greater than $\bar{\ell}$ have weight greater than or equal to d_{free}. This path length must satisfy $d_{free} \leq d_0 \bar{\ell} + d_1$, so that $\bar{\ell} \geq (d_{free} - d_0)/d_0$. The smallest integer $\bar{\ell}$ which will satisfy this requirement is therefore given by

$$\bar{\ell} \triangleq \left\lceil \frac{d_{free} - d_1}{d_0} \right\rceil \tag{14}$$

The weight of all paths of length $\leq K + 2$ which have returned to the all-*zero* state, the number of input *ones* in each path is given by

$$\begin{aligned} B_{K+2}(M, N) &\simeq NM^{d_0 \bar{\ell} + d_1} + N^2 M^{n + d_0(\bar{\ell}-1) + d_1} \\ &= NM^{d_0(\bar{\ell}-1)+d_1} (M^{d_0} + NM^n) \end{aligned} \tag{15}$$

where the path of length $K + 2$ resulting from two input *ones* has one of the branches of weight n and the rest of the branches of average weight d_0. For $\ell = K + 3$, there is one path resulting from two input *ones* and one path resulting from three input *ones*. Thus,

$$\left. \begin{aligned} B_{K+3}(M, N) &= NM^{d_0 \bar{\ell} + d_1} + 2N^2 M^{n + d_0(\bar{\ell}-1) + d_1} \\ &\quad + N^3 M^{2n + d_0(\bar{\ell}-2) + d_1} \\ B_{K+3}(M, N) &= NM^{d_0(\bar{\ell}-2)+d_1} (M^{d_0} + NM^n)^2 \end{aligned} \right\} \tag{16}$$

where a branch of weight n replaces a branch of weight d_0 for each input *one* into the convolutional encoder after the first *one*. Therefore, we are approximating all the intermediate weight paths of length ℓ by combinations of the branch weights n and d_0. Continuing this procedure, for $K + 1 \leq \ell \leq \bar{\ell} + K + 1$,

$$B_\ell(M, N) = NM^{d_0(\bar{\ell}+K+1-\ell)+d_1} (M^{d_0} + NM^n)^{\ell-K-1} \tag{17}$$

The representation for $B_\ell(M, N)$ in Eq. (17) enumerates all paths of length less than or equal to ℓ, when $K + 1 \leq \ell \leq \bar{\ell} + K + 1$, which have departed from the all-*zero* state at time zero, and returned at some time less than that corresponding to ℓ branches. The reason for approximating the weights of the various paths by $B_\ell(M, N)$ in this manner is to force the approximation to be such that the smallest weight path at each length ℓ, $K + 1 \leq \ell \leq \bar{\ell} + K + 1$, be equal to d_{free}.

For $\ell > \bar{\ell} + K + 1$, we know that all paths through the modified state diagram have weight greater than d_{free}, so that the above restriction need no longer be imposed. We proceed, therefore, as with $A_\ell(M, N)$ so that

$$B_\ell(M, N) = NM^{d_1} (M^{d_0} + NM^n)^{\bar{\ell}} \cdot \left[\sum_{k=0}^{\ell-(\bar{\ell}+K+1)} (M^{d_0} + NM^n)^{\lceil k/2 \rceil} (NM^{d_0} + N^n)^{\lfloor k/2 \rfloor} \right] \tag{18}$$

By expanding $B_\ell(M, N)$ in a power series as was similarly done for $A_\ell(M, N)$ in Eq. (10) and again making the substitution $M^r = P_r$, we obtain

$$B_\ell(M, N) \Bigg|_{\substack{N=1 \\ M^r = P_r}} = \sum_{k=0}^{\ell-\bar{\ell}-K-1} \sum_{i=0}^{\lceil (k+\bar{\ell})/2 \rceil} \sum_{j=0}^{\lfloor (k+\bar{\ell})/2 \rfloor} \binom{\lceil (k+\bar{\ell})/2 \rceil}{i} \binom{\lfloor (k+\bar{\ell})/2 \rfloor}{j} P_r \tag{19}$$

where

$$r = d_1 + d_0(i + j) + (k + \bar{\ell} - i - j)n \tag{20}$$

For the approximation of probability of error per bit, we use the power series

$$\frac{\partial B_\ell(M, N)}{\partial N} \Bigg|_{\substack{N=1 \\ M^r = P_r}} = \sum_{k=0}^{\ell-\bar{\ell}-K-1} \sum_{i=0}^{\lceil (k+\bar{\ell})/2 \rceil} \sum_{j=0}^{\lfloor (k+\bar{\ell})/2 \rfloor} \binom{\lceil (k+\bar{\ell})/2 \rceil}{i} \binom{\lfloor (k+\bar{\ell})/2 \rfloor}{j} (1 + j - i + \lceil (k+\bar{\ell})/2 \rceil) P_r \tag{21}$$

where r is given by Eq. (20).

In summary, we have approximated the probability of error per bit for a given convolutional code employing the Viterbi maximum likelihood decoder with finite decoder memory by

$$P_b \approx \left[\frac{\partial A_l(M,N)}{\partial N} + \frac{\partial B_l(M,N)}{\partial N}\right]\Bigg|_{\substack{N=1 \\ M^r = P_r}} \qquad (22)$$

where

$$\partial A_l(M,N)/\partial N$$

is given by Eq. (12) and

$$\partial B_l(M,N)/\partial N$$

is given by Eq. (21). The first term in Eq. (22) represents the contribution to the probability of error per bit due to the fact the decoder has a finite memory, measured in terms of the finite path length l. The second term represents the undetected error from paths with length less than or equal to that of the decoder memory, which have merged with the correct path. What remains is to evaluate P_k for the particular modem that is to be used, which is considered in the next section.

IV. First Error Probability P_k for Various Quantized Channels

The approximations of the probability of error considered above apply to any memoryless channel. In the present context, by channel we mean to include all preliminary signal processing which may take place before the data are given to the Viterbi maximum likelihood sequence decoder.

The channel of primary interest is the AWGN channel with Q-levels of quantization. A block diagram of the demodulator for the pulse-code modulation (PCM)-PSK biphase signal is shown in Fig. 1. Two different demodulators of the PCM-binary FSK signal with quantization are shown in Figs. 2 and 3. More will be said about these in the following discussion.

For simplicity, we shall assume a binary-encoded signal. Regardless of the modem used, the analog voltage of the output of the matched filter, or the difference of the outputs of two envelope detectors, is assumed to be quantized into Q equally spaced levels. This quantized output is mapped via a metric, once under the assumption the transmitted symbol represents a *one*, and once for a *zero*. The metric outputs $w_{ij}^{(0)}$ and $w_{ij}^{(1)}$ in Figs. 1–3 represent the ith symbol in the jth branch under the assumption that a 0 and 1 were transmitted respectively.

The optimal map which minimizes the probability of error is the log likelihood functional, for which $w_{ij}^{(n)}$ is analog and is given by

$$w_{ij}^{(n)} = \log P(y_{ij} \,|\, H_n), \qquad n = 0, 1 \qquad (23)$$

The evaluation of the error event probability P_k is then determined by considering two code sequences, x and x', which disagree in k symbols. Assume x is the correct sequence and is the all-*zero* sequence, so that x' is *one* in each of the specified k positions. Then

$$P_k = \text{Prob}\left\{\sum_{r=1}^{k} [\ln P(y_r|x'_r) - \ln P(y_r|x_r)] > 0\right\} \qquad (24)$$

if the optimal log likelihood functional is used. The summation in Eq. (24) is over the k symbols in which x and x' disagree.

For ease of implementation, the log likelihood functional is quantized and mapped into the set of integers $0, \cdots, Q-1$. When the quantization levels are assumed to be equally spaced, extensive computation of the PSK modem has demonstrated that the map is sufficiently nonlinear, so that $w_{ij}^{(n)}$ is not a good approximation of $\ln P(y_r \,|\, H_n)$. The function that is the primary contributor to P_k, however, is the difference of log likelihood functionals, as indicated in Eq. (24), for the Viterbi maximum likelihood sequence decoder. The map of $\ln P(y_r|1) - \ln P(y_r|0)$ into $w_r^{(1)} - w_r^{(0)}$, for the PSK modem, is satisfactorily linear over an extensive range of equally spaced quantization levels and ratios of signal energy to noise spectral density, E_s/N_0. Examples are shown in Figs. 4 and 5. In Fig. 4, with eight equally spaced levels of 0.5, the linearity of the interior regions is almost perfect. The only deviation is in the two extreme quantization bins $(-\infty, -1.5)$ and $(1.5, \infty)$, which increase in probability as the signal-to-noise ratio E_s/N_0 increases. In Fig. 5, this becomes extensive when the size of the equal spacing is decreased to 0.25. The linearity of the interior regions predominates over all E_s/N_0 and quantization spacings.

Because of this approximate linearity as well as the simplicity which results from this approximation, most implementations of the Viterbi decoder employ equally spaced quantization levels and linear metrics. The extension to arbitrarily spaced bins is straightforward. For the PSK modem, the relationships are as shown in Table 1.

Table 1. Relationships for the PSK modem

z_{ij}	0	1	2	$\cdots$	$Q-2$	$Q-1$
$w_{ij}^{(1)}$	0	1	2	$\cdots$	$Q-2$	$Q-1$
$w_{ij}^{(0)}$	$Q-1$	$Q-2$	$Q-3$	$\cdots$	1	0

We shall adopt the following notation:

$$P(w_{ij}^{(1)} = q \mid x_{ij} = 1) = P_q, \qquad q = 0, \cdots, Q-1 \quad \text{(25a)}$$

so that

$$P(w_{ij}^{(1)} = q \mid x_{ij} = 0) = P_{Q-1-q}, \qquad q = 0, \cdots, Q-1 \quad \text{(25b)}$$

Since $w_r^{(0)} = Q - 1 - w_r^{(1)}$, we have the result that

$$P_k = \text{Prob}\left\{\sum_{r=1}^{k} w_r^{(1)} > \frac{k(Q-1)}{2} \mid x_r = 0\right\} \quad (26)$$

for the quantized system.

Therefore, P_k is equal to the probability that the sum of discrete, identically distributed, statistically independent random variables is greater than a threshold, where each random variable can take on the integer values $0, \cdots, Q-1$.

V. Binary FSK Modem With Quantization

If the channel degrades the signal sufficiently so that coherent tracking of the RF reference phase cannot be satisfactorily maintained, an alternative is binary FSK. This is anticipated to be the case in a descending atmospheric entry probe where an RF reference phase may not be adequately maintained. In this section the use of the quantized FSK modem is described. Configurations are suggested for the binary FSK modem, which are directly extendable to multiple-frequency-shift keying (MFSK).

The optimal choice of $M = 2^K$ in MFSK from the point of view of maximizing channel capacity or R_{comp} is given by I. Bar-David and S. Butman (Ref. 4), where it is shown that choosing $M = 2$ is not best at any signal-to-noise ratio.

The simplest way to implement a binary FSK demodulator with Q-levels of quantization is shown in Fig. 2, which we have called system A. The output of each envelope detector is sampled at the end of each symbol time. Perfect synchronization is assumed. Under the assumption, for example, that frequency f_1 was transmitted over the channel during a given symbol time, the probability density function (PDF) of r_1 in Fig. 2 will be Rician distributed, and r_0 will be Rayleigh distributed. These analog samples are differenced and quantized into one of Q levels or bins. This output $\{z_{ij}\}$ is then mapped into a metric under each of the two hypotheses. The simplest metric is linear and the question immediately arises as to how representative this metric is of the log likelihood.

The envelope detectors are assumed to output r_1^2 and r_0^2 respectively, so that in system A,

$$y \triangleq y_{ij} = r_1^2 - r_0^2 \quad (27)$$

The envelope detector outputs are assumed to be appropriately normalized so that

$$p(r_0) = r_0 \exp\left(-\frac{1}{2} r_0^2\right), \qquad \text{Rayleigh, } r_0 \geq 0$$

and

$$p(r_1) = r_1 \exp\left[-\frac{1}{2}(r_1^2 + \lambda^2)\right] I_0(\lambda r_1), \qquad \text{Rician, } r_1 \geq 0$$

where $\lambda^2 = 2E_s/N_0$, $E_s = ST_s$ being the symbol energy.

The cumulative density of y under the assumption that H_1 is true can be shown to be

$$F(y) = \begin{cases} \frac{1}{2}\exp\left(-\frac{\lambda^2}{4} + \frac{y}{2}\right), & y \leq 0 \\ 1 - Q(\lambda, \sqrt{y}) + \frac{1}{2}\exp\left(-\frac{\lambda^2}{4} + \frac{y}{2}\right) \\ \quad \times Q(\lambda/\sqrt{2}, \sqrt{2y}), & y \geq 0 \end{cases} \quad (28)$$

where $Q(\alpha, \beta)$ is the Marcum Q-function (Ref. 5).

As in PSK, we assume y is quantized with equally spaced levels and the metric maps are linear as in Table 1. How representative this metric is of the difference of log likelihood functionals has been determined for binary FSK using $F(y)$ in Eq. (28). Examples are shown in Figs. 6 and 7. Examination of the Rayleigh and Rician PDFs indicates that a reasonable choice for the size of equally spaced quantization interval is given by the point

where the two PDFs intersect.[2] In the case $Q = 8$, two equally spaced intervals are placed between the origin and the point of intersection. For a given λ^2, the quantization interval is then given by that Δ which satisfies

$$\exp(\lambda^2/2) = I_0(\lambda\sqrt{Q\Delta/2}), \qquad Q = 8 \tag{29}$$

In Fig. 6, the Δ corresponding to Eq. (29) was used. At all signal-to-noise ratios considered, the difference of the log likelihoods of the probability of being in a given quantization region under H_1 and H_0 is quite linear, particularly at $E_s/N_0 = 2$ dB. Thus choosing the quantization interval based on Eq. (29) is a satisfactory rule of thumb. This assumes, of course, *a priori* knowledge of E_s/N_0. It is also reasonable to expect this choice of Δ to be very close to that Δ which will maximize the capacity of the quantized channel.

In Fig. 7, the quantization interval is fixed at $\Delta = 1$, and the difference of the log likelihoods is shown for different E_s/N_0. It is noted that $\Delta = 1$ is too small a quantization interval at $E_s/N_0 = 2$ dB, so poor in fact that the difference of the log likelihoods is no longer monotonic. Also, binary FSK does not have the satisfying property that is consistent with binary PSK, namely, of being linear over the interior quantization regions over a wide range of Δ and E_s/N_0.

In a given application, it is of much more importance to have *a priori* knowledge of E_s/N_0 when employing FSK than when employing PSK, if linear metrics and equally spaced quantization intervals are going to be representative of the log likelihood probabilities.

For a given E_s/N_0 and Δ, the probability

$$p(w_{ij}^{(1)} = q \mid x_{ij} = 1), q = 0, \cdots, Q-1$$

can be determined from $F(y)$ in Eq. (28), and P_k in Eq. (26) is then determined as for binary PSK.

The above discussion applies to System A in Fig. 2. This implementation, namely the differencing of the analog envelope detection outputs before quantization, is easily implemented only for binary FSK. Since there is significant interest in MFSK because of its increased capacity (Ref. 5) we consider System B in Fig. 3, which is directly extendable to the M-ary case as shown in Fig. 8. With System B, each envelope detector is sampled and immediately quantized before any signal processing is carried out. In the binary case, the quantized outputs are linearly indexed over $0, \cdots, Q-1$, and differenced, with the result, designated as z_{ij} in Fig. 3, mapped into each of the two metrics $w_{ij}^{(1)}$ and $w_{ij}^{(0)}$. Under the assumption frequency f_1 was transmitted, hypothesis H_1, the PDF of r_1 and r_0 are again Rician and Rayleigh respectively.

[2]Suggested by B. Levitt, Communications Systems Research Section, Jet Propulsion Laboratory.

To determine if $w_{ij}^{(1)}$ and $w_{ij}^{(0)}$ are representative of the log likelihood as is the case for the modems considered above, we must consider the likelihood ratio of the quantized received vector

$$z \stackrel{\Delta}{=} (z_{ij}^{(1)}, z_{ij}^{(0)})$$

The log likelihood ratio is given by

$$\begin{aligned} LL(z) \stackrel{\Delta}{=} & \ln P(z_{ij}^{(1)} \mid H_1) + \ln P(z_{ij}^{(0)} \mid H_1) \\ & - \ln P(z_{ij}^{(1)} \mid H_0) - \ln P(z_{ij}^{(0)} \mid H_0) \end{aligned} \tag{30}$$

since r_1 and r_0 are statistically independent random variables. Under H_1, the cumulative probability function of $y_{ij}^{(0)} \stackrel{\Delta}{=} y$ is

$$F(y) = 1 - \exp(-y/2) \quad y \geqq 0 \tag{31}$$

and $y_{ij}^{(1)} \stackrel{\Delta}{=} x$ has cumulative probability function

$$F(x) = 1 - Q(\lambda, \sqrt{x}), \qquad x \geqq 0 \tag{32}$$

where again

$$\lambda^2/2 = E_s/N_0 = ST_s/N_0$$

Since linear indexing is assumed as well as equally spaced quantization $z_{ij}^{(1)}$ and $z_{ij}^{(0)}$ can take on the values $0, \cdots, Q-1$, and z_{ij} can take on the values

$$-(Q-s), \cdots, -1, 0, 1, \cdots, Q-1$$

Computation has shown that the linear matrices

$$\left.\begin{aligned} w_{ij}^{(1)} &= z_{ij} \\ w_{ij}^{(0)} &= -z_{ij} \end{aligned}\right\} \tag{33}$$

are reasonably representative of the log likelihood. As shown above, the primary random variable in determining the performance of the Viterbi maximum likelihood sequence decoder is the difference of the log likelihood,

namely $LL(z)$ in Eq. (30), which we desire to be represented by $w_{ij}^{(1)} - w_{ij}^{(0)}$.

Sample calculations are shown in Fig. 9. The difference of the log likelihood, $LL(z)$, is plotted against $w_{ij}^{(1)} - w_{ij}^{(0)}$ for $Q = 4$ quantization regions at the output of each envelope detector, and a quantization interval of $\Delta = 1.25$. The quantized outputs of each envelope detector are assigned the values 0, 1, 2, 3 for each of the four regions respectively. The difference can take on integral values over $[-3, 3]$. With the metric map in Eq. (33), this is identical to $w_{ij}^{(1)} - w_{ij}^{(0)}$. For each of the 16 possible values of the vector z, the difference of the log likelihoods versus $w_{ij}^{(1)} - w_{ij}^{(0)}$ is shown in Fig. 9 for $E_s/N_0 = 0$ dB and 1 dB. Multiple values appear, since values of $w_{ij}^{(1)} - w_{ij}^{(0)}$ can be obtained in several ways, each with its own value of $LL(z)$. The combination of $\Delta = 1.25$ and $E_s/N_0 = 0$ dB corresponds to the choice given by Eq. (29). It appears that this quantization procedure and choice of metrics is representative of $LL(z)$.

VI. Summary

A method is presented for determining an analytic approximation to the probability of error per bit for the Viterbi maximum likelihood sequence decoder which employs an arbitrary modem. The method is applied to the quantized binary PSK modem, and two implementations of the quantized binary FSK modem. Simple linear metrics are assumed and it is determined that they are quite representative of the log likelihood, the purpose being to demonstrate that implementation of a very simple metric is close to the optimum for a given Δ and E_s/N_0. If off-line decoding is to be performed, exact values of the metric could easily be employed, as used for example in the simulation carried out in Ref. 7.

References

1. Heller, J. A., and Jacobs, I. M., "Viterbi Decoding for Satellite and Space Communication," *IEEE Trans. on Communication Technology*, Vol. COM-19, No. 5, pp. 835–849, Oct. 1971.

2. Layland, J., "Performance of Short Constraint Length Convolutional Codes and a Heuristic Code-Construction Algorithm," in *The Deep Space Network*, Space Programs Summary 37-64, Vol. II, pp. 41–44, Jet Propulsion Laboratory, Pasadena, Calif., Aug. 31, 1970.

3. Viterbi, A. J., "Convolutional Codes and Their Performance in Communication Systems," *IEEE Trans. on Communication Technology*, Vol. COM-19, No. 5, pp. 751–772, Oct. 1971.

4. Huth, G. K., and Weber, C. L., "Minimum Weight Convolutional Code Words of Finite Length," *IEEE Trans. on Information Theory*, submitted.

5. Bar-David, I., and Butman, S., "Performance of Coded, Noncoherent, Hard-Decision MFSK Systems," in this volume of *The Deep Space Network Progress Report*.

6. Marcum, J. I., "A Statistical Theory of Target Detection by Pulsed Radar," *I.R.E. Trans. Info. Theory*, IT-6, Apr. 1960.

7. Richardson, R. J., Korgel, C. C., and Blizard, R. B., "Coding for Low Data Rate Noncoherent Channels," Report No. T-70-48813-001, Martin Marietta Aerospace Group, Denver, Colorado, Dec. 1970.

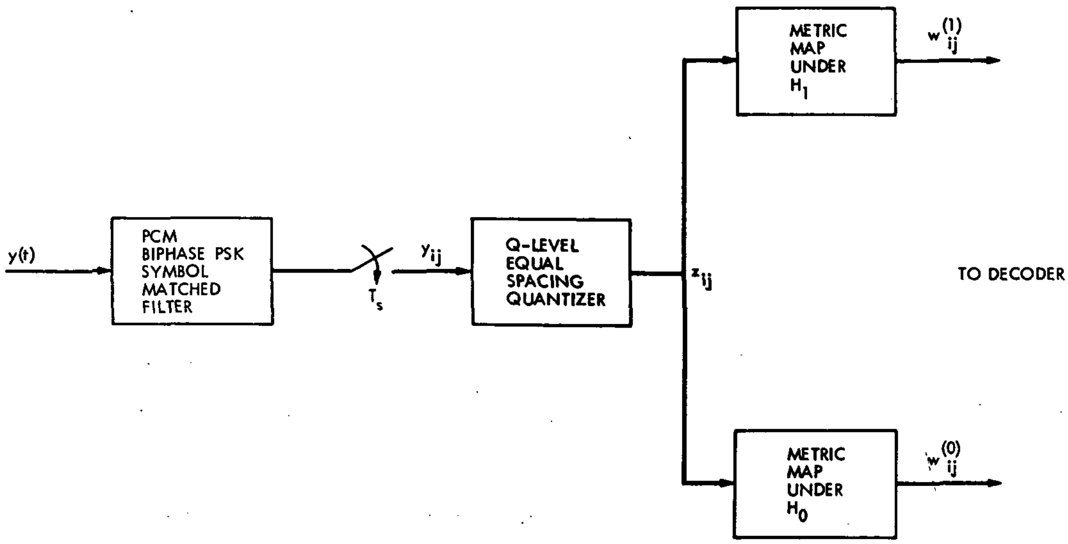

Fig. 1. PCM-PSK Biphase demodulator for the AWGN channel with Q-levels of quantization

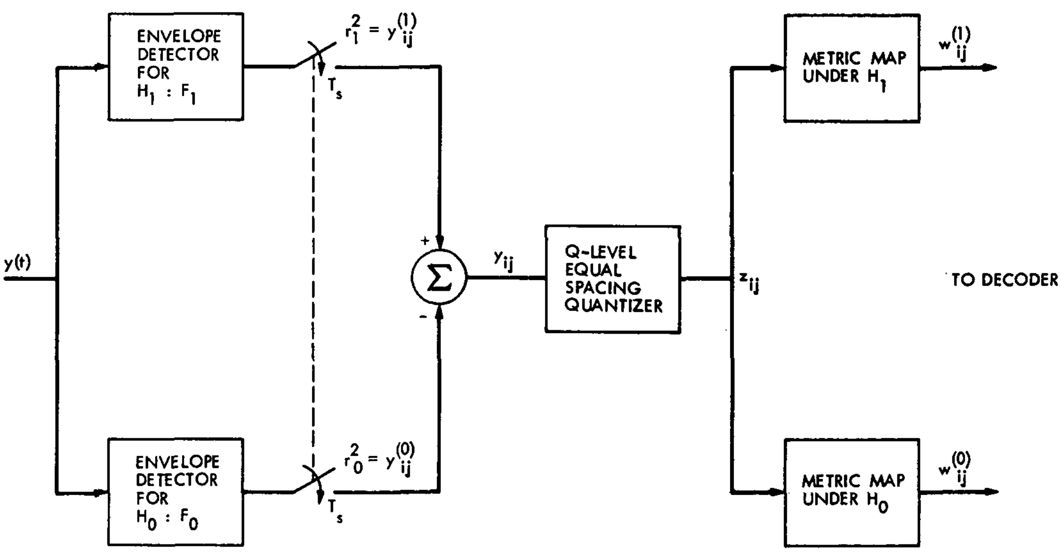

Fig. 2. PCM-binary FSK demodulator with Q-levels of quantization—System A

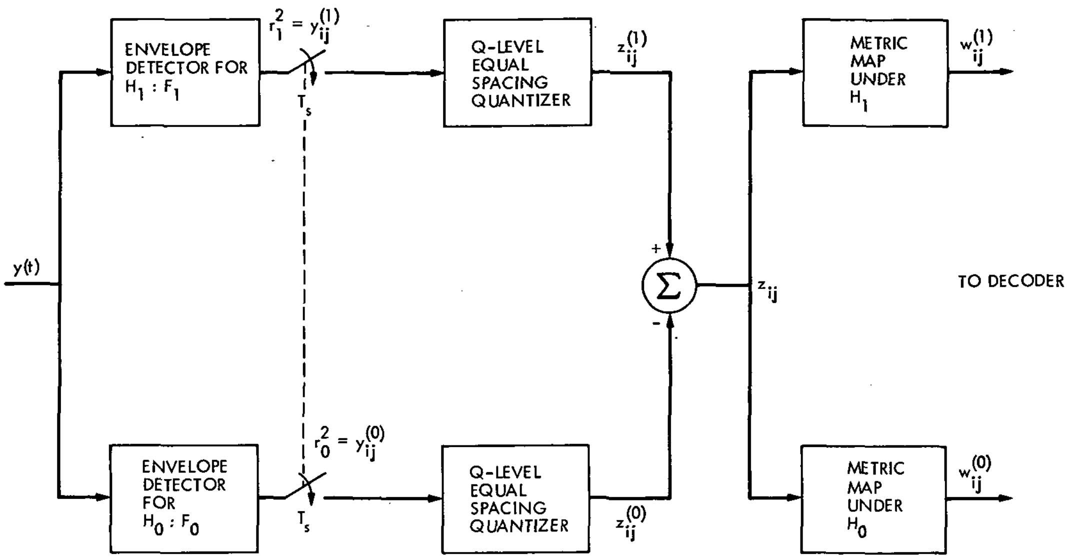

Fig. 3. PCM-binary FSK demodulator with Q-levels of quantization—System B

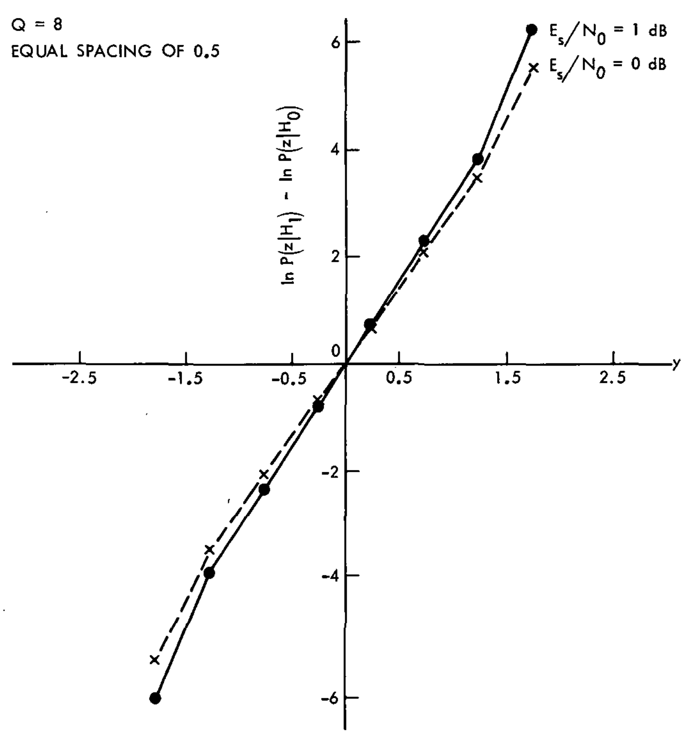

Fig. 4. Linearity of the difference of log likelihood with equally spaced quantization and the PSK modem

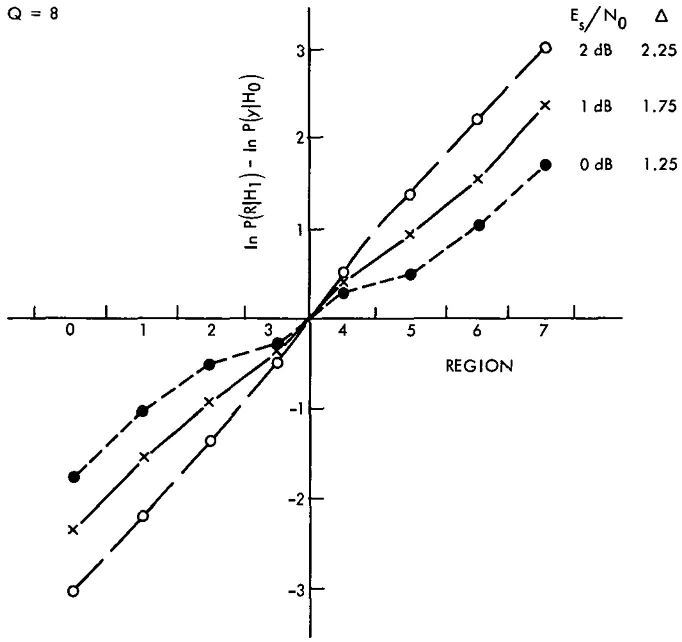

Fig. 6. Difference of log likelihoods of quantized outputs in binary FSK

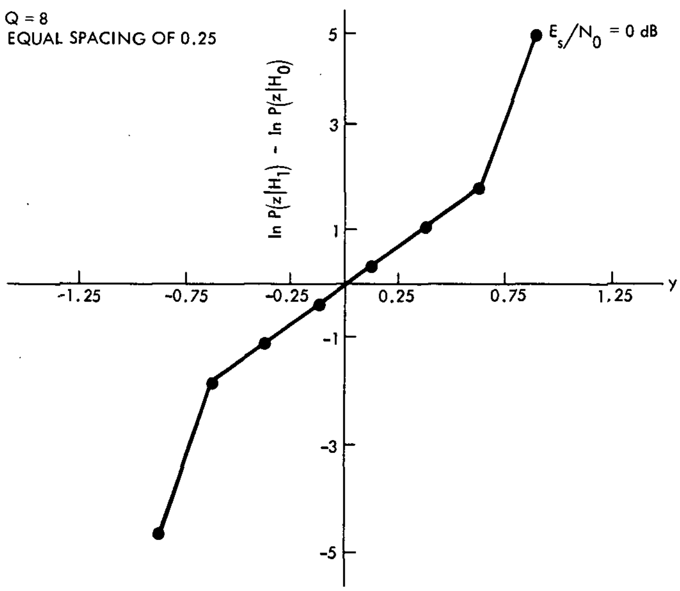

Fig. 5. Linearity of the difference of log likelihood with equally spaced quantization and the PSK modem

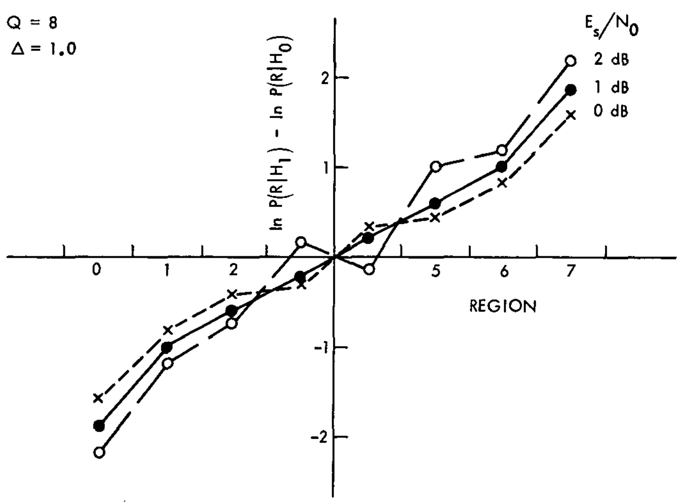

Fig. 7. Difference of log likelihoods of quantized outputs in binary FSK

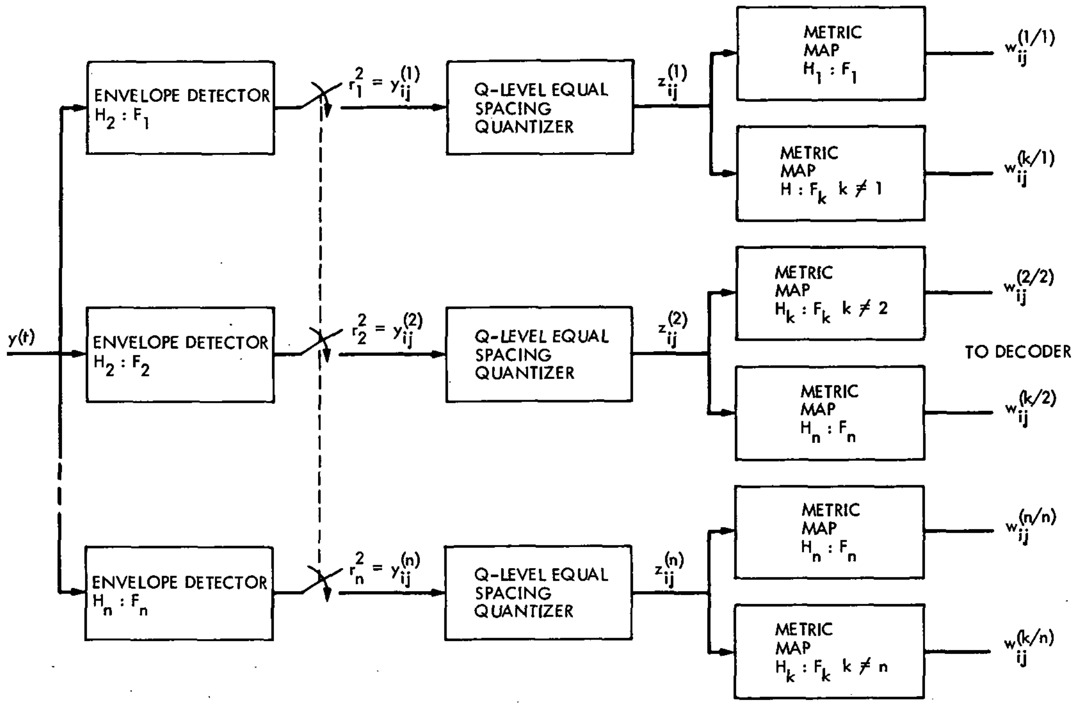

Fig. 8. PCM MFSK demodulator with Q-levels of quantization

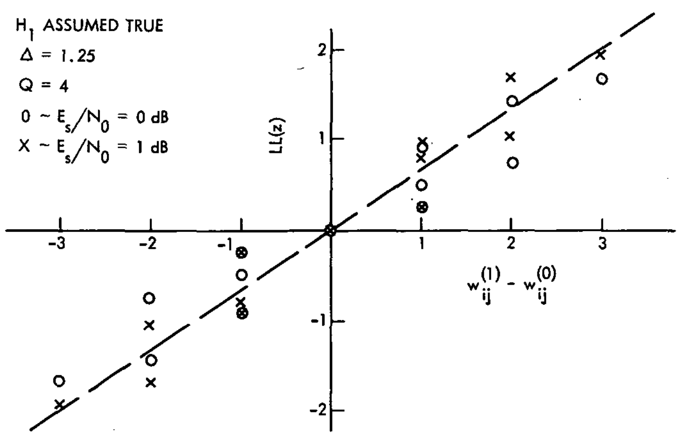

Fig. 9. Log likelihood ratio for System B, binary FSK, vs the difference of quantized, linearly indexed, envelope detector outputs

Development Support Group

E. B. Jackson and A. L. Price
RF Systems Development Section

The activities of the Development Support Group in operating the Venus Deep Space Station (DSS 13) and the Microwave Test Facility (MTF) for the period October 16 through December 15, 1972, are presented and categorized by facility and section supported. Major activities include an extensive test program of dual uplink carrier generation and measurement of intermodulation products in the downlink band resulting therefrom. A description of the progress of this test program, along with work required to minimize production of intermodulation products, is given. Progress in precision antenna gain measurements, continuing planetary radar experiments, and weak source observations are other activities noted.

During the two months ending December 15, 1972, the Development Support Group was engaged in the following activities.

I. DSS 13 Activities

A. In Support of the Communications Systems Research Section

1. Pulsars. The routine observation of pulsars was interrupted by requirements of the Dual-Carrier Project, but a total of 38 hours of observations was made.

2. Planetary radar. Continuing support of the Mariner Venus/Mercury 1973 (MVM 73) spacecraft mission, ranging measurements to the planet Mercury have been regularly made. These measurements are made using the 64-m-diameter antenna and the 400-kW transmitter at DSS 14 for transmission and reception, with pseudonoise code generation, data processing, and control being performed at DSS 13. Ranging measurements with a resolution of 5 μs were made of Mercury for a total of 66 good signal runs during this period.

B. In Support of the Communications Elements Research Section

1. Precision antenna gain measurement. Radio sources 3C123 and Virgo A were used as calibration sources from which data were obtained to calculate the absolute gain of the 26-m-diameter antenna. A total of 56 hours was devoted to these measurements using the SDS-930 computer to do automatic boresighting and tracking of the radio sources.

2. ***Weak source observation.*** Measurements were made for a total of 33 hours on radio sources 3C123, 3C348, 3C353, Cygnus X3, and the planet Jupiter. An additional 55 hours were spent on sky survey measurements with the antenna in a fixed position. Data taking is automated using the SDS-910 computer for antenna pointing and boresighting and an HP 5360A computing counter for control, measurement, and data recording.

3. ***Side lobe pattern (26-m antenna).*** Continuing the measurement of the magnitude and location of the side lobe pattern responses of the 26-m-diameter antenna, the ALSEPs left on the moon by Apollo missions are used as a calibration source across which the antenna is scanned in a raster scan with the output signal level being automatically recorded by the computer. Results have been very good and additional data will be taken with the quadripod legs on the antenna covered. These "before and after" data sets will be compared to see if significant reduction in side lobe response can be achieved by covering the quadripod legs. A total of 91 hours of tracking was obtained during this reporting period.

C. In Support of the RF Systems Development Section

1. ***Acceptance testing of 400-kW klystrons.*** A repaired 400-kW, 2115-MHz klystron (X3075) was received from Varian Associates and has undergone acceptance testing at the High Power Test Area at DSS 13. The initial tests revealed a possible problem with excessive outgassing in the tube and further tests were performed. However, an additional 2 days of testing were successful in "pumping down" the tube and it now meets all acceptance criteria.

2. ***Dual uplink carrier testing.*** Evaluation of the intermodulation products (IMPs) present in the downlink as a result of dual uplink carriers being transmitted by a single transmitter klystron has continued. An intensive program of elimination of possible noise producing sources, e.g., welding of all bolted joints above the dish surface, removal of all unshielded cables and wires, and careful taping of the antenna panel joints, resulted in a reduction of the intermodulation product levels to approximately -145 dBm. However, testing out the sidelooking feedhorn, which does not utilize the subreflector or main reflector, demonstrated intermodulation product levels of approximately -175 dBm.

To isolate further IMP producing elements, the quadripod and subreflector were removed, the waveguide system, polarizer, feedhorn, and waveguide switches were disassembled and carefully cleaned in nitric acid, and the system reassembled and tested. Although a further reduction in IMP levels was noted, it was determined that radio frequency currents on the outside of the feedhorn were still generating IMPs and noise.

A different feedcone, with all-welded exterior seams and structure, containing the feedhorn previously used as the sidelooking feedhorn (which is of a new design and has minimum exterior currents at 2115 MHz), a minimum amount of waveguide, and no switches, was installed onto the antenna in place of the existing feedcone. This simplification of the feedcone required the 2295/30-MHz converter to be removed from the S-Band Radar Operational (SRO) feedcone and temporarily installed in the 26-m-diameter antenna electronics room. Only a minimum receiving system instrumentation system is provided, and a measurement of maser gain requires physical changeover of cabling in the electronics room. If adjustment of maser gain and bandwidth is required, additional test equipment must be moved into the electronics room to substitute for the equipment that was not transferred from the SRO feedcone.

Testing with this new feedcone, without the quadripod, produced acceptable IMP-level performance and the quadripod and subreflector were reinstalled for further testing. Prior to reinstallation, the "spillover reduction" skirt around the subreflector was welded to the subreflector, and the vertex plate (in the center of the subreflector) was welded to prevent, insofar as possible, any noise production by arcing between different radio frequency potentials. Intermodulation product levels with this configuration are now -165 dBm, with further testing scheduled.

The Block II maser, utilized in all measurements of IMP levels in the downlink band, has performed without fault since original cooldown and tuning on October 12, 1972. However, the spare Block II maser was found to be unusable because of an inability to maintain a vacuum in the refrigerator jacket. Replacement of the refrigerator ion pump corrected this problem, but the associated helium compressor required overhaul before proper operation was obtained. After again starting testing of the spare maser, after ion pump replacement, the oil pump in the compressor failed and required replacement. However, the spare maser refrigerator and spare helium compressor have been tested, the refrigerator successfully

cooled to liquid helium temperature, and these items are now fully functional.

3. *Clock synchronization transmitter.* Periodic testing of the 100-kW X-band transmitter has continued. This is required to maintain the transmitter in operational condition and also to protect the transmitter during cold weather.

A new nitrogen (N_2) manifold is being installed at the 9-m-diameter antenna to enable operation of the transmitter from one (N_2) pressure source instead of the three previously required. The manifold will also provide a "loss of pressure" alarm. Work is also underway to weatherproof the electronics room on the 9-m-diameter antenna. At the present time, whenever the antenna is at zenith and it rains, most of the water caught in the dish is funneled along the waveguide run into the electronics room. Until this work is completed, storing the antenna at about 60 deg elevation serves to keep most of the water out of the electronics room.

D. In Support of the DSIF Operations Section

1. *Clock synchronization transmissions.* Although routine transmission of clock synchronization signals has ceased, three transmissions were made to DSS 41 in support of a Mariner 9 spacecraft experiment, and one transmission was made to DSS 42 at their request. Periodic testing, as described earlier, also continues.

II. Microwave Test Facility (MTF) Activities In Support of the RF Systems Development Section

During this reporting period, the primary activity has been supporting the Dual Uplink Carrier and associated transmitter testing. The disassembly, cleaning, and reassembly of the SRO feedcone was performed by MTF personnel, who also lapped all waveguide, polarizer, and feedcone joints as well as fabricated special stainless steel hardware required for reinstallation.

Efficient Signal Generation for High-Power Dual-Spacecraft Command

S. Butman
Communications Systems Research Section

This article describes a frequency multiplex scheme that is potentially 1.6 times as efficient (+2 dB) as the one currently under consideration, without exceeding the peak voltage rating of the Klystron.

I. Introduction

The possibility of transmitting to two spacecraft simultaneously from a single antenna has arisen in the forthcoming Viking 1975 Project that will place two orbiters and two landers at Mars. Two of the spacecraft will be simultaneously controlled from the ground. Therefore, there is a requirement to send two command signals (on two separate carrier frequencies) from a single transmitter, comprised of a single Klystron power amplifier and antenna. In this article, we describe a frequency multiplex scheme that is potentially 1.6 times as efficient (+2 dB) as the one currently under consideration, without exceeding the peak voltage rating of the Klystron.

II. Discussion and Description

We are concerned about amplifying two phase-modulated carrier signals

$$S_1(t) = \sin(\omega_1 t + \theta_1)$$

$$S_2(t) = \sin(\omega_2 t + \theta_2)$$

without exceeding the peak voltage limit $\sqrt{2P_{\max}}$ on the Klystron, where $P_{\max}$ is the maximum rms power rating.

If we blindly add the two signals, the result is

$$\sqrt{2P}S_1(t) + \sqrt{2P}S_2(t) = 2\sqrt{2P}\sin(\omega_+ t + \theta_+)\cos(\omega_- t + \theta_-) \leq \sqrt{2P_{\max}} \tag{1}$$

where

$$\omega_+ = \frac{1}{2}(\omega_1 + \omega_2); \qquad \theta_+ = \frac{1}{2}(\theta_1 + \theta_2)$$

$$\omega_- = \frac{1}{2}(\omega_2 - \omega_1); \qquad \theta_- = \frac{1}{2}(\theta_2 - \theta_1)$$

Obviously, from (1), the value of P is limited to

$$P \leq \frac{1}{4} P_{\max}$$

and the total power output is at most 50% of the Klystron rating, since

$$2P \leq \frac{1}{2} P_{\max}$$

The scheme proposed next can achieve an output efficiency of $\sim$80%, and should be "easy" to implement.

The idea is to biphase-modulate $\sin(\omega_+ t + \theta_+)$ by the squarewave $\sqsubset\mathrm{os}(\omega_- t + \theta_-) = \mathrm{sgn}[\cos(\omega_- t + \theta_-)]$, amplify, and then filter to remove undesired frequencies, as shown in Fig. 1.

Note that ω_- is several orders of magnitude less than $\omega_+ = (1/2)(\omega_2 + \omega_1)$: $\omega_- \approx 1$ to 10 MHz, while $\omega_+ \approx 2$ GHz. Also observe that $(4/\pi)\cos(\omega_- t)$ is the fundamental of the unit amplitude squarewave $\sqsubset\mathrm{os}(\omega_- t)$. With the above in mind, we next note that

$$z_0(t) = \sqrt{2P_{\max}} \sin(\omega_+ t + \theta_+) \sqsubset\mathrm{os}(\omega_- t + \theta_-) \leq \sqrt{2P_{\max}}$$

for all t. But

$$\sqsubset\mathrm{os}(\omega_- t + \theta_-) = \frac{4}{\pi} \sum_{k=0}^{\infty} \frac{(-1)^K}{2K+1} \cos[(2K+1)(\omega_- t + \theta_-)]$$

Therefore,

$$z_0(t) = \frac{2}{\pi}\sqrt{2P_{\max}} \sin(\omega_1 t + \theta_1) + \frac{2}{\pi}\sqrt{2P_{\max}} \sin(\omega_2 t + \theta_2)$$

+ higher harmonics of ω_- on ω_+ that can be filtered. It is crucial to note that this filtering must take place after the signal has been amplified. For example, the nearest two sidebands to the desired signal are at $\omega_+ \pm 3\omega_-$, hence at $2\omega_2 - \omega_1$ and at $\omega_1 - 2\omega_2$, and are each about 9.5 dB down. Suitable bandpass filtering will attenuate them and their higher- and lower-frequency brethren to negligible proportions. Since the filtering is on the Klystron output, the filters must be capable of dissipating approximately 20% of $P_{\max}$ or about 80 kW for a 400-kW tube.

To summarize, the signal $\sqrt{2P_{\max}} \sin(\omega_+ t + \theta_+) [(\omega_- t + \theta_-)]$ satisfies the voltage rating of the amplifier, but contains many undesirable intermodulation products that can be filtered out with some effort. The resulting benefit is an increase in output power to

$$\left(\frac{2}{\pi}\right)^2 P_{\max} \sim 0.4 P_{\max}$$

for each signal, which is only 1 dB below the maximum 50% limit for each command link and ~2 dB better than the linear multiplex scheme previously mentioned.

Incidentally, time multiplexing of the two carriers with a switching frequency of the order of ω_- also produces intermodulation products of the same size and has none of the advantages of the present scheme.

III. Implementation

Filtering of the high- (as opposed to the low-) frequency harmonics of $\sqsubset\mathrm{os}\,\omega t$ can be accomplished at low power levels in the exciter because absence of the higher harmonics places only a small ripple onto the squarewave, thus having a negligible effect on efficiency. Thus, referring to Fig. 1, starting with two signals at about 66 MHz which will be multiplied up to 2 GHz in the $\times 32$ multiplier, we have first the desired command signals at 66 MHz:

$$e_1 = \sin\left(\frac{\omega_1 t + \theta_1}{32}\right) + \cos\left(\frac{\omega_2 t + \theta_2}{32}\right)$$

Their hard limited version becomes

$$e_2 = \mathrm{sgn}[e_1(t)]$$

and prefiltering yields

$$e_3 = \text{bandpass filtered } e_2(t)$$

bandwidth of, say, 5 MHz centered at 66 MHz, so that

$$e_3(t) = \sin\left(\frac{\omega_+ t + \theta_+}{32}\right) \sqsubset\mathrm{os}\left(\frac{\omega_- t + \theta_-}{32}\right)$$

where $\sqsubset\mathrm{os}(\omega t/32) = \sqsubset\mathrm{os}(\omega t/32) -$ harmonics greater than 5 MHz. After frequency multiplication, the result is

$$e_4 = \sin(\omega_+ t + \theta_+) \sqsubset\mathrm{os}(\omega_- t + \theta_-)$$

where $\sqsubset\mathrm{os}(\omega_- t) = \sqsubset\mathrm{os}(\omega_- t) -$ harmonics greater than 160 MHz. After amplification in the Klystron,

$$e_5 = \sqrt{2P_{\max}}\, e_4$$

Finally, high-power filtering yields

$$e_6 = e_5$$

filtered to remove all but ω_1 and ω_2.

IV. Conclusions

Further studies of the high-power filter required to demonstrate this efficient dual-carrier multiplex scheme are in progress, including the question as to whether such filtering is needed at all. This last point is based on the fact that the harmonics that can cause interference in the receiver, which is about 200 MHz removed, are eliminated before amplification, while the high-power harmonics radiated by the antenna can be blocked by the front end of the spacecraft receiver.

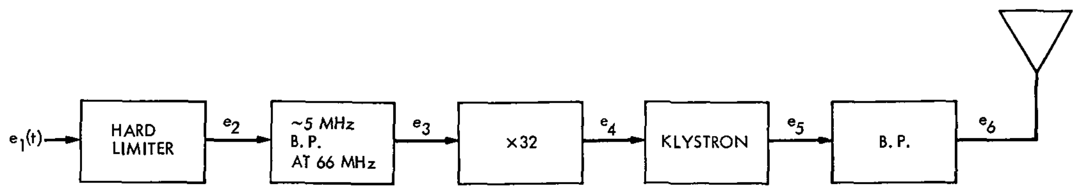

Fig. 1. Dual-carrier multiplex scheme

A New Pulsar Timer

A. Slekys
Communications Systems Research Section

The times-of-arrival of pulses of radiation from pulsating radio sources (pulsars) have been measured at the Venus Deep Space Station (DSS) by Downs and Reichley (Ref. 1). This article describes a programmable high-speed timing source, designed to control the data sampling. A possible use of the timer, as part of a DSN navigation system, is to determine a spacecraft's position in inertial space. It is easily controllable by computer and is intended to be part of a demonstration of remote experiment operation in which the Sigma 5 at JPL will configure pulsar experiments at DSS 13.

I. Introduction

This article describes a new timer that operates under program control of the XDS 930 computer, providing entirely variable major and minor cycle pulse rates, with automatic start, delay, and stop features. Incorporating a fast analog-to-digital converter (ADC), with a maximum sampling rate of 250 kHz, and having a selectable sampling interval within each period, the duty cycle of the sampling scheme can now be more closely matched to that of the pulsar. Data resolution is thus improved by over a factor of 10, to 4 μs per sample. Signals are also available from the timer to control the operation of the noise-adding radiometer (Ref. 2), which functions in complement with pulsar sampling. It is intended to demonstrate this timer in an experiment in which DSS 13 is remotely configured from the Sigma 5 at JPL.

A suggested novel use of the timer is as part of a DSN radio navigation system. Comparison of times-of-arrival of three pulsars (approximately orthogonal to the craft) measured on board and on Earth gives an accurate fix of the spacecraft's position relative to Earth when simultaneous ranging is carried out.

II. System Description

The times-of-arrival of pulses of radiation from pulsating radio sources are measured relative to a 1-s pulse derived from a cesium standard operating at 1 MHz and

accurate to 1 part in 10^{12}. The 1-MHz signal from the cesium standard also drives a frequency synthesizer. In the existing system, an operator presets the frequency synthesizer for $f_p \times 10^6$ Hz, where f_p is the apparent pulsar frequency, and then arms a start gate, which allows the cesium clock to trigger the sampling of data at a predetermined time. The frequency of the synthesizer output is divided to produce signals controlling the data sampling.

As shown in Fig. 1, the synthesizer signal is divided by $D1$, giving the major cycle signal, f major, at a frequency $(f_p \times 10^6)/D1$ Hz, and by $D2$, giving the basic minor cycle timing signal. The minor cycle signal externally drives the ADC, and hence, $(f_p \times 10^6)/D2$ samples are obtained per pulsar period. These samples are uniformly distributed over a given period, and since the actual pulsar width lies well within the period (typically, pulsar duty cycles are about 5%), the sampling is not optimized over the region of interest. Furthermore, the major cycle divisor is fixed ($D1 = 10^6$), and there are only four available values for $D2$, namely, 200, 100, 50, and 25, with a maximum ADC sampling rate of 20 kHz.

The new timer similarly divides down the synthesizer signal to create f major and f minor. The interface to the XDS computer allows for variable dividers and complete control over pulsar data sampling and subsequent processing in the machine.

A. Software

A flow chart of the pulsar timer program *PUT*, written in SYMBOL assembly language for the XDS 930 computer, is shown in Fig. 2. Given the following integer parameters, entered with individual requests on the typewriter, the program allows for complete control of all data flow into the machine, subsequent integration, processing, and output of data. Automatic start, delay, or stop during any operation is obtained without loss of time sync with the pulsar data.

TS = Start time (GMT) (entered as a 6-digit integer)

X = major cycle divisor

Y = minor cycle divisor

Δ = sampling delay (in number of minor cycles pulses)

ΔL = sampling length (in number of minor cycle pulses)

N = pulse integration number (in number of major cycle pulses)

f_s = synthesizer frequency (Hz)

From the above,

$$f_{major} = \frac{f_s}{X}, \qquad f_{minor} = \frac{f_s}{Y}$$

The limiting values for the parameters are listed below:

$$00{:}00{:}00 \leq TS \leq 23{:}59{:}59$$

$$1 \leq X < 10^8$$

$$1 \leq Y < 2^{20} \qquad Y < \frac{X}{Y} < 2^{20}$$

$$0 \leq \Delta < 2^{20}$$

$$0 \leq \Delta L < 2^{20} \qquad \Delta < \Delta + \Delta L < 2^{20}$$

$$0 < N < 2^{12}$$

Thus, for each of N major cycles, after a sampling delay of Δ minor cycle pulses, ΔL samples of pulsar data are taken at the minor cycle rate and stored in core. At this point, data flow into core is halted, and the data in core are integrated and loaded onto magnetic tape, while the hardware maintains time sync by monitoring major cycle pulses. After all further processing (plotting, etc.) is completed and the time required for the processing recorded on magnetic tape, data flow into core is resumed with the original divider parameters intact.

The breakpoints on the console allow for the following interruptions:

BPT 2: SET for DELAY. The program allows data flow into core for the current major cycle. At the end of this cycle, the program stops data flow. Time sync is maintained by the timer until either BPT 2 is RESET, or BPT 4 is SET. In the former instance, data flow into core is resumed, the delay time is written on tape, and the pulse integration number counter is reset to zero. In the latter case, time sync is abandoned, and the program enters the HALT state.

BPT 3: SET for accumulation. The program accumulates data samples in core for as many periods as BPT 3 is SET. With BPT 3 RESET, core is cleared before each period of N major cycles of data.

BPT 4: SET for immediate HALT. The program stops data flow into core and tests for BPT 4 to be RESET, indicating a RESTART. No time sync is maintained, since this is considered an emergency stop. At RESTART, all breakpoints should be in the RESET position.

B. Hardware

A block sketch of the pulsar timer hardware appears in Fig. 3. The program reads the *TS* clock (which is synced with the cesium standard), and upon reaching the preprogrammed start time (*TS*) minus 1 s, arms a start gate. Sampling of data commences on the next 1-s pulse from the *TS* clock. The first two programmable dividers with 20-bit binary divisors reduce the input signal from a frequency of $f_p \times 10^6$ Hz to create the minor cycle signal at a frequency $(f_p \times 10^6)/Y$ Hz and the major cycle signal at a frequency $(f_p \times 10^6)/X$ Hz.

High-speed switching of data from the Δ and $\Delta + \Delta L$ registers into the third programmable divider via the multiplexer allows for this divider to perform the dual function of deleting Δ pulses and passing ΔL pulses. During each major cycle, a count of Δ minor cycle pulses enables the output gate *G*. This enabling signal also switches the $\Delta + \Delta L$ divisor into the divider in midstream. When the count reaches $\Delta + \Delta L$, gate *G* is disabled and the output is terminated until the next major cycle pulse.

The fourth divider, which is limited to a 12-bit binary divisor [*N*], provides a 2-μs interrupt to the computer when the count equals the pulse integration number. In a delay mode, the divide function is inhibited via the delay gate, gate *G* is disabled, and the divider merely counts major cycle pulses, thus maintaining sync with the clock. Upon termination of the delay, the program accesses the current number in the counter via a read gate, resets the counter to zero, and reactivates the divide function. The major cycle signal is also sent to the program via an interrupt line to provide appropriate timing for the control of the *N* divider, as described.

III. System Performance

Preliminary checkout of the timer was performed at JPL and at the Venus Deep Space Station, utilizing a known pulse source as a pseudo-pulsar. Various sampling rates (to a maximum 20 kHz, limited by the ADC) and duty cycles were tested. The program and timer performed to specifications. With the divisors set to their upper-limit values, the timer has a maximum operating speed of about 14 MHz. The basic limitation is the speed of the comparators used in the divider design. With the divisors set to their lower-limit values, 20-MHz operating speed is achieved, which is the upper speed limit on the integrated circuits used.

Delivery of a high-speed ADC is expected shortly, at which time results of high-speed-sampled pulsars will be published.

References

1. Reichley, P. E., Downs, G. S., and Morris, G. A., "Time of Arrival Observations of Eleven Pulsars," *Astrophys. J.*, Vol. 159, Jan. 1970.
2. Batelaan, P. D., Goldstein, R. M., and Stelzreid, C. T., "A Noise-Adding Radiometer for Use in the DSN," in *The Deep Space Network*, Space Programs Summary 37-65, Vol. II, pp. 66–69, Jet Propulsion Laboratory, Pasadena, Calif., Sept. 30, 1970.

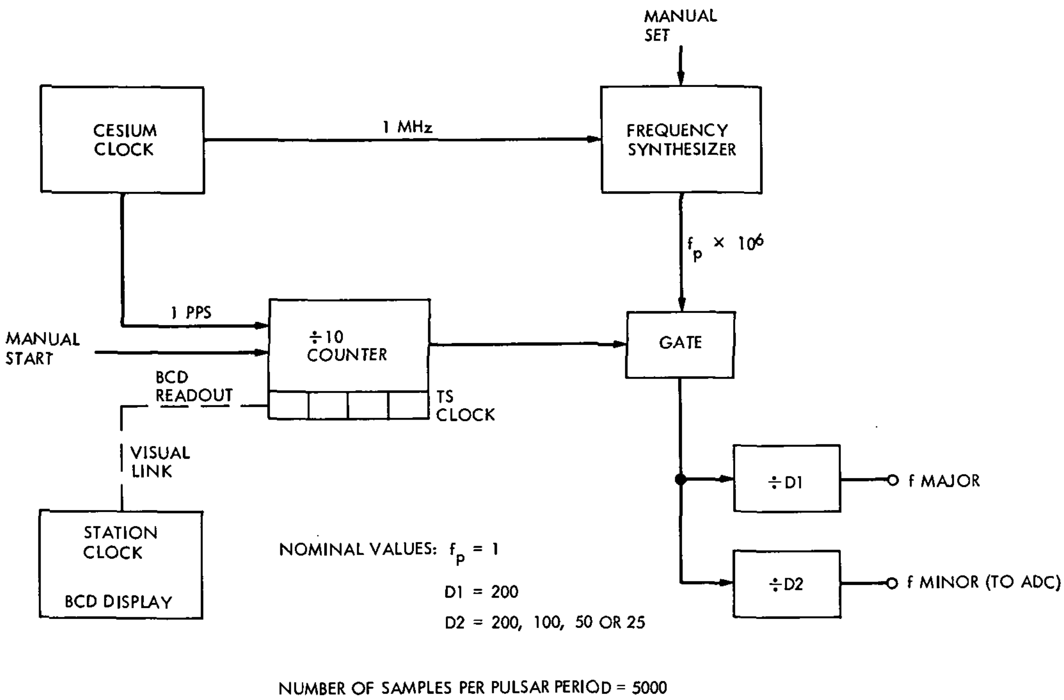

Fig. 1. Old timer functions

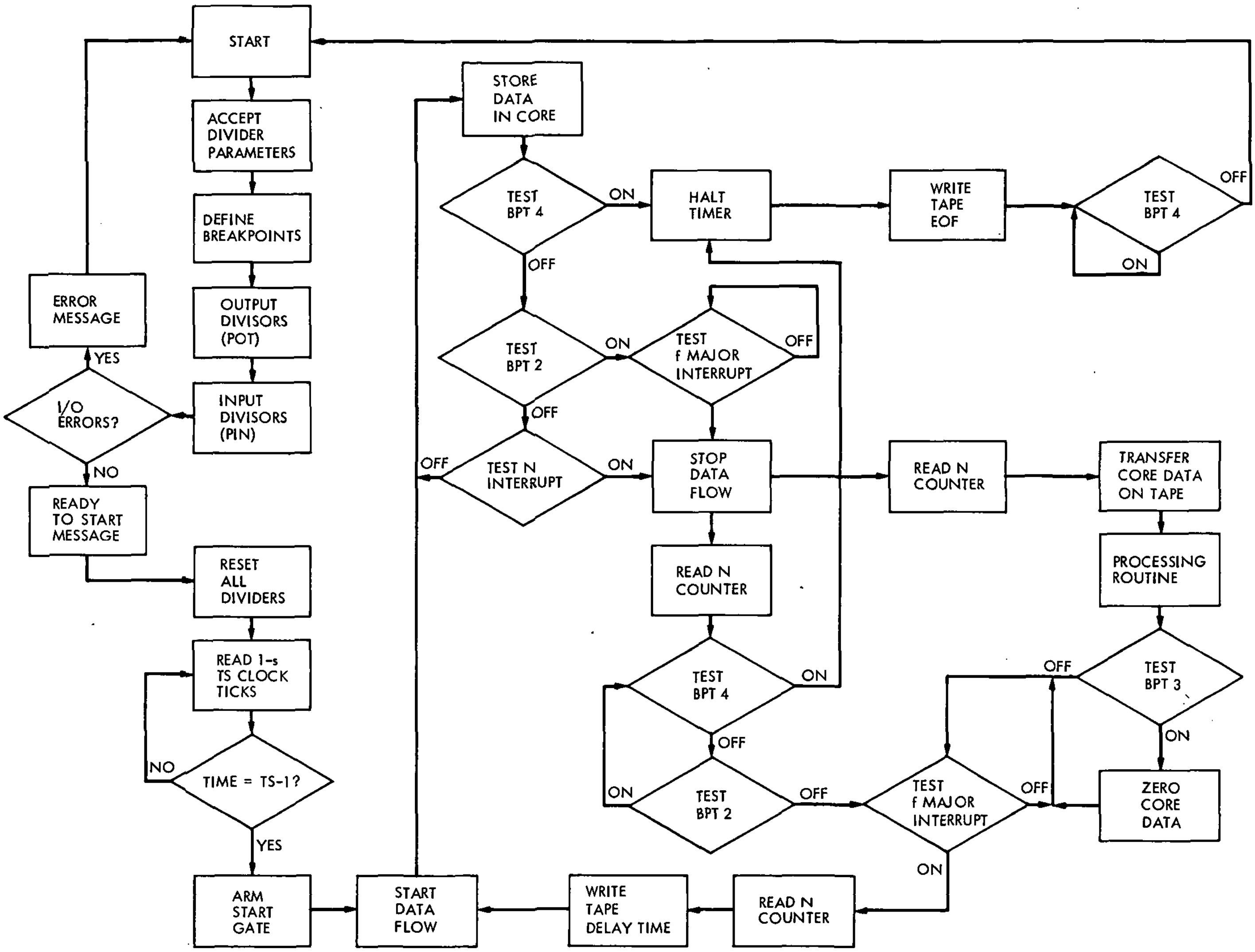

Fig. 2. Pulsar timer program *PUT*

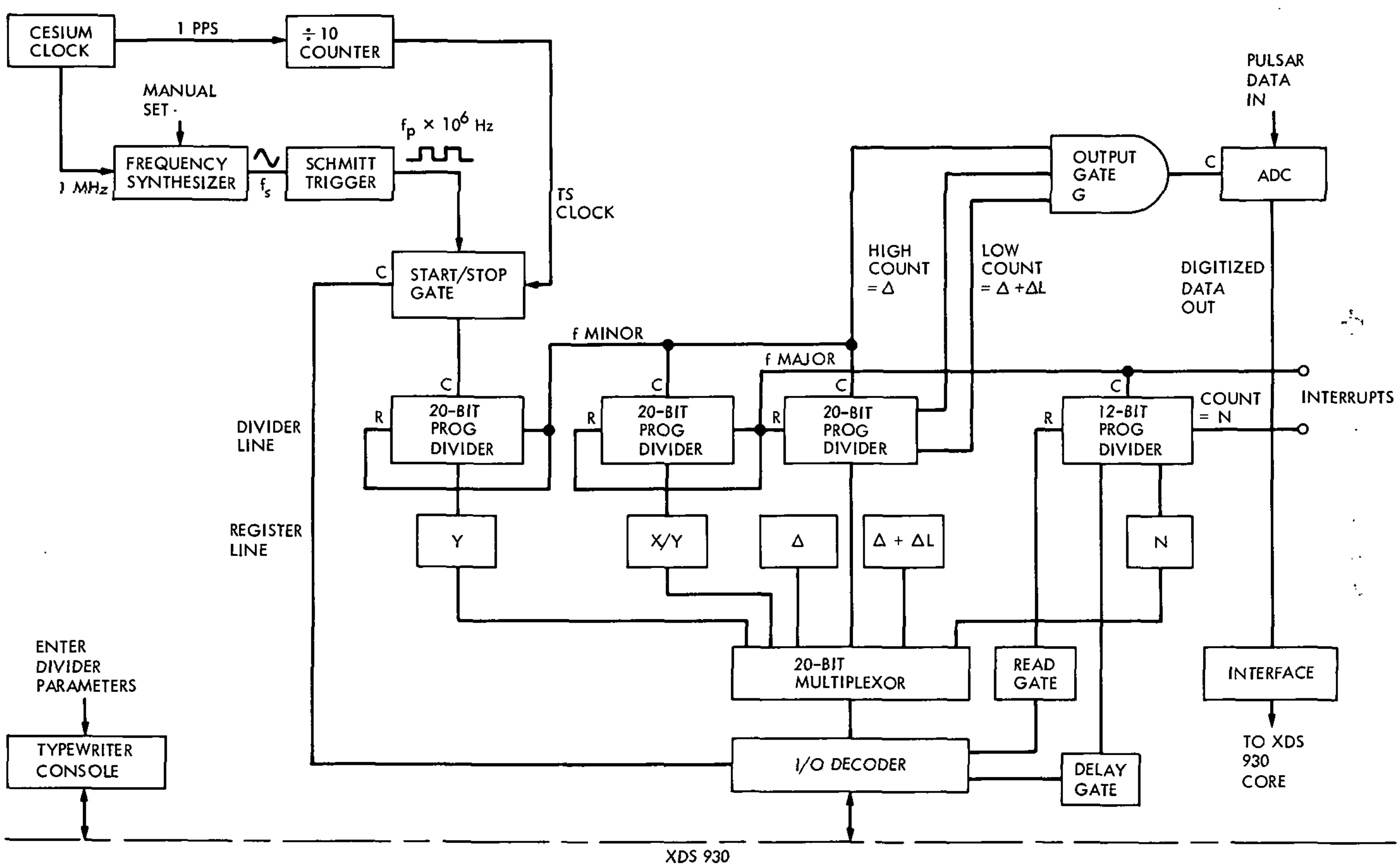

Fig. 3. Pulsar timer hardware

An Information-Theoretic Model for the Ground Communications Facility Line

O. Adeyemi
Communications Systems Research Section

This article presents a three-state Markov chain as a model for the errors occurring on the Ground Communications Facility (GCF). An analytic expression for the capacity of the channel in terms of the model parameters is obtained, and comparison is made with the capacity of a binary symmetric channel (BSC) with the same bit-error rate. For a better understanding of the channel's intrinsic behavior and for use in estimating the performances of different error-detecting and error-correcting codes, we obtain analytic expressions for three sets of channel parameters. These are the bit error statistics, the block error statistics, and the distribution of burst lengths and error-free (gap) intervals.

I. Introduction and the Model

This article will report the progress made so far in constructing a theoretical model for the Ground Communications Facility (GCF) high-frequency (50-kbps) wideband error distribution using the results of the test runs reported by J. P. McClure (Refs. 1 and 2). In those reports, the "bursty" nature of the errors is clearly noticeable; there are error-free gaps of up to 3-min duration (10,000,000 bits), followed by up to ½ s of sputtering errors.

The data from the test runs, stored in twenty-five tape reels, consisted of records of relative positions of consecutive errors in the sequence of noise digits $z = \{z_n\}$ (in which $z_n = 1$ if the nth digit is in error and equal to 0 otherwise). Because of certain problems with the recordings, only twelve of these reels were found usable, with a total of about 5.73×10^8 bits and an average bit error rate of less than 10^{-4}.

Figure 1 is the histogram for the (error-free) gap lengths X, for $X \geqq 10^3$ bits (or a transmission time of 1/50 s or more). The ordinate represents the number of times a gap of length X occurred in the twelve tape reels. Not shown on the histogram are frequencies for the gap lengths of 100 bits or less. The frequencies for this range of gap lengths are much higher, showing again that the errors

occur in bursts. The modal frequencies at $X = 10^3$ and $X = 10^6$ are denoted by $\bar{A}$ and $\bar{B}$, respectively.

Pioneered by Gilbert (Ref. 3), many attempts have been made at using Markov processes as theoretical models for burst-noise channels. For example, Elliot (Ref. 4) and Berkovits, Cohen, and Zierler (Ref. 5) have successfully generalized the original Gilbert model (Fig. 2) for fitting data from telephone networks. Gilbert's model consisted of one perfectly good state G and one error state B; i.e., an error bit can occur only in state B.

In the generalization, an error bit can occur in either the good state G or the bad state B, but with different probabilities. In Fig. 2, transitions between the states occur in the direction of the arrows, and if $P(j|i)$ denotes the one-step transition probability of going from state i to state j, then

$$P(G|B) = p, \qquad P(B|G) = P$$

and $q = 1 - p$, $Q = 1 - P$ are the probabilities of remaining in B and G, respectively. If we let k and h denote the probabilities of correct reception of a bit when the channel is, respectively, in states G and B, then $k' = 1 - k$, $h' = 1 - h$ are the respective probabilities of a bit being in error in those states.

The two-state model is not adequate, however, for the type of gap distribution obtained on the GCF channel (see Fig. 1). For very short gap lengths ($X \leqq 10^3$) and medium to larger values of the (error-free) gaps ($10^3 < X \leqq 10^5$), one may successfully characterize the communication channel by the generalized Gilbert model. But no two-state Markov chain would suffice to represent the whole range of the gap distribution (especially to include the other modal frequency at $\bar{B}$ for gap lengths of about 10^6 bits or more). We are therefore forced to consider a model with more than two states to account for the (error-free) gaps of length $\geqq 10^6$, even though the analysis of such a model may be mathematically unwieldy.

The following is the suggested model for the GCF. A Markov chain with three states B, G_1, and G_2 will be used to generate the gap lengths (Fig. 3). Because of the low bit error rate recorded in the data, we take both states G_1 and G_2 to be perfectly good, i.e., $z_n = 0$ always in G_1 or G_2; the error bursts are produced in state B. Since actual bursts contain good digits interspersed with errors, we let the probability of having a good digit in this state equal $h > 0$. In other words,

$$P(z_n = 1 | B) = 1 - h < 1$$

and we write $1 - h = h'$. As explained for Fig. 2,

$$P(G_2|B) = p$$
$$P(B|G_2) = b$$
$$P(G_1|G_2) = g$$
$$P(G_2|G_1) = P$$

are the one-step transition probabilities: $q = 1 - p$, $r = 1 - g - b$, $Q = 1 - P$ are the probabilities of remaining in B, G_2, and G_1, respectively. For example, for a bit error rate $P_1 = 4 \times 10^{-5}$, which is of the order of the average bit error recorded in the GCF data, if we assume $h' = 0.5$, calculations using the data give

$$p = 0.20; \qquad (q = 0.80)$$
$$b = 0.36; \qquad r = 0.21 \times 10^{-2}; \qquad g = 0.6379$$
$$P = 0.29 \times 10^{-4}; \qquad Q = 0.999971$$

Let $\underleftarrow{\overrightarrow{TU}}$ denote transitions between states T and U, including sojourns in T and U; and let TUV denote a particular (transition) path between states T and V passing through state U; $T, U, V = B, G_1,$ or G_2. Then the following transitions between the states can produce the pattern of gap distributions observed in the data:

(1) A long sojourn in state B (with probability $q = 0.8$ of remaining in B at any instant of time, once having got there) accounts for the very short gaps (long bursts of errors, including cases of consecutive errors).

(2) $\underleftarrow{\overrightarrow{BG}}_2$ ($\equiv BG_2G_2, \cdots, BBG_2, \cdots, BG_2B, \cdots, G_2BB, \cdots, G_2BG_2, \cdots$) accounts for gap lengths of about 10^2–10^3 bits.

(3) $BG_2G_1, \cdots, G_1G_2B, \cdots$ account for gap lengths of 10^3–10^4 bits.

(4) $\underleftarrow{\overrightarrow{G_1G_2}}$ (including sojourns in G_1 and G_2) accounts for gap lengths of 10^5 bits or more.

Unfortunately, the twelve reels on which our model is based suffer from certain recording problems which have the effect of increasing the gap lengths at the end of each test run, thereby lowering the measured bit error rate. It is assumed that the current test run being conducted on the same channel but at a much lower rate (4.8 kbps) will provide reliable data from which to estimate the parameters of this model. It is even likely that we may have to modify our model to fit the new data. In such an eventuality, however, our method of analysis here is general enough to handle an increase in the number of states of the Markov chain.

Let us mention here that in 1970, Daniel Stern (Ref. 6) of GSFC computed a number of useful empirical probabilities from high-speed data collected from selected NASCOM channels. Thus, we have some data in hand with which to compare the results of the current test run.

II. Summary of Results

For a better understanding of the channel's intrinsic behavior and for use in estimating the performance of different error-detecting and -correcting codes on the channel, analytic expressions in terms of the model parameters are obtained for three groups of channel parameters. These are the bit error statistics, the block error statistics, and the distributions of the burst lengths and the gap intervals.

Section III contains the first group of statistics, consisting of (1) the distribution of distances between consecutive errors, (2) the autocorrelation of bit errors, and (3) the probability of a sequence of consecutive errors. Distribution of distances between consecutive errors will be used to estimate the number of gaps of a given length. For estimating significant error patterns, we require the autocorrelation of bit errors, and the distribution of a sequence of consecutive errors will show how clustered the errors are.

In Section IV we evaluate the capacity of the channel (the maximum rate at which arbitrarily reliable information can be transmitted over the channel). This capacity is then compared with that of a binary symmetric channel (BSC) with the same bit error rate. The capacity of the three-state channel must always be larger than that of the equivalent BSC; ironically, forward error correction is, nevertheless, more difficult.

A very important group of statistics for estimating the performance of error-correcting codes on the channel are the block error distributions; a *block* is defined as a sequence of n bits for a fixed integer n. This group of statistics, discussed in Section V, consists of

(1) The probability of an error block

(2) The distribution of the number of errors in a block

(3) The distribution of the number of errors in the information digits of an interleaved code with a given constant of interleaving (A block code C is said to be interleaved with constant of interleaving t if successive letters of individual code words are separated on the channel by t time units.)

(4) The distribution of distances between extreme errors (i.e., between the first and the last errors) in a block, which statistic is to be used to estimate the performance of codes that can correct error bursts in a block, provided they are confined to a given length

(5) The distribution of symbol errors in an n-symbol word where a symbol is a fixed number, say m, of consecutive bits

Section VI presents the last group of the channel parameters: the distribution of burst lengths. For this analysis, a burst will be defined as a sequence (1) beginning and ending with an error, (2) separated from the nearest preceding and following error by a gap of no less than a given number, say $\mathcal{G}$, called the *guardspace*, and (3) containing within it no gap equal to or greater than the given guardspace.

Since burst correction codes can generally correct bursts up to some fraction of the guardspace, say 1/3 (see Ref. 7), it is important to note what percentage of the burst lengths falls below the given fraction of a guardspace. The optimum value of the guardspace is therefore that which has the highest percentage of bursts less than this correctable fraction (1/3) of $\mathcal{G}$. This group also contains the distribution of the number of errors in a burst of a given length. This statistic is significant because for low error densities within a burst, burst-correcting codes can cope with occasional errors in what should be an error-free guardspace.

III. Bit Error Statistics

To shorten the length of this article, detailed proofs of every proposition will not be presented. Henceforth all references to model parameters will be to those presented in Fig. 3.

The fractions of times spent in states B, G_2, and G_1 are given, respectively, by

$$P(s_0 = B) = \frac{bP}{w_0}$$

$$P(s_0 = G_2) = \frac{pP}{w_0}$$

$$P(s_0 = G_1) = \frac{pg}{w_0} \tag{1}$$

where $w_0 = pg + pP + bP$.

Since errors occur only in state B, and then just with probability h', the bit error probability $P(1)$ is given by

$$P(1) = \frac{bPh'}{w_0}$$

Let $v(k)$ denote the probability of getting k error-free bits between a given error and the one immediately following it (i.e., a gap of length k):

$$v(k) = P(0^k 1 \mid 1) \tag{2}$$

where $\{0^k 1 \mid 1\}$ is the event that a given initial error is followed by a gap of length k. It follows that

$$\begin{aligned} v(k) &= P(0^k \mid 1) - P(0^{k+1} \mid 1) \\ &= u(k) - u(k+1) \end{aligned} \tag{3}$$

where we have denoted $P(0^k \mid 1)$ by $u(k)$ and $\{0^k \mid 1\}$ is the event that a given error is followed by k error-free bits. Therefore, it suffices to find expressions only for $u(k)$ in terms of the model parameters.

Let

$$\begin{aligned} G_1(k) &= P(0^k, s_k = G_1 \mid 1) \\ G_2(k) &= P(0^k, s_k = G_2 \mid 1) \\ B(k) &= P(0^k, s_k = B \mid 1) \end{aligned} \tag{4}$$

where s_k is the state of the channel at time k. Then

$$u(k) = G_1(k) + G_2(k) + B(k)$$

and

$$\begin{aligned} G_1(k+1) &= P(0^{k+1}, s_k = G_1, s_{k+1} = G_1 \mid 1) \\ &\quad + P(0^{k+1}, s_k = G_2, s_{k+1} = G_1 \mid 1) \\ &\quad + P(0^{k+1}, s_k = B, s_{k+1} = G_1 \mid 1) \\ &= G_1(k)\,Q + G_2(k)\,g \end{aligned} \tag{5}$$

Similarly,

$$G_2(k+1) = G_2(k)\,r + G_1(k)\,P + B(k)\,p$$

$$B(k+1) = B(k)\,qh + G_2(k)\,bh$$

In matrix form,

$$\left(G_1(k+1), G_2(k+1), B(k+1)\right) = \left(G_1(k), G_2(k), B(k)\right) M \tag{6}$$

where

$$M = \begin{pmatrix} Q & P & 0 \\ g & r & bh \\ 0 & p & qh \end{pmatrix}$$

with

$$\begin{aligned} G_1(0) &= P(s_0 = G_1 \mid 1) = 0 \\ G_2(0) &= P(s_0 = G_2 \mid 1) = 0 \\ B(0) &= P(s_0 = B \mid 1) = 1 \end{aligned} \tag{7}$$

Now Eqs. (6) and (5) give

$$\begin{aligned} &\left(G_1(k+1), G_2(k+1), B(k+1)\right) \\ &\quad = \left(G_1(0), G_2(0), B(0)\right) M^{k+1} \\ &\quad = (0, 0, 1)\, M^{k+1} \end{aligned} \tag{8}$$

For the purpose of deriving

$$u(k) = G_1(k) + G_2(k) + B(k)$$

one may use Eq. (8) and a computer after estimating the model parameters. The results of such computer calculations and estimates will be presented in a fuller report. But for use in the next section in finding expression for the capacity of the channel, we give detailed solution to (8).

Write the matrix M in Eq. (6) as:

$$M = \begin{pmatrix} 1-P & P & 0 \\ g & 1-g-b & bh \\ 0 & p & (1-p)\,h \end{pmatrix} \tag{9}$$

The characteristic equation associated with M is

$$\begin{aligned} &\lambda^3 + \lambda^2 [P + ph + g + b - 2 - h] \\ &\quad + \lambda [bP + pPh + phg + 2h + 1 - h(P + p + g + b) \\ &\quad - (P + ph + g + b)] \\ &\quad + h [P + p + g + b - (pP + pg + bP) - 1] = 0 \end{aligned}$$

with roots $\lambda_1, \lambda_2, \lambda_3$ given by

$$\lambda_1 = -\left[(A + \sqrt{A^2 + B^3})^{1/3} + (A - \sqrt{A^2 + B^3})^{1/3} + \frac{\hat{b}}{3}\right]$$

$$\lambda_2 = \frac{1}{2}\left[(A + \sqrt{A^2 + B^3})^{1/3} + (A - \sqrt{A^2 + B^3})^{1/3}\right] + \frac{i\sqrt{3}}{2}\left[(A + \sqrt{A^2 + B^3})^{1/3} - (A - \sqrt{A^2 + B^3})^{1/3}\right] - \frac{\hat{b}}{3}$$

$$\lambda_3 = \frac{1}{2}\left[(A + \sqrt{A^2 + B^3})^{1/3} + (A - \sqrt{A^2 + B^3})^{1/3}\right] - \frac{i\sqrt{3}}{2}\left[(A + \sqrt{A^2 + B^3})^{1/3} - (A - \sqrt{A^2 + B^3})^{1/3}\right] - \frac{\hat{b}}{3}$$

where $\lambda_1 < \lambda_2 < \lambda_3$ are real roots and

$$\left.\begin{aligned}
A &= \frac{\hat{q}}{2}; \qquad B = \frac{\hat{p}}{3} \\
\hat{p} &= \hat{c} - \frac{\hat{b}^2}{3}; \qquad \hat{q} = \hat{d} - \frac{\hat{b}\hat{c}}{3} + \frac{2\hat{b}^3}{27} \\
\hat{b} &= P + ph + g + b - 2 - h \\
\hat{c} &= bP + pPh + pgh + 2h + 1 \\
&\quad - h(P + p + g + b) - (P + ph + g + b) \\
\hat{d} &= h[P + p + g + b - (bP + pP + pg) - 1]
\end{aligned}\right\} \tag{10}$$

To find M^n is in general complicated, but using a method described in Ref. 8 (p. 385), we get

$$M^{(n)} = c_1\lambda_1^n M_1 + c_2\lambda_2^n M_2 + c_3\lambda_3^n M_3 \tag{11}$$

where

$$M_1 = \begin{pmatrix} \dfrac{gP}{[\lambda_1 - (1-P)]^2} & \dfrac{P}{\lambda_1 - (1-P)} & \dfrac{bPh}{[\lambda_1 - (1-P)]\,[\lambda_1 - (1-p)\,h]} \\[2ex] \dfrac{g}{\lambda_1 - (1-P)} & 1 & \dfrac{bh}{\lambda_1 - (1-p)\,h} \\[2ex] \dfrac{bg}{[\lambda_1 - (1-P)]\,[\lambda_1 - (1-p)\,h]} & \dfrac{p}{\lambda_1 - (1-p)\,h} & \dfrac{pbh}{[\lambda_1 - (1-p)\,h]^2} \end{pmatrix}$$

$$M_2 = \begin{pmatrix} \dfrac{gP}{[\lambda_2 (1-P)]^2} & \dfrac{P}{\lambda_2 - (1-P)} & \dfrac{bPh}{[\lambda_2 - (1-P)]\,[\lambda_2 - (1-p)\,h]} \\[2ex] \dfrac{g}{\lambda_2 - (1-P)} & 1 & \dfrac{bh}{\lambda_2 - (1-p)\,h} \\[2ex] \dfrac{pg}{[\lambda_2 - (1-P)]\,[\lambda_2 - (1-p)\,h]} & \dfrac{p}{\lambda_2 - (1-p)\,h} & \dfrac{bph}{[\lambda_2 - (1-p)\,h]^2} \end{pmatrix}$$

$$M_3 = \begin{pmatrix} \dfrac{gP}{[\lambda_3 - (1-P)]^2} & \dfrac{P}{[\lambda_3 - (1-P)]} & \dfrac{bPh}{[\lambda_3 - (1-P)]\,[\lambda_3 - (1-p)\,h]} \\[2ex] \dfrac{g}{\lambda_3 - (1-P)} & 1 & \dfrac{bh}{\lambda_3 - (1-p)\,h} \\[2ex] \dfrac{pg}{[\lambda_3 - (1-P)]\,[\lambda_3 - (1-p)\,h]} & \dfrac{p}{\lambda_3 - (1-p)\,h} & \dfrac{bph}{[\lambda_3 - (1-p)\,h]^2} \end{pmatrix}$$

and

$$c_r = \left\{\frac{gP}{[\lambda_r - (1-p)]^2} + 1 + \frac{bph}{[\lambda_r - (1-p)\,h]^2}\right\}^{-1} \qquad r = 1, 2, 3 \tag{12}$$

Using the fact that

$$[G_1(k), G_2(k), B(k)] = (0, 0, 1)\,M^k$$

and

$$u(k) = G_1(k) + G_2(k) + B(k)$$

we obtain

$$G_1(k) = c_1\lambda_1^k \frac{pg}{[\lambda_1 - (1-P)]\,[\lambda_1 - (1-p)h]} + c_2\lambda_2^k \frac{pg}{[\lambda_2 - (1-P)]\,[\lambda_2 - (1-p)h]} + c_3\lambda_3^k \frac{pg}{[\lambda_3 - (1-P)]\,[\lambda_3 - (1-p)h]}$$

$$G_2(k) = c_1\lambda_1^k \frac{p}{\lambda_1 - (1-p)h} + c_2\lambda_2^k \frac{p}{\lambda_2 - (1-p)h} + c_3\lambda_3^k \frac{p}{\lambda_3 - (1-p)h}$$

$$B(k) = c_1\lambda_1^k \frac{bph}{[\lambda_1 - (1-p)h]^2} + c_2\lambda_2^k \frac{bph}{[\lambda_2 - (1-p)h]^2} + c_3\lambda_3^k \frac{bph}{[\lambda_3 - (1-p)h]^2}$$

and hence,

$$\begin{aligned} u(k) = {} & c_1\lambda_1^k \left\{\frac{pg}{[\lambda_1 - (1-P)]\,[\lambda_1 - (1-p)h]} + \frac{p}{\lambda_1 - (1-p)h} + \frac{bph}{[\lambda_1 - (1-p)h]^2}\right\} \\ & + c_2\lambda_2^k \left\{\frac{pg}{[\lambda_2 - (1-P)]\,[\lambda_2 - (1-p)h]} + \frac{p}{\lambda_2 - (1-p)h} + \frac{bph}{[\lambda_2 - (1-p)h]^2}\right\} \\ & + c_3\lambda_3^k \left\{\frac{pg}{[\lambda_3 - (1-P)]\,[\lambda_3 - (1-p)h]} + \frac{p}{\lambda_3 - (1-p)h} + \frac{bph}{[\lambda_3 - (1-p)h]^2}\right\} \end{aligned} \tag{13}$$

Next we find the autocorrelation of bit errors, denoted by $r(k), k = 1, 2, \cdots$. By definition then,

$$r(k) = P(z_k = 1 \mid z_0 = 1); \qquad k = 1, 2, \cdots$$

which is the probability of having an error at time k following a given initial error. The autocorrelation $r(k)$ measures the correlation of error positions, and it is useful for estimating significant error patterns.

Let

$$\begin{aligned} \bar{G}_1(k) &= P(s_k = G_1 \mid 1) \\ \bar{G}_2(k) &= P(s_k = G_2 \mid 1) \\ \bar{B}(k) &= P(s_k = B \mid 1) \end{aligned} \tag{14}$$

Then it follows that

$$r(k) = (1-h)\,\bar{B}(k)$$

To find $\bar{B}(k)$ we need the following facts:

$$\begin{aligned} \bar{B}(k+1) &= \bar{B}(k)\,q + \bar{G}_2(k)\,b \\ \bar{G}_2(k+1) &= \bar{G}_2(k)\,r + \bar{G}_1(k)\,P + \bar{B}(k)\,p \\ \bar{G}_1(k+1) &= \bar{G}_1(k)\,Q + \bar{G}_2(k)\,g \end{aligned} \tag{15}$$

which are easy to derive.

Here also, as in (8), we have

$$(\bar{G}_1(k+1), \bar{G}_2(k+1), \bar{B}(k+1)) = (\bar{G}_1(k), \bar{G}_2(k), \bar{B}(k))\,\bar{M}$$

where

$$\bar{M} = \begin{pmatrix} Q & P & 0 \\ g & r & b \\ 0 & p & q \end{pmatrix}$$

with

$$\bar{G}_1(0) = 0 = \bar{G}_2(0); \qquad \bar{B}(0) = 1$$

Hence,

$$(\bar{G}_1(k+1), \bar{G}_2(k+2), \bar{B}(k+1)) = (0, 0, 1)\,\bar{M}^{k+1} \tag{16}$$

In this case also, as in (8), we can use a computer to find the vector

$$(\bar{G}_1(k), \bar{G}_2(k), \bar{B}(k)); \qquad k = 1, 2, \cdots$$

But it is also valuable to give an explicit solution in terms of the model parameters by calculating M^k for any k. We shall do this in Section V.

The distribution of consecutive sequence of errors is easily obtained. For example, the probability of a sequence of k errors following a given error, $P(1^k \mid 1)$, is given by

$$P(1^k \mid 1) = (qh')^k$$

while the probability of k consecutive errors following a given good bit, $P(1^k \mid 0)$, is given by

$$P(1^k \mid 0) = bh'(qh')^{k-1} + (qh')^k; \qquad k = 1, 2, \cdots$$

IV. Capacity of the Channel

For estimating the maximal rate for which reliable transmission over the channel is possible, we shall find an

analytic expression for the capacity of the channel in terms of the model parameters.

Let H denote the entropy of the noise sequence $z = \{z_n\}$; then

Proposition 1

The capacity C of the burst-noise channel is given by

$$C = 1 - H$$

and

$$H = -\lim_{n\to\infty} \sum_{z_i = 0 \text{ or } 1} P(z_1, \cdots, z_{n+1}) \log P(z_{n+1} | z_1, \cdots, z_n) \tag{17}$$

Proof:

The proof is by classical information-theoretic arguments. The mutual information of the n-extension of the channel is

$$I(X^n, Y^n) = H(Y^n) - H(Y^n | X^n) \tag{18}$$

where $X(Y)$ is the input (output) and $H(\cdot)$ is the entropy function. The transmission rate is then

$$R = \lim_{n\to\infty} \frac{R(X^n, Y^n)}{n} \tag{19}$$

the capacity C is given by

$$\begin{aligned} C &= \max_{p(x)} R \\ &= \max_{p(x)} \lim_{n\to\infty} \left\{ \frac{H(Y^n)}{n} - \frac{H(Y^n|X^n)}{n} \right\} \end{aligned} \tag{20}$$

and $p(x)$ is an input distribution.

Now for additive noise—i.e., for $Y = X + Z$, Z the error sequence—we can easily show that

$$H(Y^n | X^n) = H(z_1, \cdots, z_n) \tag{21}$$

independent of X^n and that for $p(x_1, \cdots, x_n) = 2^{-n}$,

$$\frac{H(Y^n)}{n} = 1 \tag{22}$$

But

$$\frac{H(z_1, \cdots, z_n)}{n} = H(z_n | z_1, \cdots, z_{n-1})$$

So by Eqs. (20), (21), and (22), we have

$$\begin{aligned} C &= 1 - \lim_{n\to\infty} H(z_n | z_1, \cdots, z_{n-1}) \\ &= 1 - H \end{aligned} \tag{23}$$

where H denotes

$$\lim_{n\to\infty} H(z_n | z_1, \cdots, z_{n-1})$$

and

$$H(z_n | z_1, \cdots, z_{n-1}) = -\sum_{z_i = 0 \text{ or } 1} p(z_1, \cdots, z_n) \log p(z_n | z_1, \cdots, z_{n-1})$$

This completes the proof of Proposition 1.

We note that a uniformly distributed, zero-memory binary source achieves this capacity (Ref. 3).

Now let us write H as:

$$H = \lim_{n\to\infty} \sum_{\{z_1, \cdots, z_n\}} P(z_1, \cdots, z_n) h(z_1, \cdots, z_n)$$

with

$$h(z_1, \cdots, z_n) = -\sum_{z_{n+1} = 0 \text{ or } 1} P(z_{n+1} | z_1, \cdots, z_n) \log P(z_{n+1} | z_1, \cdots, z_n) \tag{24}$$

And if we assume that our model contains only one error state B, we can show easily (see Ref. 3) that $h(z_1, \cdots, z_n)$ can assume only $(n+1)$ values:

$$h(0^n), h(10^{n-1}), h(10^{n-2}), \cdots, h(10), h(1) \tag{25}$$

where $\{10^k\}$ is the event that an error is followed by k error-free bits. Using Eqs. (25) and (24), we have

$$H = \sum_{k=0}^{\infty} P(10^k) h(10^k) \tag{26}$$

In terms of $u(k)$ and $v(k)$ (see Eqs. 2 and 3), $P(10^k)$ can be written as

$$P(10^k) = P(1) u(k)$$

and hence,

$$P(0 | 10^k) = \frac{u(k+1)}{u(k)} \tag{27}$$

Equation (24) then becomes

$$h(10^k) = -\frac{u(k+1)}{u(k)}\log\frac{u(k+1)}{u(k)} - \left(1-\frac{u(k+1)}{u(k)}\right)\log\left(1-\frac{u(k+1)}{u(k)}\right) \tag{28}$$

Hence, by Eq. (26), H becomes

$$H = -P(1)\sum_{k=0}^{\infty} u(k)\left\{\frac{u(k+1)}{u(k)}\log\frac{u(k+1)}{u(k)} + \left(1-\frac{u(k+1)}{u(k)}\right)\log\left(1-\frac{u(k+1)}{u(k)}\right)\right\} \tag{29}$$

The entropy H can also be written in terms of $v(k)$, using the fact that

$$v(k) = u(k) - u(k+1)$$

We see from (26) that H then becomes

$$H = -P(1)\sum_{k=0}^{\infty} v(k)\log v(k) \tag{30}$$

For actual computations, however, it is convenient to use Eq. (29) because, as shown in (12),

$$u(k) = c_1\lambda_1^k + c_2\lambda_2^k + c_3\lambda_3^k \tag{31}$$

where c_1, c_2, c_3 are constants. And since $\lambda_1 < \lambda_2 < \lambda_3$, with λ_1 and λ_2 very much less than 1, we have

$$\frac{u(k+1)}{u(k)} \rightarrow \lambda_3 \tag{32}$$

By (29), then,

$$h(10^k) \rightarrow -\lambda_3\log\lambda_3 - (1-\lambda_3)\log(1-\lambda_3) = h_0, \text{ say} \tag{33}$$

The convergence in (32) is very fast. For example, for $P(1) = 4 \times 10^{-5}$, $h' = 0.5$, the transition probabilities are

$$p = 0.2, \qquad q = 0.8$$

$$b = 0.356, \qquad r = 0.002, \qquad g = 0.642$$

$$P = 0.0003, \qquad Q = 0.99997$$

and $[u(k+1)]/[u(k)] = 0.999991$ (to six decimal places) for $k \geqq 21$, while $\lambda_3 = 0.999989$.

Thus, in general the approximation $h(10^k) = h_0$ is good for all $k \geqq k_0$, some k_0 large enough. Therefore, using Eq. (33) in (29), we get

$$H = -P(1)\sum_{k=0}^{k_0-1} u(k)\left\{\frac{u(k+1)}{u(k)}\log\frac{u(k+1)}{u(k)} + \left(1-\frac{u(k+1)}{u(k)}\right)\log\left(1-\frac{u(k+1)}{u(k)}\right)\right\} + h_0P(1)\sum_{k=k_0}^{\infty} u(k) \tag{34}$$

But

$$P(1)\sum_{k=k_0}^{\infty} u(k) = \sum_{k=k_0}^{\infty} P(10^k) = 1 - \sum_{k=0}^{k_0-1} P(10^k) = 1 - P(1)\sum_{k=0}^{k_0-1} u(k)$$

Hence, the capacity of the channel is given by

$$C = 1 - H$$

$$\simeq 1 + P(1)\sum_{k=0}^{k_0-1} u(k)\left\{\frac{u(k+1)}{u(k)}\log\frac{u(k+1)}{u(k)} + \left(1-\frac{u(k+1)}{u(k)}\right)\log\left(1-\frac{u(k+1)}{u(k)}\right)\right\} - h_0\left[1 - P(1)\sum_{k=0}^{k_0-1} u(k)\right] \tag{35}$$

Comparison between the model capacity C and that of an equivalent binary symmetric channel C (BSC), for two sets of parameter values, is shown in Table 1.

V. Block Error Statistics

We turn now to computing the group of parameters which has the most direct application to block codes. Specifically, for estimating the performances of burst-correcting codes we find (A) the probability of getting an

error block; (B) the distribution of the number of errors in a block, denoted by $P(k,n)$; (C) the probability, denoted by $P_t(k,n)$, of k information-bit errors in n-information-bit word in an interleaved code with constant of interleaving t; (D) the distribution of symbol errors in an n-symbol word; and (E) the distribution of distances between extreme errors in a block.

A. Proportion of Blocks in Error

As in Ref. 5, let

$$TOU(n) = P(z_1 = \cdots = z_n = 0, s_n = U \mid s_0 = T); \quad U, T = B, G_1, G_2 \tag{36}$$

Thus, $TOU(n)$ is the probability, starting from a given initial state T, of having a gap of length n and ending at a final state U at time n. Then

$$\begin{aligned}
BOB(1) &= qh \\
BOG_2(1) &= p \\
BOG_1(1) &= 0 \\
G_2OB(1) &= bh \\
G_2OG_2(1) &= r \\
G_2OG_1(1) &= g \\
G_1OB(1) &= 0 \\
G_1OG_2(1) &= P \\
G_1OG_1(1) &= Q
\end{aligned}$$

and

$$\begin{aligned}
BOB(n) &= BOB(n-1)\,qh + BOG_2(n-1)\,bh \\
BOG_2(n) &= BOB(n-1)\,p + BOG_2(n-1)\,r \\
&\quad + BOG_1(n-1)\,P \\
BOG_1(n) &= BOG_2(n-1)\,g + BOG_1(n-1)\,Q \\
G_2OB(n) &= G_2OB(n-1)\,qh + G_2OG_2(n-1)\,bh \\
G_2OG_2(n) &= G_2OB(n-1)\,p + G_2OG_2(n-1)\,r \\
&\quad + G_2OG_1(n-1)\,P \\
G_2OG_1(n) &= G_2OG_2(n-1)\,g + G_2OG_1(n-1)\,Q \\
G_1OB(n) &= G_1OB(n-1)\,qh + G_1OG_2(n-1)\,bh \\
G_1OG_2(n) &= G_1OB(n-1)\,p + G_1OG_2(n-1)\,r \\
&\quad + G_1OG_1(n-1)\,P \\
G_1OG_1(n) &= G_1OG_2(n-1)\,g + G_1OG_1(n-1)\,Q
\end{aligned} \tag{37}$$

$$\begin{aligned}
P(z_1 = 0 = \cdots = z_n = 0) = {} & P(s_0 = B)\,[BOB(n) \\
&+ BOG_2(n) + BOG_1(n)] \\
&+ P(s_0 = G_2)\,[G_2OB(n) \\
&+ G_2OG_2(n) + G_2OG_1(n)] \\
&+ P(s_0 = G_1)\,[G_1OB(n) \\
&+ G_1OG_2(n) + G_1OG_1(n)]
\end{aligned}$$

and

$$P(\text{block error}) = 1 - P(z_1 = \cdots = z_n = 0) \tag{38}$$

B. $P(k,n)$

Following Ref. 5 again, let $TU(n,k) = P(k$ bit errors in n-bit words, $s_n = U \mid s_0 = T)$, which as before is the probability, given initial state T, of getting k errors in n-bit word and ending at a final state U. Then

$$\begin{aligned}
BB(1,0) &= BOB(1) = qh \\
BG_2(1,0) &= BOG_2(1) = p \\
BG_1(1,0) &= BOG_1(1) = 0 \\
G_2B(1,0) &= G_2OB(1) = bh \\
G_2G_2(1,0) &= G_2OG_2(1) = r \\
G_2G_1(1,0) &= G_2OG_1(1) = g \\
G_1B(1,0) &= G_1OB(1) = 0 \\
G_1G_2(1,0) &= G_1OG_2(1) = P \\
G_1G_1(1,0) &= G_1OG_1(1) = Q \\
BB(1,1) &= B1B(1) = qh' \\
BG_2(1,1) &= B1G_2(1) = 0 \\
BG_1(1,1) &= B1G_1(1) = 0 \\
G_2B(1,1) &= G_21B(1) = bh' \\
G_2G_2(1,1) &= G_21G_2(1) = 0 \\
G_2G_1(1,1) &= G_21G_1(1) = 0 \\
G_1B(1,1) &= G_11B(1) = 0 \\
G_1G_2(1,1) &= G_11G_2(1) = 0 \\
G_1G_1(1,1) &= G_11G_1(1) = 0
\end{aligned} \tag{39}$$

In general, for $k = 0, 1, \cdots, n$, we have

$$\begin{aligned}
BB(n,k) &= BB(n-1,k)\,qh + BG_2(n-1,k)\,bh \\
&\quad + BB(n-1,k-1)\,qh' \\
&\quad + BG_2(n-1,k-1)\,bh' \\
BG_2(n,k) &= BB(n-1,k)\,p + BG_2(n-1,k)\,r \\
&\quad + BG_1(n-1,k)\,P
\end{aligned}$$

$$BG_1(n,k) = BG_2(n-1,k)\,g + BG_1(n-1,k)\,Q$$

$$\begin{aligned} G_2B(n,k) &= G_2B(n-1,k)\,qh + G_2G_2(n-1,k)\,bh \\ &\quad + G_2B(n-1,k-1)\,qh' \\ &\quad + G_2G_2(n-1,k-1)\,bh' \end{aligned}$$

$$\begin{aligned} G_2G_2(n,k) &= G_2B(n-1,k)\,p + G_2G_2(n-1,k)\,r \\ &\quad + G_2G_1(n-1,k)\,P \end{aligned}$$

$$G_2G_1(n,k) = G_2G_2(n-1,k)\,g + G_2G_1(n-1,k)\,Q$$

$$G_1G_1(n,k) = G_1G_2(n-1,k)\,g + G_1G_1(n-1,k)\,Q$$

$$\begin{aligned} G_1B(n,k) &= G_1B(n-1,k)\,qh + G_1G_2(n-1,k)\,bh \\ &\quad + G_1B(n-1,k-1)\,qh' \\ &\quad + G_1G_2(n-1,k-1)\,bh' \end{aligned}$$

$$\begin{aligned} G_1G_2(n,k) &= G_1B(n-1,k)\,p + G_1G_2(n-1,k)\,r \\ &\quad + G_1G_1(n-1,k)\,P \end{aligned} \tag{40}$$

$$\begin{aligned} P(k \text{ errors in } n\text{-word}) &= P(s_0 = B)\,[BB(n,k) \\ &\quad + BG_2(n,k) + BG_1(n,k)] \\ &\quad + P(s_0 = G_2)\,[G_2B(n,k) \\ &\quad + G_2G_2(n,k) + G_2G_1(n,k)] \\ &\quad + P(s_0 = G_1)\,[G_1B(n,k) \\ &\quad + G_1G_2(n,k) + G_1G_1(n,k)] \end{aligned} \tag{41}$$

where $P(s_0 = B)$, $P(s_0 = G_2)$, $P(s_0 = G_1)$ are as given in (1).

C. Distribution of Symbol Errors

To find P(k-symbol errors in n-symbol word), in which we take a symbol to be in error if at least one of its m bits is in error, we note that the algorithm above works here also if we replace n by nm. We omit the details.

D. $P_t(k, n)$

It is clear that $P_t(k,n)$ is the same as the probability of getting k errors in a block of length tn on our channel sampled at every tth step. That is, if, as in (15), we put

$$\bar{M} = \begin{pmatrix} Q & P & 0 \\ g & r & b \\ 0 & p & q \end{pmatrix} \equiv \begin{pmatrix} 1-P & P & 0 \\ g & 1-g-b & b \\ 0 & p & 1-p \end{pmatrix} \tag{42}$$

to calculate $P_t(k,n)$, all we need is the t-step transition matrix $M^{(t)}$; we use the $M^{(t)}$ entries as our transitions instead of M and get $P_t(k,n)$ using the algorithm (Eqs. 39–41) which gave us $P(k,n)$.

By the method of Ref. 8 (p. 385) used in Section III, we get

$$\bar{M}^{(t)} = \frac{1}{pP + bP + pg} M_1 + \frac{1}{D_1}\left(\frac{2-A}{2}\right)^t M_2 + \frac{1}{D_2}\left(\frac{2-B}{2}\right)^t M_3$$

where

$$M_1 = \begin{pmatrix} pg & pP & bP \\ pg & pP & bP \\ pg & pP & bP \end{pmatrix}$$

$$M_2 = \begin{pmatrix} 4(2p-A)^2 Pg & 2(2p-A)^2(2P-A)\,P & 4(2P-A)(2p-A)\,bP \\ 2(2p-A)^2(2P-A)\,g & (2p-A)^2(2P-A)^2 & 2(2P-A)^2(2p-A)\,b \\ 4(2P-A)(2p-A)\,pg & 2(2P-A)^2(2p-A)\,p & 4(2P-A)^2 pb \end{pmatrix}$$

$$M_3 = \begin{pmatrix} 4(2p-B)^2 Pg & 2(2p-B)^2(2P-B)\,P & 4(2P-B)(2p-B)\,Pb \\ 2(2p-B)^2(2P-B)\,g & (2p-B)^2(2P-B)^2 & 2(2P-B)^2(2p-B)\,b \\ (2P-B)(2p-B)\,4pg & 2(2P-B)^2(2p-B)\,p & 4(2P-B)^2 pb \end{pmatrix}$$

$$D_1 = 4Pg\,[2p - A]^2 + (2P - A)^2 (2p - A)^2 + 4pb\,(2P - A)^2$$

$$D_2 = 4Pg\,[2p - B]^2 + (2P - B)^2 (2p - B)^2 + 4pb\,(2P - B)^2$$

$$A = X + \sqrt{X^2 - 4Y}$$

$$B = X - \sqrt{X^2 - 4Y}$$

$$X = P + p + g + b$$

$$Y = pP + bP + pg$$

For example, the $P(s_t = G_1 | s_1 = B)$ of being in state G_1 after t steps starting from state B is given by

$$P(s_t = G_1 | s_1 = B) = \frac{pg}{pg + pP + bP} + \frac{4(2P - A)(2p - A)}{D_1}\left(\frac{2 - A}{2}\right)^t + \frac{4(2P - B)(2p - B)}{D_2}\left(\frac{2 - B}{2}\right)^t$$

E. Distances Between Extreme Errors in a Block

Denote by P_k the probability of k bits between extreme errors in a block of length n, given there are at least two errors in the block. Then, by definition,

$$P_k = \frac{P\,(k \text{ bits between extreme errors and} \geqq 2 \text{ errors in the block}}{P\,(\geqq 2 \text{ errors in the block})}$$

By definition, the numerator is equal to

$$\sum_{x=0}^{N-k-2} P(0^x 1 \underset{k}{\leftrightarrow} 10^y); \qquad y = N - k - 2 - x$$

$$= \sum_{x=0}^{N-k-2} P(0^x 1)\, P(z_{k+1} = 1 | z_0 = 1)\, P(0^y | 0^x 1 \underset{k}{\leftrightarrow} 1)$$

$$= \sum_{x=0}^{N-k-2} P(0^x 1)\, r(k+1)\, P(0^y | 1)$$

$$= P(1)\, r(k+1) \sum_{x=0}^{N-k-2} P(0^x | 1)\, P(0^{N-k-2-x} | 1)$$

$$= P(1)\, r(k+1) \sum_{x=0}^{N-k-2} u(x)\, u(N - k - 2 - x)$$

where we have used the fact that

$$u(x) = P(0^x | 1) \text{ and } u(N - k - x - 2) = P(0^{N-k-2-x} | 1)$$

for which expressions in terms of the model parameters were found in Section III.

Also,

$$(P \geqq 2 \text{ errors in block}) = 1 - P(0, n) - P(1, n)$$

Hence,

$$P_k = \frac{P(1)\, r(k+1) \sum_{x=0}^{N-k-2} u(x)\, u(N - k - 2 - x)}{1 - P(0, n) - P(1, n)} \tag{43}$$

VI. The Burst Statistics

A. Distribution of Burst Lengths

We start with the distribution of burst lengths. Denote the guardspace by $\mathcal{G}$ and the probability of a burst of length n, for $n = 1, 2, \cdots$, by $L(n)$. Then, by definition, it follows that

$$L(n) = \sum_{k=0}^{\min(\mathcal{G}-1,\, n-2)} P(0^k 10^l 10^m 1 \cdots 10^t | 1) \tag{44}$$

over all $l, m, \cdots$, such that

$$0 \leqq l, m, \cdots, \leqq \mathcal{G} - 1$$
$$t \geqq \mathcal{G} \tag{45}$$

and

$$0^k 10^l 10^m 1 \cdots\cdots 10^t$$

is a sequence of $(n - 1) + t$ bits.

Proposition 2

$$L(n) = \begin{cases} 0; & n \leqq 0 \\ u(\mathcal{G}) = P(0^{\mathcal{G}} | 1); & n = 1 \\ \displaystyle\sum_{k=0}^{\min(\mathcal{G}-1, n-2)} v(k) L(n-k-1); & n \geqq 2 \end{cases} \tag{46}$$

Proof:

Equation (46) is almost obvious by inspection, but let us sketch a proof. Let us note first that

(1) $L(0) = 0$

(2) $L(1) = P(0^{\mathcal{G}} | 1) = u(\mathcal{G})$

since a burst *must* start with an error, implying that the least length a burst can have is 1.

From Eq. (44),

$$L(n) = \sum_{k=0}^{\min(\mathcal{G}-1, n-2)} P(0^k 10^l 10^m 1 \cdots 10^t | 1); \qquad t \geqq \mathcal{G}$$

$$= \sum_{k \geqq 0} P(0^k 1 | 1) P\{0^l 10^m 1 \cdots 10^t | 1\} \tag{47}$$

But

$$P\{0^l 10^m 1 \cdots 10^t | 1\} = L(n-k-1)$$

and

$$P(0^k 1 | 1) = v(k)$$

Now substitute these expressions in Eq. (47) to obtain (46).

B. Distribution of Errors Within a Burst

The last parameter of interest is the distribution of errors within a burst of a given length: P (k errors in a burst of length N). We state this in the following proposition.

Proposition 3

$$P(k \text{ errors in a given burst of length } N) = \frac{Q(k, N)}{L(N)}$$

where

$$Q(k, N) = \begin{cases} 0 \text{ if } 0 = k = N; \text{ or } 0 \leqq k \leqq 1, N \geqq 2; \text{ or } k > N \\ u(\mathcal{G}) = P(0^{\mathcal{G}} | 1) \qquad \text{if } N = k = 1 \\ \displaystyle\sum_{x=0}^{\min(\mathcal{G}-1, n-k)} v(x) Q(k-1, N-x-1); \\ \qquad 2 \leqq k \leqq N \end{cases} \tag{48}$$

Here $Q(k, N)$ is the probability of getting a burst of length N that contains k errors.

Proof:

$$P(k \text{ errors in a given burst of length } N) = \frac{P(\text{burst of length } N \text{ with } k \text{ errors})}{P(\text{burst of length } N)} \tag{49}$$

Write the numerator as $Q(k, N)$. Then, by definition of a burst,

$$\begin{aligned} &Q(0,0) = 0 \\ &Q(k, N) = 0 \quad \text{for} \quad 0 \leqq k \leqq 1, N \geqq 2; \quad \text{or} \quad k > N \\ &Q(1,1) = P(0^{\mathcal{G}} | 1) = u(\mathcal{G}) \end{aligned} \tag{50}$$

Now, for $2 \leqq k \leqq N$,

$$Q(k, N) = P\{0^x \underbrace{1^y 1 \cdots 10^t}_{N-1} | 1\}$$

where the $(N-1)$ bits indicated contain $(k-1)$ errors, $0 \leqq x, y \cdots \leqq \mathcal{G} - 1; \quad t \geqq \mathcal{G}$. Hence,

$$\begin{aligned} Q(k, N) &= \sum_{x=0}^{\min(\mathcal{G}-1, n-k)} P(0^x \underbrace{10^y 1 \cdots 10^t}_{N-1} | 1) \\ &= \sum_{x=0}^{\min(\mathcal{G}-1, n-k)} P(0^x 1 | 1) P\{\underbrace{0^y 1 \cdots 10^t}_{N-x-2} | 1\} \end{aligned} \tag{51}$$

$$0 \leqq y \cdots \leqq \min(\mathcal{G} - 1, N - x - k); \qquad t \geqq \mathcal{G}$$

and the $(N - x - 2)$ bits indicated contain $(k - 2)$ errors.

Therefore,

$$Q(k,N) = \sum_{x=0}^{\min(\mathcal{G}-1,\, n-k)} v(x)\, Q(k-1, N-x-1) \qquad (52)$$

Since P (burst of length n) $= L(N)$, the proposition is proved.

VII. Conclusion

The empirical counterparts of all the probabilities are now being computed. A more detailed analysis of this model, including recommendations as to the optimal error-detecting and -correcting codes to be employed on the channel, will be contained in a more detailed report in preparation.

References

1. McClure, J. P., "GCF 50-kbps Wideband Data Error Rate Test," in *The Deep Space Network Progress Report*, Technical Report 32-1526, Vol. VI, pp. 149–151, Jet Propulsion Laboratory, Pasadena, Calif., Dec. 15, 1971.
2. McClure, J. P., "Madrid-to-JPL 50-kbit/s Wideband Error Statistics," in *The Deep Space Network Progress Report,* Technical Report 32-1526, Vol. IX, pp. 177–180, Jet Propulsion Laboratory, Pasadena, Calif., June 15, 1972.
3. Gilbert, E. N., "Capacity of a Burst-Noise Channel," *Bell Sys. Tech. J.*, Vol. 39, 1960, pp. 1253–1265.
4. Elliott, E. O., "Estimates of Error Rates for Codes on Burst-Noise Channels," *Bell Sys. Tech. J.*, Vol. 42, 1963, pp. 1977–1997.
5. Berkovits, S., Cohen, E. L., and Zierler, N., *A Model for Digital Error Distribution*, Tech. Memo, Mitre Corporation, Bedford, Mass.
6. Stern, Daniel C., *Statistical Analysis of Errors Occurring in the Transmission of High-Speed Digital Data,* Master's Thesis, Dept. of EE., University of Maryland, 1970.
7. Sussman, S. M., "Communication Channel Attributes as Related to Error Control," IEEE Annual Communications Convention, 1965, pp. 5–13.
8. Feller, W., *An Introduction to Problem Theory and its Application,* Vol. I, 2nd ed., John Wiley, New York, 1959.

Table 1. Comparison between capacity of model and that of equivalent BSC

Model parameters	C	C (BSC)	$\frac{C\,(\mathrm{BSC})}{C}$
$P(1) = 4 \times 10^{-5}, h' = 0.5$ $p = 0.20, q = 0.80$ $b = 0.356, r = 0.21 \times 10^{-2}$ $g = 1 - b - r$ $P = 0.289 \times 10^{-4}$ $Q = 0.9999711$	0.999831	0.999551	0.9970
$P(1) = 0.2$ $p = 0.25; q = 0.75$ $b = 0.205$ $r = 0.699$ $P = 0.1511$ $Q = .8489$	0.56007	0.499598	0.8920

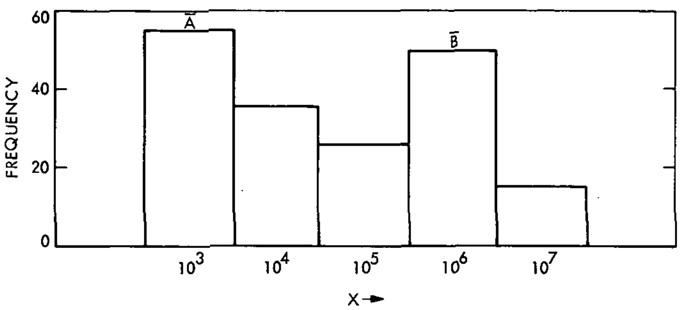

Fig. 1. Histogram for gap distribution

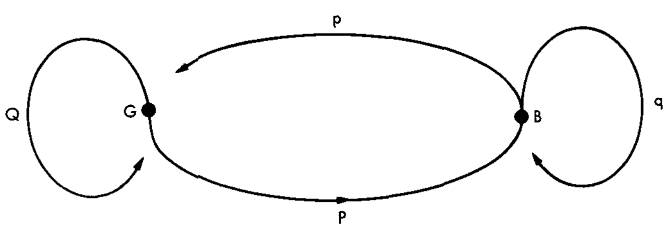

Fig. 2. Gilbert model

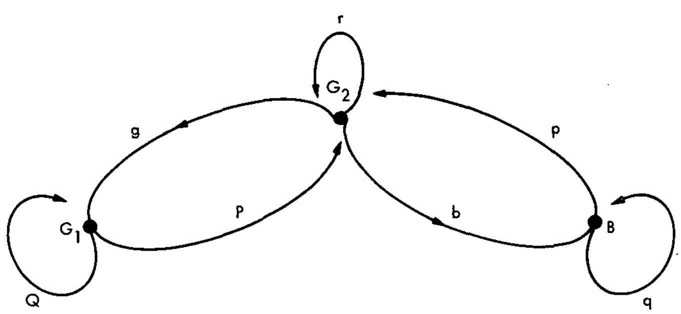

Fig. 3. Transition diagram for the Markov model

A Myopic View of Computer-Based System Design

J. W. Layland and C. C. Klimasauskas
Communications Systems Research Section

This article presents one approach to the economical allocation of resources in a complex logical system. The main goal is the understanding of systems that may involve specialized digital hardware, a computer with software, and possibly a specialized microcode within the computer processor. These components are treated as uniformly characterizable options in the design of the system that will ultimately be used.

I. Overview

In this article we present our approach to the economical allocation of resources in a complex logical system. A computer is one example of such a system, but our main goal will be the understanding of systems that may involve specialized digital hardware, a computer with software, and possibly specialized microcode for the extension of the capabilities of the computer itself. It is our intention to consider these components as uniformly characterizable options in the design of the system we will ultimately use.

The system to be designed must be represented in some unambiguous fashion in terms of a set of primitive operations. The logical n-input NAND gate is sufficient to build all systems, and in fact, is one of the alternate bases for the complexity work of Savage (Ref. 1). However, to provide a foothold for resource-allocation trade-offs, we must represent our system with a cascade of higher-level primitives, and evaluate the effect of implementing the higher-level primitives with resources of varying cost and performance. For concreteness of example, we will take our highest-level primitives to be the arithmetic and logical operators of a typical medium-scale computer, and consider several purely computational tasks as our system to be implemented.

Each primitive operator on the highest level must be implemented in some low-level operator, with the lowest-level logical operators being gates. Each can be constructed directly in the lowest level (built-in hardware) or

constructed from some intermediate-level primitive (programmed from primitives of a lower level). For all its apparent mystique, microprogramming is nothing more nor less than the programming of the machine-language-level primitive operators in terms of some lower-level set of primitives. The microprogram memory is usually higher speed than the main memory of the computer, and it is frequently read-only. Our options thus include direct construction of the primitive operators in hardware and programmed implementation in memory of various speeds and costs. The relative benefit of each type of implementation for the various primitives depends strongly upon how other primitives are implemented.

If the number of options being considered can be restricted to a relatively small number, as would occur in evaluating off-the-shelf options for a commercial computer, then an ad hoc graphical comparison can be used to evaluate them. Examples of this nature will be developed in a later section. For most real-life problems, the number of options involved will be too large to handle manually, so we expect at some future date to formulate the allocation techniques we are developing into a form suitable for solution by nonlinear mathematical programming methods.

II. Motivation

We can find motivation for our investigations in almost all aspects of computer-oriented activities today. High central processing unit (CPU) utilization is regarded as the ideal in most general purpose computer installations, and it is sought after by increasing memory to allow for multiprogramming, requiring an expanded operating system, and additional resources of other types, perhaps including a faster CPU. Is this economically sensible? To answer that, we need to know the true shape of the performance vs cost curve for computer processors. "Grosch's Law," which contends that performance is proportional to the square of the cost, is approximately valid for the IBM System/360 (Ref. 2, pg. 525), but thus may be evidence of an IBM marketing strategy and not a technical phenomenon. Minicomputers appear to violate that "law," either because of real wiggles in the performance vs complexity curves, or because they are more rapidly making use of developments in component technology. We should know which in order to plan intelligently for the future.

High utilization alone does not make for efficient use of resources. For almost any computer extant we could synthesize a job or job-stream that would almost totally occupy the CPU time and available memory space and yet very poorly utilize these resources. As an easy example, perform error-correcting code analysis or decoding on a processor with very high-speed (an expensive) floating point arithmetic operators, and without effective bit-manipulating operators. Here, a significant part of the CPU is left idle, even though the CPU itself is not. This same CPU-part will also be (mostly) idle whenever our computer is doing text editing, program compilation or assembly, and many other jobs that computers do.

TYMNET, the communications network of the TYMESHARE corporation, utilizes Varian 620i minicomputers for message concentrators and terminal controllers (Ref. 3). Data on the low-speed asynchronous communication lines to terminals are sampled on a bit-by-bit basis, and packed by software into characters (typically 8-bits). The hardware needed to interface the computer to the communication circuitry is minimized this way, but the computer moves many (18-bit) words about to enter each bit of data. Was this the economical choice? Or could they have more economically added character-assembly buffers to the communications interface hardware? Well-formulated questions such as this one can be answered directly in terms of dollars.

In the Deep Space Stations, minicomputers perform many tasks with responsibility shared with external hardware. In handling down-link telemetry, for example, computers do low-speed bit synchronization, control high-speed bit synchronizers, control block decoders, and perform (via microprogram) sequential decoding. In each case a choice must be made to partition between external equipment and software. We wish to develop criteria to guide that trade-off, and will describe some initial steps toward that goal in this article.

III. System Representation and Optimization

The first step toward an optimizing solution of a problem is the complete and unambiguous description of that problem. This is no less true in the allocation of computational resources. Most, if not all, of the computer-based systems of greatest interest are finite state machines (FSMs); or, more precisely, are *collections* of FSMs. Examples range from an Antenna Position Control Subsystem to a communications switching computer, to the operating system of a general purpose computer, to a dedicated on-line reservation system. No programming language in general use today admits a concise description of an FSM, although both high-level algebraic languages and machine-assembly languages have been

used to implement these systems. Direct FSM representation has long been used in the processing of languages (Ref. 4), and has been recently applied to communications processing (Ref. 5). There is for now, however, no clear standard language that could be used to describe both hardware and software implementation of general FSMs.

Suppose that a system under development has been described as an FSM, and that steps toward its implementation are underway. In this process, the system would be broken down into simpler, more primitive machines. These second-level machines are themselves further segmented, until a stage is reached where the direct implementation of the lowest-level machines in hardware, or in any of the myriad of programming languages, is a semitrivial exercise. In short, the system is subjected to a top-down design (Ref. 6) – not in terms of a subroutine hierarchy for an anticipated programmed implementation, but in terms of an implementation-independent FSM representation.

Given a complete description of the system as reduced to this primitive level, it should be a straightforward task to determine how total system performance depends upon the performance of each of the lowest-level submachines. And we can determine the performance and cost of each of these lowest-level machines for each of the three likely implementations: hardware, software executed from computer main memory, and software executed from high-speed memory (microcode). The implementation pattern over all primitive submachines that yields lowest system cost can be determined from these inputs by a straightforward but possibly long computational process. What will happen in this process is that those primitive submachines that most affect total system performance will be implemented in the fastest, most expensive fashion, and those primitives that little affect total performance will be implemented in the slowest, cheapest fashion.

Once the implementation mode of the lowest-level machines has been determined, those machines on the next-to-lowest level must be examined. Any of these for which the constituent submachines are implemented in hardware should probably also be implemented in hardware or microcode, but this can be ascertained by the same sort of computations that established the implementation mode of the lowest-level submachines. This type of examination should be carried through all levels of the system representation, assigning an implementation to each as it progresses.

The degree of optimality of the completed system depends upon the way in which it is modularized, or broken into its constituent submachines. Modularization is a difficult and, even if well understood, not a well documented process (Refs. 6 and 7). From the designer's viewpoint, the best criterion appears to be understandability. This may or may not be a good criterion from the standpoint of system performance, but we expect that performance is not critically dependent upon the specific modularization selected. A poor modularization will at worst prevent the suboptimized restricted problem from closely approaching the true optimum. However, refusal to modularize the system will present the optimizer with a massive, unmanageable problem.

The process we have just described is similar to the tuning process that is frequently applied to working software modules. In tuning software, the software module is instrumented to determine where it spends the majority of its time, and that region subjected to an intense optimization effort. Tuning has been defended on the basis that it is difficult to know before software is implemented where the most critical areas are. We believe that those critical areas will be quite obvious during the course of design using an implementation-independent representation, and that the additional flexibility that exists before implementation will yield a much superior result from the attempted optimization.

Virtual memory systems (Ref. 8) and systems using a high-speed buffer or cache (Ref. 9) attempt to perform automatically an optimization process similar to what we have described. In each, the main memory is a relatively slow, relatively inexpensive memory. Data are moved from main memory to the expensive high-performance memory in blocks, so that most accesses to memory can be satisfied by accesses to the fast unit, only rarely requiring that data be moved between levels of memory. In theory, at least, the more critical parts of the software reside permanently in the fast memory, while the remainder is only transiently in the fast memory, and hence executes more slowly due to the time required to access it in main memory.

We do not have a well-defined FSM representation technique, so for a concrete example of the evaluation and trade-off methods just discussed, we turn in the next section to an area where we have a complete representation – working software modules – and evaluate implementation alternatives for the "primitive submachines", represented by the machine instructions.

IV. Computer Processor Evaluation/Design

A method of computer performance evaluation known as the "instruction mix" method (Ref. 10) compares computer processors on the basis of the execution times for the instructions that are used most heavily in the jobs that the computer is to perform. This is not a widely accepted method because it ignores all of the subtleties of input/output queuing, memory usage, and all features of the vendor-supplied software that interface the typical user to his machine. These objections can mostly be waived if the job to be done is in process control where the computers are small and their operating system minimal or nonexistent. The user's problem-solving machine is then built almost directly from the machine instructions.

The user's system must in any case be built from the base computer's instruction set, whether it is built directly overall, or partially indirectly via instructions interpreted by an operating system. The computer instructions form the lowest-level primitive operator that is readily visible. We can determine the relative importance of the various instructions with respect to any specific task by tracing the execution of working software that performs this task. A companion article by Klimasauskas describes the interpretive tracing program that we used to gather data (Ref. 11). The program runs on the Xerox Sigma 5, so all data are specifically relevant to that computer and its software.

Execution data have been gathered on the instruction usage of three different types of software: the FORTRAN IV compiler, the on-line text EDITor, and user programs written in FORTRAN. The FORTRAN IV compiler was probed initially to determine how sensitive its instruction usage was to the statement types being compiled. Sensitivity was found to be very small – a few percent – which meant that we could realistically identify the instruction usage of a "typical" compilation. Figure 1 is a bar graph of the selected "typical' 'compilation data. Each column of Fig. 1 corresponds to one of the Sigma instructions, and the mnemonic (Ref. 12) for the associated instruction is written vertically beneath the column. Height of the column of asterisks is proportional to the percentage usage of that instruction on a logarithmic scale. The character "=" on the bottom line designates unused instructions, and "#" designates usage below 1%. By way of example, load immediate (LI) is the first instruction on the graph, and it accounts for about 2.4% of the total instruction executions.

EDIT proved to be a less stable subject, perhaps due to the greater diversity of services provided to the user. The "typical" instruction usage depends upon the user statistics, which we have neither the facility nor the real need to measure. Our need for exemplary material is satisfied by considering the extremes of EDIT instruction usage that are shown in Fig. 2a and 2b.

A set of user-written programs could obviously show a great variability. To avoid either a massive statistics-gathering project or extensive arguments relative to what constitutes a typical user job or mix of jobs, we arbitrarily selected matrix inversion as being one identifiable user task that occurs frequently enough to be worthy of investigation. We traced the inversion of matrices of varying dimensions from 2×2 to 100×100. The dependence of the total floating-point instruction usage relative to total instructions is shown in Fig. 3. The detailed instruction usage summary graph appears as Fig. 4 for the inversion of the largest matrix.

It is a relatively easy matter to go from the statistics of the sort shown in Figs. 1 to 4, plus published execution times of the Sigma 5 instructions (Ref. 12) to an effective execution time for that computer relative to the task to which the statistics apply. This effective execution time is proportional to the cost of performing that particular task on that computer. We can evaluate processor options, such as floating-point hardware vs software floating-point simulators, using this cost-indicator. With slightly more effort we can determine an effective execution time for other processors by first determining what instructions or sequences of instructions on the processor being considered perform the same functions for the program as each of the Sigma instructions used. The individual instruction execution times so devised then determine the effective execution time for the processor. This process has been carried out for the Digital Equipment Corporation PDP-11, and on several IBM processors. The result of this is shown in Table 1.

The processor itself is only one of the cost-contributing elements of a computer. Both main memory and input/output equipment usually cost far more than the CPU. The performance of the CPU, however, determines how much time the entire system is occupied by a specific task, except when that task is I/O-bound, or executing at a rate constrained by one or more pieces of external equipment. We shall assume in the following that the tasks of interest are not I/O-bound, and in fact, that cost involved in the external equipment is not of interest. Memory cost is of interest, and since we do not have a

good characterization for memory requirements, memory size is treated as a free parameter. Our specific comparisons will be between the PDP-11/20 and the Sigma 5 with various processor options. We will assume a fixed cost, say 1 unit per 8×10^3 bytes, for the main memory of these computers, and normalize all other item costs to this figure. (We believe that the difference in memory prices established by the manufacturers is an indicator of overall technological advance during the period between the design of the computers.) If we assume that the relative costs of CPU and memory depends predominantly on CPU architecture and complexity, and little upon the technology-base for construction and the manufacturer's marketing strategy, then normalization to a nominal memory cost allows direct cost-wise comparison of the CPU complexities. The relative cost figures for the components of each of the computers have been derived from the manufacturers advertised prices, and are only approximate. The modifications to our work to perform true cost evaluation of various computers from quoted prices and to include peripheral equipment costs would be routine.

We assume that the computers of interest will be uniprogrammed. Multiprogramming has no advantage unless at least some of the tasks to be performed are I/O-bound, and for this article at least, we wish to avoid the queuing intricacies that arise there. For each task, the computer is totally occupied by it from start to finish. The cost of performing that task is simply the cost of the computer configuration, times the execution time of the task, divided by the total lifetime of the equipment. Lifetime is assumed to be the same for all equipment. Since we are comparing units rather than estimating exact costs, we can normalize execution times by the execution time of one of the configurations. The effective execution time for the task and processor is then used for the time the task occupies the processor. Since the configuration cost is a straight-line function of the memory size allocated, the task execution cost is also a straight-line function of memory size. Table 2 lists the configurations considered, together with the relevant cost parameters. Figure 5 shows the relative costs of executing the matrix inversion task for these configurations, and Fig. 6 shows the relative cost of executing the FORTRAN compiler. Minimum cost for all configurations occurs at zero memory, but this is illusory because no work could be accomplished without some minimum memory allocated. For large memory sizes, the cost of the processor is significantly below that of the memory. Hence, more complex processors with faster execution times become increasingly economical with increasing memory size.

V. A Computer Design Exercise

It is a conceptually easy step to go from evaluation of computer processors to investigating the design of one. In designing a computer, we must be aware that it is not the computer per se that we are interested in, but it is in fact the economical implementation and operation of the users machine that is to be built using the computer and possibly other components. Let us suppose that the machine under design is to perform a known specific task and that we have reduced that task to an intermediate-level machine representation called the Sigma Instruction Set. In this form, the remaining system design is equivalent to the design of a Sigma-like computer that has been optimized for the specific task at hand.

There are many options available in this design. As one extreme, we could build a separate hard-wired machine to perform the operations of each of the Sigma instructions. As the other extreme we could build a very simple machine and make it interpret the Sigma instructions. If the simple machine program (the control program) were stored in a fast read-only memory, this would be a typical microprogramming situation. The control program could be stored in read-only memory, or in read-write memory of varying speeds and costs. In this environment, optimization consists of determining which parts of the control program belong in which type of memory.

A wide range of intermediate configurations is possible. A machine might be able to directly execute a basic subset of the Sigma instructions, but trap to an interpreting control program for the more complex instructions. The obvious basic subset would include a LOad, STore, Shift-by-one, and the ADD, SUBtract, logical AND, logical OR, and logical Exclusive OR available in a single medium-scale integration (MSI) logical array. This base machine could have the indexing and indirect addressing operations of the Sigma, but it need not as these could be made available in the same fashion as the more complex instructions. The set of primitive operators of the system has in this case been implemented in so simple a fashion that we believe little or no manipulation of its cost and performance is possible. Optimization is to be performed by varying the memory type to which each segment of the control program is to be allocated. But we also have the option of implementing some of the other instructions directly in hardware, or adding non-Sigma instructions that would make interpretation of the more complex Sigma instructions easier and faster.

We can write the control program to interpret the complex Sigma instructions without knowing what type of memory it will be executed from. The control program does depend upon instructions that are added to the base machine, but mostly these represent replacement of parts of the control program by hardware features. The greatest effort is thus involved with developing the Sigma instructions from the basic machine. In today's market, there are essentially three memory technologies that could readily be considered: core ($\sim$ 1 μs), MOS semiconductor (0.5 μs), and Bipolar semiconductor (0.1 to 0.3 μs). The cost of these on a per-bit basis is monotone-increasing with speed. In implementing 100 instructions, we have 3^{100} options out of which to select the optimum. We would not wish to compute through this space many times because of iterations in the base machine structure, nor would we be able to compute through it even once without some sensitive heuristic to reduce its effective dimensionality.

Let us label the instruction set as $\{I_i\}_{i=1}^n$, and denote as p_i the usage probability for instruction I_i within some user's task of interest. The program to implement I_i sequences through s_i steps in the control memory. This parameter s_i depends only upon the operation performed by I_i, and not upon the implementation chosen. Let the control memory segment for I_i be implemented from components with step-time t_i, where t_i in the above paragraph can have any one of three values. The cost-per-step is known to be a function of t_i; call it $c(t_i)$. The total cost of the submachine that implements instruction I_i is thus $s_i \cdot c(t_i)$. The net execution time for I_i is $max\ \{1, s_i \cdot t_i\}$, where the 1 represents the time necessary to fetch an I_i from the computer's main memory.

For convenience, we will let both the step-time and the per-unit cost of the main memory be unity, and normalize other items appropriately. Let B be the normalized cost of the base machine, and M_u be the number of units (and cost) of the main memory assigned to the end user. Then the total cost of our processor is

$$B + M_u + \sum_{i=1}^{n} s_i \cdot c(t_i)$$

The effective execution time is

$$\sum_{i=1}^{n} p_i \cdot max\ \{s_i \cdot t_i, 1\}$$

The net normalized cost of a job is proportional to the product of these two

$$C_{eff} = \left(\sum_{i=1}^{n} p_i \cdot max\ \{s_i \cdot t_i, 1\}\right)\left(B + M_u + \sum_{i=1}^{n} s_i \cdot c(t_i)\right) \tag{1}$$

The memory allocation, that is, the choice of t_i, which minimizes C_{eff} is the sought-for optimum. The allocation, of course, depends on the assumed cost function c.

At this point, let us approximate our real problem with an easily solvable one. Assume first that the unity minimum on the execution time of I_i can be ignored. This means either that the instructions are all longer than that minimum, or that we have interposed a cache or buffer memory between main memory and CPU. Assume second that there is a continuum of memory speeds available, instead of the above three, and approximate the cost function by $c(t) \approx t^{-\beta}$ for some power β. (This is not unlike current pricing with $\beta \approx 1.5$.) By optimizing in this fashion, we risk finding a t_i either above or below the accessible range; both extremes suggest that reorganization of the base machine is necessary. Differentiating C_{eff} with respect to each of the t_i's produces

$$\frac{\partial}{\partial t_j} C_{eff} = 0, \qquad \text{so}$$

$$\frac{p_j s_j t_j}{\sum_{i=1}^{n} p_i s_i t_i} = \beta \frac{s_j t_j^{-\beta}}{B + M_u + \sum_{i=1}^{n} s_i t_i^{-\beta}} \tag{2}$$

We can derive several conclusions by manipulating Eq. (2). By summing over j, we see that the optimum occurs when

$$\sum_{i=1}^{n} s_i t_i^{-\beta} = \frac{1}{\beta - 1} (B + M_u) \tag{3}$$

which means that the total machine control cost is proportional to total costs of base machine and main memory. If Eq. (3) is inserted into Eq. (2), we see that the optimum occurs when

$$\frac{p_j s_j t_j}{\sum_{i=1}^{n} p_i s_i t_i} = \frac{s_j t_j^{-\beta}}{\sum_{i=1}^{n} s_i t_i^{-\beta}} \tag{4}$$

or in words: when the fraction of total time spent in I_j is equal to the fraction of total instruction-building costs expended on I_j. We can in fact reduce Eqs. (3) and (4) to show that

$$t_j = \left(\frac{(\beta - 1) \sum_{i=1}^{n} s_i \left(\frac{p_i}{p_j} \right)^{\beta/(\beta+1)}}{B + M_u} \right)^{1/\beta} \tag{5}$$

Establishing allocations from Eq. (5) is far easier than numerically minimizing Eq. (1), but we must still interpret these results in terms of the real-world problem. If any of the t_j are significantly outside of the range covered by current technology, we should revise the overall design by adding or deleting instructions from the base machine, then recheck the allocation of control memory. It may also happen that the overall performance of the resultant machine is inadequate to fulfill some external requirement, or is too fast and is always waiting for something to do. We can accommodate these factors within Eq. (5) by pretending that M_u is larger or smaller than anticipated. We should also, at this point, return to the basic design and question whether M_u was properly estimated in the first place, since the selected figure produced unrealistic results when applied to the processor design. Once all t_j are within the technically feasible range, they can be approximated by the nearest available step-time, and the result used as a starting value for the numerical minimization of Eq. (1).

The initial steps of this process have been performed for a fully microprogrammed implementation of the Sigma instructions used by the FORTRAN compiler. The base machine was assumed to have logic for segmenting the Sigma instructions into their constituent fields, basic arithmetic/logical instructions, plus a shift by 2^n instruction class, and test/add/shift combination instructions for facilitating multiplies and divides. Figure 7 shows the pertinent parameters that result from the application of Eq. (5) to this task. Most of the control-program memory times were close together and within the feasible range. However, the multiply and divide operations had relatively long memory times, indicating that, for this job at least, they were constrained more by memory cost than execution time. Most likely, the combination instructions added to speed up the multiply/divide operations should be deleted from the base machine, and replaced by a conditional jump, which saves storage at the expense of time. Neither this iteration, nor the next step of assigning allowed memory times to the instruction control memory have yet been performed.

VI. Where We Are Now

It should be clear at this point that we could continue almost forever with design examples of processor and memory structures. The design exercise initiated in Section V could of itself consume several months of effort. We are not at the moment prepared to expend that effort on that particular example.

The viewpoint we have developed for the efficiency characterization of computer processors is a slight refinement of the instruction-mix method (Ref. 10) for computer performance evaluation. It is a useful tool for the evaluation of computer processor options, and a tractable measuring device for an end-use-oriented optimization of processor design.

Although the work presented here has been specifically processor oriented, the general results obtained have turned out to be functions of the memory allocated to the user's process: the optimized processor cost is proportional to the user's memory cost. Thus, a way is needed to characterize the memory required in the performance of user tasks. Given that characterization, we should be able to optimize operations with the user's memory in much the same way as we have attempted here for the control memory.

We are also as yet unable to say anything about economy-of-scale in computer systems. Again, we need a characterization of memory requirements, and possibly other parameters to permit us to estimate the overall performance vs overall cost relationship. In addition, we may need to investigate the behavior of I/O boundedness; queuing; and multiprogramming as they relate to the synchronization of real-time events, such as those that exist within a DSN tracking station, with computational events within a controlling computer.

Finally, we believe that future progress along the path initiated here depends upon the development of a system description technique, such as the Finite State Machine representation discussed in Section II, that will allow a significant portion of the system design process to be performed without prior commitment to hardware, firmware, or software for implementation. Both computer assembly languages and current high-level algebraic languages correspond to implementation languages, rather than description languages, when applied to systems instead of to calculation problems.

References

1. Savage, J. E., "A Collection of Results on Computational Complexity", in *Supporting Research and Advanced Development*, Space Programs Summary 37-65, Vol. II, pp. 42-47, Jet Propulsion Laboratory, Pasadena, Calif., Sept. 30, 1970.

2. Bell, C. G., and Newell, A., *Computer Structures; Readings and Examples,* Part 6, Section 3, McGraw-Hill Book Company, New York, N.Y., 1971.

3. Beere, M. P., and Sullivan, N. C., "Tymnet – A Serendipitous Evolution," *IEEE Transactions on Communications Technology*, Vol. COM-20, N.3, p. 511-515, June 1972.

4. Gries, D., *Compiler Construction for Digital Computers* (especially Chap. 3) John Wiley & Sons, New York, N.Y., 1971. (NB: this reference is a modern entry to a wealth of past literature, part of which is specifically referenced in paragraph 3.6.)

5. Birke, D. M., "State Transition Programming Techniques and Their Use in Producing Teleprocessing Device Control Programs," *IEEE Transactions on Communications Technology*, Vol. COM-20, No. 3, p. 569-575, June 1972.

6. *Software Engineering*, Edited by P. Naur and B. Randell, NATO Science Committee Conference Report, Jan. 1969.

7. Parnas, D. L., *On the Criterion to be used in Decomposing Systems into Modules*, Carnegie-Mellon University Report – CMU-CS-71-101, Aug. 1971.

8. Denning, P., "Virtual Memory," *Computing Surveys*, Vol. 2, No. 3, pp. 153-189, Sept. 1970.

9. Conti, C. J., "Concepts for Buffer Storage," *IEEE Computer Group News*, pp. 9-13, Mar. 1969.

10. Lucas, H. C., "Performance Evaluation and Monitoring," *Computing Surveys*, Vol. 3, No. 3, pp. 79-91, Sept. 1971.

11. Klimasauskas, C. C., "An Execution Analyzer for the Sigma 5 Computer," *The Deep Space Network Progress Report*, Volume XII, pp. 176-188, Jet Propulsion Laboratory, Pasadena, Calif., Dec. 15, 1972.

12. *XDS Sigma 5 Computer Reference Manual*, Xerox Publication #90-09-59D, Feb. 1970.

Table 1. Computer configuration speed comparison

Computer item	FORTRAN compiling time	Matrix inverse time
Sigma 5 with floating hardware	1.0	1.0
Basic Sigma 5 CPU	1.0	9.7
Basic PDP-11/20 CPU	2.7	16.0
PDP-11/20 with floating hardware	2.7	2.9
IBM 360/44	2.0	1.7
370/135	1.6	1.7
360/65	0.66	0.54
370/155	0.40	0.34
360/85	0.15	0.09

Table 2. Computer configuration cost comparison

Computer item	Normalized cost
8×10^3 bytes of storage	1.0
Basic PDP-11/20 CPU	1.6
PDP-11/20 with floating-point hardware	4.3
Basic Sigma 5 CPU	7.8
Sigma 5 with floating-point hardware	10.5

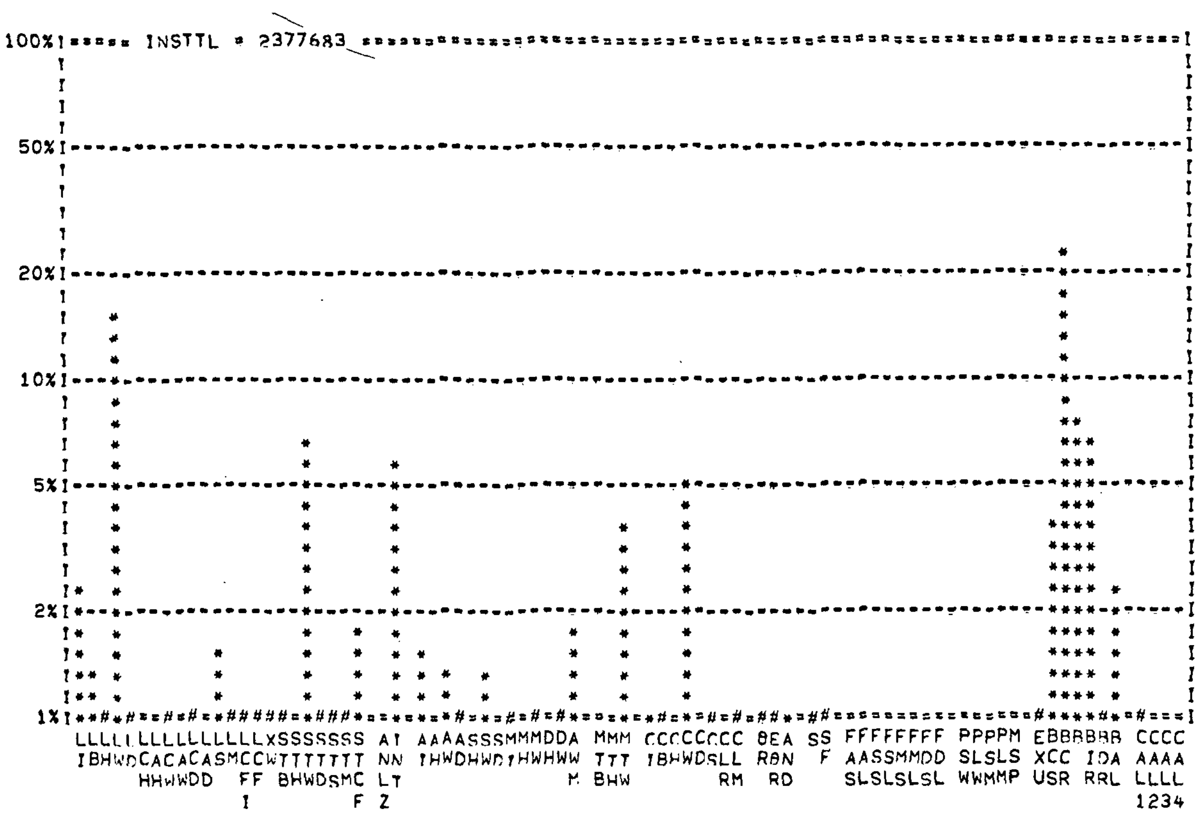

Fig. 1. Instruction usage of typical compilation

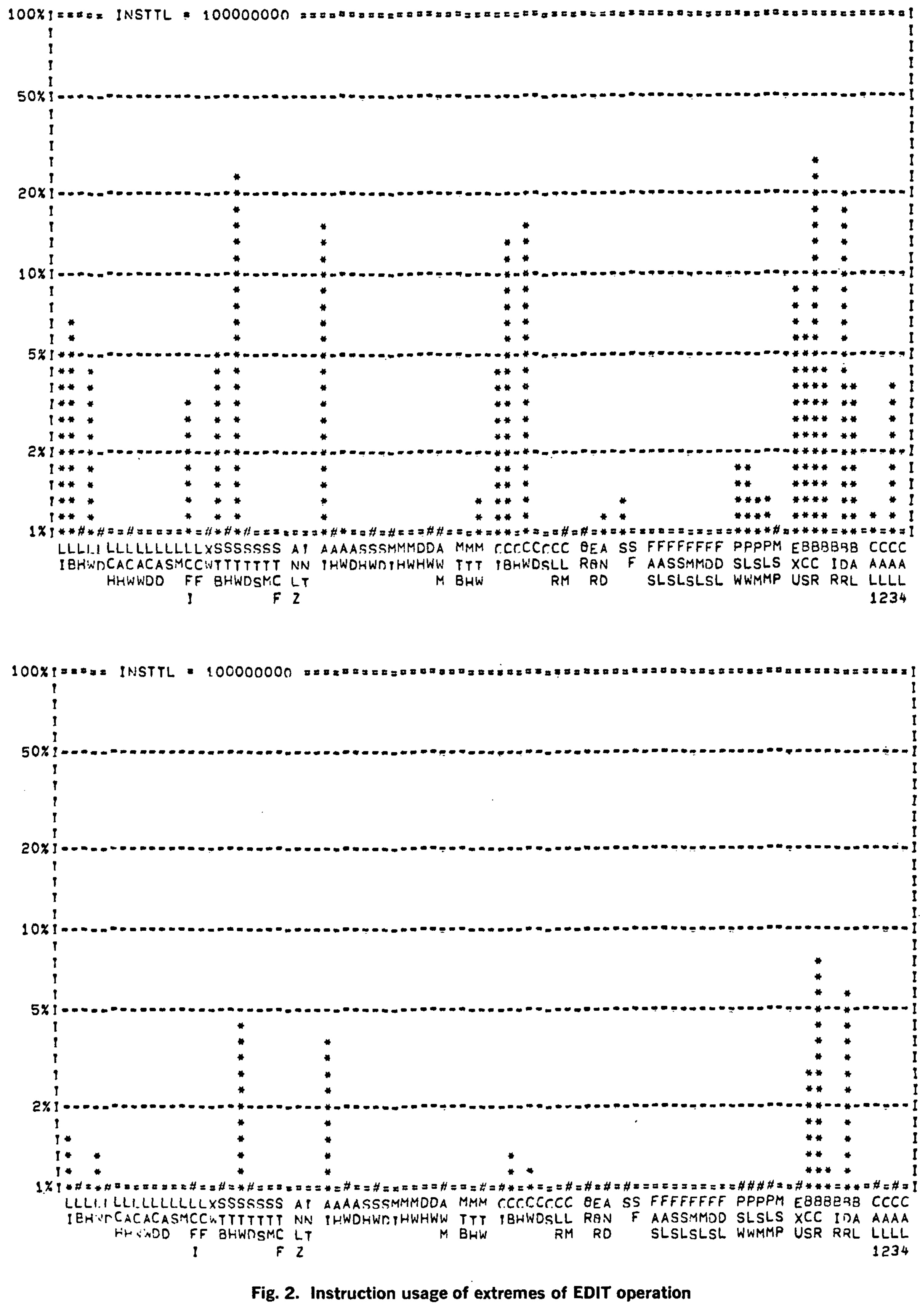

Fig. 2. Instruction usage of extremes of EDIT operation

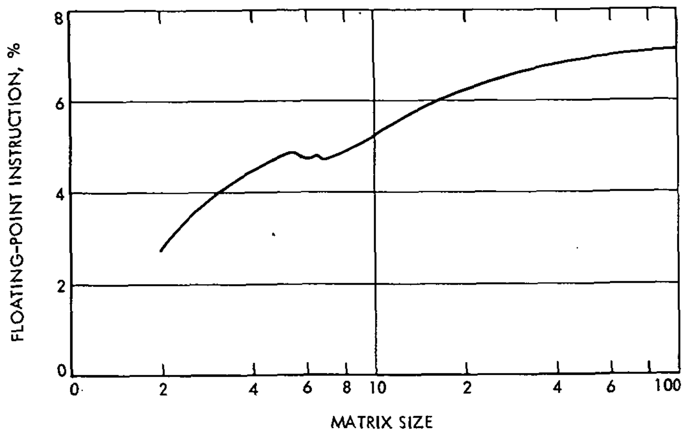

Fig. 3. Usage of floating point instructions in matrix inversion

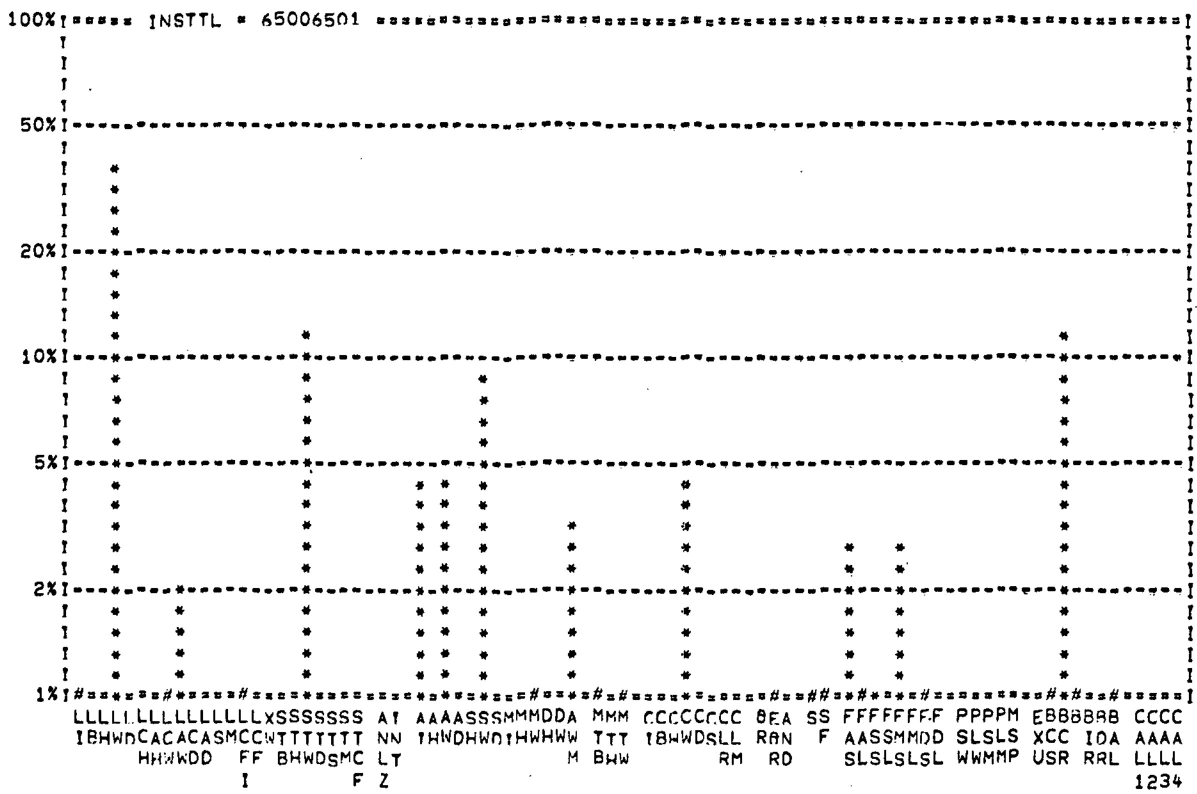

Fig. 4. Instruction usage of matrix inversion, $n = 100$

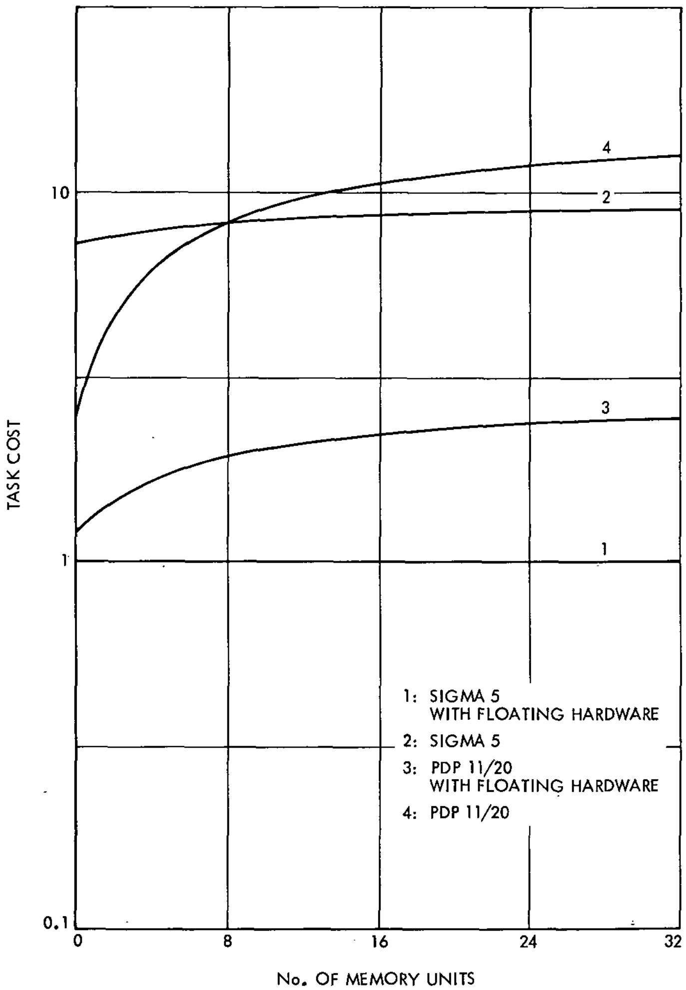

Fig. 5. Relative cost of executing matrix inversion

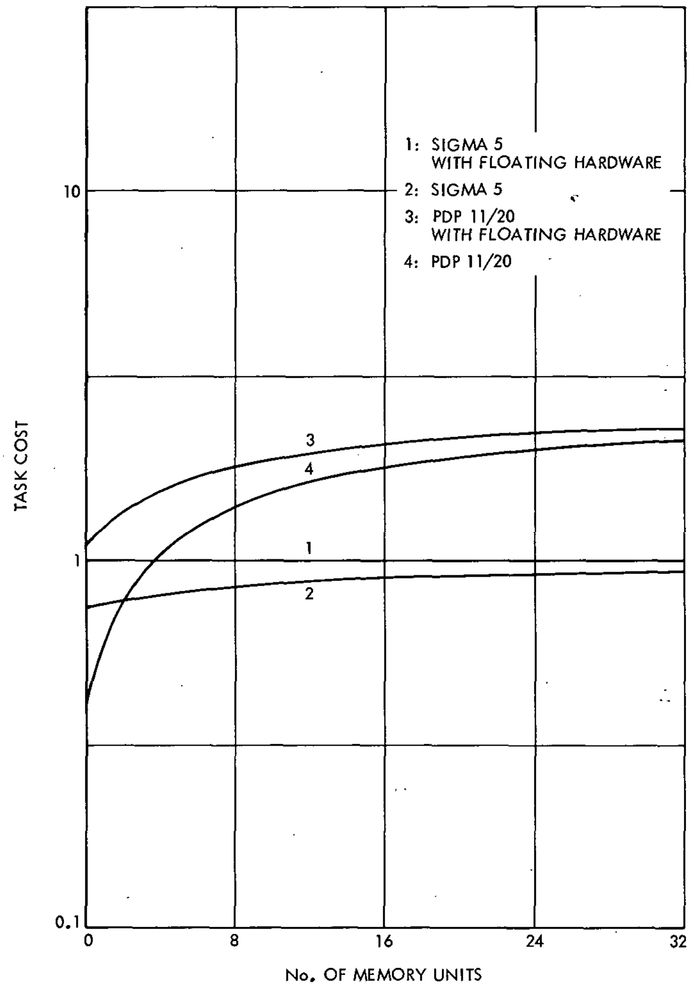

Fig. 6. Relative cost of FORTRAN compilation

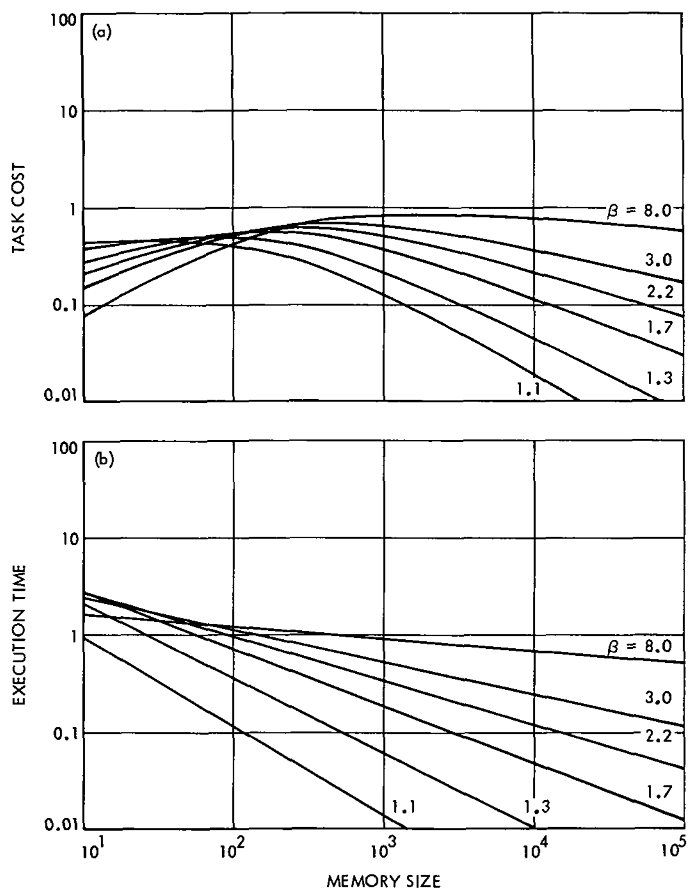

Fig. 7. Performance parameters of hypothetical machine: (a) C = 1: control memory of same speed as main; (b) T = 1: control memory of same speed as main

Optimum Control Logic for Successive Approximation Analog-to-Digital Converters

T. O. Anderson
Communications Systems Research Section

Optimum control logic is a popular subject with designers and manufacturers of high-resolution high-speed low-cost modular analog-to-digital converters of the successive approximation type which are found in abundance in today's module market. Also, with miniaturization being a strong consideration, it may not be long before the complete control logic will be available in a single medium-scale integrated circuit chip. The designs described here may be a strong contender for such chips. One novelty of the designs presented here is found in their optimum logic and in their minimum component count, considering presently available components. Another novelty is that they are modular or iterative, i.e., the logic structure is the same for all bits. A high-resolution converter logic is then simply an extension of the logic for a low-resolution converter.

I. Introduction

This article describes another step in DSN analog-to-digital converter development that provides possible circuits for large-scale integrated circuit (LSI) production which would make the analog-to-digital converters (ADCs) more attractive as to cost, size, power, etc. This would make the Deep Space Station data acquisition and preprocessing system designs more attractive. Optimum design is first qualified in terms of minimum logic and component count for implementation. Because of the rapidly advancing medium-scale integrated circuit (MSI) technology, component count is referenced to the present state of development.

The most common design strategies are discussed in general. Two fundamentally different schemes are elaborated on, and for each one of these, several different logic designs are described in detail. The designs presented here are logically simpler and their component count smaller than those most commonly found. Of special interest in these designs is the fact that they are

modular or iterative, i.e., the logic structure is the same for all bits. A high-resolution converter logic is then simply an extension of the logic for a low-resolution converter.

II. Qualification of the Optimum Claim

The claim for these circuits to be optimum, speed of operation being equal or notwithstanding, refers to the total involvement of their implementation. Due to the rapidly decreasing cost of MSI/LSI circuits and due to presently emerging high-speed versions of complex low-power metal-oxide semiconductor (MOS) circuits, the optimum claim also refers to the present state of the art of component technology. The circuits presented here are logically minimum and, in combination with a selective choice of presently available components, should be safely claimed to be optimum.

III. Successive Approximation Logic

The operation in successive approximation logic is well known. It is, in fact, self-evident: the most common operational strategy is as follows: A flip-flop FF1 is set at clock time t_0. It contributes its particular weight to a summing bus, which is one input term to a comparator amplifier. The other is the analog signal to be converted. The output of the comparator amplifier becomes the control bus which determines whether the FF1 shall remain set or whether it shall be reset at t_1. At t_1 the next most significant flip-flop FF2 is set and the same simple procedure is repeated. Any FF is operable for only two clock pulses per conversion cycle which proves to be a useful observation in deriving a design strategy for optimum implementation.

To set a FF and then again reset it if its weight contribution was too large appears at a first consideration to be cumbersome. A design was explored in which a sequencer functioned as a trial-register and a final register was set only if the trial was affirmative. This design, however, required an OR function between the two registers and, therefore, was abandoned as less than optimum, even though its reasoning appeared attractive.

IV. Two Fundamentally Different Designs

One consists of one sequencer and one code register, and the other consists of a single set of FFs connected so as to simultaneously function both as sequencer and code register, referred to in the following as sequencer/code register design.

V. Sequencer and Register Design No. 1

Figure 1 is a logic diagram of one of the most commonly used sequencer and code register designs. This connection is very simple and straightforward.

The sequencer is a shift register which is initially reset for each conversion cycle and shifts as "1" through the register. An output from the sequencer sets a FF in the code register through its DC set input. The output from the FF that is being set is then used as a clock for conditional reset of the previous FF. The control bus is the data input to all code register FFs.

Shown in Fig. 2 are some additional connections, for example, how to conditionally turn off the code register FF for the least-significant bit (LSB). One additional FF in the sequencer is used. This FF is also used in the CONTINUOUS MODE/MANUAL MODE mechanism. In the manual mode its output is used to control the clock enable gate. As the last FF turns on, it inhibits the clock, and the sequencer "hangs up" until manually reset through the manual start signal. In the continuous mode the turn on of the last FF will automatically reset the sequencer and a new conversion cycle will start automatically. The last FF will then also turn itself off. With present components designed for high-speed of operation, this type of connection can easily be made to operate reliably with very little delay or energy storage in the reset line.

The component count for the design discussed above can be reduced as the price for MSI serial in-parallel out (SIPO) shift register packages decreases. Typical shift register packages presently available that would be applicable are 74164, which is an 8-bit SIPO, and 8273, which is a 10-bit SIPO shift register.

VI. Sequencer and Register Design No. 2

In the design discussed above, the conditional turn-off of a FF in the code register is clocked by the secondary effect of the succeeding FF that is turning on. This mechanism then exhibits a slight but unnecessary delay when considering the connection shown in Fig. 3. This is also a simple connection and it works as follows: as the output from the sequencer turns on a code register FF,

the same output from the sequencer turns off the preceeding FF. As shown in the figure, the Q output from the sequencer will DC set a code register FF while the positive transition of the Q output from the same stage of the sequencer provides the clock for the conditional turn-off of the preceeding code register FF.

VII. Sequencer and Register Design No. 3

As mentioned previously, each FF in the code register is set and conditionally reset once per conversion cycle. This reasoning suggests a scheme in which the outputs from the sequencer are two-pulse outputs used as clock terms for code register FFs of the J/K type. The first pulse will set and the second will conditionally reset the FF. For a maximum speed of operation, the second pulse of one output should coincide with the first pulse of the succeeding output. Figure 4 is a logic diagram of such a connection.

The sequencer is simply a shift register which is initially reset to 11000 . . . 00 and shifted right. The shift clock is a common term in the output enable gates. This connection assures overlapping double pulse outputs. Figure 5 shows the truth table for the sequencer outputs.

VIII. Maximum Speed Sequencer

The sequencers described in the previous three designs have been designed as shift registers where a single '1' or '1' have been shifted through a register from a reset condition. The shift occurs on a transition of the shift clock which then must be a pulse train with pulses of a certain duration occuring at a certain rep rate. At higher speeds the clock then looks like a square wave of a certain symmetry. At maximum speed the clock may be an entirely symmetrical square wave.

If one would operate every other stage in such a shift register on the complement of the clock square wave, as shown in Fig. 6, a '1' (or any other preset pattern) would travel through the register at twice the rate it would if all stages operated on the same clock. The code output from any one tap would overlap that of the preceding stage with half a clock period. For distinctive nonoverlapping pulse outputs, the output should be enabled with the clock to that stage as shown in Fig. 6.

A timing chart for this connection is shown in Fig. 7. A single '1' is considered propagating through the register. The general scheme of fast propagation of successive approximation logic described here for a sequencer is also valid for designs where a single set of FFs simultaneously functions both as sequencer and code register.

IX. Sequencer/Register Design No. 1

The sequencer/register expression implies that a single set of FFs is connected so as to simultaneously function both as a sequencer and a code register. The design strategy is as follows:

With all FFs reset their zero condition is serially AND-ed in a series of AND gates from the least significant to the most significant, from right to left as shown in Fig. 8.

A shift "1" connection from the most significant bit to the least significant bit from left to right is easily identifiable.

In Fig. 8 the clock is common to all FFs; however, for maximum speed, every other stage may be operated on the complement of the clock as described above. The turn-off term is also common and so is the control bus, the output from the comparator amplifier. Both the turn-on and turn-off terms for each FF are controlled by the AND-ed zero condition for all the bits of lesser significance.

J/K FFs with 2 term AND functions for both the J and the K inputs such as SN 74105 are used.

The operation is as follows: All FFs are reset. On the next clock pulse the most significant FF will set, since it is the only one that has a true input. The control bus is not true; even if it were, the first FF would still set, since it is a J/K FF. On the next clock pulse the first FF will conditionally reset. The second FF will set because the first FF is set and provides a true input. All other FFs are reset and provide the enable term through the series AND gates. Once the second FF is set, both inputs to the first FF are entirely disconnected for the remainder of the conversion cycle. On the third clock pulse the second FF may turn off but the third FF will turn on and disconnect both the first and the second FFs. Each FF is then enabled or operative for exactly two clock pulses.

Of special interest is the fact that the series propagation of the all-zero condition, through a series of AND-

gates, occurs between conversion cycles at which time the analog circuits must be allowed the settling time for zero to full-scale excursion. During the conversion cycle the gates are then settled and in a "waiting" condition.

Because of pin limitation, a 16-pin dual in-line package (DIP) can accommodate only a single J/F FF with two enable terms for each input. This makes the chip count for this connection somewhat less than optimum. A slight modification will improve this condition.

X. Sequencer/Register Design No. 2

The component count can be reduced if one uses a simpler FF of which there are two per package. This connection then requires external gates. Two J/K FFs are available in one 16-pin DIP; for example, SN7476. Four 2-input gates are contained in one 16-pin DIP; for example, SN7408.

A simple design which will decrease the component count is shown in Fig. 9. The basic strategy of series propagating of the all-zero condition as discussed in the previous case is maintained. The enable term operates on a single gate for each FF. This gate is then the clock gate. In the previous case the J/K inputs were enabled for two clock pulses. In this case the J/K inputs are never disconnected, only the clock gates are enabled for two clock pulses each.

XI. Conclusion

Because of the large number of systems in the DSN using analog-digital-analog conversion, the subject of optimum logic for a successive approximation analog-to-digital conversion is important. This article has given examples of logic which are presently used as well as examples which are not used presently. Two basic types have been discussed, one with a sequencer and a code register as two separately distinguishable items and one where a single set of FFs is connected through auxiliary gates to simultaneously function both as a sequencer and a register. Auxiliary control logic is suggested as well as a connection for speeding up the conversion cycle. Components are suggested but not specified.

The purpose of this article is then to provide guidance for the design of DSN standard analog-to-digital converter modules rather than to provide an absolute or rigid detail design. Also, the article can provide a first step in the design and layout of a single LSI component as a DSN standard analog-to-digital conversion module. Such a module is expected to be more important in future DSIF systems as more and higher frequency operations become digitized.

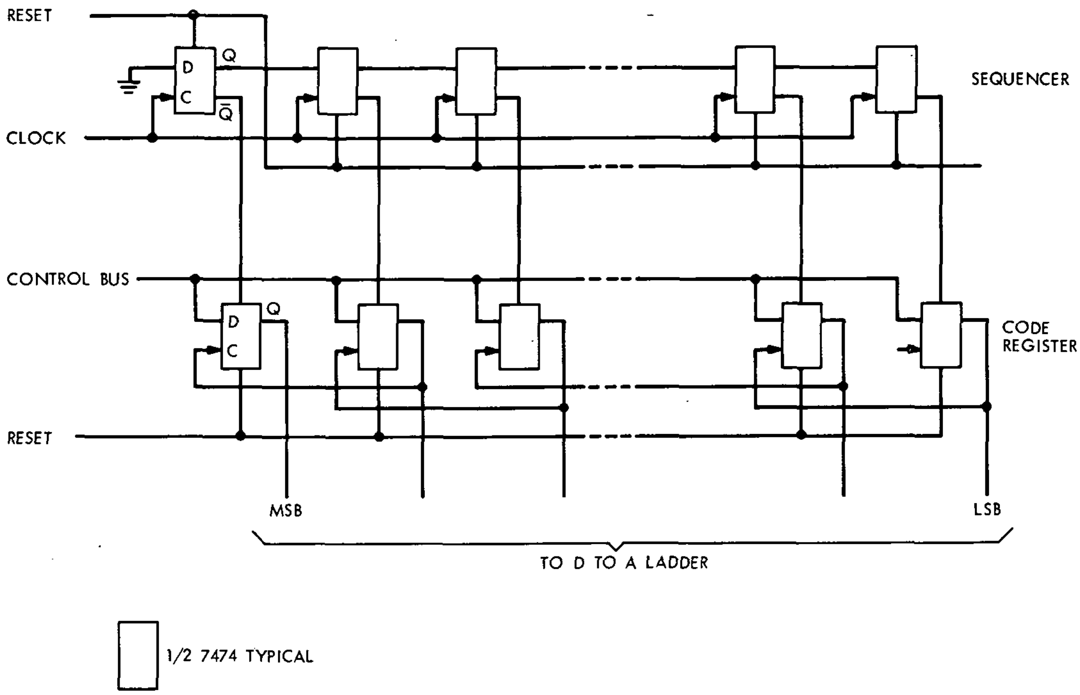

Fig. 1. Sequencer and code register with conditional secondary effect turn-off of code register FFs

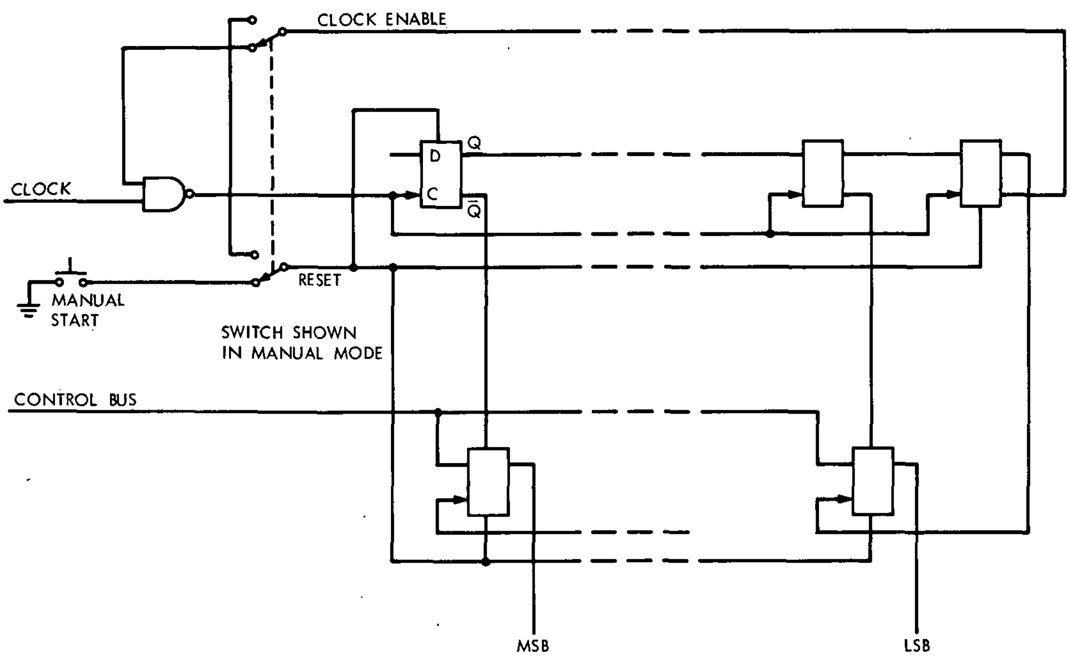

Fig. 2. Continuous or external start conversion control logic

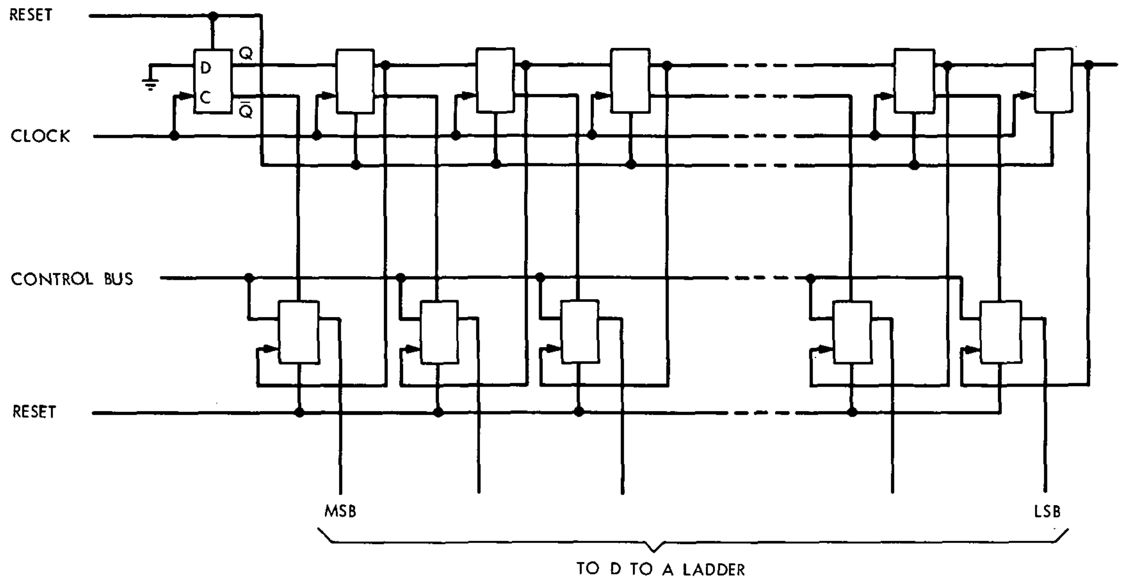

Fig. 3. Sequencer and code register with conditional direct sequencer turn-off of code register FFs

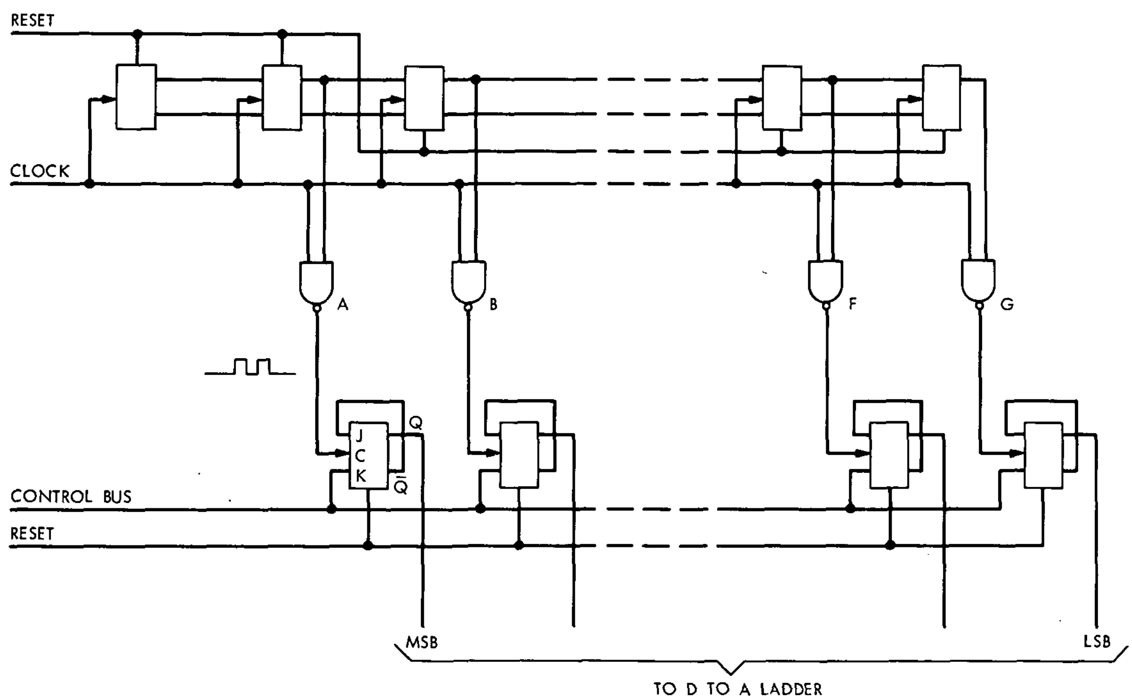

Fig. 4. Overlapping double pulse sequencer and simple J/K code register

A	B	C	D	E	F	G	H
1	1	0	0	0	0	0	0
0	1	1	0	0	0	0	0
0	0	1	1	0	0	0	0
0	0	0	1	1	0	0	0
0	0	0	0	1	1	0	0
0	0	0	0	0	1	1	0
0	0	0	0	0	0	1	1
0	0	0	0	0	0	0	1

Fig. 5. Overlapping double pulse sequencer truth table

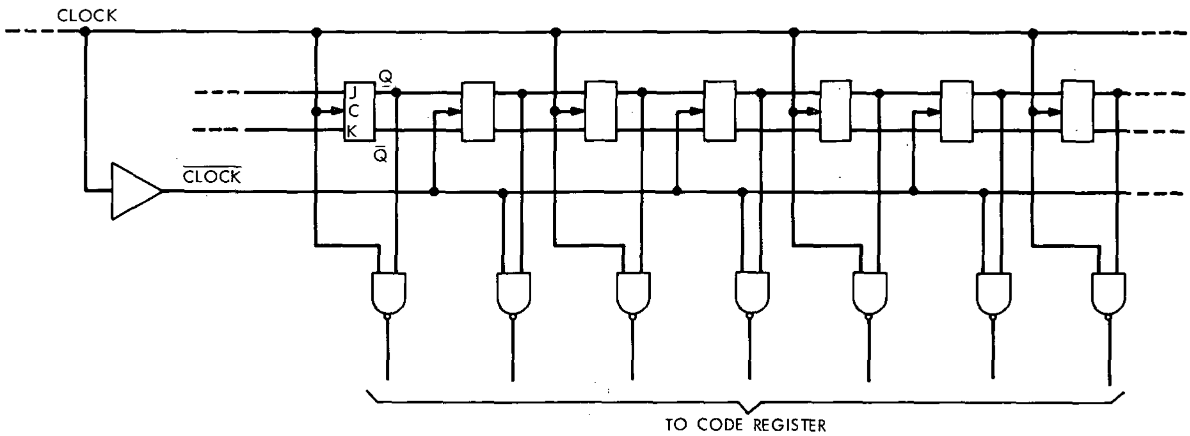

Fig. 6. Maximum speed sequencer connection using alternating true and complement clock phase

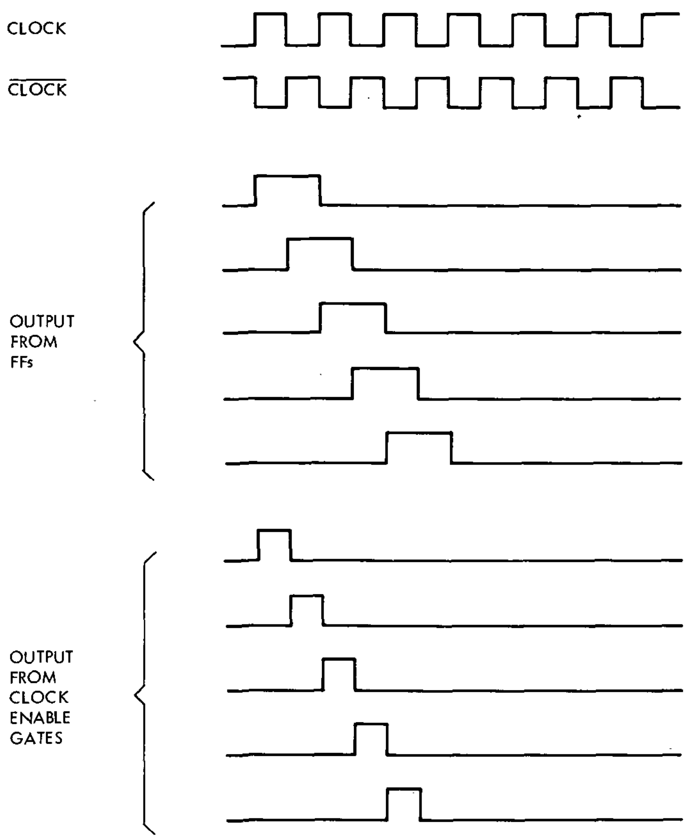

Fig. 7. Timing chart for maximum speed sequencer connection

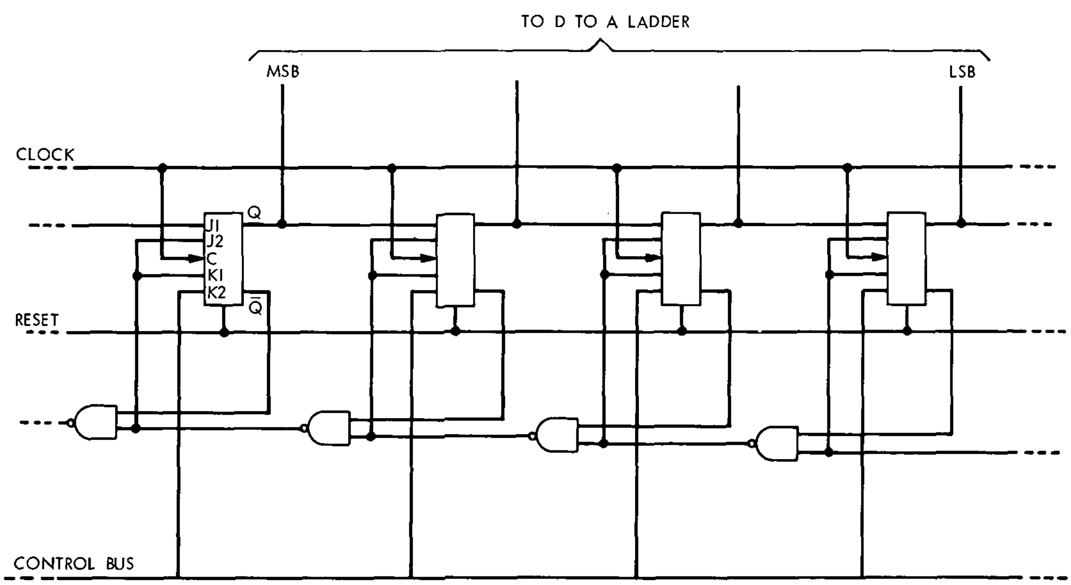

Fig. 8. Sequencer and code register using a single set of J/K FFs plus steering gates

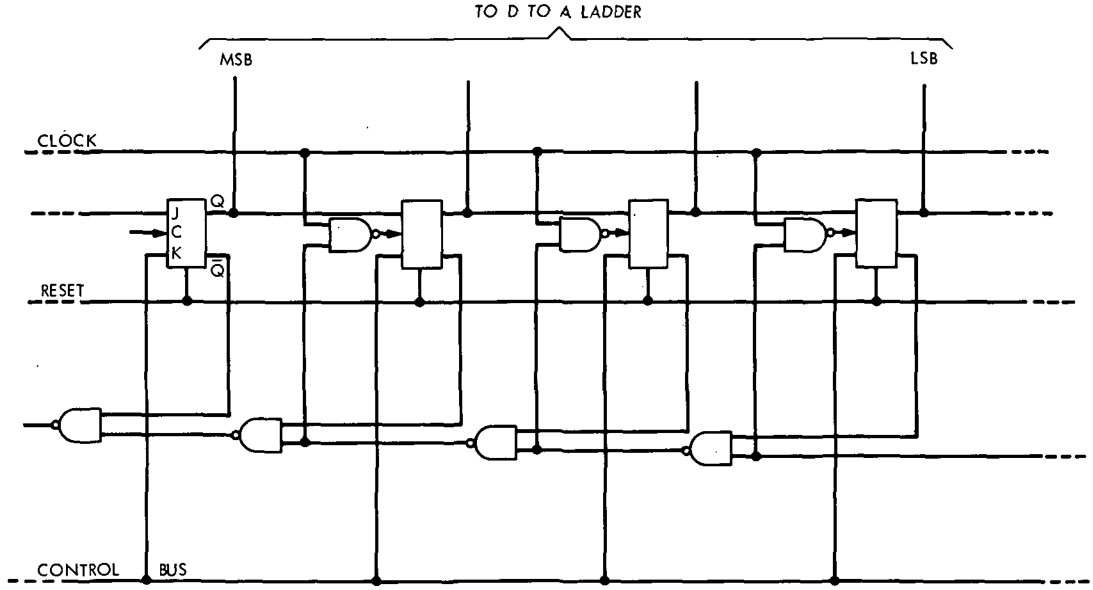

Fig. 9. Sequencer and code register using a single set of simple J/K FFs plus steering gates

The LEAPSIG Sigma 5-Mac 16 Cross-Assembler

H. C. Wilck
Communications Systems Research Section

A cross-assembler, called LEAPSIG, has been developed to permit the Sigma 5 computer to assemble programs for the Mac 16 minicomputer. It was obtained by translating the Mac 16 assembler into a Sigma 5 program by means of Sigma 5 METASYMBOL "procedures." This article describes the LEAPSIG program and discusses the method by which it was generated. Information for using LEAPSIG on the Sigma 5 is also given.

I. Introduction

LEAPSIG runs on the Sigma 5 computer and is used to assemble software for the Mac 16 minicomputer. This cross-assembler accepts standard LEAP 8 (Lockheed Mac 16 assembler) source language as input and produces the same object code and listing as LEAP 8. LEAPSIG is a two-pass assembler with macro capability.

The need for this cross-assembler stems from fact that the Mac 16 minicomputers, used by JPL in control applications, lack the peripherals, particularly a fast line printer and card reader, necessary for efficient program preparation. Since the assembly process is typically input/output (I/O) limited, shifting this task from the minicomputer to a larger machine with a good set of peripherals can cut assembly time by a factor of ten or more. A further discussion of minicomputer software support can be found in an article by J. W. Layland (Ref. 1). The XDS Sigma 5 was chosen as a host computer because of its availability at JPL and because it has a very flexible assembler (METASYMBOL) which made it possible to build the LEAPSIG program in an efficient manner.

This article primarily discusses the development of the LEAPSIG program. In addition, operating instructions for LEAPSIG are provided in Section IV. Some familiarity with the Sigma 5 computer, METASYMBOL, the Mac 16 minicomputer, and LEAP 8 on part of the reader is assumed. The respective manufacturers' manuals are recommended as a source of additional information (Refs. 2, 3, 4, and 5).

II. The Method Used to Implement LEAPSIG

The most direct method to obtain a cross-assembler on the Sigma 5 would be to write it completely in Sigma 5 assembly language. This approach demands a large amount of programmer time.

An alternative technique that requires less programming work is to develop a set of procedures (macro definitions) which allow Sigma 5 METASYMBOL to assemble programs written in a modified version of the minicomputer assembly language. A second program must also be provided to translate the resultant Sigma 5 load modules into

the format required by the minicomputer loader. This method has been used by C. C. Klimasauskas and D. E. Erickson to assemble programs for the XDS 930 and the PDP 11 on the Sigma 5 (Refs. 6 and 7). This process requires an input source language compatible in syntax and format with METASYMBOL. Since, in general, minicomputer languages do not meet this requirement, each minicomputer program to be assembled by this method must be written in a special METASYMBOL-compatible language.

A different approach, the translation of the Mac 16 LEAP 8 assembler into a Sigma 5 program, has been chosen for the implementation of LEAPSIG. This translation was accomplished in several steps. First the LEAP 8 assembler source program, written in a subset of the LEAP 8 language itself, was modified to make it syntactically compatible with METASYMBOL. Next a set of procedures was written to define the operation codes contained in the LEAP 8 source to the METASYMBOL assembler. Then the METASYMBOL assembler was used to translate the LEAP 8 assembler source program according to those procedures into a Sigma 5 machine language program. This program, augmented by a set of short I/O routines written in METASYMBOL, constitutes the LEAPSIG cross-assembler.

It is important to note that only the LEAP 8 assembler itself is translated by METASYMBOL procedures. The result of this translation is LEAPSIG. Assembly of other Mac 16 programs by means of LEAPSIG is not done by these procedures. LEAPSIG, in its object form, is a Sigma 5 machine language program. Language compatibility problems are therefore confined to the development of LEAPSIG and do not affect its use.

LEAPSIG is the functional equivalent of LEAP 8. LEAPSIG accepts standard LEAP 8 source language and outputs the same object and listing when run on a Sigma 5 as does LEAP 8 operating in a Mac 16. Any Mac 16 program can be assembled either by LEAPSIG on the Sigma 5 or by LEAP 8 on the Mac 16 with identical results.

III. The Translation Process

Some aspects of the translation process used to generate LEAPSIG are discussed in greater detail below.

A. Preprocessing

The LEAP 8 assembler is written in a subset of the LEAP 8 language not entirely compatible with METASYMBOL. Therefore, the LEAP 8 source program had to be preprocessed to make it suitable for translation by the METASYMBOL assembler. The LEAP 8 source program was inspected, analyzed, and modified with the aid of a set of FORTRAN routines written for this purpose. These routines take advantage of the fact that the LEAP 8 is written in fixed field form. It was found that only 60% of the LEAP 8 instructions and only half of the directives were used in the LEAP 8 source and that there were no instances of macros, logical operators, Boolean operators, or floating point constants. LEAP 8 almost agrees with METASYMBOL in the definition of source statement fields and subfields, symbols, operators, and expressions, at least to the extent of their actual presence in the LEAP 8 source. Usage of * for indirection and comment and usage of = for literals is the same in both languages. Furthermore, the only three cases of mnemonics common to both languages, NOP, EQU, and END, also have equivalent definitions in LEAP 8 and METASYMBOL. All of this simplifies translation and contributes significantly to the feasibility of this technique of cross-assembler building. However, there were some compatibility problems that had to be resolved by modifying the LEAP 8 source, as outlined below:

(1) *Hexadecimal constants.* The symbol $ followed by a string of hexadecimal digits (the LEAP 8 representation for hexadecimal constants) had to be changed to a string of hexadecimal digits surrounded by quotation marks and preceded by X.

(2) *Binary scaling.* All constants with binary scaling were interpreted and replaced by their unscaled equivalents.

(3) *Character strings.* It was necessary to change all character strings into hexadecimal constants, according to the USASCII code, since leaving their interpretation to METASYMBOL would lead to EBCDIC representation, which is incorrect for LEAPSIG.

(4) *Location counter references.* The symbol $ had to be substituted for * where used as reference to the location counter.

(5) *Assembler directives.* A number of LEAP 8 directives for which METASYMBOL procedures cannot be written had to be handled by source editing. EJECT was replaced by PAGE. The conditional assembly directives SKIPT and SKIPF were interpreted and then deleted together with the skipped source lines. EXTRN, LSTSY, and TITLE were expunged because their use was found unnecessary.

(6) *Storing into instructions at run time.* This practice causes problems if a Mac 16 instruction being

changed at run time translates into more than one Sigma 5 instruction or into an instruction that does not allow the type of modification attempted. Although any instruction can be modified or replaced at execution time, some are more likely targets than others. Eight instances of run time instruction changing were found in the LEAP 8 program by scanning its source for labeled NOPs and instructions of the immediate type with zero arguments. Analysis showed that seven of these cases would still work after translation, and the remaining one required rewriting a segment (12 source lines) of the LEAP 8 program.

B. The LEAP 8 Procedure Set

The LEAP 8 procedure set, which consists of 500 statements, allows the METASYMBOL assembler to translate each LEAP 8 operation code into one or more Sigma 5 instructions. Writing these procedures was greatly eased by the fact that only those LEAP 8 operations and pseudo-operations that actually occur in the LEAP 8 assembler source program needed to be defined.

Two Sigma 5 registers were set aside for representing the Mac 16 accumulator and index register. Another two Sigma registers were assigned to the Mac 16 carry and overflow indicators. (The other four Mac 16 status indicators are never used in LEAP 8.)

Since Mac 16 is a 16-bit machine while the Sigma 5 word is 32 bits long, the procedures for data generating directives store data words into the lower halfword with the sign extended 16 bits to the left. Because of this difference in word length, carry and overflow do not occur in the same manner in both machines. Therefore, procedures for arithmetic instructions must make provision for detecting and saving Mac 16 carry and overflow and for extending the sign of the result of the operation.

To avoid address arithmetic problems all Mac 16 instructions that resulted in more than one Sigma 5 instruction were translated into a branch to a separate auxiliary program section where the actual translation was stored, followed by a branch back to the next location in the main section. The METASYMBOL directives CSECT and USECT allow easy switching between two assembly sections.

Figure 1 shows a procedure for a number of Mac 16 instructions, each of which translates into one Sigma 5 instruction.

The procedure in Fig. 2 is an example of a Mac instruction (STL) expanding into several Sigma instructions. Line 109 shows the branch to the auxiliary section. The branch instruction itself is assembled into the main section. Line 110 establishes an address for the branch back from the auxiliary section. Line 111 switches assembly to the auxiliary section. Lines 112 through 116 contain the actual translation of the STL instruction. Line 117 is the branch back to the main section. Line 118 sets the address for the next branch to the auxiliary section and line 119 returns assembly to the main section. XTWO and XONE on lines 114 and 115 refer to two index registers that contain a 2 and a 1 respectively.

Excluding the symbol table and the I/O routines, LEAP 8 occupies roughly 4000 words of Mac 16 storage. Translation expands it into approximately 6000 Sigma 5 words.

C. I/O Routines

Five Sigma 5 routines, comprising a total of 200 source statements, have been written in METASYMBOL to enable LEAPSIG to communicate with the outside world. These routines replace the I/O programs used by LEAP 8 when running on the Mac 16.

During pass 1 of the LEAPSIG assembler the *source input* routine reads the source from the input device (usually the card reader) and translates it from EBCDIC (the character code used by the Sigma 5) to USASCII (the character code required by LEAPSIG). The translated source is also saved on the RAD and later retrieved from there for use by the second pass.

The *list output* routine translates the assembly listing from USASCII to EBCDIC and outputs it on the listing device.

The *object output* subprogram punches the Mac 16 binary object on the paper tape punch.

The *device ready* routine performs a check for I/O completion. This is necessary in order to take advantage of the LEAP 8 I/O buffer switching feature, designed to speed execution.

The *executive* routine reads and interprets control messages that govern the execution of LEAPSIG. (See Section IV below.)

IV. Using LEAPSIG on the Sigma 5

The I/O routines used by this assembler require assignments for the following logical devices:

F:CTL	Control input device (usually assigned to the card reader).
F:CRD	Source input device (usually assigned to the card reader).
F:PRT	Listing output (usually assigned to the line printer).
F:PCH	Object output (usually assigned to the paper tape punch).
F:RAD	Scratch file (usually assigned to the RAD).

The execution of the LEAPSIG program is controlled by special control cards. These cards must contain a / in column 1 followed in column 2 by 0, 1, 2, 3, 4 or /. Columns 3 through 80 are ignored. The meaning of these control cards is explained below:

/0	Execute pass 1 (similar to the Mac 16 control message 'EX,,400').
/1	Execute pass 2, punch object and print listing (similar to 'EX,,401').
/2	Execute pass 2, print listing (similar to 'EX,,402').
/3	Execute pass 2, punch object (similar to 'EX,,403').
/4	Execute pass 2, print errors only (similar to 'EX,,404').
//	Exit to Monitor.

If F:CTL and F:CRD are assigned to the same device (e.g., the card reader) the control messages must be contained in the source input stream. The assembler looks for control messages when it starts execution and after finishing each pass.

The typical deck shown below will produce an assembly with listing and object paper tape. It is assumed here that the LEAPSIG program is available from the RAD.

```
!JOB ACCOUNT,NAME
!ASSIGN F:CTL, (DEVICE CRA03)
!ASSIGN F:CRD, (DEVICE CRA03)
!ASSIGN F:PRT, (DEVICE,LPB02), (VFC)
!ASSIGN F:PCH, (DEVICE PPA01), (BIN)
!ASSIGN F:RAD, (FILE,SCRATCH), (OUTIN)
!RUN (LMN,LEAP,ACCOUNT)
!DATA
/0
(Source deck in LEAP 8 language)
/1
//
!FIN
```

V. Conclusion

The LEAPSIG cross-assembler has been extensively used in the preparation and documentation of the Programmed Oscillator software.

The relatively small programming effort required for generating LEAPSIG makes it worthwhile to investigate the applicability of the techniques described here to other cross-assemblers. The feasibility of this approach is primarily governed by the amount of preprocessing involved and by the expansion of assembler core size caused by the translation.

References

1. Layland, J. W., "An Introduction to Minicomputer Software Support," in *The Deep Space Network Progress Report*, Technical Report 32-1526, Vol. VII, pp. 84–85. Jet Propulsion Laboratory, Pasadena, Calif., Feb. 1972.
2. *XDS Sigma 5 Computer Reference Manual*, 90 09 59D. Xerox Data Systems, El Segundo, Calif., Feb. 1970.
3. *SYMBOL/META-SYMBOL Reference Manual for Sigma 5/7 Computers*, 90 09 52C. Xerox Data Systems, El Segundo, Calif., Dec. 1969.
4. *Mac 16 Computer Reference Manual, TM13010009800*. Lockheed Electronics Company, Los Angeles, Calif., Nov. 1970.
5. *Mac 16 LEAP Assembler Manual, TM13013041101*. Lockheed Electronics Company, Los Angeles, Calif., Dec. 1970.
6. Klimasauskas, C. C., "The X930 Program Set for Sigma 5 Assembly," in *The Deep Space Network Progress Report*, Technical Report 32-1526, Vol. VII, pp. 86–90. Jet Propulsion Laboratory, Pasadena, Calif., Feb. 1972.
7. Erickson, D. E., "The SAPDP Program Set for Sigma 5 Assembly," in *The Deep Space Network Progress Report*, Technical Report 32-1526, Vol. VII, pp. 91–96. Jet Propulsion Laboratory, Pasadena, Calif., Feb. 1972.

```
*
JMP      CNAME    O,X'68'
JMM      CNAME    X,X'6A'
LDA      CNAME    A,X'32'
LDX      CNAME    X,X'32'
STA      CNAME    A,X'35'
STX      CNAME    X,X'35'
ANA      CNAME    A,X'48'
ORA      CNAME    A,X'49'
         PROC
         BOUND    4
LF       GEN,1,7,4,3,17 AFA(1),NAME(2),NAME(1),AF(2),AF(1)
         PEND
*
```

Fig. 1. Example of a procedure for one-to-one translation of Mac 16 instructions into Sigma 5 instructions

```
*
STL      CNAME
         PROC
LF       B        BB
RR       SET      $
         USECT    AUXF
         BOUND    4
         GEN,1,7,4,3,17 AFA(1),X'32',A1,AF(2),AF(1)
         STB,A    A1,XTWO
         LH,A1    A1,XONE
         GEN,1,7,4,3,17 AFA(1),X'35',A1,AF(2),AF(1)
         B        RR
BB       SET      $
         USECT    PROG
         PEND
*
```

Fig. 2. Example of a procedure that expands one Mac 16 instruction into several Sigma 5 instructions

Models for Flicker Noise in DSN Oscillators

C. A. Greenhall
Communications Systems Research Section

A mathematically tractable model for flicker noise is presented. The model is not stationary, but has stationary increments. It behaves like flicker noise when subjected either to high-pass filtering or to direct spectral measurements. Effects of a detrending operation on these measurements are investigated. The model is expressed as a limit of stationary processes. The model of Barnes and Allan is reviewed, and the performances of the two models are compared.

I. Heuristic Description of the Model

The paradox of flicker noise appears in the study of certain types of time series, which include oscillator frequency fluctuations and noise in semiconductors. Experiments that attempt to measure the spectral density of such time series at low angular Fourier frequencies ω have yielded densities of the order $1/|\omega|$ or even $1/|\omega|^\alpha$, $\alpha > 1$ (Refs. 1 and 2). No rolloff from this behavior has been observed down to frequencies of the order 1 cycle per year. Since $1/|\omega|^\alpha$, $\alpha > 1$, is not integrable over the low-frequency range, there is no stationary process with such a spectral density.

This situation has been dealt with by two approaches (Refs. 3–8):

(1) Assume that a stationary formalism can still be used. Plug $1/|\omega|$ into formulas as if it were the spectral density of a stationary process. If the resulting integrals converge, those results are meaningful. An objection to this approach is that it is mathematically unsound.

(2) Assume that the $1/|\omega|$ behavior cuts off in some way below a frequency ϵ lower than any frequency of interest. Then use a mathematically sound stationary formalism and obtain results depending perhaps on ϵ. Investigate what happens as $\epsilon \to 0$. An objection here is that one has to assume the existence of something never observed, namely, an artificially imposed cutoff.

We believe that there really is no cutoff. Hence we must look to nonstationary processes to find a sound mathematical model for the phenomenon. This is not to say that we abandon the idea that flicker noise is produced by a stationary mechanism; after all, an ordinary random walk is a nonstationary process, but consists of the partial sums of a stationary sequence. This idea is the germ of our model. It is often said that when you pass a stationary process $X(t)$ with spectral density $f(\omega)$ through a perfect integrator, you get a process $Y(t)$ with spectral density $f(\omega)/\omega^2$. However, such a Y is not stationary, but has stationary increments, i.e., the processes $Y_\delta(t) = Y(t+\delta) - Y(t)$ are stationary. We will not say

that Y has spectral density $f(\omega)/\omega^2$, but will show that $f(\omega)/\omega^2$ can be associated with Y in an experimentally meaningful way.

To make a model for flicker noise, define $f(\omega) = |\omega|$, at least for small ω. The mathematics of the model will require a high-frequency rolloff from the $1/|\omega|$ behavior. Accordingly, our model is as follows: Send white noise through a high-pass filter that attenuates low frequencies at a rate of 3 dB per octave. This gives a stationary process $X(t)$ with spectral density $|\omega|$ for small ω. Then our model $Y(t)$ for flicker noise is given by

$$Y(t) = \int_0^t X(s)ds \tag{1}$$

We will also add a constant term and a linear drift term, since such dc components are natural to processes with stationary increments. Besides, oscillators often exhibit linear frequency drift, with random fluctuations superimposed.

We will not try to "prove" that the process Y has a spectral density $1/|\omega|$. There is no such thing. We will simply subject Y to the same measurements on paper that have been performed on flicker noise in the laboratory. These include (1) passages through high-pass filters, and (2) attempts to measure spectral density directly. If Y behaves like flicker noise, then to this extent our model is successful. We can then entertain hopes of finding a physical mechanism that generates the model.

Fortunately, the calculations are easy to carry out, for processes with stationary increments are mathematically tractable. They are an immediate generalization of stationary processes, and their spectral theory is almost as simple (Refs. 9, 10, and 11). On the way, we will point out how the two approaches fit into the picture.

II. Stationary Processes and Processes with Stationary Increments

We will be concerned here only with first and second moment properties of processes. Accordingly, "stationary" means "weakly stationary," i.e., that the covariance depends only on time differences.

If $X(t)$, $-\infty < t < \infty$, is a continuous-time, complex-valued, mean-continuous, stationary process with spectral distribution function F, then

$$X(t) = \int_{-\infty}^{\infty} \exp(i\omega t)dZ(\omega) \tag{2}$$

where Z is a process with orthogonal increments such that $E|dZ(\omega)|^2 = dF(\omega)$. The function F is increasing and bounded on $(-\infty, \infty)$. If X has a spectral density f, then $dF(\omega) = f(\omega)d\omega$.

A stochastic integral

$$\int_{-\infty}^{\infty} \phi(\omega)\, dZ(\omega)$$

of which Eq. (2) is an example, is defined for functions ϕ such that

$$\int_{-\infty}^{\infty} |\phi(\omega)|^2 dF(\omega) < \infty \tag{3}$$

The main property of this integral is

$$E\left(\int_{-\infty}^{\infty} \phi dZ\right)\left(\overline{\int_{-\infty}^{\infty} \psi dZ}\right) = \int_{-\infty}^{\infty} \phi(\omega)\overline{\psi(\omega)}\, dF(\omega) \tag{4}$$

if ϕ and ψ satisfy Eq. (3).

The theory of stationary processes can be found in Refs. 9–14. A process $Y(t)$, $-\infty < t < \infty$, is said to have stationary increments if $E[Y(s) - Y(t)] = a(s - t)$ for some number a, and if

$$E[Y(t + \tau_1) - Y(t)][\overline{Y(t + \tau_2) - Y(t)}]$$

does not depend on t. If Y is mean-square differentiable, then its derivative Y' is stationary, mean-continuous, and satisfies

$$Y(t) - Y(0) = \int_0^t Y'(s)\, ds$$

the integral being in the mean-square sense. If Y' is the process X of Eq. (2), then

$$\begin{aligned} Y(t) - Y(0) &= \int_0^t ds \int_{-\infty}^{\infty} dZ(\omega) \exp(i\omega s) \\ &= \int_{-\infty}^{\infty} dZ(\omega) \int_0^t ds \exp(i\omega s) \end{aligned}$$

$$Y(t) = Y(0) + \int_{-\infty}^{\infty} \frac{\exp(i\omega t) - 1}{i\omega}\, dZ(\omega) \tag{5}$$

The interchange of orders of integration leading to Eq. (5) may be carried out because $\int dF < \infty$; see Rozanov's book (Ref. 14, p. 12) for the relevant theorem.

By considering the stationary processes $Y(t+\delta) - Y(t)$, it can be shown that any mean-continuous process with stationary increments, differentiable or not, has a representation of form (5), where the increasing function F that corresponds to Z via $E\,|\,dZ\,|^2 = dF$ no longer need be bounded, but merely satisfies

$$\int_{-\infty}^{\infty} \frac{dF(\omega)}{1+\omega^2} < \infty \tag{6}$$

This is equivalent to Eq. (3), where $\phi(\omega) = [\exp(i\omega t) - 1]/i\omega$. For example, if $F(\omega) = \omega/(2\pi)$, then $Y(t) - Y(0)$ has the same covariances as Brownian motion. This may be shown by using Eqs. (5) and (4).

More detailed accounts of these processes may be found in Ref. 11, p. 86 ff., and in Ref. 10.

We will concentrate our attention on the case in which F has a jump at 0, but elsewhere has a density f. Then Z has a jump Z_0 at 0, orthogonal to $dZ(\omega)$ when $\omega \neq 0$. Since $[\exp(i\omega t) - 1]/i\omega$ is considered as having the value t when $\omega = 0$, the contribution of Z_0 to Eq. (5) is $Z_0 t$. Indeed, the presence of linear drift is part of the nature of processes with stationary increments. Removing this jump from Z, and calling the remaining process again Z, we write this case of Eq. (5) as

$$Y(t) = Y(0) + Z_0 t + \int_{-\infty}^{\infty} \frac{\exp(i\omega t) - 1}{i\omega}\, dZ(\omega) \tag{7}$$

where $E\,|\,dZ(\omega)|^2 = f(\omega)\,d\omega$, f being a nonnegative function such that

$$\int_{-\infty}^{\infty} \frac{f(\omega)}{1+\omega^2}\, d\omega < \infty \tag{8}$$

In this situation we will say that Y has the *formal spectral density* $f(\omega)/\omega^2$. The point is that maybe

$$\int_{-1}^{1} \frac{f(\omega)}{\omega^2}\, d\omega = \infty \tag{9}$$

in which case $f(\omega)/\omega^2$ cannot be the spectral density of any stationary process. The main purpose of this article is to make some sense of this terminology.

Now it is evident what our model for flicker noise shall be, namely, a process Y with stationary increments having a formal spectral density $1/|\,\omega\,|$. This would make $f(\omega) = |\,\omega\,|$, which violates Eq. (8). Accordingly, we demand a $1/|\,\omega\,|$ behavior only for low frequencies. We will require that

$$\frac{f(\omega)}{|\,\omega\,|} \rightarrow 1 \qquad \text{as } \omega \rightarrow 0 \tag{10}$$

and that f roll off enough at high frequencies to satisfy Eq. (8). The exact nature of the rolloff will not affect our results.

III. Quadratic Means

We wish to know how these processes behave under certain measurements. Let X be a stationary process with spectral density f. We will consider only measurements of the following form:

$$P = \left|\int_{-\infty}^{\infty} X(t)h(t)dt\right|^2 \tag{11}$$

where h is a complex-valued "time window" such that

$$\int_{-\infty}^{\infty} |\,h(t)\,|\,dt < \infty \tag{12}$$

(We may include δ-functions in h.) Further, we will look only at the expectation of P, ignoring the problem of finding its variance under assumptions about higher moments of X. It is a familiar fact that

$$EP = \int_{-\infty}^{\infty} |\,H(\omega)\,|^2 f(\omega)d\omega \tag{13}$$

where

$$H(\omega) = \int_{-\infty}^{\infty} h(t)\exp(i\omega t)dt \tag{14}$$

Now suppose that we make the same measurement on a process Y with stationary increments and a formal spectral density $f(\omega)/\omega^2$. Assume $Y(0) = 0$ for now. Let

$$Q = \left|\int_{-\infty}^{\infty} Y(t)h(t)dt\right|^2 \tag{15}$$

The integral can be transformed as follows:

$$\int_{-\infty}^{\infty} Y(t)h(t)dt - Z_0\int_{-\infty}^{\infty} th(t)dt$$

$$= \int_{-\infty}^{\infty} dth(t) \int_{-\infty}^{\infty} dZ(\omega)\frac{\exp(i\omega t) - 1}{i\omega}$$

$$= \int_{-\infty}^{\infty} dZ(\omega)\frac{1}{i\omega}\int_{-\infty}^{\infty} dth(t)[\exp(i\omega t) - 1]$$

$$= \int_{-\infty}^{\infty} \frac{H(\omega) - H(0)}{i\omega}\, dZ(\omega) \qquad (16)$$

The condition

$$\int_{-\infty}^{\infty}(1 + |t|)\,|h(t)|\,dt < \infty \qquad (17)$$

plus Eq. (8), is sufficient to validate the interchange of orders of integration leading to Eq. (16). Condition (17) also makes H differentiable. From Eqs. (16), (4), and the orthogonality of Z_0 to dZ, we get

$$EQ = |H'(0)|^2 E|Z_0|^2 + \int_{-\infty}^{\infty} |H(\omega) - H(0)|^2 \frac{f(\omega)}{\omega^2}\, d\omega \qquad (18)$$

valid when $Y(0) = 0$ (or, what is the same, if h is applied to $Y(t) - Y(0)$). The formal spectral density $f(\omega)/\omega^2$ appears in somewhat the same role as spectral density $f(\omega)$ does in Eq. (13), the analogous formula for stationary processes. The next two sections examine some special cases of these measurements.

IV. High-Pass Filters

We say that a time window h satisfying Eq. (17) is a high-pass filter if $H(0) = 0$, i.e.,

$$\int_{-\infty}^{\infty} h(t)dt = 0 \qquad (19)$$

In this situation, we no longer need to require $Y(0) = 0$, and Eq. (18) becomes

$$EQ = |H'(0)|^2 E|Z_0|^2 + \int_{-\infty}^{\infty} |H(\omega)|^2 \frac{f(\omega)}{\omega^2}\, d\omega \qquad (20)$$

The first term of Eq. (20) is due to linear drift. The second term is exactly what we would get if a stationary process with spectral density $f(\omega)/\omega^2$ were subjected to the same measurement. This is what the first approach (1) of Section I gives. Of course, if Eq. (9) holds, there is no such stationary process. Moreover, if h is not high-pass, then approach (1) fails, for the integral in Eq. (20) diverges.

In the study of oscillator stability, $Y(t)$ is the frequency of an oscillator at time t, relative to some nominal average frequency. To measure the instability of Y, one often uses a family of high-pass filters

$$h_\tau(t) = \frac{1}{\tau}k\left(\frac{t}{\tau}\right)$$

depending on an integration-time parameter τ. Here, $k(x)$ is a fixed high-pass filter function of dimensionless time x. Perhaps the simplest of these is given by

$$\begin{aligned} k(x) &= -1/2^{1/2}, && 0 < x < 1 \\ &= 1/2^{1/2}, && 1 < x < 2 \\ &= 0, && \text{otherwise} \end{aligned}$$

The corresponding Q is called the Allan variance. It is the sample variance of two successive averages over adjacent time intervals. Let

$$K(y) = \int_{-\infty}^{\infty} \exp(ixy)k(x)dx$$

Then

$$EQ = \tau^2|K'(0)|^2 E|Z_0|^2 + \int_{-\infty}^{\infty} |K(\omega\tau)|^2 \frac{f(\omega)}{\omega^2}\, d\omega \qquad (21)$$

For the flicker noise case, let us assume for simplicity that $f(\omega) = |\omega|$ for $|\omega| \leq \omega_1$. (Actually, conditions (8) and (10) are sufficient.) The integral in Eq. (21) becomes

$$\int_{-\omega_1\tau}^{\omega_1\tau} |K(y)|^2 \frac{dy}{|y|} + \int_{|\omega|>\omega_1} |K(\omega\tau)|^2 \frac{f(\omega)}{\omega^2}\, d\omega$$

If $K(y)$ tends to 0 fast enough as $y \rightarrow \infty$, this expression tends to

$$\int_{-\infty}^{\infty} |K(y)|^2 \frac{dy}{|y|} \qquad (22)$$

as $\tau \rightarrow \infty$. In the case of Allan variance, this integral is

$$\int_0^{\infty} \sin^4 \frac{1}{2}y \frac{1}{y^3}\, dy = 4 \log 2$$

A standard test for the presence of flicker noise is the leveling off of the Allan variance to a nonzero limit as τ gets large. Since $K'(0) \neq 0$ in this case, the linear drift term in Eq. (21) grows like τ^2. Thus it is obviously necessary to remove linear drift from Y before making the measurement, and this is in fact done (Ref. 5). Of course, this surgery cannot be performed without damaging the second term of Eq. (21); we will examine this situation in detail in Section VI. This difficulty can be avoided by using a filter h such that $H'(0) = 0$, i.e.,

$$\int_{-\infty}^{\infty} th(t)dt = 0 \tag{23}$$

Then the linear drift term vanishes. When Barnes (Ref. 4) considers the third difference of the phase of an oscillator, he is using such a filter.

V. Spectral Estimates

We wish to see what happens when we perform experiments on our model that are designed to measure spectral density f of a stationary process X. One estimate of f at a chosen frequency ω_0 is a modified periodogram (Refs. 15 and 16). Let k be an integrable function on (0,1). The estimate of $f(\omega_0)$ using an integration time of τ is

$$I_\tau(\omega_0) = \frac{1}{2\pi\tau}\left| \int_0^\tau X(t)k\left(\frac{t}{\tau}\right) \exp(-i\omega_0 t)\, dt \right|^2 \tag{24}$$

To get stable estimates of $f(\omega_0)$ we would have to average $I_\tau(\omega)$ over a band of frequencies that is wide compared with $1/\tau$. We will not do this here.

Let

$$K(y) = \int_0^1 \exp(ixy)k(x)dx \tag{25}$$

The measurement $I_\tau(\omega_0)$ is of the Eq. (11) type. By Eq. (13),

$$EI_\tau(\omega_0) = \frac{\tau}{2\pi}\int_{-\infty}^{\infty} |K((\omega - \omega_0)\tau)|^2 f(\omega)d\omega \tag{26}$$

Assume that k is square-integrable, and that f is a bounded, continuous function on $(-\infty, \infty)$. Then

$$EI_\tau(\omega_0) \to f(\omega_0)\int_0^1 |k(x)|^2 dx$$

as $\tau \to \infty$; in other words, $I_\tau(\omega_0)$ is an asymptotically unbiased estimate of $f(\omega_0)\int |k|^2$.

Let $J_\tau(\omega_0)$ be defined as in Eq. (24), except that X is replaced by a process Y with stationary increments and a formal spectral density $f(\omega)/\omega^2$. Assume again that $Y(0) = 0$. By Eq. (18),

$$EJ_\tau(\omega_0) = \frac{1}{2\pi}\tau^3 |K'(-\omega_0\tau)|^2 E|Z_0|^2 + \frac{\tau}{2\pi}\int_{-\infty}^{\infty} |K((\omega-\omega_0)\tau) - K(-\omega_0\tau)|^2 \frac{f(\omega)}{\omega^2}d\omega \tag{27}$$

Suppose that $K(y)$ and $K'(y)$ tend to 0 faster than $|y|^{-3/2}$ as $|y| \to \infty$. As $\tau \to \infty$, the linear drift term goes to 0. In the integral, the $1/\omega^2$ divergence is cancelled by the $|\cdots|^2$ factor. For ω near ω_0, the term $K(-\omega_0\tau)$ is insignificant compared to $K((\omega-\omega_0)\tau)$. As a result, when $\tau \to \infty$, expression (27) behaves like (26), this time picking off the value $f(\omega)/\omega_0^2$ of the formal spectral density. For flicker noise we set $f(\omega) \sim |\omega|$ as $\omega \to 0$, and we see again how the model manages to masquerade as a nonexistent stationary process with spectral density $\sim 1/|\omega|$ for small ω.

Here is a precise statement about the behavior of $EJ_\tau(\omega_0)$: *Let k be an absolutely continuous function on [0,1] such that $k(0) = k(1) = 0$, and let K be its Fourier transform Eq. (25). Let f be a continuous function satisfying Eq. (8). Then for $\omega_0 \neq 0$, the second term of Eq. (27) tends to*

$$\frac{f(\omega_0)}{\omega_0^2}\int_0^1 |k(x)|^2 dx \tag{28}$$

as $\tau \to \infty$.

Proof: The conditions on k imply

$$K^{(n)}(y) = o\left(\frac{1}{|y|}\right), \qquad \text{as } |y| \to \infty \tag{29}$$

for $n = 0, 1, 2, \cdots$.

It will be enough to prove the result when $\omega_0 > 0$. We break up the integral in Eq. (27) as follows:

$$\frac{\tau}{2\pi}\left(\int_{-\infty}^{-1/\tau} + \int_{-1/\tau}^{1/\tau} + \int_{1/\tau}^{\omega_0/2} + \int_{\omega_0/2}^{3\omega_0/2} + \int_{3\omega_0/2}^{\infty}\right)$$
$$= I_1 + I_2 + I_3 + I_4 + I_5$$

We will show that I_4 tends to Eq. (28) as $\tau \to \infty$, and the other I_j tend to 0. Let $q = \omega_0 \tau$, and let

$$g(x) = \frac{f(\omega_0(1+x))}{\omega_0^2(1+x)^2}$$

Then

$$I_4 = \int_{-q/2}^{q/2} |K(y) - K(-q)|^2 g\left(\frac{y}{q}\right) \frac{dy}{2\pi}$$
$$= \int_{-m}^{m} + \int_{m<|y|<q/2} \tag{30}$$

As $q \to \infty$, the first integral in Eq. (30) tends to

$$\frac{g(0)}{2\pi} \int_{-m}^{m} |K(y)|^2 dy \tag{31}$$

The second integral in Eq. (30) is less than

$$\frac{1}{\pi} max \left\{ g(x) : |x| < \frac{1}{2} \right\} \left(\int_{|y|>m} |K(y)|^2 dy + q |K(-q)|^2 \right)$$

By choosing m large we can make this expression as small as we like for all q sufficiently large, and can also make Eq. (31) as close as we like to

$$\frac{g(0)}{2\pi} \int_{-\infty}^{\infty} |K(y)|^2 dy = \frac{f(\omega_0)}{\omega_0^2} \int_0^1 |K(x)|^2 dx$$

This establishes the limiting behavior of I_4.

To estimate I_1 we simply observe

$$\tau | K((\omega - \omega_0)\tau) - K(-\omega_0\tau)|^2 = o\left(\frac{1}{\tau}\right)$$

as $\tau \to \infty$, uniformly for $\omega < 0$. Hence

$$I_1 \le o\left(\frac{1}{\tau}\right) \int_{-\infty}^{-1/\tau} \frac{f(\omega)}{\omega^2} d\omega$$
$$= o\left(\frac{1}{\tau}\right) O(\tau) = o(1)$$

The estimates for I_3 and I_5 are similar.

Only I_2 remains. By a version of the mean value theorem for complex-valued functions of a real variable,

$$|K(\omega\tau - \omega_0\tau) - K(-\omega_0\tau)|^2 \le \omega^2\tau^2 |K'(c)|^2$$

for some number c between $\omega\tau - \omega_0\tau$ and $-\omega_0\tau$. If $|\omega| \le 1/\tau$ and $\tau \ge 2/\omega_0$, then $c \le -\omega_0\tau/2$ and $|K'(c)|^2 = o(1/\tau^2)$. Therefore

$$I_2 \le o(1)\, \tau \int_{-1/\tau}^{1/\tau} f(\omega) d\omega = o(1)$$

The proof is complete.

When $f(0) = 0$, as in the flicker noise model, we can replace o by O in Eq. (29). Then even a boxcar function will serve for k. Of course, to make the linear drift term in Eq. (27) tend to 0 we need $K'(y) = o(1/|y|)^{3/2}$. This problem goes away when we remove drift before doing the spectral analysis; we treat this situation in the next section.

VI. Removal of Linear Trends

Before taking the kinds of measurements we have described, it is common practice to fit a linear trend to the data and subtract it off. Measurements are then taken on the residual data. In spectral measurements this avoids interaction of dc components with minor lobes of the spectral window.

Least-squares fitting on an interval $-1/2\tau \le t \le 1/2\tau$ is convenient for us here. Given a signal $u(t)$, we produce a residual signal

$$u_r(t) = u(t) - a_0 - a_1 t$$

where

$$a_0 = \frac{1}{\tau} \int_{-½\tau}^{½\tau} u(t)dt, \qquad a_1 = \frac{12}{\tau^3} \int_{-½\tau}^{½\tau} tu(t)dt$$

Then

$$\int_{-½\tau}^{½\tau} u_r(t)dt = 0, \qquad \int_{-½\tau}^{½\tau} tu_r(t)dt = 0 \tag{32}$$

and for any two given signals u and v,

$$\int_{-½\tau}^{½\tau} u_r(t)v(t)dt = \int_{-½\tau}^{½\tau} u(t)v_r(t)dt \tag{33}$$

Let Y be the process of Eq. (7). We will look at quadratic means Q_r of the reduced process $Y_r(t)$:

$$Q_r = \left| \int_{-½\tau}^{½\tau} Y_r(t)h(t)dt \right|^2$$

If h is integrable on $[-\tau/2, \tau/2]$,

$$\int_{-\frac{1}{2}\tau}^{\frac{1}{2}\tau} Y_r(t)h(t)dt = \int_{-\frac{1}{2}\tau}^{\frac{1}{2}\tau} Y(t)h_r(t)dt \tag{34}$$

Let

$$H(\omega) = \int_{-\frac{1}{2}\tau}^{\frac{1}{2}\tau} h(t) \exp(i\omega t)dt$$

$$H_r(\omega) = \int_{-\frac{1}{2}\tau}^{\frac{1}{2}\tau} h_r(t) \exp(i\omega t)dt \tag{35}$$

Because of Eq. (32), not only is h_r a high-pass filter, $H_r(0) = 0$, but also $H'_r(0) = 0$. Hence, by Eq. (20),

$$EQ_r = \int_{-\infty}^{\infty} |H_r(\omega)|^2 \frac{f(\omega)}{\omega^2} d\omega \tag{36}$$

Take the situation

$$h(t) = \frac{1}{\tau} k\left(\frac{t}{\tau}\right)$$

where k is a function with residual k_r defined with respect to the interval $[-1/2, 1/2]$. Then

$$h_r(t) = \frac{1}{\tau} k_r\left(\frac{t}{\tau}\right)$$

and Eq. (21) gives

$$EQ_r = \int_{-\infty}^{\infty} |K_r(\omega\tau)|^2 \frac{f(\omega)}{\omega^2} d\omega \tag{37}$$

where

$$K_r(y) = \int_{-\frac{1}{2}}^{\frac{1}{2}} k_r(x) \exp(ixy)dx$$

For the flicker noise case, $f(\omega) \sim |\omega|$ as $\omega \to 0$, EQ_r tends to

$$\int_{-\infty}^{\infty} |K_r(y)|^2 \frac{dy}{|y|}$$

as $\tau \to \infty$, and there is no linear drift term to interfere with our observations. This happens whether or not k is a high-pass filter.

Before we look at spectral measurements on the reduced process Y_r, we need a formula for H_r in terms of H. By Eqs. (35) and (33),

$$H_r(\omega) = \int_{-\frac{1}{2}\tau}^{\frac{1}{2}\tau} h(t)e(\omega,t)\, dt$$

where $e(\omega,t)$ is the reduced form of the function $\exp(i\omega t)$ on $-\tau/2 \leq t \leq \tau/2$. We calculate

$$e(\omega,t) = \exp(i\omega t) - \phi_0(\omega\tau/2) - \phi_1(\omega\tau/2)i\omega t$$

where

$$\phi_0(x) = \frac{\sin x}{x}, \qquad \phi_1(x) = 3\frac{\sin x - x\cos x}{x^3}$$

Therefore the desired formula is

$$H_r(\omega) = H(\omega) - \phi_0(\omega\tau/2)H(0) - \phi_1(\omega\tau/2)\omega H'(0) \tag{38}$$

We apply Eqs. (36) and (38) to the spectral estimate $J_T(\omega_0)$ of Section V, where Y is replaced by Y_r, and k is on $[-1/2, 1/2]$ instead of $[0,1]$. We get

$$EJ_T(\omega_0) = \frac{\tau}{2\pi}\int_{-\infty}^{\infty} |K((\omega-\omega_0)\tau) - \phi_0(\omega\tau/2)K(-\omega_0\tau) - \phi_1(\omega\tau/2)\omega\tau K'(-\omega_0\tau)|^2 \frac{f(\omega)}{\omega^2} d\omega \tag{39}$$

Although this is messier than Eq. (27), it is actually better behaved. There is no linear drift term. When $|\omega\tau| \geq 1$, the perturbing terms in (39) go to 0 at least as fast as the old $K(-\omega_0\tau)$, and even faster when ω is bounded away from 0. In the region $|\omega\tau| \leq 1$, the integrand of (39) is like that of (27) except for the extra terms

$$(1 - \phi_0(\omega\tau/2))K(-\omega_0\tau) - \phi_1(\omega\tau/2)\omega\tau K'(-\omega_0\tau)$$

which are both $|\omega| o(1)$ as $\tau \to \infty$, $|\omega\tau| \leq 1$. Hence this part of the integral behaves as well as before.

We conclude that the reduced $EJ_T(\omega_0)$ tends to the right side of Eq. (28). In general, the detrending operation enhances the ability of our measurements to provide information about the formal spectral density $f(\omega)/\omega^2$ of a process with stationary increments.

VII. Approximation by Stationary Processes

The purpose of this section is to give a concrete interpretation of the method of cutoffs, the second approach of Section I. Rather than creating out of nothing a sta-

tionary process with spectral density that cuts off below $\omega = \epsilon$, we will generate one by sending the process Y of Eq. (7) through a high-pass filter. This will give a stationary process X_ϵ which in a certain sense converges to Y as $\epsilon \to 0$.

We will need to assume that the linear drift term $Z_0 t$ is absent from $Y(t)$. Take a high-pass filter with impulse response

$$h_\epsilon(t) = \delta(t) - \epsilon k(\epsilon t)$$

where $\epsilon > 0$ and k is a function such that

$$\int_{-\infty}^{\infty} (1 + |x|)\,|k(x)|\,dx < \infty, \int_{-\infty}^{\infty} k(x)dx = 1$$

and δ is the Dirac delta. This time, let

$$K(y) = \int_{-\infty}^{\infty} \exp(-ixy)\,k(x)dx$$

a bounded, differentiable function that tends to 0 as $|y| \to \infty$. Define the process X_ϵ by

$$X_\epsilon(t) = \int_{-\infty}^{\infty} Y(s)h_\epsilon(t-s)ds$$

Then Eq. (16) gives

$$X_\epsilon(t) = \int_{-\infty}^{\infty} \exp(i\omega t)\frac{1 - K(\omega/\epsilon)}{i\omega}\,dZ(\omega)$$

Hence, X_ϵ is a stationary process with spectral density

$$\left|1 - K\left(\frac{\omega}{\epsilon}\right)\right|^2 \frac{f(\omega)}{\omega^2} \tag{40}$$

a cutoff version of $f(\omega)/\omega^2$ which tends to $f(\omega)/\omega^2$ as $\epsilon \to 0$. If Eq. (9) holds, the random variables $X_\epsilon(t)$, t fixed, $\epsilon \to 0$, do not converge to anything, since $E\,|X_\epsilon(t)|^2 \to \infty$ as $\epsilon \to 0$. Nevertheless, for each t we do have

$$X_\epsilon(t) - X_\epsilon(0) \to Y(t) - Y(0)$$

in mean-square, as $\epsilon \to 0$.

Proof: Let $\Delta Y(t) = Y(t) - Y(0)$, and similarly for X_ϵ. Then

$$\Delta X_\epsilon = \int_{-\infty}^{\infty} \frac{\exp(i\omega t) - 1}{i\omega}\left(1 - K\left(\frac{\omega}{\epsilon}\right)\right) dZ(\omega) \tag{41}$$

Equations (41), (7), and (4) give

$$E\,|\Delta Y(t) - \Delta X_\epsilon(t)|^2 = \int_{-\infty}^{\infty}\left(\frac{\sin \omega t/2}{\omega/2}\right)^2 \left|- K\left(\frac{\omega}{\epsilon}\right)\right|^2 f(\omega)d\omega$$

Since

$$\left(\frac{\sin \omega t/2}{\omega/2}\right)^2 (1 + \omega^2) \leq t^2 + 4$$

we have

$$E\,|\Delta Y(t) - \Delta X_\epsilon(t)|^2 \leq (t^2 + 4) \int_{-\infty}^{\infty} \left|- K\left(\frac{\omega}{\epsilon}\right)\right|^2 \frac{f(\omega)}{1 + \omega^2}\,d\omega \tag{42}$$

which, by Lebesgue's dominated convergence theorem, tends to 0 as $\epsilon \to 0$.

If h is a time window satisfying Eq. (17), then (42) implies

$$\int_{-\infty}^{\infty} \Delta X_\epsilon(t)h(t)dt \to \int_{-\infty}^{\infty} \Delta Y(t)h(t)dt \tag{43}$$

in mean-square, as $\epsilon \to 0$. If h is also a high-pass filter, then

$$\int_{-\infty}^{\infty} X_\epsilon(t)h(t)dt \to \int_{-\infty}^{\infty} Y(t)h(t)dt$$

so that in this case, the method of cutoffs fits smoothly into our model.

Strictly speaking, we have not expressed $\Delta Y(t)$ as a limit of stationary processes, but rather as the limit of $\Delta X_\epsilon(t)$, which is not stationary but has stationary increments [and a *formal* spectral density (Eq. 40)]. The stationary process X_ϵ, ϵ very small, would not be a good model for flicker noise because in this case $E\,|X_\epsilon(t)|^2$ is large for all t. An appropriate model might be ΔX_ϵ, but then we might as well use Y, which does not have an extra parameter ϵ to make calculations messier.

VIII. The Barnes–Allan Model

In 1966, Barnes and Allan (Ref. 17) exhibited a flicker noise model and calculated its Allan variance. (See Section IV for a definition.) We have examined the behavior of our own model under a general class of measurements, and will now do the same for the Barnes–Allan model. The details of the derivations will be omitted.

Their model for the frequency $\Phi'(t)$ of an oscillator (Φ is the phase) is given by

$$\Phi'(t) = \frac{1}{\sqrt{\pi}} \int_0^t \frac{1}{(t-u)^{1/2}}\, dW(u), \qquad t \geq 0 \tag{44}$$

where dW is white noise. Actually, this stochastic integral does not exist, since

$$\int_0^t \frac{du}{t-u} = \infty$$

Nevertheless, Eq. (44) defines a *generalized* process; that is, we can give a meaning to

$$\int_0^\infty \Phi'(t)h(t)dt \tag{45}$$

for suitable time windows h by formally plugging Eq. (44) into (45) and reversing orders of integration. (The real reason that Φ is not an ordinary process is that there is no high-frequency cutoff of the $1/|\omega|$ spectral behavior.)

From here on, let h be of bounded variation and equal to 0 outside some interval $[0,b]$. Let R be the square of the absolute value of Eq. (45). We are able to show that

$$ER = \frac{1}{2\pi} \int_{-\infty}^{\infty} |H(\omega) - H^*(\omega)|^2 \frac{d\omega}{|\omega|} \tag{46}$$

where H is given by (14) and

$$H^*(\omega) = \int_0^\infty H(\omega\xi)p(\xi)d\xi \tag{47}$$

$$p(\xi) = \frac{1}{\pi(1+\xi)\xi^{1/2}}$$

Since $\int p = 1$, $H^*(\omega)$ is a weighted average of H. Formula (46) is analogous to (18). In our own model Y, we set $Z_o = 0$ and $f(\omega) = |\omega|\, g(\omega)$, where $g(\omega) \to 1$ as $\omega \to 0$. Then (18) becomes

$$EQ = \int_{-\infty}^{\infty} |H(\omega) - H(0)|^2 g(\omega) \frac{d\omega}{|\omega|} \tag{48}$$

Since Y has stationary increments, the starting time T of measurements does not matter, provided we replace $Y(t) - Y(0)$ by $Y(T+t) - Y(T)$. This is not the case for Φ', as Barnes and Allan recognize. Therefore we first consider h of form

$$h(t) = \frac{1}{\tau} k\left(\frac{t-T}{\tau}\right)$$

where k is not necessarily high-pass. If we set $Y(T) = 0$, then EQ depends only on τ, namely,

$$EQ = \int_{-\infty}^{\infty} |K(y) - K(0)|^2 g\left(\frac{y}{\tau}\right) \frac{dy}{|y|} \tag{49}$$

and

$$EQ \to \int_{-\infty}^{\infty} |K(y) - K(0)|^2 \frac{dy}{|y|} \qquad \text{as } \tau \to \infty \tag{50}$$

On the other hand, ER depends only on $\rho = T/\tau$, and we can show that

$$ER \to \frac{1}{2\pi} \int_{-\infty}^{\infty} |K(y) - K^*(y)|^2 \frac{dy}{|y|} \qquad \text{as } \rho \to 0 \tag{51}$$

$$ER \to \frac{1}{2\pi} \int_{-\infty}^{\infty} |K(y)|^2 \frac{dy}{|y|} \qquad \text{as } \rho \to \infty \tag{52}$$

If K is high-pass, $K(0) = 0$, then all these limits are finite. For the special case of Allan variance, Barnes and Allan keep τ fixed and let $T \to \infty$ since (Ref. 17) "flicker noise is normally observed on equipment which has been operating for long periods of time." From Eqs. (52) and (50), we see that $2\pi \lim_{T\to\infty} ER = \lim_{T\to\infty} EQ$. Thus, $2\pi ER$ and EQ are almost equal for large τ and $T >> \tau$. If we keep T fixed and let $\tau \to \infty$, then EQ approaches the right side of (50), whereas ER approaches the right side of (51).

If K is not high-pass, $K(0) \neq 0$, then the right sides of (50) and (52) are infinite, whereas (51) is still finite. If τ is large and $T >> \tau$, then EQ and ER are both large. If T is fixed and $\tau \to \infty$, then $EQ \to \infty$, while ER remains finite. Because of the ambiguity of T, the Barnes–Allan model cannot be used to predict the dependence of R on τ if $K(0) \neq 0$, while (49) does exactly that for Q. In fact, it is easy to see that EQ grows like $\log \tau$.

We have also calculated the expected modified periodogram of Φ' for the case $T = 0$. This is the expectation of the expression (24) with X replaced by Φ'. If k is of bounded variation on $[0,1]$, an effort as in Section V shows that the expected modified periodogram tends to

$$\frac{1}{2\pi|\omega_o|} \int_0^1 |k(x)|^2 dx$$

as $|\omega_0|\tau \rightarrow \infty$. Thus, the Barnes–Allan model does display a $1/|\omega|$ behavior when subjected to a spectral measurement.

The two models Y and Φ' are closely related. Formulas (46) and (48) display the relationship in the spectral domain. It is possible to generate a formula for $Y(t)$ in the time domain by passing white noise through a certain realizable filter, then integrating. The resulting expression splits naturally into two parts, one of which resembles (44). This part is actually a version of the Barnes–Allan model that cuts off the $1/|\omega|$ behavior at high frequencies.

IX. Future Prospects

We see two directions for further work. First of all, we would like to make more comparisons of the behavior of actual flicker noise with the behavior of our model Y and the Barnes–Allan model Φ'. These models already agree with the experiments involving high-pass filter averaging and direct measurements of spectral density, but Φ' has some difficulty predicting the result of non-high-pass filter averages. Averaging experiments could be done on flicker noise data to search for the logarithmic dependence on integration time that Eq. (49) predicts for Y.

Secondly, it would be desirable to search for physical mechanisms that could generate either model Y or Φ'. Since we have described only second-moment properties of these models, each model can be realized in a variety of ways. Instead of using Brownian motion to generate the model, we can start with other processes with orthogonal increments. For example, if we started with a suitably modified Poisson process, we would get some form of nonstationary shot noise. Such a noise might occur in the frequency of an oscillator subject to infrequent but sudden random disturbances.

References

1. Atkinson, W. R., Fey, R. L., and Newman, J., "Spectrum Analysis of Extremely Low Frequency Variations of Quartz Oscillators," *Proc. IEEE* (Correspondence), Vol. 51, 1963, p. 379.
2. Firle, T. E., and Winston, H., "Noise Measurements in Semiconductors at Very Low Frequencies, *J. Appl. Physics,* Vol. 26, pp. 716–717.
3. Allan, D. W., "Statistics of Atomic Frequency Standards," *Proc. IEEE*, Vol. 54, No. 2, Feb. 1966, pp. 221–230.
4. Barnes, J. A., "Atomic Timekeeping and the Statistics of Precision Signal Generators," *Proc. IEEE,* Vol. 54, No. 2, Feb. 1966, pp. 207–220.
5. Cutler, L. S., and Searle, C. L., "Some Aspects of the Theory and Measurement of Frequency Fluctuations in Frequency Standards," *Proc. IEEE,* Vol. 54, No. 2, Feb. 1966, pp. 136–154.
6. Vessot, R., Mueller, L., and Vanier, J., "The Specification of Oscillator Characteristics From Measurements Made in the Frequency Domain," *Proc. IEEE,* Vol. 54, No. 2, Feb. 1966, pp. 199–207.
7. Barnes, J. A., et al., *Characterization of Frequency Stability,* NBS Technical Note 394, National Bureau of Standards, U. S. Department of Commerce, Washington, D. C., 1970.
8. Gray, R. M., and Tausworthe, R. C., "Frequency Counted Measurements and Phase Locking to Noisy Oscillators," *IEEE Trans. Communications Technology,* Vol. COM-19, 1971, pp. 21–30.

References (contd)

9. Cramér, H., and Leadbetter, M. R., *Stationary and Related Stochastic Processes,* John Wiley & Sons, Inc., New York, N. Y., 1967.

10. Yaglom, A. M., *Correlation Theory of Processes With Random Stationary n^{th} Increments,* American Mathematical Society Translations, Series 2, Vol. 8, American Mathematical Society, Providence, R. I., 1958, pp. 87–141.

11. Yaglom, A. M., *An Introduction to the Theory of Stationary Random Functions,* Prentice-Hall, Inc., Englewood Cliffs, N. J., 1962.

12. Grenander, U., and Rosenblatt, M., *Statistical Analysis of Stationary Time Series,* John Wiley & Sons, Inc., New York, N. Y., 1957.

13. Rosenblatt, M., *Random Processes,* Oxford University Press, New York, N. Y., 1962.

14. Rozanov, Yu. A., *Stationary Random Processes,* Holden–Day, San Francisco, Calif., 1967.

15. Bingham, C., Godfrey, M. D., and Tukey, J. W., "Modern Techniques of Power Spectrum Estimation," *IEEE Trans. Audio and Electroacoustics,* Vol. AU-15, 1967, p. 56 ff.

16. Tukey, J. W., "Spectrum Calculations in the New World of the Fast Fourier Transform," Lecture Notes from the Advanced Seminar on Spectral Analysis of Time Series at the Army Mathematics Research Center and Statistics Department, University of Wisconsin, Madison, Wis., Oct. 3, 1966.

17. Barnes, J. A., and Allan, D. W., "A Statistical Model of Flicker Noise," *Proc. IEEE,* Vol. 54, No. 2, Feb. 1966, pp. 176–178.

Matrix Multiplication With Fixed Matrices and Polynomial Evaluation With Fixed Polynomials

J. E. Savage[1]
Communications Research Section

Others have shown that the conventional method for computing $m \times n$ matrix-vector products and Horner's rule for evaluating polynomials are optimal when matrix and vector elements as well as polynomial coefficients and polynomial variables are indeterminate. In this article, the calculation of matrix-vector products and the evaluation of polynomials are treated when the matrix elements and polynomial coefficients are known and drawn from a set of size s. It is shown that the algorithms which are optimal for indeterminate matrix entries and polynomial coefficients are nonoptimal when s is fixed and the entries and coefficients are known. Good algorithms for this case are given and tight bounds are derived on the combinational complexity of the most complex matrix-vector function and the most complex polynomial evaluation function. These are operations used in the Deep Space Station computers for decoding telemetry and interpolating ephemerides for antenna pointing and programmed oscillators.

I. Introduction

The two problems treated in this article are the calculations of matrix-vector products and the evaluation of a set of polynomials. The first problem causes most of the combinational complexity in DSN telemetry decoders, and the second tends to overload programmable oscillator minicomputers in high doppler situations such as in planetary orbiters (see Ref. 1 for a data decoder assembly article).

The multiplication of an $m \times n$ matrix A with entries $\{a_{ij}\}$ by an n-vector

$$\mathbf{x} = (x_1, \cdots, x_n)$$

[1]Division of Engineering and Center for Computer and Information Science, Brown University, Providence, Rhode Island, and consultant, Communications Research Section. A portion of the research reported here was completed at Brown University with the support of grants NSF GJ-32 270 and DA-ARO-D-31-124-73-G65.

is defined by

$$f_i(x_1, \cdots, x_n) = a_{i1} * x_1 + \cdots + a_{in} * x_n, \qquad 1 \leq i \leq m \tag{1}$$

where $*$ denotes multiplication and $+$ denotes addition. The evaluation of m polynomials, $b_1(z), \cdots, b_m(z)$ of degree n in one variable z is defined by

$$b_i(z) = b_{i0} + b_{i1} * z + b_{i2} * z^2 + \cdots + b_{in} * z^n, \qquad 1 \leq i \leq m \tag{2}$$

where $*$ and $+$ are the multiplication and addition operators and $z^j = z \cdot z^{j-1}$ denotes the j-fold product of z with itself.

The obvious way to do matrix-vector multiplication is that indicated by Eq. (1) and requires mn $*$ operations and $m(n-1)$ $+$ operations. Polynomials can be evaluated with Horner's rule, namely,

$$b_i(z) = b_{i0} + z(b_{i1} + \cdots) \cdots)$$

which is not so obvious and which uses mn $*$'s and mn $+$'s. It can be shown (Refs. 2, 3, and 4) that no fewer than these numbers of operations are sufficient when the matrix entries, vector entries, polynomial coefficients, and the parameter z are indeterminates (or are isomorphic to indeterminates).

In this article, it is assumed that the vector elements $\{x_1, x_2, \cdots, x_n\}$ and the parameter z are the only indeterminate elements and that the matrix entries $\{a_{ij}\}$ are known, fixed, and drawn from a set of size s, a typical DSN situation. Then the functions $\{f_1, f_2, \cdots, f_m\}$ are functions of n variables and the polynomials $\{b_1(z), \cdots, b_m(z)\}$ are functions of one variable. By exhibiting algorithms, we shall show that the set $\{f_1, \cdots, f_m\}$ can be computed with approximately $mn \, \ell n(s)/\ell n(m)$ operations and the set $\{b_1(z), \cdots, b_m(z)\}$ can be computed with about $mn \, \ell n(s)/\ell n(mn)$ operations, for m and n large. Furthermore, counting arguments will be derived to show that under suitable conditions these upper bounds can be improved upon by at most constant factors for the worst-case matrix and worst-case set of polynomials.

We conclude that algorithms for computing matrix-vector products for fixed matrices and for evaluating a specific set of polynomials are asymptotically less expensive to realize than algorithms which compute any $m \times n$ matrix-vector product or for evaluating any set of m n-degree polynomials. These results also hold when the number of values assumed by matrix elements and by polynomial coefficients is bounded.

II. Preliminaries

Let $\mathbf{f} = \{f_1, \cdots, f_m\}$ be the set of functions realized by the matrix-vector product and let

$$\mathbf{f} = A\mathbf{x} \tag{3}$$

represent the m expressions defined in Eq. (1), where $\mathbf{x} = (x_1, \cdots, x_n)$. Assume that the x_i are indeterminate over the set S so that $\mathbf{f}: S^n \rightarrow S^m$, where S^n denotes the n-fold Cartesian product of S with itself. Since the coefficients $\{a_{ij}\}$ in Eq. (1) are assumed drawn from a finite set, without loss of generality, we let a_{ij} be chosen from among $\{1, 2, \cdots, s\}$ and regard the $*$ operation $a_{ij} * x_j$ to be the pth unary operation $U_p(x_j)$, $U_p: S \rightarrow S$, when $a_{ij} = p$. We also define $+: S^2 \rightarrow S$ to be an associative binary operation and call it addition. Also, we assume that S contains the additive unit o satisfying $o + x = x + o = x$.

The following examples illustrate the generality of this formulation:

(1) Let $s = 2$, $U_1(x_j) = 0$, $U_2(x_j) = x_j$. Then, the algebraic system $< S, + >$ is a semigroup such as:

- (a) $S = R$ (reals), $+$ denotes either multiplication or addition.
- (b) $S = \{0, 1\}$, $+$ denotes the Boolean AND, OR, or EXCLUSIVE OR.

(2) (a) $S = R$, $U_p(x) = r_p * x$, $r_p \varepsilon R$, $*$ denotes multiplication on reals and $+$ denotes addition on reals.

- (b) $S = D^{q \times q}$ (set of $q \times q$ matrices over D), $U_p(x) = x^p$, the pth power of the matrix x, $+$ denotes matrix addition.
- (c) $S = \{0, 1\}$, $U_1(x) = \bar{x}$ (Boolean complement), $U_2(x) = x$, f_i are called minterms.

The polynomials defined by Eq. (2) are $\{b_1(z), \cdots, b_m(z)\}$ as above. Let $z \varepsilon S$ so that $b_i: S \rightarrow S$ and let b_{ij} be in $\{1, 2, \cdots, s\}$, $b_{ij} * z^j$ denote the unary operation $U_p(z^j)$, $U_p: S \rightarrow S$, when $b_{ij} = p$. Also, let $\cdot$ and $+$ be binary associate operations, $\cdot: S \times S \rightarrow S$, $+: S \times S \rightarrow S$, let $\cdot$ distribute over $+$ and let z^j be defined by $z^j = z \cdot z^{j-1}$. Examples are:

(1) $S = R$ (reals), $U_p(z^j) = r_p * z^j$, $r_p \varepsilon R$, and $* = \cdot$ and is multiplication on reals, and $+$ is real addition.

(2) $S = D^{q\times q}$, $s = 2$, $\cdot$ and $+$ denote matrix product and addition and $U_1(z^j) = 0$, $U_2(z^j) = z^j$.

The complexity of a set of functions $\{g_1, g_2, \cdots, g_m\}$ over S, $g_i : S^{t_i} \to S$, will be measured by the minimum number of steps to realize the set with *straight-line algorithms* (SLAs). The relationships between this measure and conventional measures of complexity such as storage and time are discussed in Ref. 5.

Definition. Let $\Omega = \{h_i \mid h_i : S^{n_i} \to S\}$ be a finite set of functions over S, called the *basis*, and let $\Gamma = \{x_1, \cdots, x_k, K\}$, called the *data set*, be a set of k indeterminates over S and $K \subset S$, a set of constants. Then a q-step SLA, $\beta = (\beta_1, \cdots, \beta_q)$, is an ordered set of q-steps $\{\beta_1, \cdots, \beta_q\}$ where either $\beta_j \in \Gamma$ (a data step), or

$$\beta_j = (h_i\,; \beta_{j_1}, \cdots, \beta_{j_{n_i}}), \qquad j_1, \cdots, j_{n_i} < j$$

that is, β_j is a computation step which results from a basis function operating on previous steps. The SLA computes the set of functions $\{\overline{\beta}_1, \cdots, \overline{\beta}_q\}$ where

$$\overline{\beta}_j = \begin{cases} \beta_j & \text{if } \beta_j \in \Gamma \\ h_i(\overline{\beta}_{j_1}, \cdots, \overline{\beta}_{j_{n_i}}) & \text{otherwise} \end{cases}$$

Definition. To each basis element h_i, assign cost $c_i > 0$. Then, the cost of an SLA β, $x(\beta)$, is defined by

$$x(\beta) = \sum_{i=1}^{|\Omega|} q_i c_i$$

where q_i is the number of occurrences of h_i in β and $|\Omega|$ is the number of basis functions. The *combinational complexity* of the set of functions $g = \{g_1, \cdots, g_m\}$, $g_i : S^{t_i} \to S$, $C_\Omega(g)$, is the minimum of $x(\beta)$ over all SLAs β which compute g and undefined (or infinite) if there is no β with basis Ω which computes g.

III. Upper Bounds

Let $C_{m,n}$ denote the maximal combinational complexity of the $m \times n$ matrix-vector product functions and let $D_{m,n}$ be the same for the most complex set of m polynomials of degree n. In this section, upper bounds to $C_{m,n}$ and $D_{m,n}$ are derived by construction of SLAs. Lower bounds to these quantities are derived in the next section.

We sketch SLAs for evaluation of $\mathbf{f} = A\mathbf{x}$ and of $\{b_1(z), \cdots, b_m(z)\}$. We begin with the matrix-vector product problem. Represent the n-vector $\mathbf{x}$ as

$$t_0 = \left\lceil \frac{n}{k} \right\rceil$$

($\lceil x \rceil$ is the smallest integer $\geq x$) subvectors

$$\mathbf{x} = (\mathbf{x}^1, \mathbf{x}^2, \cdots, \mathbf{x}^{t_0})$$

where

$$\mathbf{x}^i = (x_{(i-1)k+1}, \cdots, x_{ik})$$

for $1 \leq i \leq t_0 - 1$ and

$$\mathbf{x}^{t_0} = (x_{(t_0-1)k+1}, \cdots, x_n)$$

Let A be subdivided into t submatrices $B_1, B_2, \cdots, B_{t_0}$

$$A = [B_1 \quad B_2 \quad \cdots \quad B_t]$$

where B_i is $m \times k$, $1 \leq i \leq t_0 - 1$ and B_{t_0} is $m \times r$ where $r = n - (t_0 - 1)k$. Then, $\mathbf{f} = A\mathbf{x}$ can be computed as follows:

(1) Form the t_0 matrix-vector products

$$\mathbf{y}^i = B_i \mathbf{x}^i \qquad 1 \leq i \leq t_0 \tag{4}$$

(2) Do vector addition of these products to form $\mathbf{f}$.

$$\mathbf{f} = \mathbf{y}^1 + \cdots + \mathbf{y}^{t_0} \tag{5}$$

This decomposition is possible because the binary operation of addition is associative. Also, we shall show that the products $B_i\mathbf{x}^i$ can be done with significantly fewer operations than are required for the obvious method of matrix-vector multiplication. This will translate into a savings for the computation of $\mathbf{f}$.

Consider polynomial evaluation next. Represent a polynomial $b_i(z)$ as

$$b_i(z) = P_{i1}(z) + P_{i2}(z) \cdot z^k + \cdots + P_{it}(z) \cdot z^{(t_1-1)k} \tag{6}$$

where each $P_{ij}(z)$ is a polynomial of degree $k - 1$ and

$$t_1 = \left\lceil \frac{n+1}{k} \right\rceil$$

This representation is unique and possible because $+$ and $\cdot$ are associative and $\cdot$ distributes over $+$. The algorithm which shall be given for evaluating a set of polynomials will generate all polynomials of degree $k - 1$, use them in the appropriate places, and follow them with the

necessary multiplications by terms z^j and the necessary additions.

Theorem 1. Let Ω contain the binary operation $+$ and the unary operators $\{U_1, \cdots, U_s\}$. If c_a is the cost of $+$, then

$$C_{m,n} \leq \left(\left\lceil \frac{n}{k} \right\rceil - 1\right) C_{m,k} + C_{m,r} + \left(\left\lceil \frac{n}{k} \right\rceil - 1\right) mc_a \tag{7}$$

Proof. In the decomposition of Eqs. (4) and (5),

$$\left(\left\lceil \frac{n}{k} \right\rceil - 1\right) C_{m,k} + C_{m,r}$$

is the cost of computing $\mathbf{y}^1, \cdots, \mathbf{y}^{t_0}$. With a total of

$$\left(\left\lceil \frac{n}{k} \right\rceil - 1\right)$$

additions per component of $\mathbf{f}$, $\mathbf{f}$ can be formed. Since this decomposition may not be the best way to realize $\mathbf{f}$, Eq. (7) follows.

Theorem 2. Let Ω contain the two binary operations $+$ and $\cdot$ and the unary operators $\{U_1, \cdots, U_s\}$. Also, let $U_s(x) = x$ be the identity operator. If c_a is the cost of $+$ and c_b is the cost of $\cdot$, then

$$D_{m,n} \leq D_{N,k-1} + \left(\left\lceil \frac{n+1}{k} \right\rceil - 1\right) (mc_a + (m+1)c_b) \tag{8}$$

where $N = s^k$ is the number of polynomials of degree $k-1$.

Proof. In the decomposition of Eq. (6), all of the polynomials $P_{ij}(z)$ are fixed. There are at most $N = s^k$ of them and they can *all* be realized with a combinational complexity of $D_{N,k-1}$. To form Eq. (6), compute $z^k, \cdots, z^{(t_1-1)k}$. This can be done with $(t_1 - 1)$ $\cdot$'s since z^{k-1} is available as a polynomial of degree $k-1$. Form the $t_1 - 1$ products $P_{ij}(z) \cdot z^j$, $1 \leq j \leq t_1 - 1$, for each $i, 1 \leq i \leq m$ and do the indicated additions. A total of $m(t_1 - 1)$ additions and $(m+1)(t_1-1)$ multiplications will be done. Then Eq. (8) follows since this is but one method for computing $\{b_1(z), \cdots, b_m(z)\}$.

These two theorems will prove useful when bounds to $C_{m,k}$ and $D_{N,k-1}$ have been derived. This is the next task.

Lemma 1. Let Ω contain $+$ and $\{U_1, \cdots, U_s\}$.

Let $\varepsilon = 1$ if one of the unary operators, say U_1, is the o-ary operator, $U_1(x_j) = 0$, and let $\varepsilon = 0$, otherwise. Let c_p be the cost of U_p, $1 \leq p \leq 2$, and let

$$K_1 = mk\left(\max_{1 \leq l \leq s} c_l\right) + m(k-1)c_a$$

$$K_2 = \begin{cases} k(c_1 + \cdots + c_s) + c_a(s^{k+1} - s^2)/(s-1) & \varepsilon = 0 \\ k(c_1 + \cdots + c_s - (s-1)c_a) + c_a(s^k - 1) & \varepsilon = 1 \end{cases}$$

then

$$C_{m,k} \leq \min(K_1, K_2)$$

Proof. The K_1 bound follows from the standard aglorithm for matrix-vector multiplication.

The K_2 bound is derived by first noting that all s unary operations on $x_1, \cdots, x_k$ can be performed at a cost of $k(c_1 + c_2 + \cdots + c_s)$ and then determining the number of additions to form all s^k sums of the form

$$U_{l_1}(x_1) + \cdots + U_{l_k}(x_k)$$

If all such sums are available, all functions $\mathbf{f} = A\mathbf{x}$ can be computed since there are at most s^k such distinct functions.

We show by induction that all s^k sums can be formed with at most $s^2 + s^3 + \cdots + s^k = (s^{k+1} - s^2)/(s-1)$ additions. Clearly, all sums in two variables can be formed with s^2 additions. Assume that all s^{k-1} sums in $k-1$ variables $k \geq 3$ can be performed with $s^2 + \cdots + s^{k-1}$ additions. For each of these s^{k-1} sums, s additions are formed to adjoin $\{U_l(x_k), 1 \leq l \leq s\}$, for a total of s^k new additions. Thus, all sums of k variables can be done with $s^2 + s^3 + \cdots + s^k$ additions, and the induction hypothesis holds.

If there is a unary operator $U_1 = 0$, some additions are unnecessary. Form all sums

$$U_{l_i}(x_i) + U_{l_j}(x_j), \quad l_i \geq 2, \quad l_j \geq 2, \quad i \neq j, \quad 1 \leq i, \quad j \leq k$$

with one addition per sum. All sums

$$U_{l_i}(x_i) + U_{l_j}(x_j) + U_{l_p}(x_p), \quad l_i \geq 2, \quad l_j \geq 2, \quad l_p \geq 2$$

can be formed with one more addition per sum. Hence, all the sums can be formed with a number of additions

equal to the number of terms requiring one or more additions. Since there is one 0 sum and $k(s-1)$ sums involving one nonzero unary operation, all sums can be formed with $s^k - k(s-1) - 1$ additions when $\varepsilon = 1$.

The next result is a bound on $D_{N,k-1}$.

Lemma 2. Let Ω contain $+$, $\cdot$, and $\{U_1, \cdots, U_s\}$. Let c_a, c_b, and c_p be the costs of $+$, $\cdot$, and U_p, $1 \leq p \leq s$, respectively. Also, assume that $U_s(x) = x$, $c_s = 0$, and let $\varepsilon = 1$ if $U_1(x) = 0$ and let $\varepsilon = 0$ if $U_1(x) \neq 0$. Then, when $N = s^k$,

$$D_{N,k-1} \leq h(k)\, c_b + k(c_1 + c_2 + \cdots + c_{s-1}) + K_2$$

where K_2 is defined above and $h(k) = k - 2$ if $k \geq 2$ and $h(k) = 0$, otherwise.

Proof. $D_{N,k-1}$ is the combinational complexity of the most complex set of s^k polynomials of degree $k-1$. Clearly, this is the set of all polynomials of degree $k-1$.

Realize these polynomials as follows: (1) construct the sequence $1, z, z^2, \cdots, z^{k-1}$ *using* $h(k)$ $\cdot$*'s; (2) to each term* apply $U_1, U_2, \cdots, U_{s-1}$ at a cost of $k(c_1 + c_2 + \cdots + c_{s-1})$; (3) then add the k terms. This last step has cost K_2, as shown in the proof of Lemma 1.

These two lemmas and two theorems are combined to give asymptotic bounds on the combinational complexity of matrix-vector multiplication and polynomial evaluation.

Theorem 3. Under the conditions of Theorem 1 and Lemma 1,

$$C_{m,n} \leq \left\lceil \frac{n}{k} \right\rceil (K_2 + mc_a) - mc_a$$

and for m, n large

$$C_{m,n} \leq \frac{mnc_a}{\log_s m}\left(1 + 0\left(\frac{1}{\log_s m}\right) + 0\left(\frac{1}{n}\right)\right)$$

Proof. The first inequality follows directly from Theorem 1 and Lemma 1 since $C_{m,r} \leq C_{m,k}$.

The second inequality follows from a long but uncomplicated set of steps when

$$k = \lceil \log_s [(m/s)/\log_s (m/s)] \rceil$$

Theorem 4. Under the conditions of Theorem 2 and Lemma 2,

$$D_{m,n} \leq \frac{n(mc_a + (m+1)c_b)}{\log_s (mn)} (1 + 0(1/\ln(mn)))$$

for large n where c_a and c_b are the cost of $+$ and $\cdot$, respectively.

Proof. The theorem follows from Theorem 2 and Lemma 2 when

$$k = \lceil \log_s ((mn)/s(\log_s (mn/s))^2) \rceil$$

Table 1 shows the first bound of Theorem 3 to $C_{m,n}$ optimized under variation of k, when $m = n$ is a power of 2, $s = 2$, $c_a = 1$, $c_1 = c_2 = 0$ and $\varepsilon = 1$ (i.e., $U_1(x) = 0$). It also shows the ratio of the K_1 bound to this bound. The improvement over the K_1 bound is substantial and for large binary matrices recommends the method of matrix-vector multiplication by decomposition.

Table 2 shows the bound to D_{1n} when $c_a = c_b = 1$, $c_1 = c_2 = 0$ and $\varepsilon = 1$, which follows from Theorem 2 and Lemma 2. Also shown is the ratio of $2n$, the number of operations for Horner's rule, and this bound. The improvement is substantial for large n and warrants use of the algorithm introduced above.

IV. Lower Bounds

In this section, an upper bound is derived on the number of distinct sets of m functions $\{g_1, \cdots, g_m\}, g_j : S^n \to S$, with $C_\Omega(g_1, \cdots, g_m) \leq C$. If C is not large enough, not all sets of such functions can be realized at a cost $\leq C$. Consequently, at least one set must have combinational complexity $> C$. This result is used to derive lower bounds to $C_{m,n}$ and $D_{m,n}$ and to show that the upper bounds given above are tight under suitable conditions.

Let $N_\Omega(C, m, p)$ be the number of distinct sets of m functions in p variables $\{g_1, \cdots, g_m\}, g_j : S^p \to S$, with $C_\Omega(g_1, \cdots, g_m) \leq C$.

Lemma 3. Let all operations in Ω be either unary or binary. *Then, for* $p \geq 6$,

$$N_\Omega(C, m, p) < |\Omega|^{C/c^*} (p + |K| + C/c^*)^{2(p+|K|+C/c^*+(m-1)/2)}$$

where $c^* > 0$ is the cost of the minimum cost operation and $K \subset S$ *is the set of constants in the data set.*

Proof. Consider SLAs in which variable data steps precede constant data steps and these precede computation steps. There is no loss of generality in this assumption.

Let an SLA β have $p' \leq p$ variable data steps $x_{i_1}, \cdots, x_{i_{p'}}$, drawn without replacement from $\{x_1, \cdots, x_p\}$. There are

$$\binom{p}{p'} < 2^p$$

ways to do this.

Let the SLA β have $d \leq |K|$ constant data steps. There are

$$\binom{|K|}{d} < 2^{|K|}$$

ways to choose these d constants.

Also, let β have t computation steps $(h_i; \beta_{i_1}, \beta_{i_2})$ where β_{i_2} may be empty if h_i is unary. There are at most $M(p', d, t)$ such steps, where

$$M(p', d, t) = |\Omega|^t \prod_{j=p'+d}^{p'+d+t} (j-1)^2$$

To β we associate sets of m functions. One function of each set must be associated with the last step (otherwise, the SLA is not optimal) and the remaining $m-1$ functions of each set can be assigned in at most $(p' + d + t - 1)^{m-1}$ ways.

There are at most $L(p', d, t)$ sets of m functions associated with SLAs with p' variable data steps, d constant data steps, and t computation steps, and

$$L(p', d, t) \leq 2^{p+|K|} (p' + d + t)^{m-1} M(p', d, t)$$

This bound is clearly monotonically increasing in p', d, and t.

Since $N_\Omega(C, m, p)$ is the sum of $L(p', d, t)$ over $0 \leq p' \leq p$, $0 \leq d \leq |K|$ and $0 \leq t \leq T$ where $T = \lfloor C/c^* \rfloor$ ($\lfloor x \rfloor$ is the largest integer $\leq x$) and $c^* > 0$ is the cost of the minimum cost basis function,

$$N_\Omega(C, m, p) \leq (p+1)(|K|+1)(T+1) 2^{p+|K|} \times (p + |K| + T)^{m-1} M(p, |K|, T)$$

It is easily shown that

$$\sum_{v=L}^{Q} \ln v \leq \int_L^{Q+1} \ln x \, dx = x \ln\left(\frac{x}{e}\right)\Bigg|_L^{Q+1}, \qquad L \geq 0$$

so that

$$M(p, |K|, T) \leq |\Omega|^T \left(\frac{p + |K| + T}{e}\right)^{2(p+|K|+T)} \times \left(\frac{p + |K| - 1}{e}\right)^{-2(p+|K|-1)}$$

Then, combining terms, we have

$$N_\Omega(C, m, p) \leq \left[\frac{(p+1)(T+1)}{e^{2(p+|K|+T)}}\right]\left[\frac{(|K|+1) 2^{p+|K|}}{\left(\frac{p+|K|-1}{e}\right)^{2(p+|K|-1)}}\right] \cdot |\Omega|^T (p + |K| + T)^{2(p+|K|+T+(m-1)/2)}$$

It can be shown that the first bracketed term is monotonically decreasing in T and p and has value ≤ 1 at $T = p = 0$. The second bracketed term is monotonically decreasing in increasing $|K|$ for $p \geq 4$ and is < 1 for $p \geq 6$. From this and $T \leq C/c^*$, the theorem follows.

It remains to apply Lemma 3 in order to derive lower bounds for $C_{m,n}$ and $D_{m,n}$.

Theorem 5. Let Q be the number of distinct sets of m functions $\{g_1, \cdots, g_m\}$, $g_j : S^p \to S$, in the set $\mathcal{N}$. Then, if $C(\mathcal{N})$ is the maximum of $C_\Omega(g_1, \cdots, g_m)$,

$$C(\mathcal{N}) \geq \frac{c^*}{2} \frac{\ln Q}{\ln(\ln Q) + \ln(|\Omega|/2)} - c^*(p + |K| + (m-1)/2)$$

for $p \geq 6$ when $|\Omega| \ln Q \geq 2e$ and $c^* > 0$ is the cost of the minimum cost basis function.

Proof. Let C_0 satisfy

$$2x(\ln x + \ln|\Omega|) = \ln Q$$

where

$$x = p + |K| + (C_0/c^*) + (m-1)/2$$

Then, it is easy to show that $N_\Omega(C_0, m, p) < Q$. Consequently, for some set

$$\{g_1, \cdots, g_m\} \in \mathcal{N}, \qquad C_\Omega(g_1, \cdots, g_m) \geq C_0$$

We solve for C_0. The equation above is rewritten as

$$y \ln y = \frac{|\Omega|}{2} \ln Q = B$$

where $y = x|\Omega|$. The function $y \ln y$ is monotonically increasing for $y \geqq 1$ and at $y = y_1 = B/\ln B$ we have

$$y_1 \ln y_1 = \frac{B}{\ln B}(\ln B - \ln\ln B) < B$$

if $\ln\ln B \geqq 0$ or $B \geqq e$. Therefore, the solution y is

$$y \geqq y_1 = \frac{\frac{|\Omega|}{2}\ln Q}{\ln(\ln Q) + \ln(|\Omega|/2)}$$

if $|\Omega|\ln Q \geqq 2e$ and it follows from

$$y = (p + |K| + (C_0/c^*) + (m-1)/2\,|\Omega|$$

that

$$C_0 \geqq \frac{c^*}{2}\,\frac{\ln Q}{\ln(\ln Q) + \ln(|\Omega|/2)} - c^*(p + |K| + (m-1)/2)$$

This completes the proof.

Note that the proof of Theorem 5 and Lemma 3 requires that the cost of all basis functions be greater than zero. Thus, if basis functions of zero cost exist, they cannot be used if these results are to apply. We now specialize these results to matrix-vector multiplication and polynomial evaluation.

Corollary 1. If all of the s^n $1 \times n$ matrix-vector functions are distinct and if there are α_1, α_2 with $0 < \alpha_1 < \alpha_2 < \infty$ such that $\alpha_1 \leqq m/n \leqq \alpha_2$, then

$$C_{m,n} \geqq \frac{c^*\,mn}{4\log_s(m)}(1 + 0(1/\ln(m)))$$

for $|\Omega|$, $|K|$, and s fixed and m, n large.

Proof.

$$Q = \binom{s^n}{m}$$

since there are this many ways to construct m distinct functions in $p = n$ variables. Then,

$$Q = s^{nm}(1 - 1/s^n)\cdots(1 - (m-1)/s^n)/m!$$

Using the inequality

$$(1 - a_1)(1 - a_2) \geqq 1 - a_1 - a_2$$

for $a_1, a_2 \geqq 0$, we have

$$Q \geqq s^{nm}(1 - m(m-1)/(2s^n))/m! > s^{nm}(1 - m^2/s^n)/m!$$

Then,

$$\ln Q \geqq nm\ln s + \ln(1 - m^2/s^n) - m\ln m$$

or

$$\ln Q \geqq nm\ln s\left(1 + 0\left(\frac{m}{ns^n} + \frac{\ln m}{n}\right)\right)$$

since $\ln(1-x) \leqq x$ and $m^2/s^n << 1$ under the conditions stated.

From the monotonicity of $x/(\ln x + a)$ for $\ln x \geqq 1 - a$ and from the discussion above, it follows that

$$\frac{\ln Q}{\ln\ln Q + \ln(|\Omega|/2)} \geqq \frac{nm}{\log_s(nm)}\left(1 + 0\left(\frac{m}{ns^n} + \frac{\ln m}{n}\right) + 0\left(\frac{\ln|\Omega|}{\ln(mn)}\right)\right)$$

and since $\alpha_1 \leqq m/n \leqq \alpha_2$, m and n large, the dominant term is the last one. Finally $\log mn \leqq 2\log m - \log \alpha_1$, from which the theorem follows.

Comparing this corollary with the upper bound of Theorem 3, it is clear that when m and n are comparable and large and all the $1 \times n$ matrix-vector functions are distinct, the upper bound to $C_{m,n}$ can be improved by at most a constant factor. Certainly all the $1 \times n$ matrix-vector functions are distinct when $s = 2$ and $U_1(x) = 0$, $U_1(x) = x$, and $x_i \in S = R$ (reals).

Corollary 2. If all of the s^{n+1} n-degree polynomials in z are distinct and if there is an α with $0 < \alpha < \infty$ such that $m < \alpha n$, then for large n

$$D_{m,n} \geqq \frac{c^*}{2}\,\frac{mn}{\log_s(mn)}(1 + 0(1/\ln(mn)))$$

for $|\Omega|$, $|K|$, and s fixed.

Proof. The number of distinct sets of m functions Q equals

$$\binom{s^{n+1}}{m}$$

Using the lower bound of the proof of Corollary 1 with $n+1$ replacing n, we have

$$\frac{\ln Q}{\ln \ln Q + \ln(|\Omega|/2)} \geq \frac{(n+1)m}{\log_s (n+1)m}$$

$$\times \left(1 + 0\left(\frac{m}{(n+1)s^{n+1}} + \frac{\ln m}{n+1}\right) + 0\left(\frac{1}{\ln(n+1)m}\right)\right)$$

Under the condition $m \leq \alpha n$, $0 < \alpha < \infty$, the dominant term for large n is the last term.

Since the polynomials depend on $p = 1$ variable, from Theorem 5 we have

$$D_{m,n} \geq \frac{c^*}{2} \frac{(n+1)m}{\log_s (n+1)m} (1 + 0(1/\ln(nm)))$$

$$- c^*(1 + |K| + (m-1)/2)$$

For n large, the theorem follows from the suitable approximation to this bound.

The result for polynomial evaluation is somewhat stronger than that for matrix multiplication since the bounds of Corollary 2 and Theorem 4 differ by at most a constant for large n only. It is not necessary that m, the number of polynomials, also be large. Hence, when $m = 1$ and one polynomial of degree n is to be evaluated, the combinational complexity of the worst such function behaves as $n/\log_s n$, for n large, for those cases where there are s^n distinct n-degree polynomials. One such case is that in which $s = 2$, $U_1(z^j) = 0$, $U_2(x^j) = z^j$ and $z \varepsilon R$.

V. Conclusions

The matrix-vector functions and the polynomial functions examined here are restrictions of the functions which obtain when the matrix elements and the polynomial coefficients are treated as indeterminates. From this vantage point, it is not surprising that these two problems are considerably less complex than the general problems. Nevertheless, the algorithms presented here promise considerable reductions in the number of operations to do matrix-vector multiplication with fixed matrices and to do polynomial evaluation with fixed polynomials. These reductions, however, will be realized only in those applications where the matrix-vector multiplication and polynomial evaluation are to be done many times, since the algorithms offered above must be constructed from a search of the matrix entries and of the polynomial coefficients and this search time will be comparable to the time to evaluate the functions using the algorithms for the general problem.

References

1. Grauling, C. R., and Jones, N. J., "Performance Capabilities of the Data Decoder Assembly Through the Viking Era," in *The Deep Space Network Progress Report,* Technical Report 32-1526, Vol. X, pp. 164–168, Jet Propulsion Laboratory, Pasadena, Calif., Aug. 15, 1972.
2. Pan, V. Ya., "Methods of Computing Values of Polynomials," *Russian Mathematical Surveys,* Vol. 21, No. 1, Jan.–Feb. 1966, pp. 105–136.
3. Winograd, S., "On the Number of Multiplications Necessary to Compute Certain Functions," *Communications on Pure and Applied Mathematics,* Vol. 23, 1970, pp. 165–179.
4. Winograd, S., *On the Algebraic Complexity of Functions,* IBM Report, International Business Machines Corp., Armonk, N.Y., Nov. 1968.
5. Savage, J. E., "Computational Work and Time on Finite Machines," *Journal of the Association for Computing Machinery,* Vol. 19, No. 4, Oct. 1972, pp. 660–674.

Table 1. Bound on $C_{n,n}$

n	Best k	$C_{n,n} \leq$	$n(n-1)$	Ratio
4	2	6	12	2
8	2 or 3	28	56	2
16	4	92	240	2.61
32	4	312	992	3.18
64	5	1,106	4,032	3.65
128	5	3,876	16,256	4.19
256	6	13,203	65,280	4.94
512	7	46,256	261,632	5.66
1024	8	161,664	1,047,552	6.48
2048	9	585,472	4,192,256	7.16
4096	10	2,090,594	16,773,120	8.02

Table 2. Bound on $D_{1,n}$

n	Best k	$D_{1,n} \leq$	$2n$	Ratio
3	2	4	6	1.5
7	2	10	14	1.4
15	3	20	30	1.5
31	4	34	62	1.82
63	4	58	126	2.17
127	5	104	254	2.44
255	5	182	510	2.80
511	6	322	1022	3.17
1023	7	563	2046	3.63
2047	7	1001	4094	4.09
4095	8	1786	8190	4.59

DSS Command System Redesign

J. Woo
DSIF Digital Systems Development Section

The existing Deep Space Station (DSS) Command System cannot meet project requirements through the Viking era (1975). The DSS Command System redesign, described herein, will be used to support Mission Command requirements through 1975. Major areas of redesign include command stack capacity and allocation of command stack manipulating functions from the DSS computer to the Mission Control and Computing Center. This article describes the system configuration and the functional operation of the redesign.

I. Introduction

The Deep Space Station (DSS) Command System redesign was initiated on September 1, 1972. The primary reason for the redesign effort is that the existing command software system is no longer capable of supporting project requirements through the Viking era (1975). The Telemetry and Command Processor (TCP) at the DSS has reached its limits of capability, in both processing cycle time and storage capacity, when telemetry and command functions must be performed simultaneously.

The primary objective of the command redesign is to develop new TCP command software that will operate with existing DSS equipment to satisfy project command requirements (such as command rates higher than 1 symbol/s) through the Viking era. In order to accomplish this, two major areas, command stack manipulation and command storage, in the existing TCP command software require redesign. The result of the redesign was to (1) reallocate the command stack manipulation (stack sorting, merging, and searching) control logic from TCP to the Mission Control and Computing Center (MCCC) and (2) limit the command storage to four High-Speed Data (HSD) blocks of 6–71 bit command elements each for remote-controlled operation and one HSD block for manual commanding.

The command software redesign reduced TCP command activity loading as well as TCP input HSD processing because of decreased HSD loading. Thus, the implementation of this new command software will permit the DSS Command System to operate at 8 symbols/s simultaneously with telemetry processing.

The following describes the DSS equipment configuration for command and the detailed functional operation of the new TCP command software. [After the command software is developed, it will be integrated into the Telemetry and Command Data Handling Subsystem (TCD) Multiple Mission Software.]

II. System Configuration

The purpose of the command software is to provide uplink communication capability to spacecraft. The command software, which is located in the TCP computer, utilizes the Command Modulator Assembly (CMA) as its connection to the Exciter/Transmitter Subsystem. The primary method of operation is the automatic mode, in which the TCP receives command inputs from the HSD lines; the second method of operation is the manual mode, in which the TCP receives local command inputs from the DSS typewriter and/or paper tape reader. In both modes, the TCP logs information on a magnetic tape [called the Original Data Record (ODR)], displays status information at the DSS through the Station Monitor [called the Digital Instrumentation Subsystem (DIS)] or teletype output printer, and receives time from the Frequency and Timing Subsystem (FTS) for time tag of command events. Figure 1 shows the DSS system configuration for command, and the following sections describe the functions of the components.

A. Control Center

Any control center can interrogate the TCP at any time by sending HSD blocks requesting information to the TCP. Configuration tables, standards and limits tables, and mode control and command stack modules and status can be obtained. In either the automatic or manual mode, the TCP will address and transmit HSD blocks describing events that are asynchronous to other HSD communications to one control center, called the control source.

B. Typewriter/Paper Tape Reader

The typewriter and paper tape reader are input devices used to perform software initialization and to control the command software in the manual mode.

C. FTS Inputs

The FTS timing interrupts and GMT time information are utilized by the command software to time-tag transmission of the first bit of a command element and HSD outbound messages, and to time initiation of transmission of timed command elements. In addition, command partial status periodic messages are generated for display in the DIS.

D. ODR Output

All input HSD blocks to the TCP are logged on the ODR, as are all acknowledge blocks. All HSD block images constructed in response to typewriter input are logged on the ODR regardless of HSD communications to the control center.

E. DIS Output

The DIS displays information generated by the command software on the station line printer. If the DIS is inoperable, information will be displayed on a teletype output printer. The information displayed includes display requests, command partial status messages, and command event messages.

F. CMA

The CMA accepts configuration, frequency, symbol rate, and command data from the TCP for different CMA operations as controlled by the command software. CMA status information is fed back to the TCP to allow checks to be made by the software.

G. Analog Tape

Modulated subcarrier output from the CMA is recorded on analog tape for post-operation analysis.

H. Exciter/Transmitter

Modulated subcarrier output from the CMA is input to the exciter/transmitter subsystem for signal amplification, carrier modulation, and transmission to the spacecraft.

III. Functional Operations

A. TCP/CMA Modes of Operation

The CMA, under the control of the command program, operates in various modes:

Cal-1 (Calibrate-1) – the DSS operator establishes CMA signal modulation attenuation settings.

Cal-2 (Calibrate-2) – the CMA is operating according to project specific frequency-modulation method and symbol rate, but no modulated output is transmitted to the exciter/transmitter subsystem.

IDLE-1 – a project Idle word is continuously transmitted.

IDLE-2 – a second project Idle word is continuously transmitted.

ACTIVE – project command bits are transmitted.

ABORT – command bits are no longer transmitted because of command check failures.

Figure 2 shows the relationship between each mode and the sequence of events leading to the entry and exit of the mode.

B. Initialization

During the initialization process, type-ins are made by DSS operator through the typewriter. The type-ins [Command Station-Spacecraft (CSS)] identify the DSS, computer string, spacecraft, and destination code for outbound HSD blocks. The modulation attenuation for the CMA is also established. The operator then types in CRUN to terminate the initialization process, and the command program subsequently enters formal Cal-1 mode. At this point, the program operates in either the automatic or the manual mode, depending upon the key setting of the station manager's console.

C. Automatic Mode

In the formal Cal-1 mode, the program is ready to accept all HSD blocks consisting of configuration and standards and limits tables. When it has rceived both of these tables, the program enters Cal-2. From Cal-2, the mode changes are under the control of the mode enable/disable flags of the mode control portion of the command block.

From Cal-2, the program goes to Idle-1 when that flag is enabled, and from Idle-1 to Idle-2 when the Idle-2 flag is enabled. The transfer from Idle-2 to Active occurs only when the Active flag is enabled and transmission of a command element is started. The transfer to Abort is made when an Abort directive is received, when an Abort limit is reached and the Abort-override flag is not set, when a watchdog timer (computer overload condition) occurs, or when a manual button is started.

Mode regressions also occur. From the Abort mode, return to the Cal-2, Idle-1, or Idle-2, depending on the Abort return code, occurs after the Abort duration has expired. Active regresses to Idle-2 when a command element confirms and no other command elements exist in the stack, or the next command element is timed. Idle-2 to Idle-1 and Idle-1 to Cal-2 regressions occur when the Idle-2 and Idle-1 flags are disabled (the program being in that particular mode), respectively. In the redesign, bit verification is performed on the Idle word sequence; if the Abort-override flag is not set and a bit error occurs, the program reverts to Cal-2. The return from the Abort mode plus the bit error regressions disable all mode flags higher than Cal-2. Once the program is past Cal-2, only mode control and command blocks are accepted. That is, it is necessary to revert to Cal-2 for program reconfiguration.

The Network Control System (NCS) can establish a lockout condition in which normal HSD blocks from NCS would be rejected. NCS should establish lockout after configuring the TCP to prevent interference of NCS with project commands through MCCC.

D. Command Stack Loading and Logic

Figure 3 shows the command stack and manual buffer structure. The command stack consists of four modules of six elements (71 bits per element) each, plus the extent which specifies how many modules have data in them. The loading of command stack modules is accomplished by way of HSD blocks from a control center. Recalls of the contents of any stack module can be made by HSD blocks. Only element 1 of the prime module is eligible for transmission. When transmission of the element begins, it is transferred to the active register; the remaining elements of the prime module are then pushed up one, and element 6 is filled with zeros. If element 1 of the prime module is empty (all command elements are transmitted), the extent is reduced by 1, and if the results are positive, the modules are promoted by being pushed up one and radiation of commands until the extent reaches 0.

Synchronization with a control center is based on the extent, and for the prime module references, also on the count of elements. An input module from a control center is marked as to which stack module it replaces, and also carries the expected TCP extent and a new TCP extent, plus the expected TCP count.

Synchronization is achieved by comparing the expected TCP extent against the actual and, for prime module references, the expected count against the actual. If the comparison is nonequal, the control center does not know the current TCP situation, so the module is rejected, and the resulting HSD block notifies the control center of the

actual TCP extent and count. If a module is accepted, it replaces the indicated stack module and the new extent replaces the actual extent. Note that the stack will be empty if the new extent is zero.

E. Manual Mode

Manual mode operation is, in the main, similar to automatic. Direct type-ins exist to take the TCP from Cal-1 to Cal-2 and any other mode. One type-in, CIN, exists to put the TCP back into the dormant pre-initialization stage.

All manual mode commands in Cal-1, except for the manual buffer updating and display requests, result in HSD block images which flow through the system as formal HSD blocks, are logged on the ODR, and generate an Acknowledge response. These blocks are identified as manually generated.

F. Manual Buffer

A manual buffer is exactly the same size as a stack module (six elements of 71 bits each). The manual buffer is independent of the stack. In the automatic mode, a specially earmarked module can be sent to fill the manual buffer. The contents of the manual buffer can be recalled by the HSD block. Manual entry of the command elements into the manual buffer is accomplished through type-ins. Other type-ins are used to send the whole manual buffer to the stack as a module, or to send one command element to the stack in a partially filled module. Once a command element enters the stack module, the transmission of a command is the same as described above.

IV. Summary

The implementation of the command software as described will meet project requirements through the Viking era. The following outlines the performance characteristics of the redesigned system:

(1) Command storage

Command stack: 4 modules × 6 elements/module × 71 bits/element

Manual buffer: 6 elements × 71 bits/element

The factor most limiting the capacity of command storage is that the command software shares the TCP computer with the telemetry processor.

(2) HSD input block rate: maximum of 1 block/5 s

The rate is limited by the time-consuming routine required to process input blocks. Additional time is also required in the command stack synchronization process between a control center computer and the TCP computer.

(3) CMA operations monitoring

Bit-by-bit check is performed for each command bit. Other checks, such as frequency, symbol rate, and data quality are performed once per word.

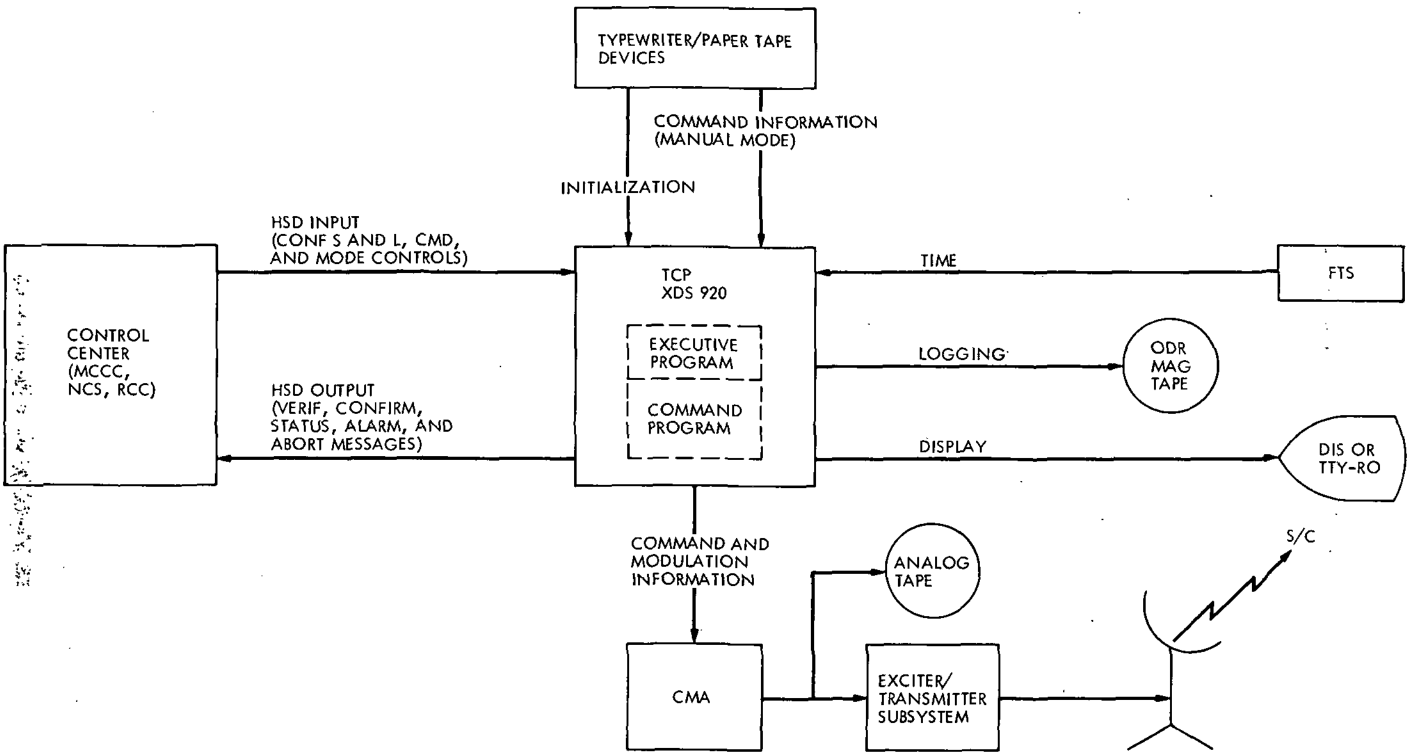

Fig. 1. DSS command configuration

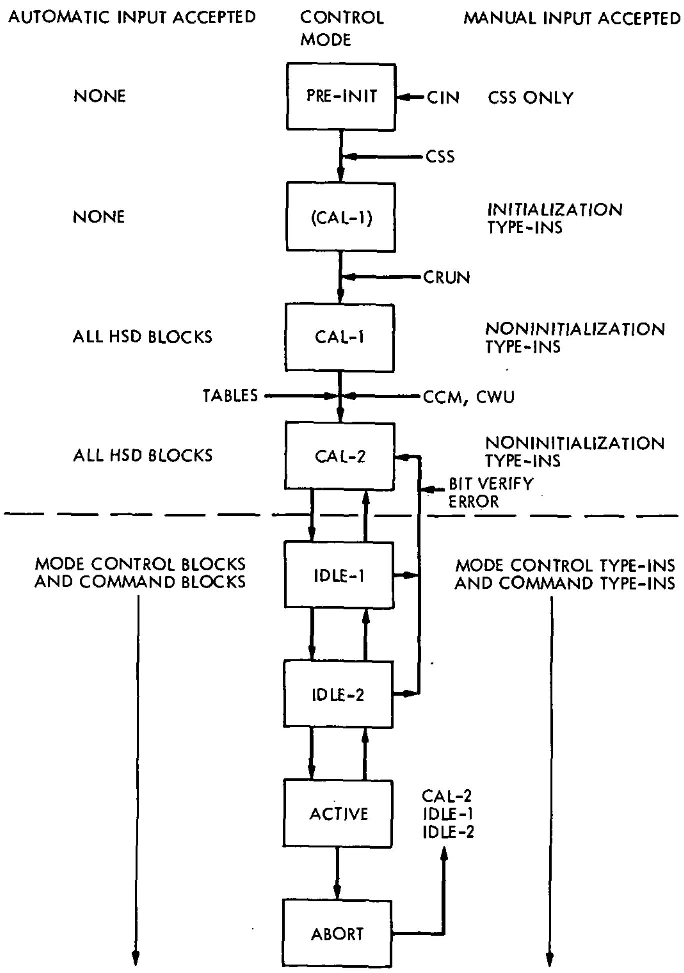

Fig. 2. Mode relationships

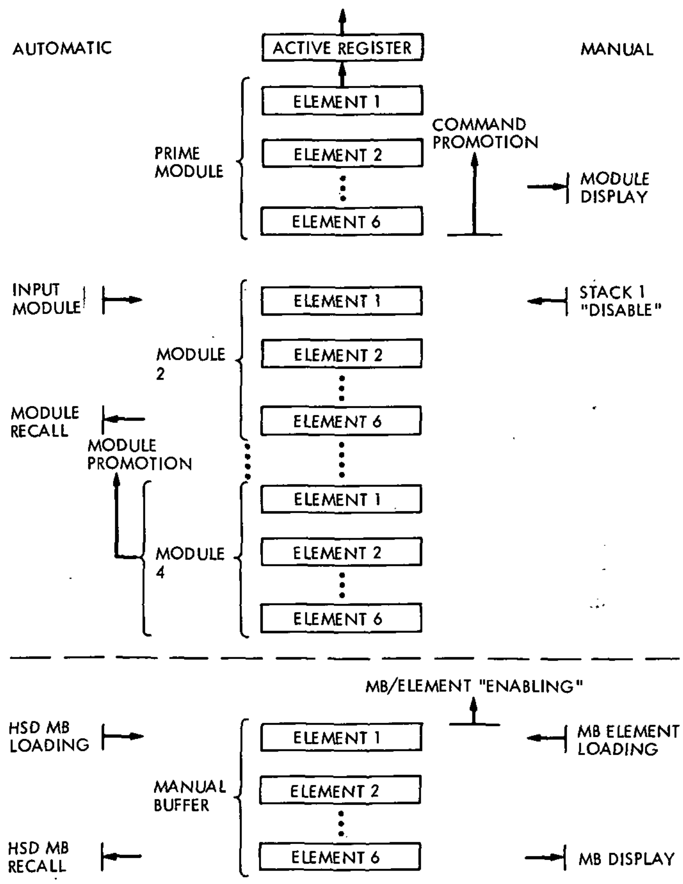

Fig. 3. Command data update/recall diagram

Network Control System

J. N. Edwards
DSIF Digital Systems Development Section

This article provides information regarding implementation project team responsibilities and activities. The final Network Control System (NCS) hardware implementation configuration and the interim NCS configuration interfaces are described, and the hardware configuration for the interim NCS is discussed.

This is the second article describing the JPL DSN Network Control System (NCS). Information including (1) DSN philosophy and functional requirements, (2) key functional characteristics, (3) subsystem functions, (4) generic subsystem data flow, and (5) overall system data flow and interface diagram was contained in Vol. XI of the DSN Progress Report (TR 32-1526).

The initial JPL document formulating the NCS baseline and implementation is the DSN Data System Development Plan (DSDP)*. This document, prepared by the JPL Tracking and Data Acquisition (TDA) Planning Office, includes baseline requirements, design, management, resources, and scheduling for the final NCS to be completed by July 1, 1974. An interim NCS, including functions which are a subset of the final system capability, will provide network control functions from July 1, 1973, to July 1, 1974.

**DSN Capabilities and Plans,* Document 803-2, Volume II—Network Control System, Data System Development Plan, Baseline Version, Sept. 1, 1972 (JPL internal document).

The NCS functional requirements identified by the DSDP are further defined in the DSN 822-Series NCS documents* for (1) General, (2) Tracking, (3) Telemetry, (4) Command, (5) Monitor/Control, (6) Display, (7) Support, (8) Test/Training, and (9) Communications Terminal Subsystems. These detailed NCS functional/performance requirements were prepared by DSN Systems Engineering. In conjunction, the supporting DSN Operations Group and NCS Implementation Project Engineering Group inputs have provided personnel operating-interface and hardware-capability requirements reflected in these documents.

*JPL internal documents.

A key function of the NCS is to reduce operations costs for the DSN, while providing required FY'74/75 mission support capability. The NCS Implementation Project Team was established on May 19, 1972, within the JPL Telecommunications Division to fulfill these requirements.

The Project will implement and direct activities and supporting group functions for (1) Planning and Schedules, (2) Budgets and Costs, (3) System Design, (4) Specifications, (5) Hardware Procurement, (6) Software Support, (7) Facilities and Services Procurement/Implementation, (8) System Testing, and (9) Operations/Training Support.

The Implementation Project Team has participated in various tasks supplemental to the basic data processing system design and hardware implementation. These activities have included:

(1) Evaluation of system requirement documents and related data processing interfaces with the Deep Space Stations (DSSs) and the Mission Control and Computing Center (MCCC).

(2) Detailed facilities evaluation studies for interim and final NCS. Factors relating to buildings, power, Ground Communications Facility (GCF) interfaces, air conditioning, backup failure modes, and cost effectivity including implementation and long-term growth of operations costs, were prepared for the Site Evaluation and Selection Board review.

(3) Investigation of industry standards for computer/peripheral/communication interfaces, preparatory to specifying Deep Space Instrumentation Facility (DSIF) standards for all hardware data interfaces within the NCS.

(4) Detailed evaluation of NCS subsystem data processing functional requirements as related to the data processing capability of mini-computers and midi-computers to be specified for NCS.

(5) Evaluation of final NCS functional requirements vs. existing hardware specified for interim NCS. Interim mission support requirements were evaluated to develop a revised set of functional requirements to be fulfilled by the interim NCS.

(6) Evaluation of the GCF communication interfaces; and definition of requirements, and design of a new GCF Filler Multiplexer (GCF-FM). The GCF-FM provides automatic bit/data-block synchronization of remote high-speed and wideband data, and also merges NCS/MCCC data with the Remote Mission Operation Control (RMOC) data on a single GCF line from JPL to any DSS.

(7) Evaluation of the final NCS functional requirements vs. resources available, to define the hardware implementation configuration.

A simplified data flow requirements diagram of the final NCS is shown in Fig. 1. The key functional characteristics of the NCS are:

(1) The DSS/MCCC data link is direct via the GCF Central Communications Terminal (CCT).

(2) All DSS/MCCC traffic is recorded in the NCS GCF log, and also routed via GCF Network Communications Equipment (NCE) to the Network Data Processing Area (NDPA) for data validation, analysis, and display generation.

(3) DSIF configuration control data are transmitted from NDPA via NCE/CCT, and merged with MCCC data on GCF lines to DSS.

(4) DSN/NCS control, display, monitor, test/training, and MCCC interfaces, are all directed by DSN Operations Personnel located in the Network Operations Control Area (NOCA).

A simplified block diagram of the final NCS data flow and hardware configuration for July 1974 is shown in Fig. 2.

The GCF CCT, MCCC and associated Mission Operation Control (MOC), and NOCA are to be located at JPL, as are the GCF NCE and NDPA.

A RMOC may be connected via GCF High-Speed Data (HSD) full duplex lines for up to three project control locations remote from JPL. All inbound DSS data are received by the GCF CCT, and are switch-routed directly to the MCCC/RMOC/NCS data interfaces. The MCCC/RMOC/NCS outbound data are routed via GCF equipment directly to the DSS. With a RMOC, the outbound data are routed via the GCF-FM and GCF data sets to the DSS. The GCF-FM allows local MCCC/NCS data to be interspersed onto the same outbound HSDL to DSSs as the RMOC data, by synchronous substitution of local MCCC/NCS data blocks for RMOC GCF filler blocks.

All inbound/outbound data are also routed to the GCF CCT Comm/Log Processors. These data are logged on magnetic tape to provide the NCS GCF data log. GCF

log data may subsequently be recalled by the NCS, RMOC, or MCCC for updating other data records. The GCF Comm/Log Processors route data bilaterally to the NOCA for NCS control and display. The GCF CCT Comm/Log Processors delete GCF filler blocks, sort, and route data to the communication processors in the GCF NCE. A 230.4-kbps full-duplex-mode data rate capability is planned between GCF CCT and GCF NCE.

The GCF NCE processors sort and route DSS data and NCS control/displays bilaterally between the GCF CCT and all processors within the NDPA. NCS Test and Training data are routed to GCF CCT for local or long-loop DSS testing.

The Real Time Monitors (RTMs) for Tracking, Telemetry, Command, and Monitor receive only their respective data from the GCF NCE. The RTMs provide input DSS data accountability, verification, validation, and respective Subsystem Data Records. Alarm and display data are generated to provide monitoring of all data streams and network performance in real time.

Designated RTM control data for configuring the DSSs are sent via the Network Support Controller (NSC) to the DSSs. RTM display data are generated and sent to the NOCA. Local RTM displays are available as backup for NOCA.

The NSC provides support computation for each RTM data type via a demand-responsive data processing interface. The NSC is the hub of NCS NDPA operation, but does not preclude stand-alone operation of each RTM. Data processed or generated by the RTM may be transferred to the NSC for subsequent transmission to the DSS via GCF NCE/GCF CCT. Data are also transferred from each RTM to the NSC for output on magnetic tape to provide System Data Records for each RTM. The NSC receives other data from the GCF data log in CCT, and from NOCA. These data may receive special processing in the NSC for analysis and records, or they may be formatted for transmission to DSSs, GCF CCT data log, NOCA, MCCC, or RMOC. The NSC backup processor runs support programs, for subsequent NSC processor transmission within NCS/GCF/DSN. The backup processor and its peripherals may be selected for NSC operation.

The Test and Training Subsystem (TTS) generates High-Speed System/Wideband System (HSS/WBS) test data for all NCS subsystems and NCS/DSS system testing. Testing is unique to NCS/DSS performance validation requirements, and is not a duplication of project flight data model simulation provided by the MCCC.

The NOCA, located in the Space Flight Operations Facility (SFOF) area at JPL, provides all NCS Operations display/control. All NCS processor modes and functions are selected in the NOCA, but may also be operated stand-alone locally. DSS/NCS data and equipment status is displayed in the NOCA. Incoming DSS data to the GCF CCT are formatted and routed per NOCA control. Video data formats are generated for local NOCA console selection of desired data display. NCS display data are also available for distribution to MCCC Operations video displays, and vice versa. Magnetic tape data may be transmitted bilaterally from NOCA to NDPA. Peripheral equipment data outputs are available for Network Analysis Team support. The equipment tabulations in Fig. 2 indicate the hardware configuration planned for July 1974 operational capability.

The implementation of the interim NCS will provide DSN Monitor/Control in a cost-effective configuration providing limited mission support requirements from July 1973 to July 1974.

The interim capability will be a subset of the NCS requirements identified in the 822-Series documents. The system configuration reflects performance requirements, existing hardware, and available resources. The interim NCS interface block diagram is shown in Fig. 3.

The interim NOCA will be located in the SFOF, and interim NCS data processing equipment will also be located at JPL. DSS data will be received via the GCF CCT at JPL.

The interim NCS will receive and process data from up to six HSD and one WBD GCF input data lines. All data will be routed directly from GCF to MCCC. One RMOC will be accommodated by a GCF-FM, as described for the final NCS.

The interim NCS processing for all real-time control, display, data validation, tracking, and monitoring is provided by a single central processor located at JPL. GCF input/output (I/O) functions are provided by a second small processor located in the GCF CCT, with a data link to the central processor. Local controls and displays are provided at the central processor. Controls and displays for interim NCS Operations are remoted in the SFOF area. A backup central processor is available for

the real-time operations. The backup processor also performs nonreal-time data processing to support the real-time operation. Magnetic tape is used for data transfer between the real-time and nonreal-time processors. The predicts/sequence of events (SOE)/schedule data transfer interfaces from the MCCC to NCS are magnetic tape for the interim system. A GCF Tracking Data Log may be recalled to MCCC via HSDL. A subsequent interim configuration (Jan. 1974) will provide for additional MCCC data processing to be accomplished in the interim NCS backup processor.

Coordination between interim NCS Operations and MCCC Operations will be via telephone in a localized area of the SFOF. In addition, existing MCCC video displays of DSS data will be viewed by interim NCS Operations on MCCC consoles. Designated NCS monitor functions will be performed at each DSS to supplement the centralized control/monitor operations.

An interim NCS hardware block diagram is shown in Fig. 4. The display area includes interim NCS hardware/data status records, displays, and controls. The real-time video displays are part of the MCCC video system, and are not included in Fig. 4.

The data processing area includes the real-time/backup processors and associated peripherals. Switched controller/data sets to the separate areas utilize existing hardware for minimum-cost implementation.

The GCF data are preprocessed in an existing I/O processor to simplify inter-building data transfer, and to reduce core requirements of the central processor.

The interim NCS hardware/software is currently in development for July 1973 operation. Design features and applications will include future use in the final NCS where applicable.

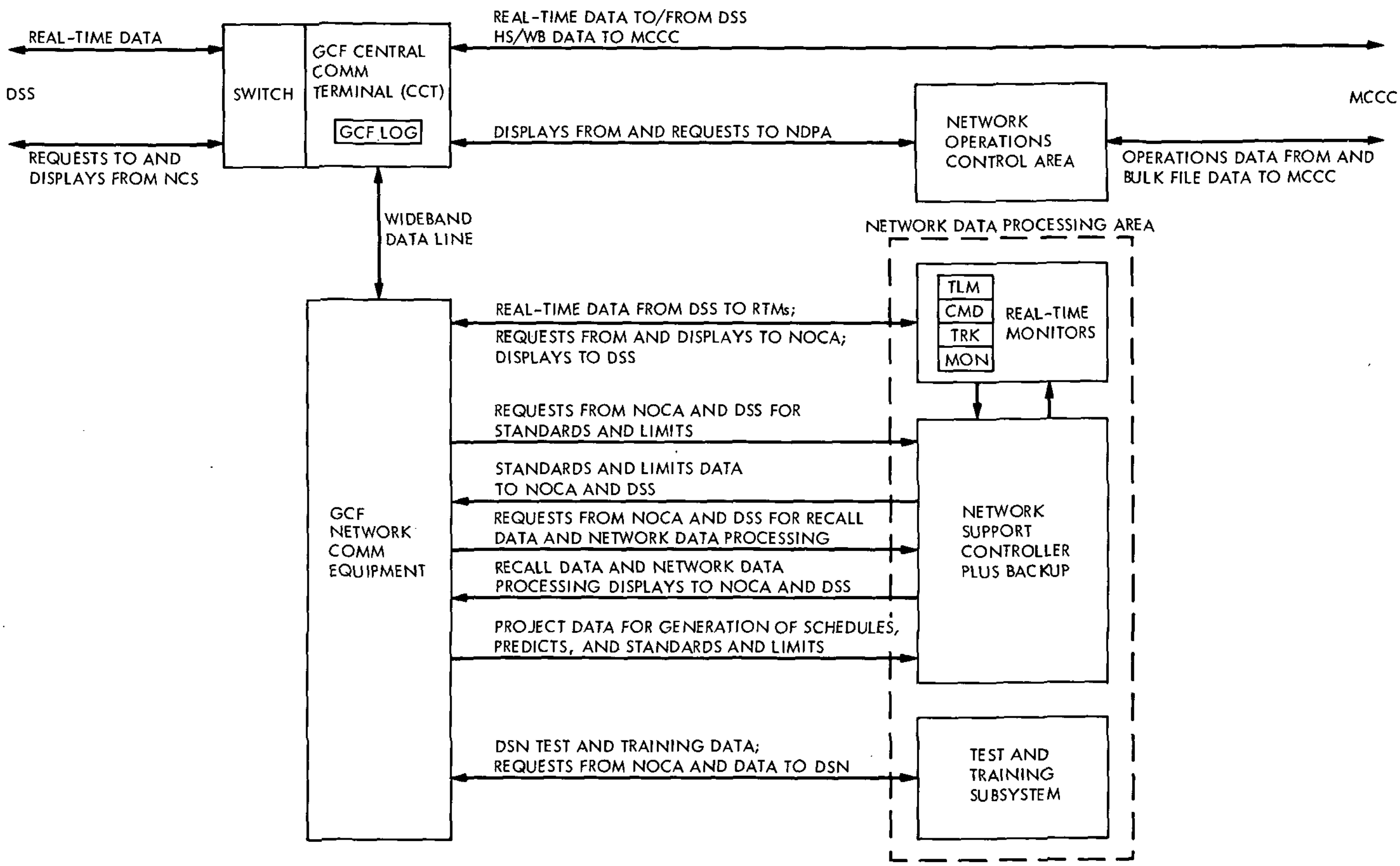

Fig. 1. NCS data and message flow requirements

"Pages missing from available version"

Pgs 214 – 216

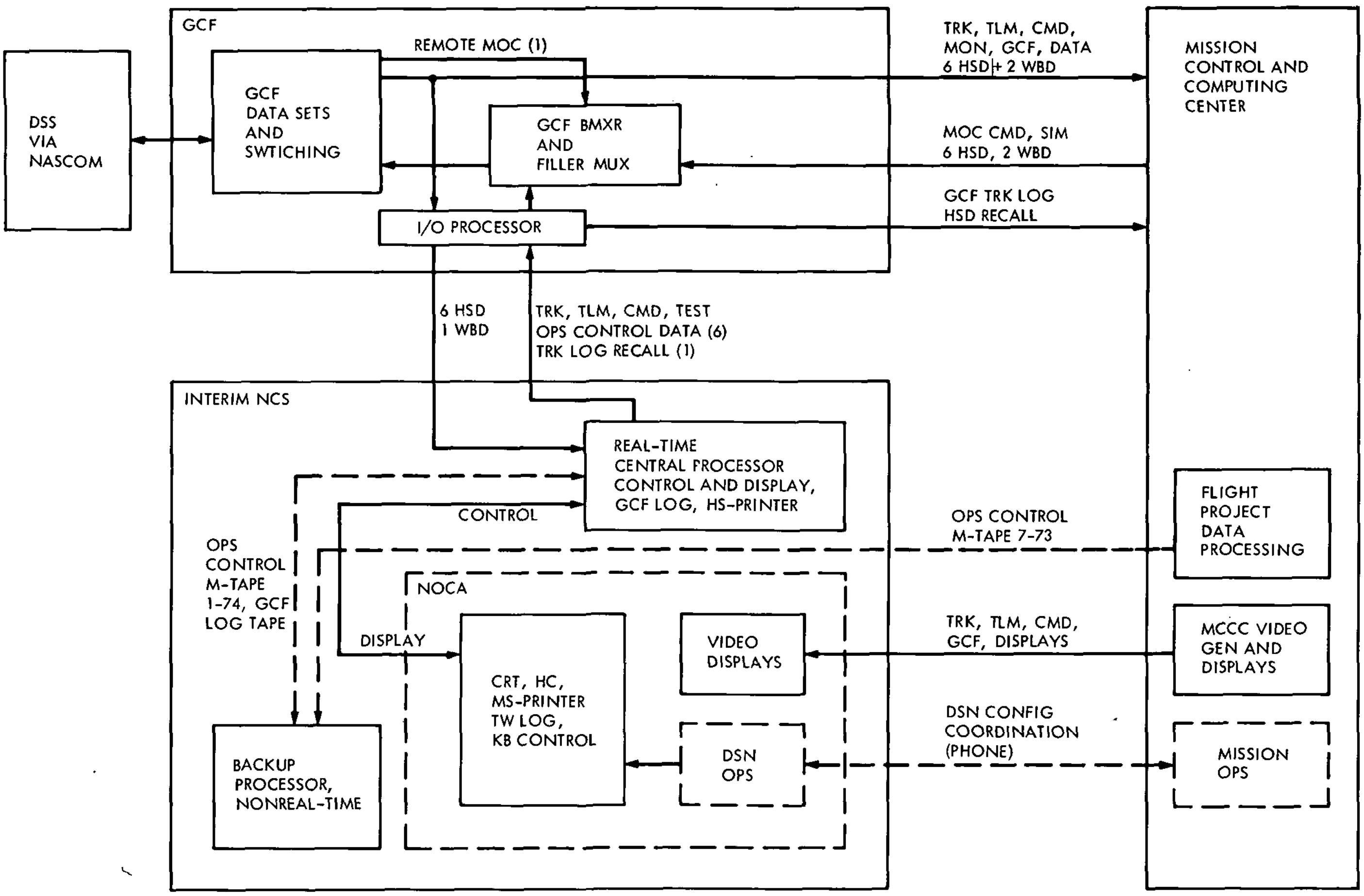

Fig. 3. Interim NCS interface block diagram

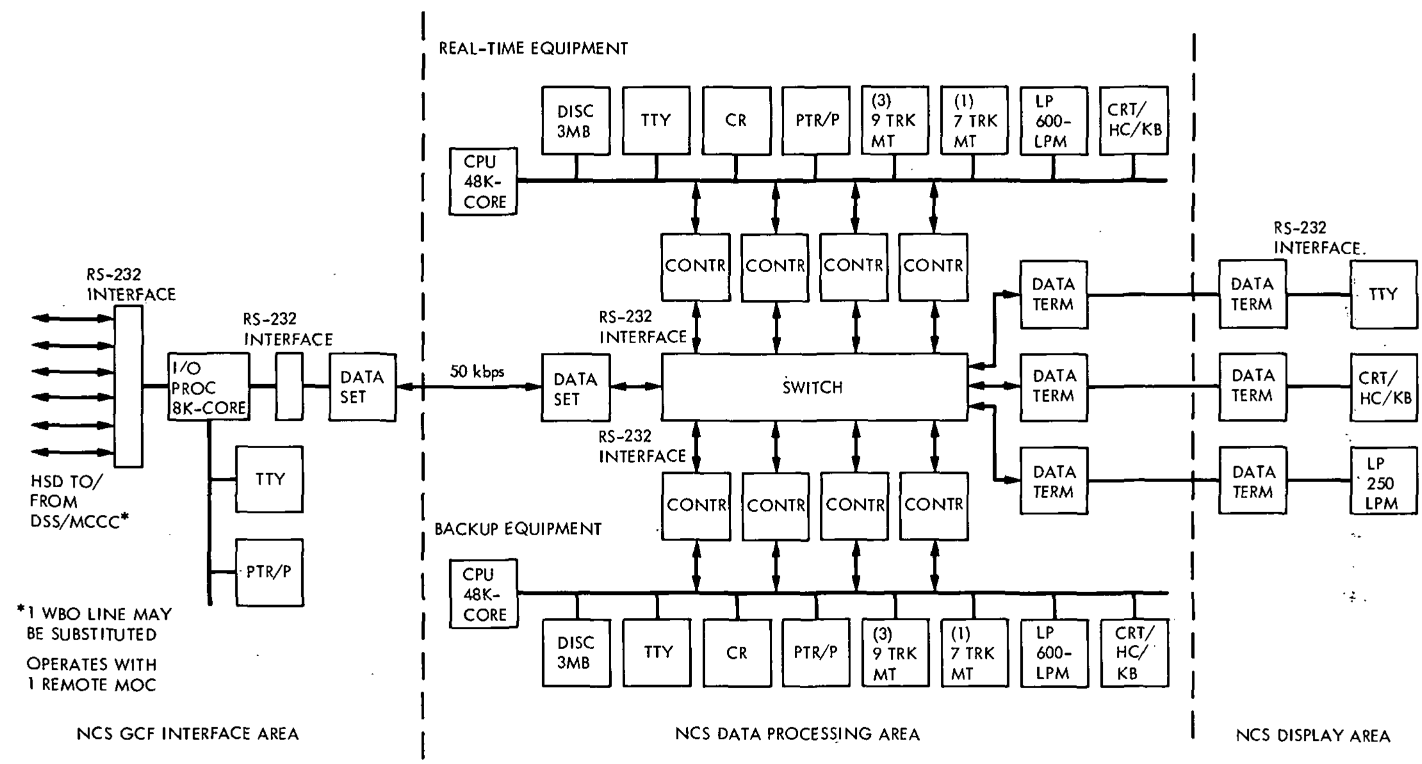

Fig. 4. Interim NCS hardware block diagram

Hydrostatic Bearing Runner Damage at the Spain 64-m-Diameter Antenna

J. Chapman
DSN Quality Assurance Section

K. Bartos
DSIF Engineering Section

On November 12, 1972 the rear pad of the 64-m-diameter antenna in Spain grounded upon a foreign object in the hydrostatic bearing runner oil trough. The rear pad and the runner were damaged. The antenna was being operated by the contractor, Collins Radio, Dallas, Texas, while conducting final analog pointing accuracy tests. This article describes the damage incurred by the three hydrostatic bearing pads and the runner surfaces and the methods of repair used by the contractor to return the antenna to testing status.

I. Introduction

The 64-m-diameter antenna rotates in azimuth on a hydrostatic bearing that consists of a 7-in.-thick steel runner of eleven segments, segments A through L less I (Fig. 1), and three pads spaced 120° apart through which high pressure oil is pumped to support or "float" the 5.5-million-lb antenna. The plan view of Fig. 1 shows a typical relative orientation of the antenna base triangle, pads, and runner segments. On November 12, 1972, the rear pad grounded upon a foreign object resulting in damage to the runner and the rear pad.

II. Damage to Runner

A. Major Damage

The major runner damage was confined to a 3-m length of runner segment K. As the antenna was being rotated clockwise, a foreign object became caught between the runner and the film height sensor (skateboard). As the antenna motion continued, the foreign object gouged the runner that in turn precipitated pad damage as the pad moved over the damaged runner area. Damage to both the pad and runner continued until the friction force equaled the antenna rotating force. The damage consisted of a gouge varying from zero depth at the start point to approximately 1 cm deep near the end of the gouge.

The width varied from 1 cm to 5 cm. Figure 2 shows the maximum point of clockwise rotation, the damaged film height sensor, and the edge of the pad acting as a machine tool for cutting metal from the runner surface. (It is noted that the antenna was moved counterclockwise about 30 cm while trying to pinpoint the reason for nonmotion immediately after the grounding occurred.)

Figure 3 shows the trailing edge of the pad, the starting point of the damage, and the typical film height sensors. Figures 4 and 5 show the characteristic print left by the foreign object on the runner at the starting point of damage and on the film height sensor.

B. Minor Damage

Nearly the entire runner showed minor damage in the form of single and multiple scratches caused by a foreign object, presumably the same object that precipitated the grounding. The scratches varied in depth and width—a maximum depth of 0.1 mm and a maximum width of 1.5 mm. The scratches also showed characteristic upset material on either side of the scratch due to Poisson's ratio effect on the order of 0.05 mm above the runner surface. The radii of the scratches near the outside of the runner (Fig. 1) can be directly attributed to the foreign object being lodged under the outside corner film height sensor assemblies of the left front and rear pads and under the film height sensor assembly corresponding to the grounding on segment K while the antenna was being rotated. These three height sensor assemblies showed the same characteristic imprint pattern (Fig. 5). The multiplicity of the scratches implies that the object was either long or that the object was in the trough during several antenna rotations. Figure 6 shows the maps of the scratches on each individual runner segments.

III. Damage of the Pads

A. Rear Pad

Rear pad damage was directly related and was a mirror image of the runner damage. Figure 7 shows the rear pad after removal. The other minor scratches are of the order of 0.07 mm in depth and correspond to the scratches that were made in the runner and then transferred to the pad, either by the upset material or small chips removed from the runner.

B. Front Pads

The front pads were removed to verify that no unknown major damage was hidden. As was expected only minor scratches existed, similar to those in Fig. 7 and of the order of magnitude of 0.05 mm deep and upset of 0.02 mm.

IV. Method of Repair

A. Runner Major Damage

The major damage of segment K was repaired by first removing all loose material. Dye penetrant was used to assure that no cracks or laminar material remained prior to welding. The gouge was filled to above the level of the runner surface with E7018 weld material placed as stringer beads with spacing techniques used to prevent heat distortion of the runner. The temperature of the work area was maintained between 20 and 30°C. After welding the repair area was ground, filed, and hand stoned to remove excess weld material. The area was carefully measured to assure that the original runner flatness of 0.07 mm was obtained. In fact the flatness was better than 0.025 mm. Four isolated instances, three related to the foreign object, required welding repair and finishing as above.

B. Runner Minor Damage

The entire runner surface was hand stoned to remove all upset material along the sides of individual and multiple scratches.

C. Rear Pad

The damaged areas on the rear pad were ground out and inspected using dye penetrant to assure that no cracks or laminar material remained before welding. The pad was then shipped to Bilbao, Spain, to be placed in an oven for preheat prior to weld repair.

The fabrication shop and oven of Talleres San Miguel, a Collins Radio subcontractor, was used to preheat the pad. The pad was preheated for 6 h to 315°C and welding by a certified welder was started. After one hour the preheat decreased to 260°C the minimum set prior to starting repair. The pad was returned to the oven and heated again for 12 h at an oven temperature of 480°C. When the pad was removed, the temperature was 425 to 460°C, as checked with temperature sensitive crayons. The welding was done using an E 8018 welding rod placed as stringer passes. Each pass was cleaned with a wire brush and the weld checked using the magnetic particle method. As in the runner repair, sufficient weld material was placed to be sure that the repair areas were above the plane of the pad surface. After welding the pad was returned to the oven and heat treated to 650°C for 20 h.

After cooling the pad surface was measured and found slightly warped, a peak-to-peak measurement of 0.25 mm. The pad surface was ground in 0.02-mm increments until flat. After machining the pad surface was phosphate coated in accordance with MIL-P-16232 D, Type Z, Class 2.

D. Front Pads

The raised material on either side of the minor scratches on both pads was removed with a hand stone. The pad faces were cleaned and the pads reassembled.

V. Reassembly of Hydrostatic Bearing

The rear pad was returned to the site after repair and all parts and cavities cleaned before reinstallation.

The runner surface was vacuumed and wiped clean with solvent to remove all foreign particles, and visually inspected before bolting down each access cover plate. The hydrostatic bearing oil was filtered before being returned to the oil trough and refiltered in the trough. All the film height recording devices were refurbished with new bearings and recalibrated. The antenna was rotated and returned to testing status on December 5, 1972.

VI. Conclusion

The repair was completed in an expeditious manner by the contractor, and operational tests and rotation checks have shown no deterioration in operation parameters.

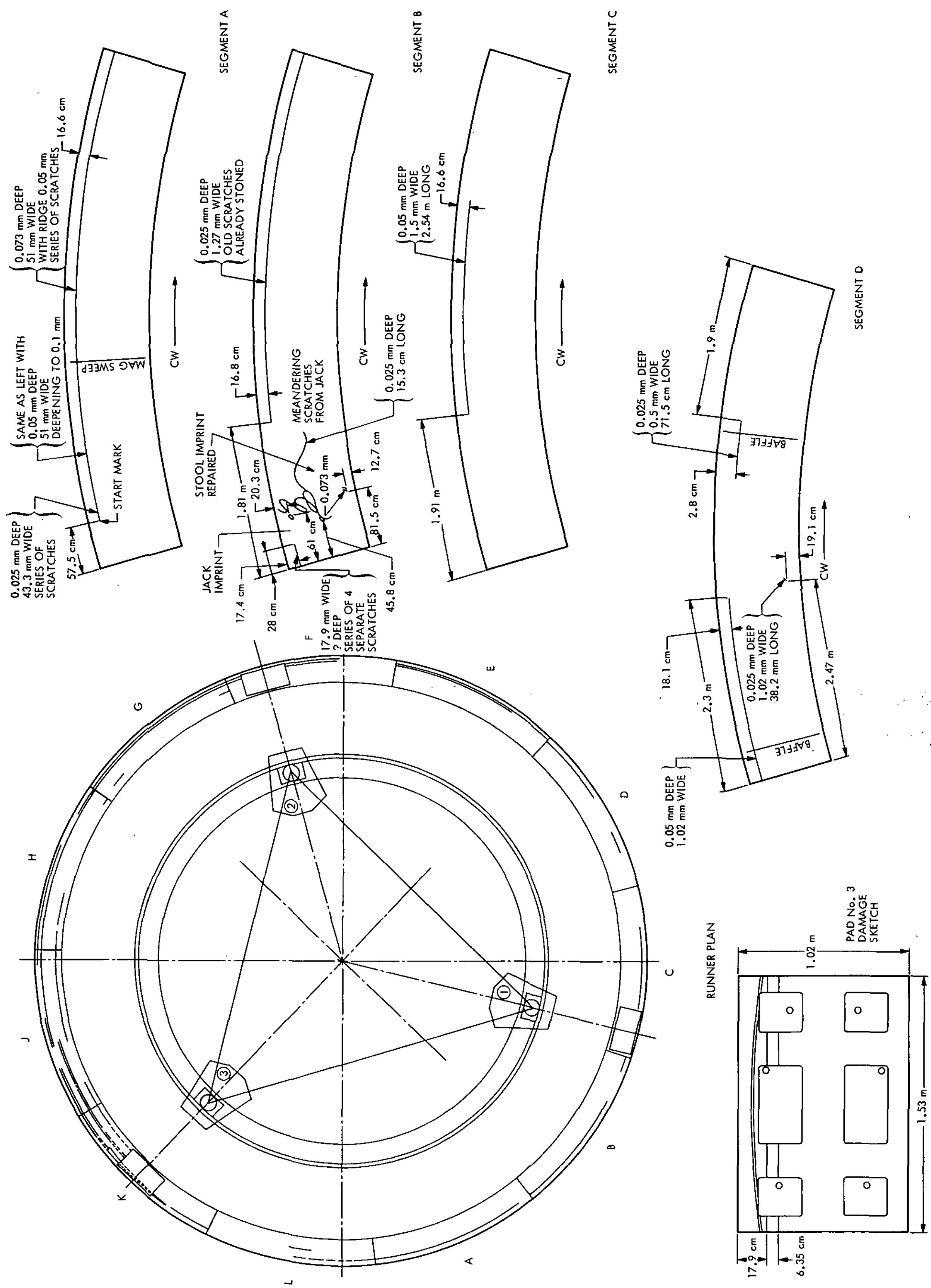

Fig. 1: Plan of Scratches

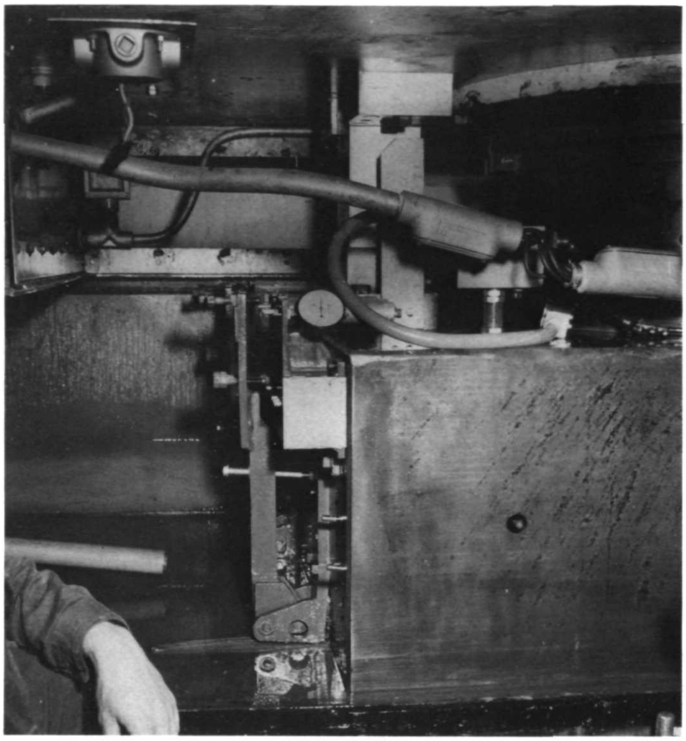

Fig. 2. Runner segment K

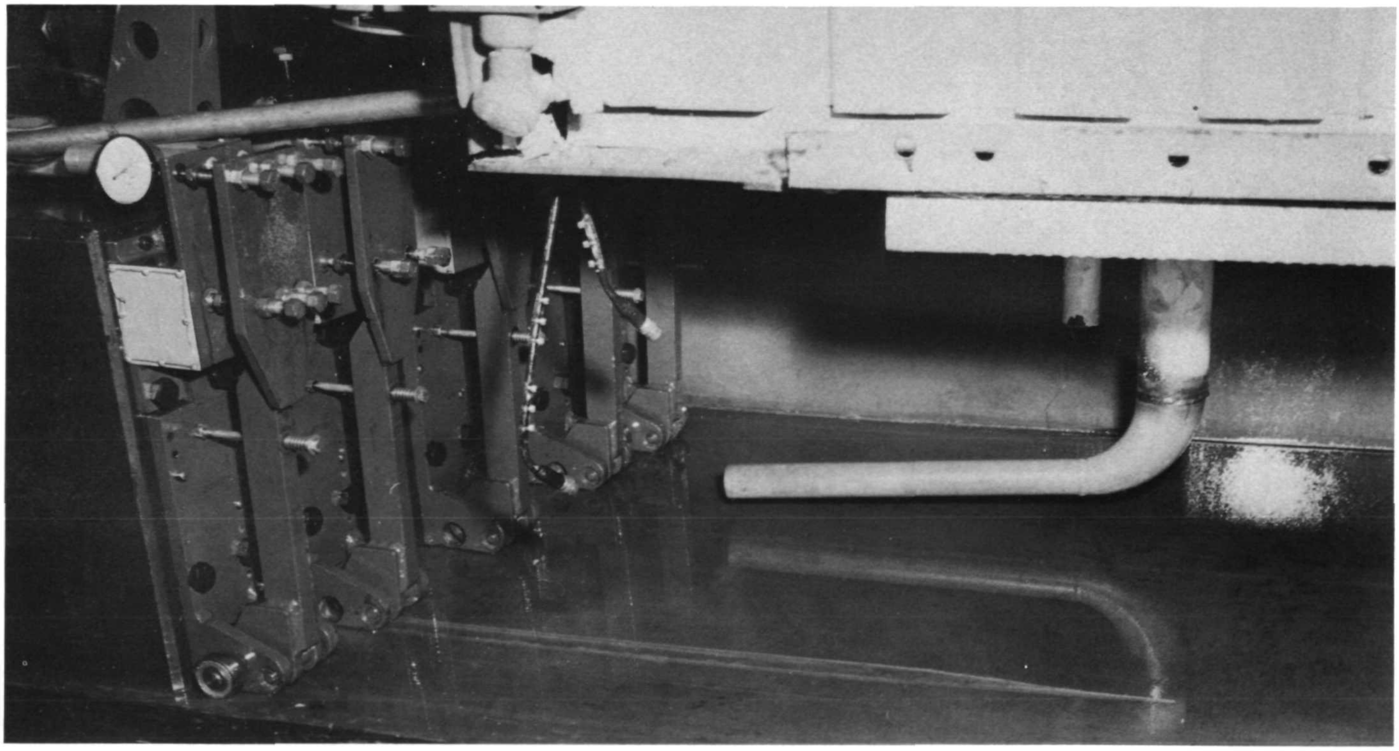

Fig. 3. Starting point of damage

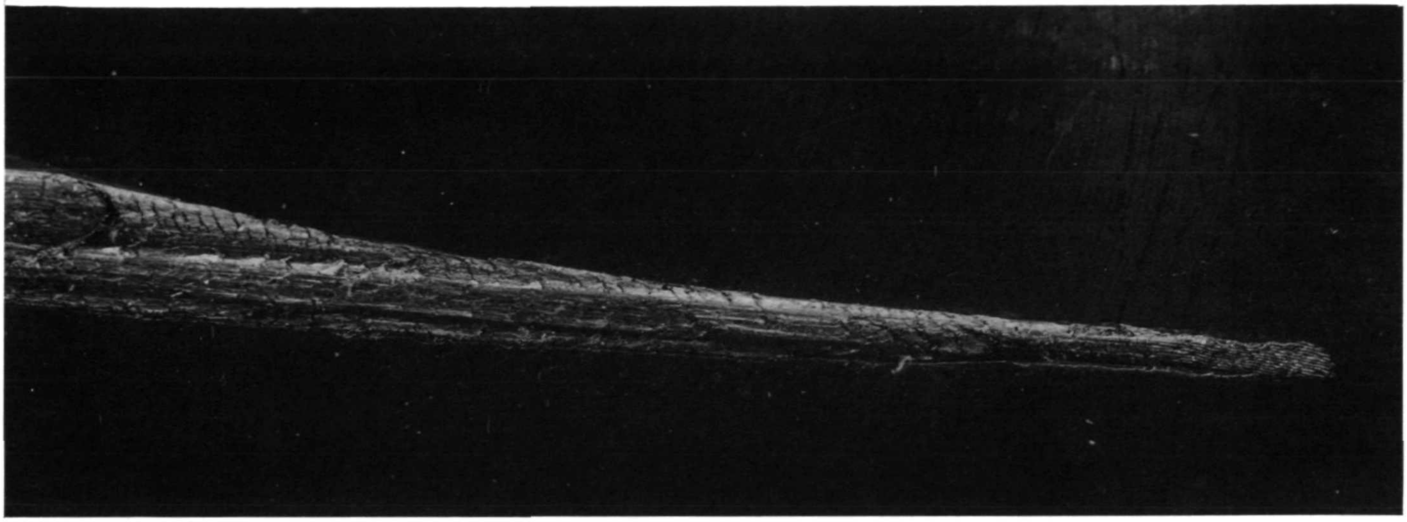

Fig. 4. Damage print on runner

Fig. 5. Damage print on the film height sensor

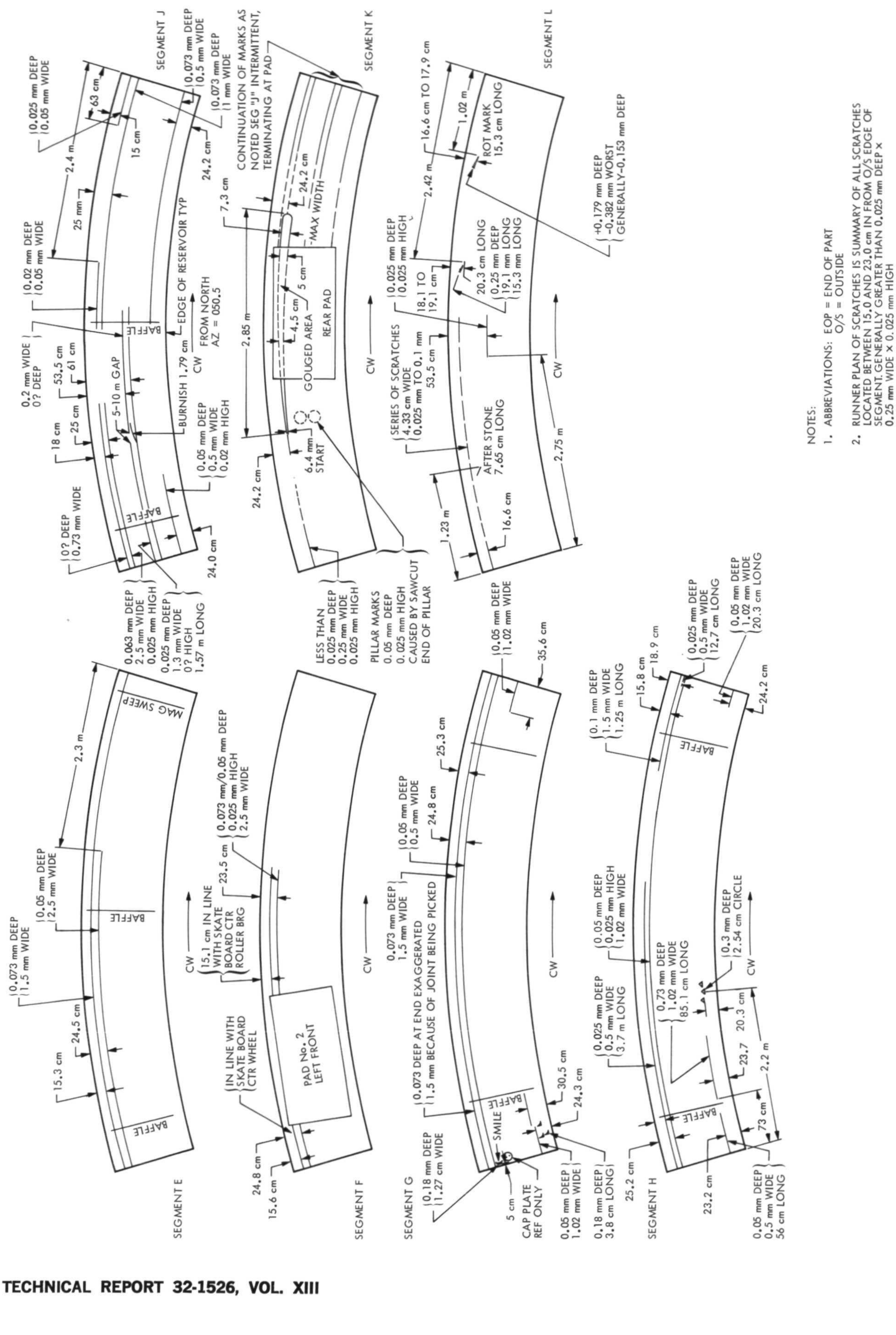

Fig. 6. Maps of individual segments

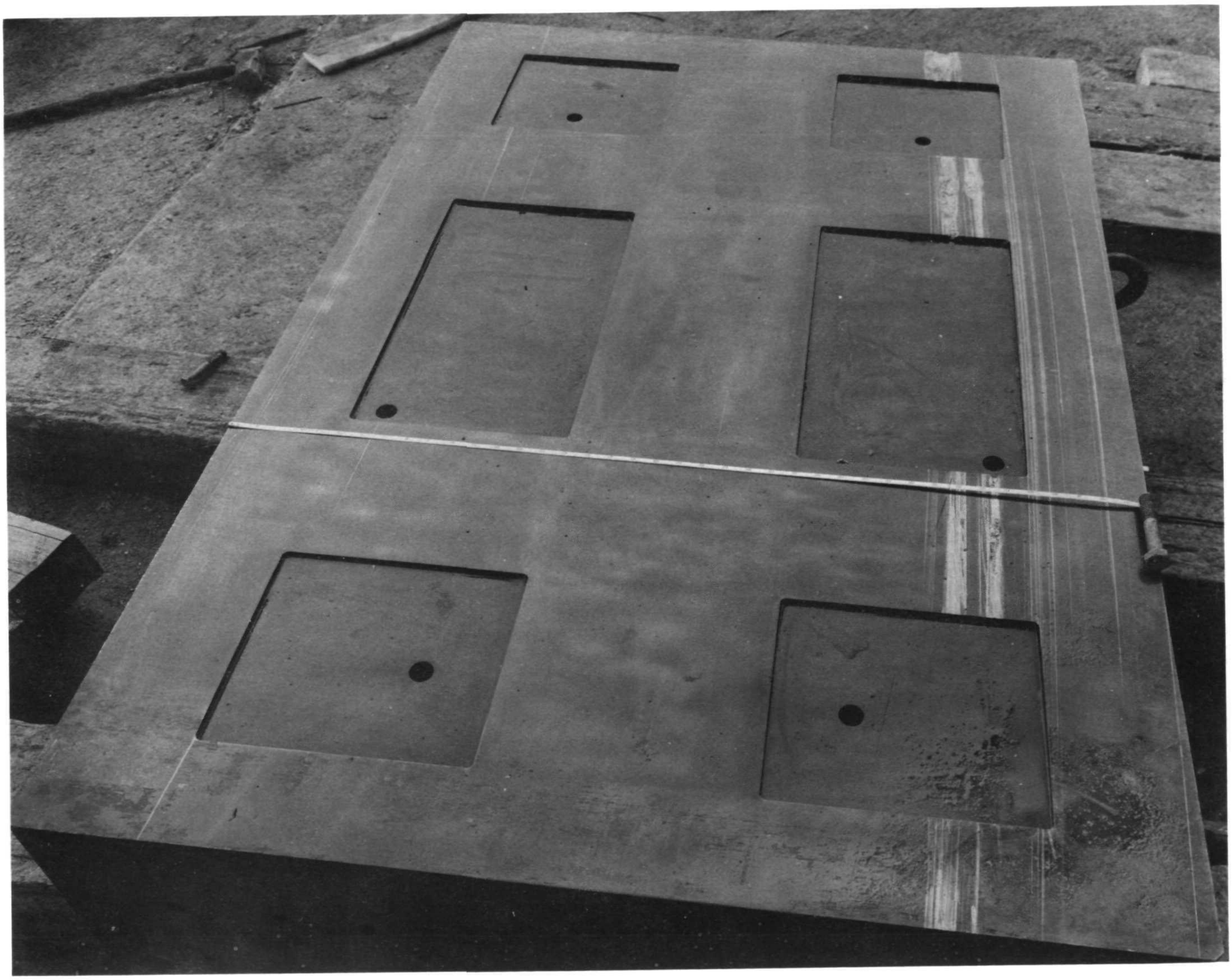

Fig. 7. Rear pad after removal

Mariner 9 Doppler Noise Study

A. L. Berman
Network Operations Office

Doppler noise data as calculated by and compiled from the near-real-time 360/75 pseudo-residual program during the Mariner 1971 mission are presented as a function of uplink and downlink signal strength. Some observations are made about the nature of this relationship, as well as about the functional dependence of doppler noise on round-trip light time and ground frequency standards.

I. Introduction

One of the strongest tools in monitoring the performance of the DSN tracking system is the doppler data standard deviation, or, as it is commonly referred to, doppler noise. However, to get maximum use out of this tool, one really needs to have a noise model as a function of the relevant parameters which determine the noise, such as doppler mode, doppler count time, ground station frequency standard, uplink signal strength, downlink signal strength, etc. The DSN is responsible for developing such a model based on the characteristics of the tracking system, but as of this date, a tracking system noise model has been unavailable. Until such time as one becomes available, it was felt that, as an interim solution, an empirical approach could be adopted whereby an attempt would be made to correlate doppler noise during the Mariner mission with ground station frequency standard, uplink signal strength, downlink signal strength, etc.

The study herein described was restricted to two-way, 60-s-count doppler. First, this would reduce the number of variables upon which doppler noise is dependent, and secondly, two-way, 60-s-count doppler data are the predominant data type taken by the DSN and are used almost exclusively by the orbit determination process.

The data base selected to provide the doppler noise during the Mariner 9 mission was the pseudo-residual program. Briefly, the pseudo-residual program is a near-real-time, 360/75 program, which, among other things, computes a running standard deviation of the last 8 to 15 doppler samples received, on a point-by-point basis. No editing is done except for gross blunder points, and the method of computation has remained constant throughout the Mariner 9 mission. The Orbit Determination Program was an alternate source of data, albeit unsatisfactory, because the data were readily available only in compressed form (alternate 600-s samples) and were subject to varying editing techniques.

The statistical technique selected for this study was intended to produce a lower limit of the standard deviation for any given pass, or to determine the least noisy data achieved for some reasonable period of time during any given pass. This was accomplished by searching each two-way, 60-s-count pass for the three lowest groups of approximately 20 points of running standard deviation. The average value of the noise of each 20-sample group was estimated, and then the three groups were averaged to produce a final figure for the pass.

The final noise value produced for each pass is plotted in Figs. 1 through 6 vs. the day of year of each pass; also plotted as a function of day of year is uplink signal strength and downlink signal strength. Finally, included on the graphs are the frequency standards used, uplink and downlink thresholds, and points at which round-trip light time (RTLT) equaled doppler count time (60 s) and when the spacecraft switched to the high-gain antenna.

The initial impression of the results was disappointing, as a strong correlation between noise and uplink and downlink signal strengths was not apparent. However, the study has proved to be useful in three areas, namely:

(1) Observations about noise when RTLT is less than the doppler sample rate (60 s), observations about the relative noise characteristics of the different ground frequency standards, and finally, some observations about noise as a function of signal strength.

(2) As an historical record of the noise encountered during the Mariner 9 mission.

(3) As a data base against which future DSN-produced noise models can be validated. The observations described in (1) above are discussed in the sections that follow.

II. Noise Characteristics When RTLT Is Less Than the Doppler Sample Rate

When the RTLT is less than the sample rate (60 s), noise is lower because any noise in the transmitted signal has an easily calculable probability of being subtracted when the received signal is beat against the transmitted frequency. The amount of noise not subtracted out would be

$$\frac{\mathrm{RTLT}}{60\ \mathrm{s}}$$

so that one might expect that, in this early mission phase, the noise might appear as

$$\text{noise} \approx A + B\left(\frac{\mathrm{RTLT}}{60\ \mathrm{s}}\right)$$

An attempt to roughly fit a linear curve through this region (Figs. 1, 2, 4, and 5) yields the following (approximate) results:

Deep Space Station (DSS)	A, Hz	B, Hz
12	0.0008	0.0023
14	0.0007	0.0032
41	0.0014	0.0048
51	0.0008	0.0019

The figure for DSS 41 is significantly higher than that for the other DSSs; therefore, restricting ourselves to DSS 12, DSS 14, and DSS 51, we would have

$$\text{noise (Hz)} \approx 0.0008 + 0.0025\left(\frac{\mathrm{RTLT}}{60\ \mathrm{s}}\right)$$

when RTLT $\leq$ 1 min and under conditions of great signal strength.

III. Different Ground Frequency Standards

A. Differences Between the R20 and H5065 Rubidium Frequency Standards

At DSS 62, a switch was made from the R20 ("old") to the H5065 ("new") Rubidium on day 301 of the Mariner mission. The spacecraft had switched to the high-gain antenna 35 days earlier, and went into orbit 20 days later, both these events having some effect on the noise. However, if one takes the average noise 30 days prior to the frequency standard change and 20 days after the change, one arrives at the rough figures:

$$\text{average noise prior to change (R20)} \approx 0.0027\ \text{Hz}$$

$$\text{average noise after change (H5056)} \approx 0.0020\ \text{Hz}$$

leading to a difference of

$$\Delta \approx 0.0007\ \text{Hz}$$

$$\Delta\,\% = 26$$

However, since the numbers are so close and the graphical analysis is so rough, the results are subject to some question. All in all, one might say that the R5065 Rubidium certainly appears at least as quiet as the R20, and possibly, somewhat quieter.

B. Differences Between the R20 Rubidium and the Hydrogen Maser

On day 265, three stations, DSS 12, DSS 41, and DSS 51, made a switch from the R20 Rubidium to the Hydrogen Maser. In all three cases, a dramatic drop in the doppler noise occurred (see Figs. 1, 4, and 5). Once again, using rough graphical techniques, the noise levels before and after the switch were as follows:

DSS	R20 Rubidium, Hz	Hydrogen Maser, Hz
12	0.0031	0.0015
41	0.0046	0.0013
51	0.0029	0.0012
Average	0.0035	0.0013

Thus, we have:

average noise prior to change (R20 Rubidium) $\approx$ 0.0035

average noise after change (Hydrogen Maser) $\approx$ 0.0013

$$\Delta \approx 0.0022 \text{ Hz}$$

$$\Delta\,\% \approx 63$$

These figures are, of course, only approximate, but they do indicate a considerable improvement from the R20 Rubidium to the Hydrogen Maser.

IV. Noise as a Function of Signal Strength

It had been hoped to arrive at some definite conclusions regarding the effect of signal strength on doppler noise level. Unfortunately, no specific statements can be made on the basis of the results as presented in Figs. 1 through 6. However, there are two regions in which we might expect to find some signal strength effects.

On day 265, the spacecraft switched to the high-gain antenna, and this produced an increase of 17 dBm in downlink signal strength over about a 2-week period. However, in the case of DSS 12, DSS 41, and DSS 51 this occurred concurrently with the switch to the Hydrogen Maser, so that any minor effect on the noise by the increase in signal strength was totally overshadowed by the noise reduction due to the implementation of the Hydrogen Maser. The one station where the effect of the 17-dBm increase in signal strength can be seen is DSS 62. However, inspection of Fig. 6 leads one to the conclusion that, at the most, it decreased the noise by only 0.0001 or 0.0002 Hz.

The second region showing some effect is where the signal strength came close to threshold. This occurred when Mariner 9 was in orbit, and at a time when the noise bandwidth reported by the pseudo-residual program had widened considerably compared to pre-insertion (day 310; see Figs. 1, 4, and 6) data. The reason was that, after insertion, the predicts supplied to the pseudo-residual program by the Navigation Team had large oscillating trends, and since the program can only fit a second-degree polynominal to the raw residuals (actual data-predicted data), some amount of trend could not be correctly accounted for in the standard deviation computation.

In Figs. 1 and 4, an increase in noise is noted from about day 035 to day 075. In both these cases, the uplink signal strength stayed almost constant at approximately −143 dBm (9 dBm above threshold), while the downlink signal strength fell from −154 (18 dBm above threshold) to −159 dBm (13 dBm above threshold), so that one might guess that the noise was sensitive to downlink signal strength and increased as downlink signal strength approached 10 dBm above threshold. However, this appears to be contradicted by the drop in downlink signal strength to about −165 dBm (7 dBm above threshold) at DSS 62 (see Fig. 6), without a noticeable increase in noise. It is known that noise is sensitive to signal strength, but the results of this study appear to yield little information about that relationship.

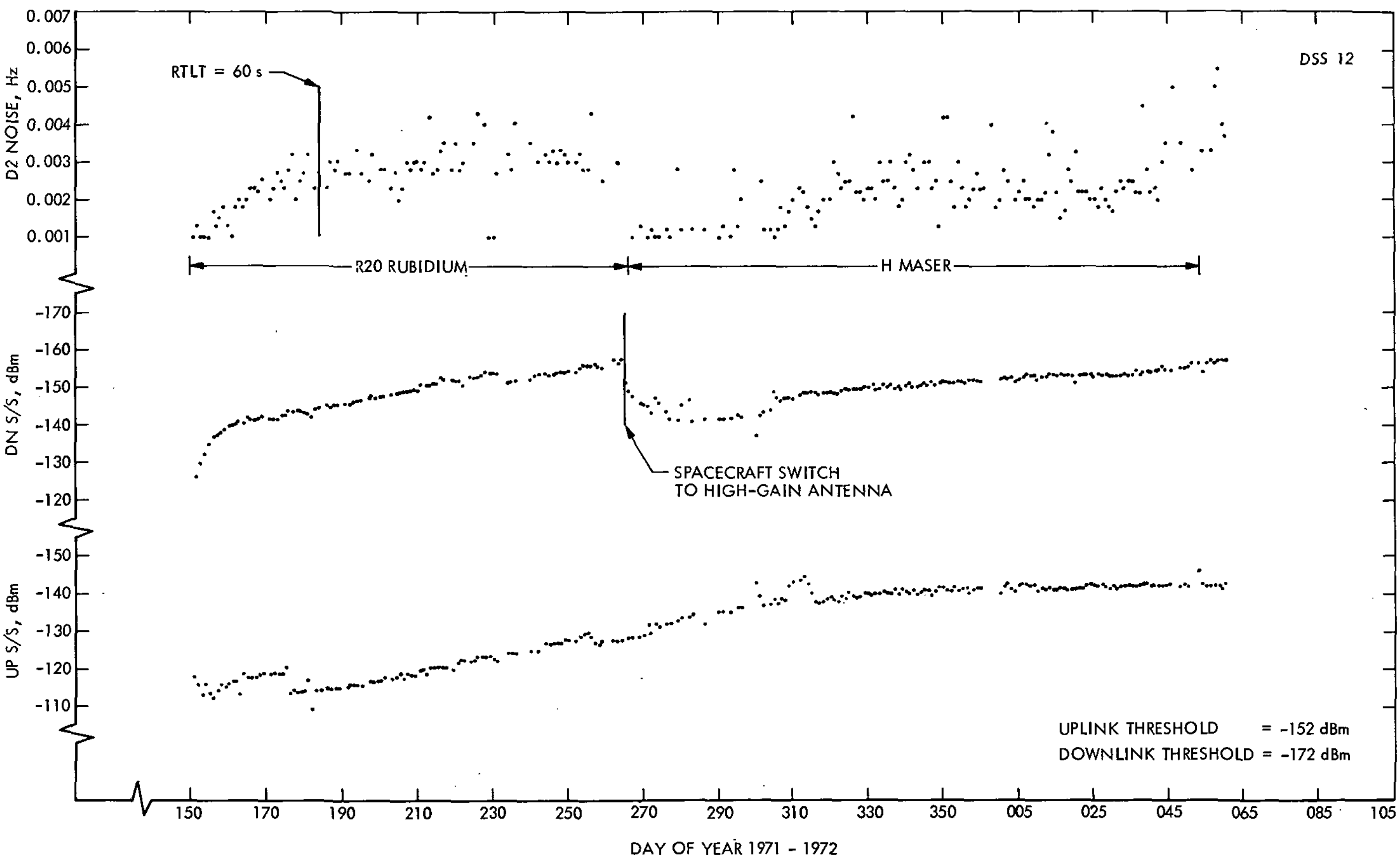

Fig. 1. Mariner 9 doppler noise and uplink and downlink signal strength vs. day of year, DSS 12

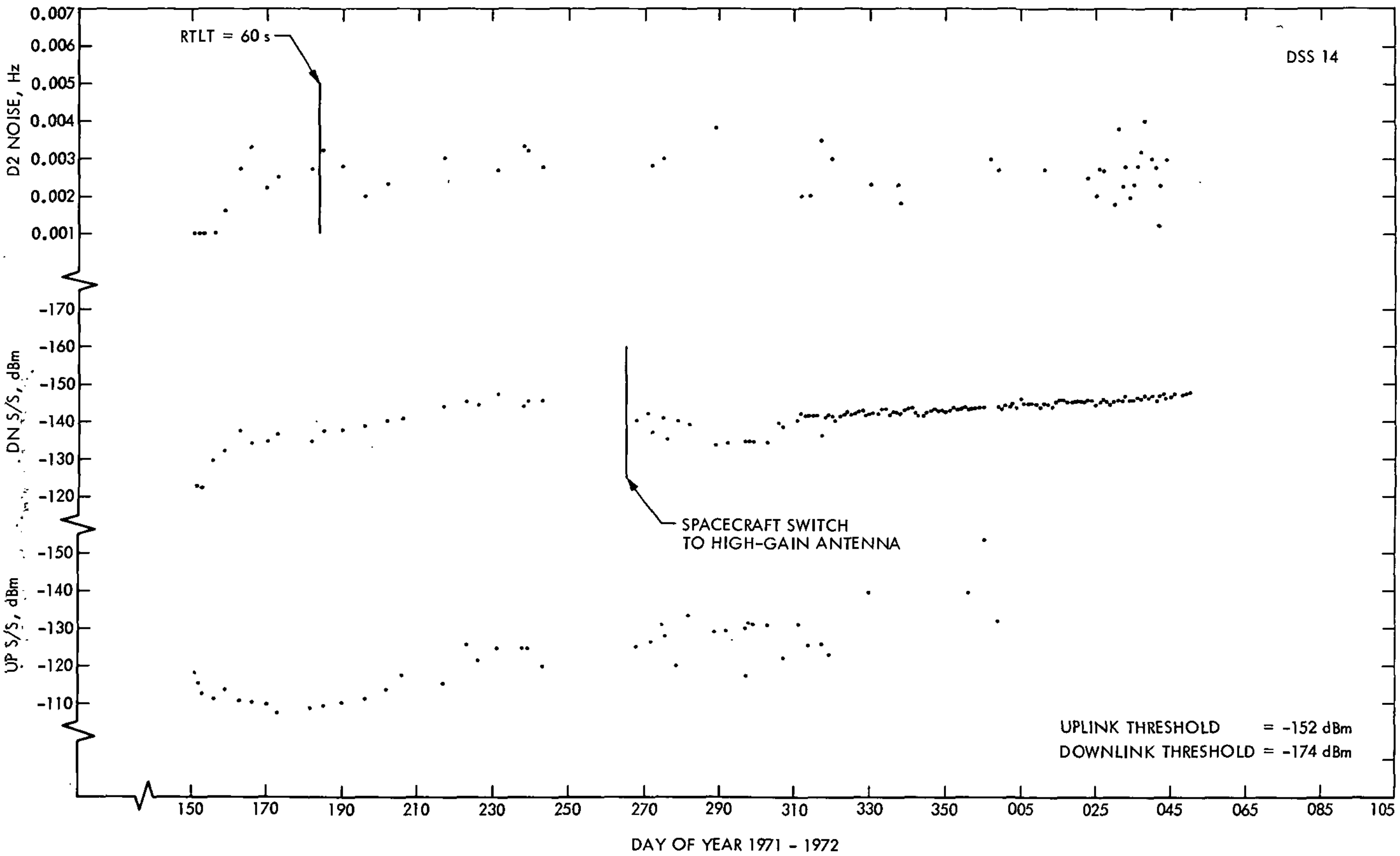

Fig. 2. Mariner 9 doppler noise and uplink and downlink signal strength vs. day of year, DSS 14 (1971–1972)

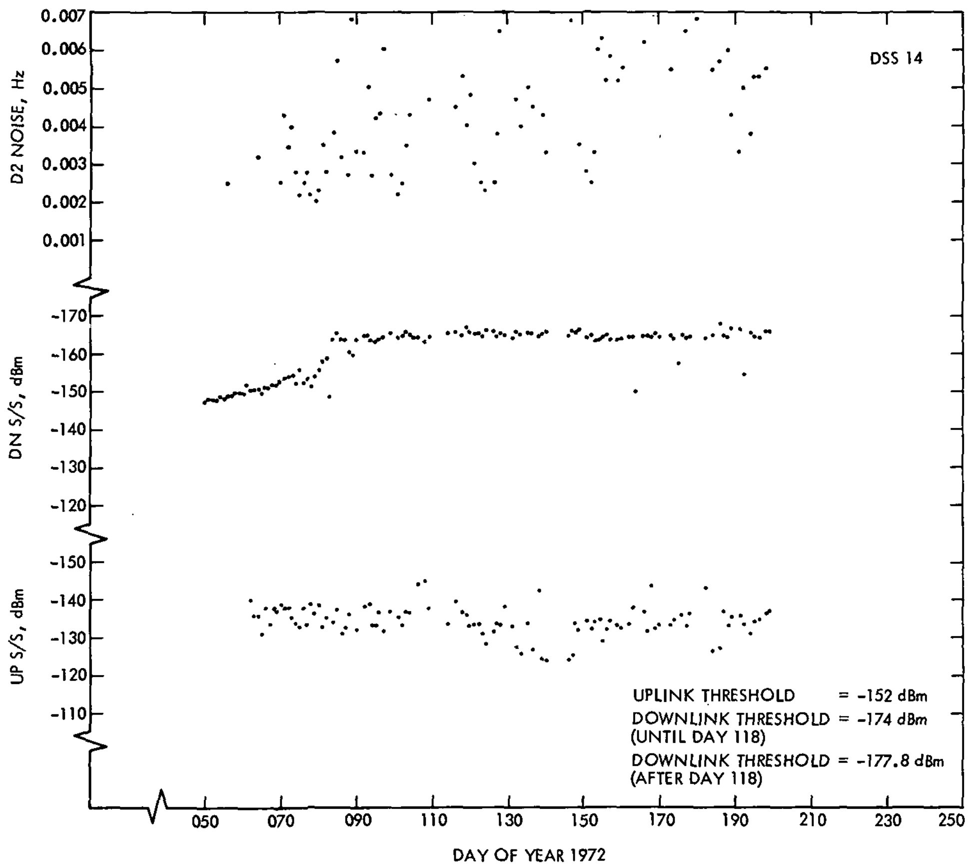

Fig. 3. Mariner 9 doppler noise and uplink and downlink signal strength vs. day of year, DSS 14 (1972)

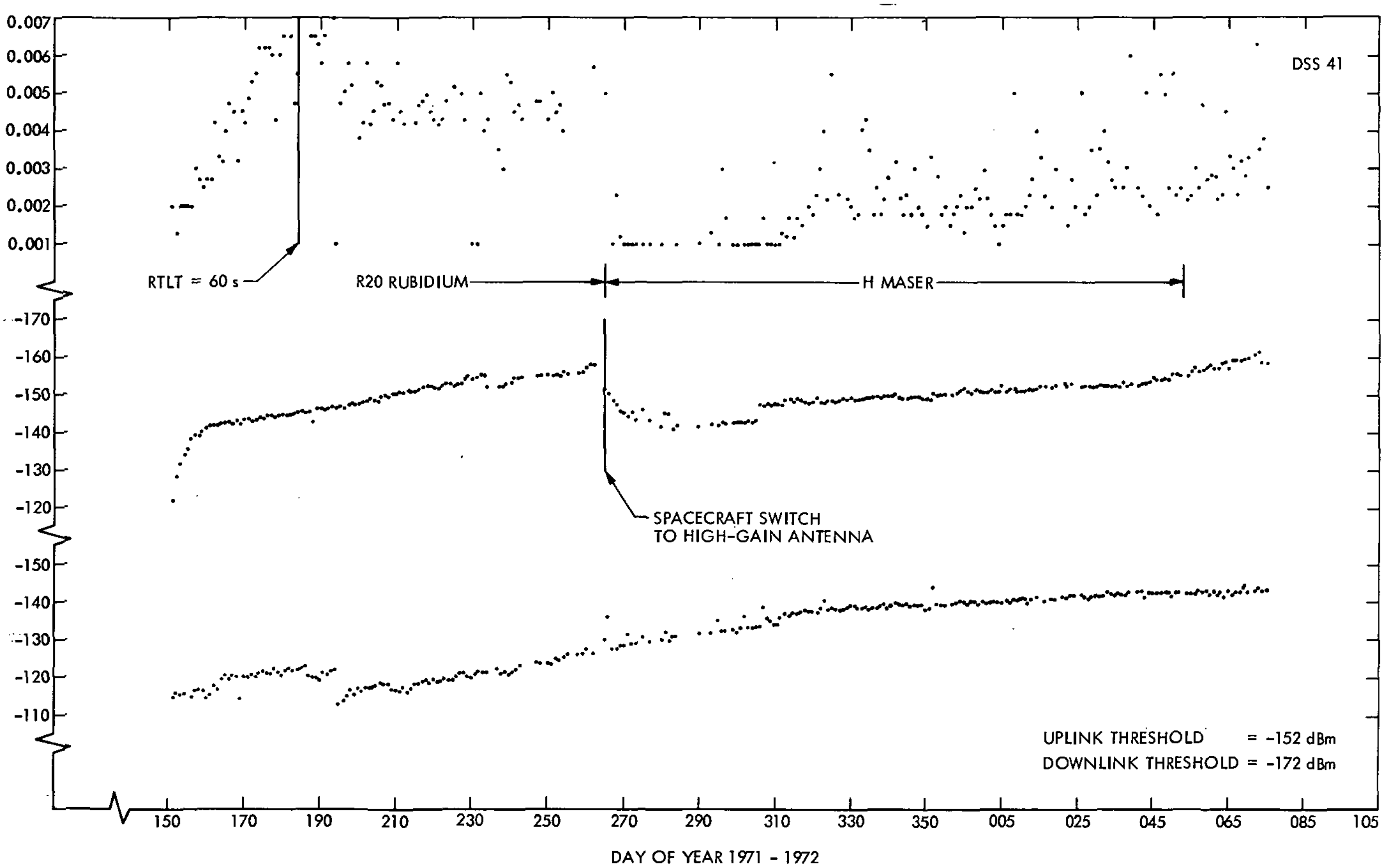

Fig. 4. Mariner 9 doppler noise and uplink and downlink signal strength vs. day of year, DSS 41

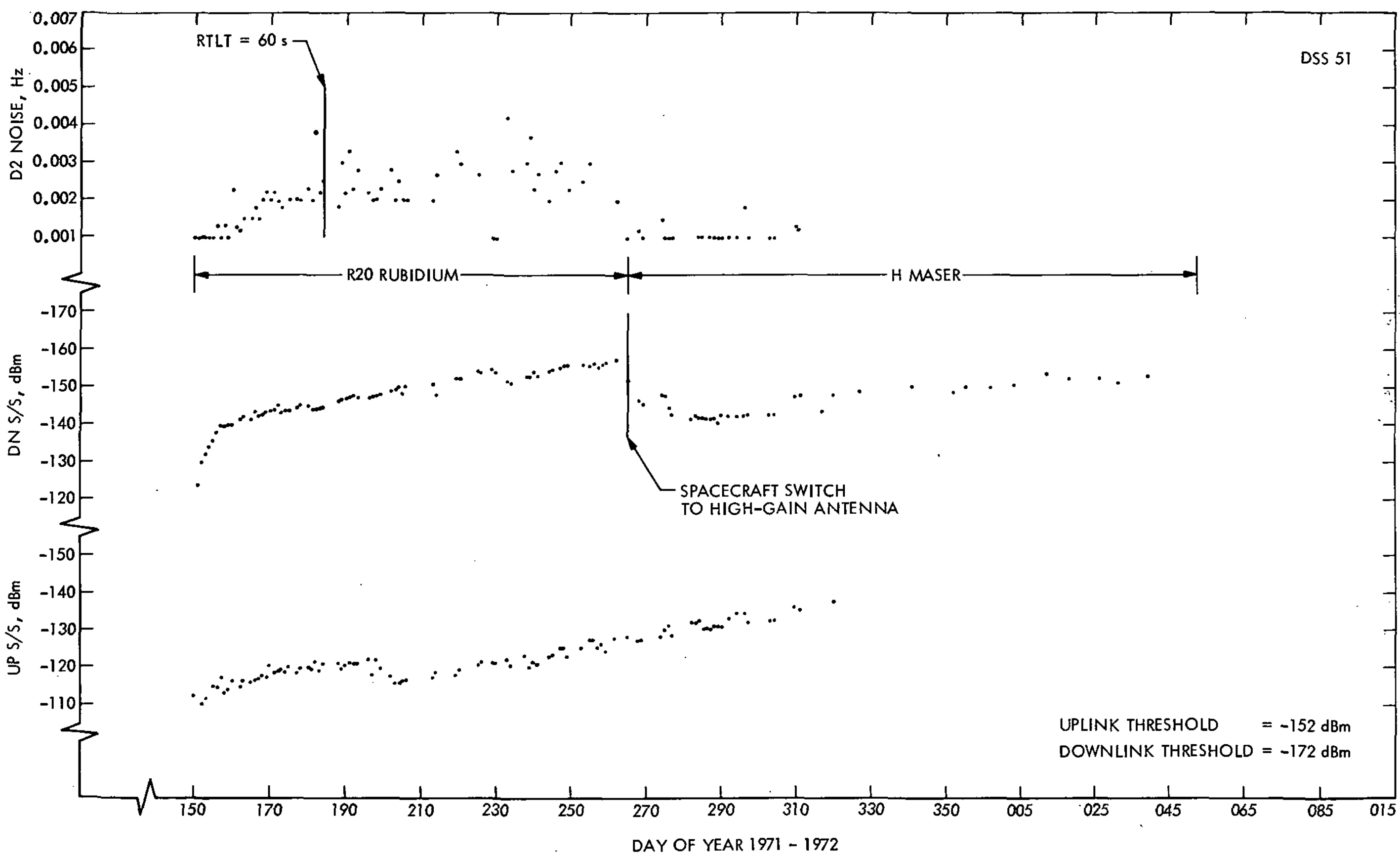

Fig. 5. Mariner 9 doppler noise and uplink and downlink signal strength vs. day of year, DSS 51

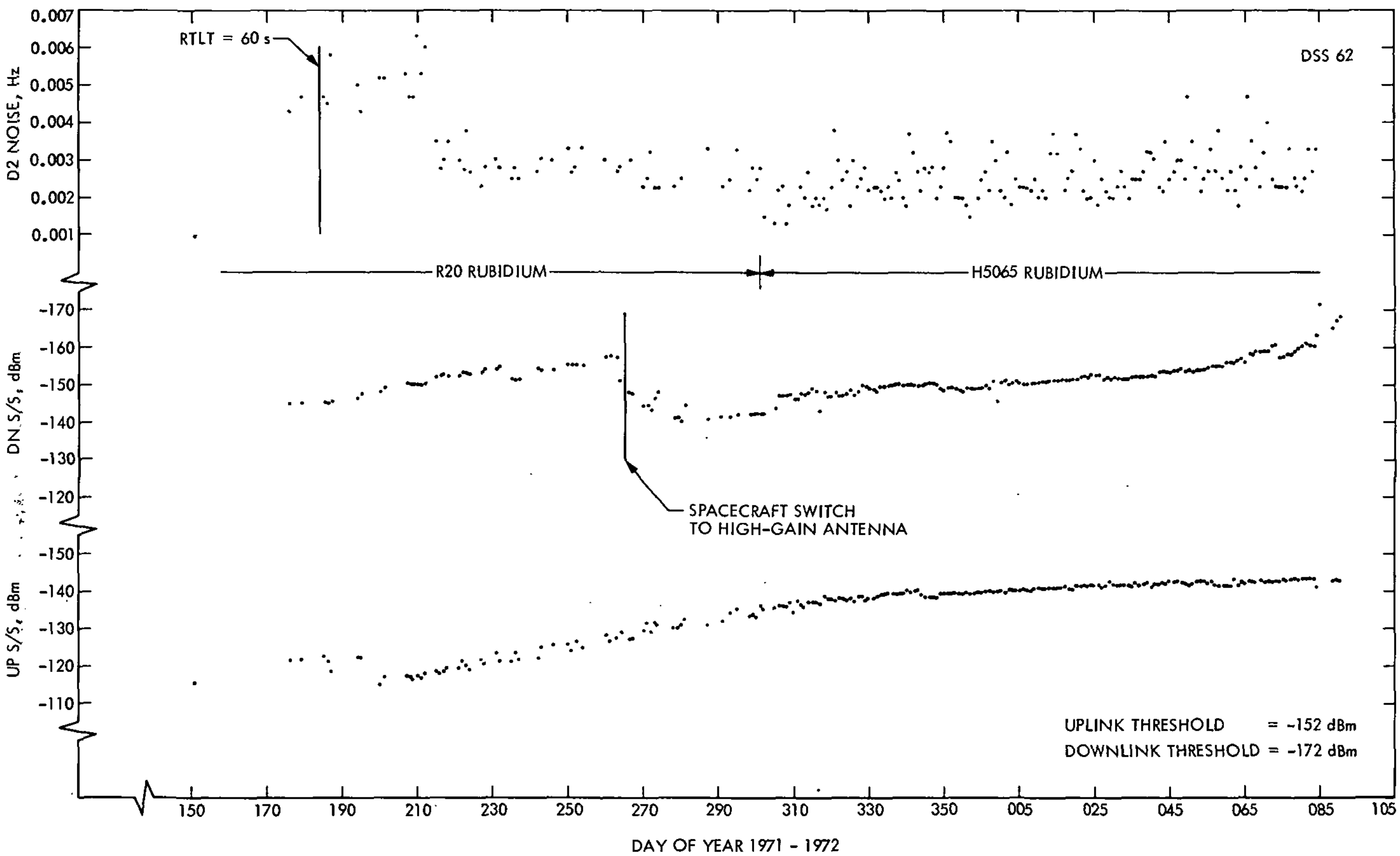

Fig. 6. Mariner 9 doppler noise and uplink and downlink signal strength vs. day of year, DSS 62

Bandlimited Power of an Asynchronously Biphase-Modulated Squarewave

J. R. Lesh
DSN Operations

Expressions for the bandlimited power of a squarewave which is biphase-modulated by an asynchronous binary data stream are determined by means of spectral integration. The utility of these expressions is demonstrated through examples using typical Mariner Venus/Mercury 1973 mission parameters.

I. Introduction

In a previous article (Ref. 1), an expression for the spectrum of a squarewave carrier biphase-modulated by an asynchronous binary data stream was determined. While this expression is useful in calculating the power spectral density at a particular frequency, it sheds little light on the calculation of the total power contained in a specified bandwidth (or equivalently, how much power is lost due to band limitations). In this article, expressions for the total power contained within an arbitrary spectral band are presented. Some sample calculations are made using Mariner/Venus Mercury 1973 mission parameters to show the utility of these expressions.

II. Derivation of Equations

Consider a squarewave carrier signal, assuming values of ± 1 with period T_S. Consider also a random binary data stream, taking on values of ± 1 with equal probability and bit period T_b. We assume that the data stream is generated asynchronously with respect to the carrier signal and that the data stream biphase-modulates the carrier. Now, if we let n denote the number of carrier half-periods which can be totally contained within one bit time, i.e.,

$$n = \text{greatest integer in} \left(\frac{2T_b}{T_S}\right) \tag{1}$$

then the spectrum of the modulated carrier $S(f)$ is given by (Ref. 1, Eq. 9)

$$S(f) = \frac{4}{T_S T_b \pi^3 f^3} \sum_{k=1}^{n} \left\{ (-1)^k \left[\sin(k\pi f T_S) - \frac{k\pi f T_S}{2} \cos(k\pi f T_S) + \pi f T_b \cos(k\pi f T_S) \right] \right\}$$
$$+ \frac{1}{2T_S T_b \pi^2 f^2}(T_S + 4T_b)$$
$$+ \frac{(-1)^n}{2\pi^2 f^2}\left[\frac{4}{T_S} - \frac{(2n+1)}{T_b}\right]\cos(2\pi f T_b)$$
$$- \frac{2(-1)^n}{\pi^3 T_S T_b f^3}\sin(2\pi f T_b) \qquad (2)$$

If we denote P_{f_1,f_2} as the power contained in the spectral window from f_1 to f_2 Hz, then

$$P_{f_1,f_2} = \int_{f_1}^{f_2} S(f)\,df$$
$$= \frac{4}{T_S T_b \pi^3} \sum_{k=1}^{n} (-1)^k \int_{f_1}^{f_2} \frac{\sin(k\pi f T_S)}{f^3}\,df$$
$$- \frac{2}{T_b \pi^2} \sum_{k=1}^{n} k(-1)^k \int_{f_1}^{f_2} \frac{\cos(k\pi f T_S)}{f^2}\,df$$
$$+ \frac{4}{T_S \pi^2} \sum_{k=1}^{n} (-1)^k \int_{f_1}^{f_2} \frac{\cos(k\pi f T_S)}{f^2}\,df$$
$$+ \frac{(T_S + 4T_b)}{2T_S T_b \pi^2}\left[\frac{1}{f_1} - \frac{1}{f_2}\right]$$
$$+ \frac{(-1)^n}{2\pi^2}\left[\frac{4}{T_S} - \frac{(2n+1)}{T_b}\right] \int_{f_1}^{f_2} \frac{\cos(2\pi f T_b)}{f^2}\,df$$
$$- \frac{2(-1)^n}{T_S T_b \pi^3} \int_{f_1}^{f_2} \frac{\sin(2\pi f T_b)}{f^3}\,df \qquad (3)$$

These integrals can be evaluated by relatively straightforward techniques to yield

$$P_{f_1,f_2} = \frac{2}{T_S T_b \pi^3} \sum_{k=1}^{n} (-1)^k \left[\frac{\sin(k\pi f_1 T_S)}{f_1^2} - \frac{\sin(k\pi f_2 T_S)}{f_2^2}\right]$$
$$+ \frac{4}{T_S \pi^2} \sum_{k=1}^{n} (-1)^k \left[\frac{\cos(k\pi f_1 T_S)}{f_1} - \frac{\cos(k\pi f_2 T_S)}{f_2}\right]$$
$$+ \frac{4}{\pi} \sum_{k=1}^{n} k(-1)^k [S_i(k\pi f_1 T_S) - S_i(k\pi f_2 T_S)]$$
$$+ \frac{(-1)^n(2n+1)}{2\pi^2 T_b}\left[\frac{\cos(2\pi f_2 T_b)}{f_2} - \frac{\cos(2\pi f_1 T_b)}{f_1}\right]$$
$$+ \frac{(-1)^n(2n+1)}{\pi}[S_i(2\pi f_2 T_b) - S_i(2\pi f_1 T_b)]$$
$$+ \frac{(-1)^n}{T_S T_b \pi^3}\left[\frac{\sin(2\pi f_2 T_b)}{f_2^2} - \frac{\sin(2\pi f_1 T_b)}{f_1^2}\right]$$
$$+ \frac{(T_S + 4T_b)}{2T_S T_b \pi^2}\left[\frac{1}{f_1} - \frac{1}{f_2}\right] \qquad (4)$$

where $S_i(x)$ is the sine integral defined by

$$S_i(x) = \int_0^x \frac{\sin u}{u}\,du \qquad (5)$$

Unfortunately, no closed form has yet been determined for the sine integral. Thus, we must resort to approximate solutions. For $|x| < 1$, we can expand $S_i(x)$ in a Taylor series, so that

$$S_i(x) \approx x - \frac{x^3}{18} + \frac{x^5}{600} - \frac{x^7}{35280} + \frac{x^9}{3265920} \qquad |x| < 1 \qquad (6)$$

For $|x| \geqq 1$, we can use the approximation (Ref. 2)

$$S_i(x) \approx \frac{\pi}{2} - f(x)\cos(x) - g(x)\sin(x) \qquad |x| \geqq 1 \qquad (7)$$

where

$$f(x) = \frac{1}{x}\left(\frac{x^8 + a_1x^6 + a_2x^4 + a_3x^2 + a_4}{x^8 + b_1x^6 + b_2x^4 + b_3x^2 + b_4}\right)$$
$$g(x) = \frac{1}{x^2}\left(\frac{x^8 + c_1x^6 + c_2x^4 + c_3x^2 + c_4}{x^8 + d_1x^6 + d_2x^4 + d_3x^2 + d_4}\right) \qquad (8)$$

and the coefficients a_j, b_j, c_j, and $d_j; j = 1, 2, 3, 4$ are given in Ref. 2.

Equation (4) can be used to compute the power in any spectral band, provided neither of the frequencies f_1 or f_2 is zero. To compute the corresponding power when one of these frequencies (say, f_1) is zero, we can use the appropriate limit expression. Thus, we find that the power within the 0 to f_2 Hz band is

$$
\begin{aligned}
P_{0,f_2} &= \lim_{f_1 \to 0} \{P_{f_1,f_2}\} \\
&= -\frac{2}{T_S T_b \pi^3} \sum_{k=1}^{n} (-1)^k \frac{\sin(k\pi f_2 T_S)}{f_2^2} \\
&\quad - \frac{4}{T_S \pi^2} \sum_{k=1}^{n} (-1)^k \frac{\cos(k\pi f_2 T_S)}{f} \\
&\quad - \frac{4}{\pi} \sum_{k=1}^{n} k(-1)^k S_i(k\pi f_2 T_S) \\
&\quad + \frac{(-1)^n (2n+1)}{2\pi^2 T_b} \frac{\cos(2\pi f_2 T_b)}{f_2} \\
&\quad + \frac{(-1)^n (2n+1)}{\pi} S_i(2\pi f_2 T_b) \\
&\quad + \frac{(-1)^n}{T_S T_b \pi^3} \frac{\sin(2\pi f_2 T_b)}{f_2^2} - \frac{(T_S + 4T_b)}{2\pi^2 T_S T_b f_2}
\end{aligned}
\qquad (9)
$$

Finally, we note that if f_2 is allowed to increase without bound, then

$$
P_{0,\infty} = \lim_{f_2 \to \infty} \{P_{0,f_2}\} = \frac{1}{2} \qquad (10)
$$

which says, as one would expect, that half of the power occupies the positive frequency region.

III. Example of Band-Limited Power Loss

Consider a squarewave subcarrier of 177.1 kHz, modulated by a data stream of 117.6 kbps. This modulated signal is to be passed through a low-pass filter having a 2.0-MHz cutoff frequency. To compute the power lost due to this finite bandwidth, we can first compute the power passed by the filter from Eq. (9). If this result is doubled to account for negative frequencies, the power passed is found to be 0.959, which corresponds to a power loss of 0.18 dB.

IV. Example of Band Interference Power

Consider the same modulated subcarrier as in the previous example. This time, however, we are interested in the percentage of this signal power that occupies the region of a lower-rate channel extending from 75.483 to 102.617 kHz. Folding the spectrum and using Eq. (4) reveals that 2.1% of the high-rate signal power occupies the low-rate channel region.

References

1. Lesh, J. R., "Spectrum of an Asynchronously Biphase Modulated Squarewave," in *The Deep Space Network Progress Report*, Technical Report 32-1526, Vol. XII, pp. 226–229, Jet Propulsion Laboratory, Pasadena, Calif., Dec. 15, 1972.

2. Abramowitz, M., and Stegum, I. A., *Handbook of Mathematical Functions*, National Bureau of Standards, June 1964, pp. 232–233.

The Traceability and Reporting Program: Mariner Mars 1971—Integration, Review, Evolution

J. A. Miccio
DSN Operations

The Traceability and Reporting Program (TARP) is the basic support software utilized by the DSN Operational Data Center (ODC). It is used during mission operations to provide administrative control and selective dissemination of information concerning transferable DSN mission data products. Significant qualitative information relative to data record production, quality, logistics, and recycleability status are entered into the data base with respective operational data. Data records covered in TARP consist of original, system, and master magnetic tapes with supplemental microfilmed hard-copy records. The execution of this program within ODC in support of Mariner Mars 1971 (MM'71) operations is reviewed in this article, focusing on the evolution of the program through MM'71, into its current status, and planned configuration for Pioneer G and Mariner Venus/Mercury 1973 mission support. The program's current organization structure is adaptive to both mission operation support and management information support environments. Thus concurrent efforts are being expended on the adaptability of the present system to data management systems involved in hierarchical reporting relationships concerned with user–operations–management interfaces.

I. Introduction

The Traceability and Reporting Program (TARP) is a file management scheme based on Informatics MARK IV software, operating in either an IBM 370/155 or 360/75 system environment. Specifically, TARP is utilized to provide data administration, i.e., the accountability of and accessibility to network data records, and the retrieval and reporting of information concerning those records for network management and users. The significant capability of TARP is the linkage developed for coordination of information from multiple network sources (Deep Space Stations, Ground Communications Facility, Monitor, Operations Support) enabling summary profiles for a particular spacecraft, station, and GMT day of year (DOY)

combination to be assembled. Linkage is established within the DSN Scheduling System by assigning a "key" to scheduled spacecraft, station, and DOY combinations. Thus, all network system records, hard copy, and magnetic data generated during a tracking sequence are commonly addressed under a key assigned to that particular sequence (Fig. 1).

There are four methods used in TARP to enable a requestor to narrow the search for a desired item. They are used sequentially, in order of selectivity and efficiency of search. The first method provides an efficient way to initially narrow the search, while in the last, a much higher selectivity of the remaining items is provided. The methods are:

(1) Hierarchical classification—basic subject category breakdown

(2) Semantical characterization—subject distinction/qualification

(3) Free-form search—specific word or phrase search

(4) Data content examination—selected item reduction and analysis

II. Mariner Performance Review

Management of information implies the understanding of the requirements acquired data must serve or meet. Of the different types of data acquired and recorded by the DSN during the Mariner Mars 1971 (MM'71) mission, engineering data concerning the functions of the spacecraft and performance data concerning the functions of the DSN operations were basic to TARP. Engineering data were used for System Data Record (SDR) and subsequent Master Data Record (MDR) production as deliverable products to the Project for Experimenter Data Record generation. The utility of DSN performance data was directed toward the effective management of the DSN itself.

A Management Information System (MIS) such as TARP, unlike most information systems designed to perform specific functions, has greater utility and potential when utilizing input information from a broad base to produce reports that enable accurate and expeditious user analysis/judgment.

TARP operates in a nonreal-time mode; data are transferred into ODC from real-time systems either by card input or manual abstraction of information from source hard-copy and/or network monitor summaries (Ref. 1). This information interface resulted in the development of forms to expedite the transfer of information, as well as to minimize the translation of information from one form to another for keypunching functions. It became obvious that in order to secure the needed inputs reliably, the information had to be accepted by the system in the form that was most useful to the source activity (Network Monitor) responsible for its submission. Resultant forms had system compatible formats requiring the entry of specific information into predefined areas from which keypunching or abstration could take place without any additional or transitional forms being required. This process enabled efficient and expeditious entry of information into TARP. In addition, it introduced a sense of discipline regarding the recording and reporting of information in such a way as to facilitate retrieval and search strategies to meet user requests.

As previously reported (Refs. 2 and 3), information system design is based on two "knowns": (1) the type of data or information generated or put into the system and (2) end user requirements—specifically, quantity, quality, format, form, and frequency of information. Throughout MM'71, the type of data entering the system remained constant; however, user request characteristics and patterns for information requests changed frequently. It was found that once data entered TARP in specific order and coding, concomitant with the frequency of change in request patterns, the program was somewhat inflexible in meeting those requests. By pursuing trade-off analysis of physical vs. logical data structure, a solution for data definition (preparation and entry) was derived. It consisted of reducing the detailed coding or indexing of specific information units, and creating "classes" of information in which specific units could be entered as well as retrieved either by unit or collectively with no loss in time.

Figure 2 represents a page generated by TARP for the DSN Monthly Operations Report showing classes of data from individual systems. In the generation of the Monthly Operations Report, the TARP process replaced a lengthy manual collection and documentation function, allowing earlier publication of the document by a minimum of 3 weeks. Additionally, owing to its flexibility, the document format has become a standard user reference, and a base for further report generation.

The information concerning magnetic tape data records, including original, system and master data records—a significant portion of the operations information—was segregated into a sub-function of TARP in terms of method for input and record structure. This information was entered

into the Traceability and Accountability (TRACC) subfile. As a subfunction, TRACC is a necessary transaction-oriented step in the DSN/project data transfer and logistics activities (Fig. 3). The occurrence which necessitated the incorporation of TRACC was the requirement to lengthen Original Data Record retention cycles and to retain SDRs until MDRs were transferred to and accepted by project. Subsequent to MM'71, the SDR/MDR production was transferred from the DSN to the Mission Control and Computing Center; future DSN emphasis, in terms of TRACC, will be oriented toward the accountability of system and Network Performance Records, along with various Ground Communications Facility and Deep Space Station log tapes.

III. Evolution and Development

The characteristics of Network Performance information requirements place limiters on the scope or latitude of possible systems design. These characteristics differ with respect to (1) the type of information storage medium to be utilized, (2) the complexity of retrieval algorithms that can be employed efficiently, and (3) the types of functional activities necessary on the part of the information analyst to effect retrieval of information. Thus, to maximize the efficiency of an existing system within a new environment (structured by data processing, hardware and software innovations, and new user requirements), the information processing flow must be segmented into its three principal modules and evaluated as to their respective individual capabilities and possibilities.

The three basic information processing modules are (1) data definition (entry and coding) and abstraction, (2) processing, and (3) selective dissemination of information. Of the three modules, only the first offers individual flexibility, yet it determines overall system performance. From this point of reasoning, TARP development has emphasized data definition and entry in software and hardware consideration. Subsequent to MM'71, TARP has been operating exclusively on the 370/155 system, allowing execution from an IBM 2780 remote job entry (RJE) terminal and offering on-line system access for data entry, deletions, reorganization controls, and report generation. In the near future, the 370 system will be upgraded to a level which allows for "virtual storage" and provisions for multiple RJE terminal access for on-line operations.

Internally, within the Network Operations Program Support element, it is hoped that a closer interface of nonreal-time software files will establish a paradigm for commonality, in terms of accessibility via a linkage concept somewhat like that within TARP. The development of such a paradigm would enhance the completeness and responsiveness of a Network Operations Information Process.

IV. Conclusion

Mariner Mars 1971 TARP operations have successfully identified areas of information acquisition and dissemination not heretofore considered. Those concepts developed during the course of MM'71 provide a basis for further development and planning toward a common network data base indifferent to software consideration, yet addressed to user requirements and satisfaction.

References

1. Allen, J. E., "DSN Monitor Performance Program," in *The Deep Space Network Progress Report*, Technical Report 32-1526, Vol. IX, pp. 5–11, Jet Propulsion Laboratory, Pasadena, Calif., June 15, 1972.
2. Miccio, J. A., "DSN Traceability and Reporting Program: Micrographic Application," in *The Deep Space Network Progress Report*, Technical Report 32-1526, Vol. VII, pp. 185–187, Jet Propulsion Laboratory, Pasadena, Calif., Feb. 15, 1972.
3. Miccio, J. A., "DSN Traceability and Reporting Program," in *The Deep Space Network Progress Report*, Technical Report 32-1526, Vol. II, pp. 145–147, Jet Propulsion Laboratory, Pasadena, Calif., Apr. 15, 1971.

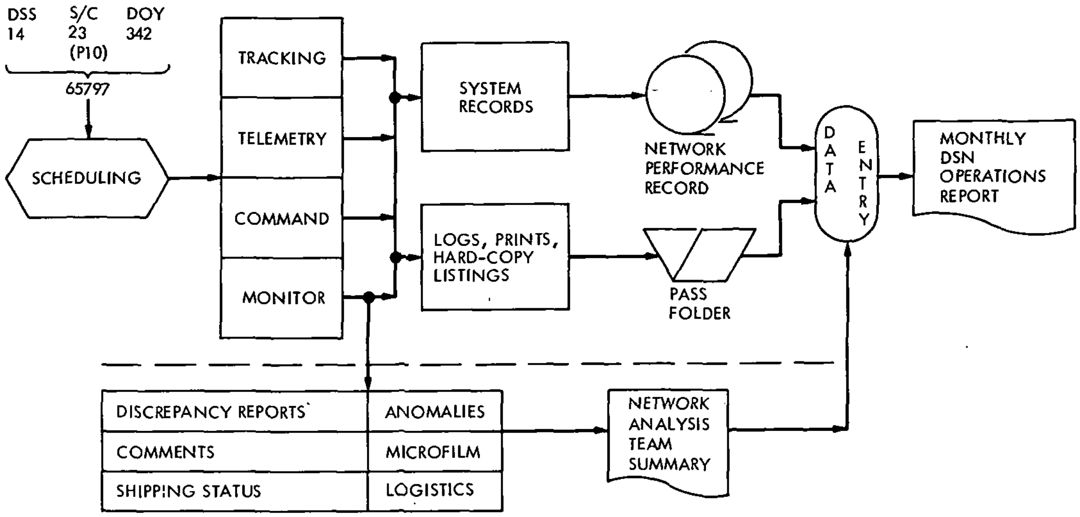

Fig. 1. Mission key assignment providing linkage association to network data records

```
                    OPERATION DATA CONTROL

                 MONTHLY REPORT FOR JUNE 1972
------------------------------------------------------------------------
PASS  GMT-START     GMT-END       DATA
NO.                               DAY
------------------------------------------------------------------------


MM9CFZ65797

0387  721711506     721720416     0387
          DSS 14 PASS 387  CL F-8 CTDN 343254 GCF S40D CPS N/A  DSS D000
          CONFIG     ---------------------------------------------------
                     ACS DOY 171  LOS DOY 172         TOTAL
                     SCHEDULED 1507Z SCHEDULED 0416Z SCHEDULED 13H 09M
                     ACTUAL    1506Z ACTUAL    0416Z ACTUAL    13H 10M
                     ST XFR    N/A Z RELEASE   0430Z DSS TIME  13H 24M
          COMMAND    ---------------------------------------------------
                     TOTAL  0   AUTO  0   MANUAL  0   ABORT  0
          TELEMETRY*----------------------------------------------------
                     POWER N/AKW  BIT RATES   8 1/3    33 1/3
                            RX 1   RX 1  TCP A ENG TCP A ENG
                     ACTUAL 164.7  149.8   8.0        6.9
                     PREDIC 164.1  149.6   6.0        6.7
                     RESID   -0.6   -0.2  +2.0       +0.2
          TRACKING   ---------------------------------------------------
                     TRACK MD  3 WAY RANGING NONEBIAS N/A RU NOISE N/A RU
                     DCP BIAS  -191  HZ C NOS  .010HZ EXP  .010HZ
          MONITOR    ---------------------------------------------------
                          LGWR  LGER  BLRC  BLER
                     DIS  2165     2     0     0
                     TCPB 3697     2    18     0

          COMMENTS   ---------------------------------------------------
          BIT RATE       4.05       8.1
                     TCP B SCI TCP B SCI
          ACTUAL         5.3        3.2
          PREDICT        4.9        3.1
          DIFFER        +0.4       +0.1
          1749Z-1752Z 360 DOWN TO LOAD VERSION 12.4 (SCHEDULED)
          2001Z-2054Z LOST ALL COMM CKTS EXCEPT WIDEBAND DATA LINE,
          ELECTRICAL FIRE AT DSS-14. DR 5703.
          2230Z-2233Z LOST HSD. DR 5707.
          0228Z-0247Z 360 DOWN - TOTAL LOCKOUT, FORCED R DUMP IPL/WARM
          AND RESTART/WARM. DR 3696.
```

Fig. 2. Individual network "data class," assembly by mission key, from DSN Monthly Operations Report

OPERATIONAL DATA CONTROL
PIONEER MAGNETIC TAPE REPORT
BY
GMT START TIME

DATA DAY	PASS NO.	GMT-START	GMT-END	DOCUMENT NO.	MSN KEY NO.	CONFIGURATION
NT-DSN NETWCRK ANALYSIS TEAM						
					TELEMETRY	
		721921315	721922359	MDR 8499	P10CGY00051 REF MDR 8499	TEL COMPOSITE
		721942359	721952359	SDR 8925	P10CGY08925 D-8973 TO OCIS 8-17-72.	TEL COMPOSITE
		721960000	721962359	SDR 8934	P10CGY08934 D-8965 TO OCIS 8-16-72.	TEL COMPOSITE
		721970000	721972359	MDR 8716	P10CGY08716 XFER TO ARC 7-24-72.	TEL COMPOSITE
		721980000	721990000	SDR 5860	P10CGY05860 D-5070 TO OCIS 8-10-72.	TEL COMPOSITE
		721990000	721992359	MDR 8431	P10CGY00052 XFER TO ARC 8-3-72. VAL CGMY	TEL COMPOSITE
		722000000	722010000	SDR 6107	P10CGY06107 D-6072 TO OCIS 8-14-72.	TEL COMPOSITE
		722020000	722022212	MDR 8755	P10CGY08755 XFER TO ARC 8-1-72. CGMY	TEL COMPOSITE
		722022212	722022359	MDR 8736	P10CGY08736 XFER TO ARC 8-1-72. CGMY	TEL COMPOSITE
		722030000	722031951	MDR 8740	P10CGY08740 XFER TO ARC 8-1-72. CGMY	TEL COMPOSITE
		722031951	722032359	MDR 8741	P10CGY08741 XFER TO ARC 8-1-72. CGMY	TEL COMPOSITE
		722040000	722041921	SDR 5210	P10CGY05210 D-8642 TO OCIS 8-10-72.	TEL COMPOSITE
		722040000	722042009	MDR 8753	P10CGY08753 XFER TO ARC 8-1-72. CGMY	TEL COMPOSITE
		722041921	722042359	SDR 6147	P10CGY06147 D-8641 TO OCIS 8-10-72.	TEL COMPOSITE
		722042009	722042359	MDR 8754	P10CGY08754 XFER TO ARC 8-1-72. CGMY	TEL COMPOSITE
		722050000	722051303	SDR 4095	P10CGY04095 D-8590 TO OCIS 8-15-72.	TEL COMPOSITE
		722051303	722052359	SDR 4287	P10CGY04287 D-6201 TO OCIS 8-15-72.	TEL COMPOSITE
		722060000	722062359	SDR 4399	P10CGY04399 D-5105 TO OCIS 8-17-22.	TEL COMPOSITE
		722060000	722062359	SDR 4403	P10CGY04403 D-4871 TO OCIS 8-8-72.	TEL COMPOSITE
		722070000	722072310	SDR 5868	P10CGY05868 D-8971 TO OCIS 8-17-72.	TEL COMPOSITE
		722072310	722072359	SDR 8951	P10CGY08951 D-8972 TO OCIS 8-17-72.	TEL COMPOSITE
		722080000	722082359	SDR 5227	P10CGY05227 D-5254 TO OCIS 8-8-72.	TEL COMPOSITE
		722090000	722092359	SDR 5173	P10CGY05173 D-6251 TO OCIS 8-1-72.	TEL COMPOSITE

Fig. 3. TRACC format in chronological sequence by spacecraft, identifying data record transfer activity

Bibliography

Anderson, J. D., *Determination of the Masses of the Moon and Venus and the Astronomical Unit from Radio Tracking Data of the Mariner II Spacecraft.* Technical Report 32-816. Jet Propulsion Laboratory, Pasadena, Calif., July 1, 1967.

Anderson, J. D., et al., "The Radius of Venus as Determined by Planetary Radar and Mariner V Radio Tracking Data," *J. Atmos. Sci.*, pp. 1171–1174, Sept. 25, 1968.

Berman, A. L., *Tracking System Data Analysis Report, Ranger VII Final Report,* Technical Report 32-719, Jet Propulsion Laboratory, Pasadena, Calif., June 1, 1965.

Berman, A. L., *ABTRAJ—On-Site Tracking Prediction Program for Planetary Spacecraft,* Technical Memorandum 33-391. Jet Propulsion Laboratory, Pasadena, Calif., Aug. 15, 1968.

Cain, D. L., and Hamilton, T. W., *Determination of Tracking Station Locations by Doppler and Range Measurements to an Earth Satellite,* Technical Report 32-534. Jet Propulsion Laboratory, Pasadena, Calif., Feb. 1, 1964.

Carey, C. N., and Sjogren, W. L., "Gravitational Inconsistency, in the Lunar Theory: Confirmation by Radio Tracking," *Science,* Vol. 160, pp. 875, 876, Apr.–June 1968.

Curkendall, D. W., and Stephenson, R. R., "Earthbased Tracking and Orbit Determination—Backbone of the Planetary Navigation System," *Astronaut. Aeronaut.*, Vol. 7, May 1970.

Curkendall, D. W., "Planetary Navigation: The New Challenges," *Astronaut. Aeronaut.*, Vol. 7, May 1970.

Efron, L., and Solloway, C. B., *Proceedings of the Conference on Scientific Applications of Radio and Radar Tracking in the Space Program,* Technical Report 32-1475. Jet Propulsion Laboratory, Pasadena, Calif., July 1970.

Flanagan, F. M., et al., *Deep Space Network Support of the Manned Space Flight Network for Apollo: 1962–1968,* Technical Memorandum 33-452, Vol. I. Jet Propulsion Laboratory, Pasadena, Calif., July 1970.

Flanagan, F. M., et al., *Deep Space Network Support of the Manned Space Flight Network for Apollo: 1969–1970,* Technical Memorandum 33-452, Vol. II. Jet Propulsion Laboratory, Pasadena, Calif., May 1, 1971.

Fjeldbo, G., and Eshleman, V. R., "Radio Occultation Measurements and Interpretations," in *The Atmospheres of Venus and Mars,* p. 225. Gordon and Breach, Science Publishers, Inc., New York, N.Y.

Georgevick, R. M., "Mathematical Model of the Solar Radiation Force and Torques Acting on the Components of a Spacecraft," Technical Memorandum 33-494. Jet Propulsion Laboratory, Pasadena, Calif., Oct. 1, 1971.

Goldstein, R. M., "Radar Time-of-Flight Measurements to Venus," *Astron. J.*, Vol. 73, No. 9, Aug. 1968.

Goldstein, R. M., and Rumsey, H., Jr., "A Radar Snapshot of Venus," *Science,* Vol. 169, Sept. 1970.

Bibliography (contd)

Gordon, H. J., et al., *The Mariner 6 and 7 Flight Paths and Their Determination From Tracking Data,* Technical Memorandum 33-469. Jet Propulsion Laboratory, Pasadena, Calif., Dec. 1, 1970.

Hamilton, T. W., et al., *The Ranger IV Flight Path and Its Determination From Tracking Data,* Technical Report 32-345. Jet Propulsion Laboratory, Pasadena, Calif., Sept. 15, 1962.

Kellermann, K. I., et al., "High Resolution Observations of Compact Radio Sources at 13 Centimeters," *Astrophys. J.*, Vol. 161, pp. 803–809, Sept. 1970.

Kliore, A., "Radio Occultation Measurements of the Atmospheres of Mars and Venus," in *The Atmospheres of Venus and Mars,* p. 205. Gordon and Breach Science Publishers, Inc., New York, N. Y.

Labrum, R. G., Wong, S. K., and Reynolds, G. W., *The Surveyor V, VI, and VII Flight Paths and Their Determination from Tracking Data,* Technical Report 32-1302. Jet Propulsion Laboratory, Pasadena, Calif., Dec. 1, 1968.

Lieske, J. H., and Null, G. W., "Icarus and the Determination of Astronomical Constants," *Astron. J.*, Vol. 74, No. 2, Mar. 1969.

Lorell, J., and Sjogren, W. L., *Lunar Orbiter Data Analysis,* Technical Report 32-1220. Jet Propulsion Laboratory, Pasadena, Calif., Nov. 15, 1967.

Lorell, J., *Lunar Orbiter Gravity Analysis,* Technical Report 32-1387. Jet Propulsion Laboratory, Pasadena, Calif., June 15, 1969.

Lorell, J., et al., "Celestial Mechanics Experiment for *Mariner,*" Icarus, Vol. 12, Jan. 1970.

McNeal, C. E., *Ranger V Tracking Systems Data Analysis Final Report,* Technical Report 32-702. Jet Propulsion Laboratory, Pasadena, Calif., Apr. 15, 1965.

Melbourne, W. G., et al., *Constants and Related Information for Astrodynamical Calculations,* Technical Report 32-1306. Jet Propulsion Laboratory, Pasadena, Calif., July 15, 1968.

Melbourne, W. G., "Planetary Ephemerides," *Astronaut. Aeronaut.*, Vol. 7, May 1970.

Miller, L., et al., *The Atlas–Centaur VI Flight Path and Its Determination from Tracking Data,* Technical Report 32-911. Jet Propulsion Laboratory, Pasadena, Calif., Apr. 15, 1966.

Moyer, T. D., "Mathematical Formulation of the Double-Precision Orbit Determination Program (DPODP)," Technical Report 32-1527, Jet Propulsion Laboratory, Pasadena, Calif., May 17, 1971.

Mulhall, B. D., et al., *Tracking System Analytic Calibration Activities for the Mariner Mars 1969 Mission,* Technical Report 32-1499. Jet Propulsion Laboratory, Pasadena, Calif., Nov. 15, 1970.

Mulholland, J. D., and Sjogren, W. L., *Lunar Orbiter Ranging Data,* Technical Report 32-1087. Jet Propulsion Laboratory, Pasadena, Calif., Jan. 6, 1967.

Bibliography (contd)

Mulholland, J. D., *Proceedings of the Symposium on Observation, Analysis, and Space Research Applications of the Lunar Motion,* Technical Report 32-1386. Jet Propulsion Laboratory, Pasadena, Calif., Apr. 1969.

Muller, P. M., and Sjogren, W. L., *Consistency of Lunar Orbiter Residuals With Trajectory and Local Gravity Effects,* Technical Report 32-1307. Jet Propulsion Laboratory, Pasadena, Calif., Sept. 1, 1968.

Muller, P. M., and Sjogren, W. L., *Lunar Mass Concentrations,* Technical Report 32-1339. Jet Propulsion Laboratory, Pasadena, Calif., Aug. 16, 1968.

Null, G. W., Gordon, H. J., and Tito, D. A., *Mariner IV Flight Path and Its Determination From Tracking Data,* Technical Report 32-1108. Jet Propulsion Laboratory, Pasadena, Calif., Aug. 1, 1967.

O'Neil, W. J., et al., *The Surveyor III and Surveyor IV Flight Paths and Their Determination From Tracking Data,* Technical Report 32-1292. Jet Propulsion Laboratory, Pasadena, Calif., Aug. 15, 1968.

Pease, G. E., et al., *The Mariner V Flight Path and Its Determination From Tracking Data,* Technical Report 32-1363. Jet Propulsion Laboratory, Pasadena, Calif., July 1, 1969.

Renzetti, N. A., *Tracking and Data Acquisition for Ranger Missions I–V,* Technical Memorandum 33-174. Jet Propulsion Laboratory, Pasadena, Calif., July 1, 1964.

Renzetti, N. A., *Tracking and Data Acquisition for Ranger Missions VI–IX,* Technical Memorandum 33-275. Jet Propulsion Laboratory, Pasadena, Calif., Sept. 15, 1966.

Renzetti, N. A., *Tracking and Data Acquisition Support for the Mariner Venus 1962 Mission,* Technical Memorandum 33-212. Jet Propulsion Laboratory, Pasadena, Calif., July 1, 1965.

Renzetti, N. A., *Tracking and Data Acquisition Report, Mariner Mars 1964 Mission: Near-Earth Trajectory Phase,* Technical Memorandum 33-239, Vol. I. Jet Propulsion Laboratory, Pasadena, Calif., Jan. 1, 1965.

Renzetti, N. A., *Tracking and Data Acquisition Report, Mariner Mars 1964 Mission: Cruise to Post-Encounter Phase,* Technical Memorandum 33-239, Vol. II. Jet Propulsion Laboratory, Pasadena, Calif., Oct. 1, 1967.

Renzetti, N. A., *Tracking and Data Acquisition Report, Mariner Mars 1964 Mission: Extended Mission,* Technical Memorandum 33-239, Vol. III. Jet Propulsion Laboratory, Pasadena, Calif., Dec. 1, 1968.

Renzetti, N. A., *Tracking and Data System Support for Surveyor: Missions I and II,* Technical Memorandum 33-301, Vol. I. Jet Propulsion Laboratory, Pasadena, Calif., July 15, 1969.

Renzetti, N. A., *Tracking and Data System Support for Surveyor: Missions III and IV,* Technical Memorandum 33-301, Vol. II. Jet Propulsion Laboratory, Pasadena, Calif., Sept. 1, 1969.

Renzetti, N. A., *Tracking and Data System Support for Surveyor: Mission V,* Technical Memorandum 33-301, Vol. III. Jet Propulsion Laboratory, Pasadena, Calif., Dec. 1, 1969.

Bibliography (contd)

Renzetti, N. A., *Tracking and Data System Support for Surveyor: Mission VI,* Technical Memorandum 33-301, Vol. IV. Jet Propulsion Laboratory, Pasadena, Calif., Dec. 1, 1969.

Renzetti, N. A., *Tracking and Data System Support for Surveyor: Mission VII,* Technical Memorandum 33-301, Vol. V. Jet Propulsion Laboratory, Pasadena, Calif., Dec. 1, 1969.

Renzetti, N. A., *Tracking and Data System Support for the Mariner Venus 67 Mission: Planning Phase Through Midcourse Maneuver,* Technical Memorandum 33-385, Vol. I. Jet Propulsion Laboratory, Pasadena, Calif., Sept. 1, 1969.

Renzetti, N. A., *Tracking and Data System Support for the Mariner Venus 67 Mission: Midcourse Maneuver Through End of Mission,* Technical Memorandum 33-385, Vol. II. Jet Propulsion Laboratory, Pasadena, Calif., Sept. 1, 1969.

Renzetti, N. A., *Tracking and Data System Support for the Pioneer Project. Pioneer VI. Prelaunch to End of Nominal Mission,* Technical Memorandum 33-426, Vol. I. Jet Propulsion Laboratory, Pasadena, Calif., Feb. 1, 1970.

Renzetti, N. A., *Tracking and Data System Support for the Pioneer Project. Pioneer VII. Prelaunch to End of Nominal Mission,* Technical Memorandum 33-426, Vol. II. Jet Propulsion Laboratory, Pasadena, Calif., Apr. 15, 1970.

Renzetti, N. A., *Tracking and Data System Support for the Pioneer Project. Pioneer VIII. Prelaunch Through May 1968,* Technical Memorandum 33-426, Vol. III. Jet Propulsion Laboratory, Pasadena, Calif., July 15, 1970.

Renzetti, N. A., *Tracking and Data System Support for the Pioneer Project. Pioneer IX. Prelaunch Through June 1969,* Technical Memorandum 33-426, Vol. IV. Jet Propulsion Laboratory, Pasadena, Calif., Nov. 15, 1970.

Renzetti, N. A., *Tracking and Data System Support for the Pioneer Project. Pioneer VI. Extended Mission: July 1, 1966–July 1, 1969,* Technical Memorandum 33-426, Vol. V. Jet Propulsion Laboratory, Pasadena, Calif., Feb. 1, 1971.

Renzetti, N. A., *Tracking and Data System Support for the Pioneer Project. Pioneer VII. Extended Mission: February 24, 1967–July 1, 1968,* Technical Memorandum 33-426, Vol. VI. Jet Propulsion Laboratory, Pasadena, Calif., Apr. 15, 1971.

Renzetti, N. A., *Tracking and Data System Support for the Pioneer Project. Pioneer VII. Extended Mission: July 1, 1968–July 1, 1969,* Technical Memorandum 33-426, Vol. VII. Jet Propulsion Laboratory, Pasadena, Calif., Apr. 15, 1971.

Renzetti, N. A., *Tracking and Data System Support for the Pioneer Project. Pioneer VIII. Extended Mission: June 1, 1968–July 1, 1969,* Technical Memorandum 33-426, Vol. VIII. Jet Propulsion Laboratory, Pasadena, Calif., May 1, 1971.

Renzetti, N. A., *Tracking and Data System Support for the Pioneer Project. Pioneers VI–IX. Extended Missions: July 1, 1969–July 1, 1970.* Technical Memorandum 33-426, Vol. IX. Jet Propulsion Laboratory, Pasadena, Calif., Aug. 15, 1971.

Sjogren, W. L., *The Ranger III Flight Path and Its Determination From Tracking Data,* Technical Report 32-563. Jet Propulsion Laboratory, Pasadena, Calif., Sept. 15, 1965.

Sjogren, W. L., et al., *The Ranger V Flight Path and Its Determination From Tracking Data*, Technical Report 32-562. Jet Propulsion Laboratory, Pasadena, Calif., Dec. 6, 1963.

Sjogren, W. L., et al., *The Ranger VI Flight Path and Its Determination From Tracking Data*, Technical Report 32-605. Jet Propulsion Laboratory, Pasadena, Calif., Dec. 15, 1964.

Sjogren, W. L., et al., *Physical Constants as Determined From Radio Tracking of the Ranger Lunar Probes*, Technical Report 32-1057. Jet Propulsion Laboratory, Pasadena, Calif., Dec. 30, 1966.

Sjogren, W. L., *Proceedings of the JPL Seminar on Uncertainties in the Lunar Ephemeris*, Technical Report 32-1247. Jet Propulsion Laboratory, Pasadena, Calif., May 1, 1968.

Sjogren, W. L., "Lunar Gravity Estimate: Independent Confirmation," *J. Geophys. Res.*, Vol. 76, No. 29, Oct. 10, 1971.

Spier, G. W., "Design and Implementation of Models for the Double Precision Trajectory Program (DPTRAJ)," Technical Memorandum 33-451, Jet Propulsion Laboratory, Pasadena, Calif., Apr. 15, 1971.

Stelzried, C. T., *A Faraday Rotation Measurement of a 13-cm Signal in the Solar Corona*, Technical Report 32-1401. Jet Propulsion Laboratory, Pasadena, Calif., July 15, 1970.

Stelzried, C. T., et al., "The Quasi-Stationary Coronal Magnetic Field and Electron Density as Determined From a Faraday Rotation Experiment," *Sol. Phys.*, Vol. 14, No. 2, pp. 440–456, Oct. 1970.

Thornton, J. H., Jr., *The Surveyor I and Surveyor II Flight Paths and Their Determination From Tracking Data*, Technical Report 32-1285. Jet Propulsion Laboratory, Pasadena, Calif., Aug. 1, 1968.

Vegos, C. J., et al., *The Ranger IX Flight Path and Its Determination From Tracking Data*, Technical Report 32-767. Jet Propulsion Laboratory, Pasadena, Calif., Nov. 1, 1968.

Winn, F. B., *Selenographic Location of Surveyor VI, Surveyor VI Mission Report: Part II. Science Results*, Technical Report 32-1262. Jet Propulsion Laboratory, Pasadena, Calif., Jan. 10, 1968.

Winn, F. B., "Post Landing Tracking Data Analysis," in *Surveyor VII Mission Report: Part II. Science Results*, Technical Report 32-1264. Jet Propulsion Laboratory, Pasadena, Calif., Mar. 15, 1968.

Winn, F. B., "Post Lunar Touchdown Tracking Data Analysis," in *Surveyor Project Final Report: Part II. Science Results*, Technical Report 32-1265. Jet Propulsion Laboratory, Pasadena, Calif., June 15, 1968.

Winn, F. B., *Surveyor Posttouchdown Analyses of Tracking Data*, NASA SP-184. National Aeronautics and Space Administration, Washington, D.C., p. 369.

Wollenhaupt, W. R., et al., *The Ranger VII Flight Path and Its Determination From Tracking Data*, Technical Report 32-694. Jet Propulsion Laboratory, Pasadena, Calif., Dec. 15, 1964.

NASA — JPL — Coml., L.A., Calif.